Kinetic and Spectroscopic Studies of Atmospheric Intermediates

Thesis by

Matthew David Smarte

In Partial Fulfillment of the Requirements for

the degree of

Doctor of Philosophy

CALIFORNIA INSTITUTE OF TECHNOLOGY

Pasadena, California

2019

(Defended May 29, 2019)

© 2019

Matthew David Smarte
ORCID: 0000-0002-4835-7880

To my grandmother, Mom-Mom

Acknowledgements

As a steadfast procrastinator, I wrote this section of the thesis last. I was worried about being unable to find the perfect words to accurately acknowledge each person who has supported me throughout my graduate education. But it eventually became clear that such a task is impossible: there exist no words that can adequately capture the enormous gratitude I have to all who have helped me on this journey.

I would first like to acknowledge the three people who have had the most substantial impact on my scientific career thus far: Professors Amy Mullin (University of Maryland), Ross Salawitch (University of Maryland), and Mitchio Okumura (California Institute of Technology). I thank Amy for introducing me to the wonders of research as a freshman and for developing my fascination with the field of chemical physics. I thank Ross for impressing upon me the importance of the problems facing our environment and for introducing me to the field of atmospheric chemistry. I thank Mitchio, my adviser, for providing an amazing graduate research program that has allowed me to simultaneously pursue my passion for both disciplines.

I would also like to acknowledge the members of my thesis committee, who have provided invaluable guidance over the years through meetings and exams: Paul Wennberg, Brian Stoltz, and Rudy Marcus (chair).

The experiments in Chapters 2 and 4 of this thesis would not have been possible without an extensive collaboration between the Okumura group and scientists at the NASA Jet Propulsion Laboratory (JPL) and Sandia National Laboratories. Stan Sander, leader of the JPL effort, has been an incredibly helpful source of knowledge on free radical chemistry. David Osborn and Craig Taatjes, leaders of the Sandia effort, have constructed a powerful instrument for the study of chemical kinetics. I was extremely fortunate to use their spectrometer across six trips to the Advanced Light Source (ALS) synchrotron.

I have learned so much from working with many members of the Okumura group over the years: Thinh Bui, Laura Mertens, Linhan Shen, Aileen Hui, Elizabeth Lunny, Gautam Stroscio, Joey Messinger, Greg Jones, Doug Ober, Hannah Szentkuti, Matt Cich, Damien Amedro, Luis Gomez, Tzu Ling Chen, Robin Miri, Caitlin Bray, Daniel Hogan, Gregory Rassolov, Camilla Kjeldbjerg, Cristina Alonso, and Denh Vuong – it has been a

privilege to be your colleague. In particular, I would like to highlight Greg Jones, who made contributions to the analysis described in Chapters 2 and 4 and Appendix C.

Many staff members in the CCE and GPS divisions have played important roles in enabling these research efforts. In CCE, I would like to acknowledge Alison Ross, Agnes Tong, Monica Brito, Elisha Okawa, and Elisa Brink. In GPS, I would like to acknowledge Kathy Young, Kathy Bravo, Bronagh Glaser, and Nora Oshima. I am convinced that Linde Robinson Laboratory is held together by the hard work and dedication of Nora.

I have shared an office in Linde Robinson with two generations of graduate students. Each generation was predominantly comprised of members of the Wennberg group: Kat Saad, Alex Teng, Becky Schwantes, Kelvin Bates, Jacob Hedelius, Harrison Parker, and Ariana Tribby. The Wennberg group performs laboratory studies of atmospheric chemistry using different methods than those used in my research. I learned much from discussing our respective approaches, as well as from our interesting conversations about science policy and higher education.

Throughout graduate school, I have been an active member of the Graduate Honor Council (GHC), serving as the co-chair for three years. In addition to upholding academic integrity, this group partakes in conversations and debates surrounding scholarly topics such as scientific ethics and plagiarism. Being a member of the GHC was one of the most enriching experiences I had at Caltech. I worked with some amazing people: my fellow co-chairs, Rob Craig and Sarah Del Ciello, and our advisers in the administration, Joe Shepherd and Felicia Hunt. Caltech would not be the same without Felica.

I have had the support of some great friends over the past several years. Many meals were shared with Crystal Chu. Many glasses of wine were consumed with Linhan Shen. Many text messages were exchanged with Alice Kunin. And many adventures were embarked upon during my incredible summer in Boulder with Abby Powell. I would particularly like to acknowledge Keith Spangler, Phylicia Kimmel, and Emma Newell, friends who I have known since eighth grade. These three individuals hold a special place in my heart and have shaped the person I am today. I could not have made it through graduate school without their friendship and unwavering support.

I have had a second family at Caltech through my roommates Annet Blom and Marcus Low, as well as our honorary roommates Asher Tenn-McClellan and Matt Rienzo.

We have lived together for five years and gone on some amazing adventures, including a trip across the world to Amsterdam. Between dim sum outings, game nights, evening drinks, and binging television shows – no other roommates will ever come close.

My time in the Okumura group would not have been the same without two particular individuals: Aileen Hui and Elizabeth Lunny. Aileen – you are the hardest-working person I know. You inspire me to be a better scientist every day. I could not have gotten through the ALS shifts without you. I will always treasure the Law & Order marathons, boba outings, ramen trips, escape rooms, and all the other activities we have enjoyed. Elizabeth – I truly do not know where to begin. We have been together in this crazy graduate school adventure since the first momentous day we met at orientation. You have saved me so many times, more than I can remember, although I am sure you can use your uncannily good memory to remind me. Graduate school was hard at times, but your friendship made even the toughest moments okay. I am going to miss the weekly meals at our favorite restaurant of the season, the near-daily Dunkin' or boba runs, and the frequent chats. But I look forward to visiting you in Boston and continuing our debates.

I would like to thank my family for their continuous encouragement: my mother and father, Kathy and David, my brother and sister-in-law, Mike and Jordan, and my nephew and niece, Carter and Kenley. Aunt Dotsy, Uncle Chris, and many other family members have also cheered for me over the years. *This thesis is dedicated to my late grandmother, Mom-Mom, who was always my biggest supporter.*

Finally, I would like to acknowledge our sources of funding. My participation in these projects was funded by an NSF Graduate Research Fellowship and a NASA Earth and Space Science Fellowship (NNX16AO36H). The research described in Chapter 2 was funded by the NASA Upper Atmospheric Research Program (NNX12AE01G). The research described in Chapters 3 and 4 was funded by the National Science Foundation (CHE-1413712). Parts of this work used resources of the Advanced Light Source, which is a DOE Office of Science User Facility under Contract No. DE-AC02-05CH11231. Parts of this work used the Extreme Science and Engineering Discovery Environment (XSEDE), which is supported by National Science Foundation Grant No. ACI-1548562.

Abstract

Atmospheric chemistry investigates the chemical transformations of atmospheric trace constituents through three complementary approaches: field observations, laboratory experiments, and computational modeling. This thesis used the laboratory experiment approach to explore persistent unknowns associated with free radical chemistry in the troposphere and stratosphere. Studies were conducted using two powerful techniques for the study of chemical kinetics: multiplexed synchrotron photoionization mass spectrometry and cavity ringdown spectroscopy.

In the first part of this thesis, we describe experiments measuring of the absolute photoionization cross sections of chlorine monoxide (ClO) and chlorine dioxide (ClOOCl). The cross sections of ClO were found to be at least a factor of three greater than a prior determination and those of ClOOCl were measured for the first time. ClO and ClOOCl play important roles in the catalytic destruction of polar stratospheric ozone and yet values of the parameters controlling the rate of atmospheric ClOOCl photolysis are uncertain. Our results show that photoionization spectroscopy is highly sensitive to the ClO radical and may be ideally suited for future experiments constraining the quantum yields of ClOOCl photolysis at wavelengths of relevance to the polar stratosphere.

We next discuss experiments investigating the kinetics of chlorine-substituted peroxy radicals ($ClRO_2$). These species are formed in the troposphere upon oxidation of alkenes by chlorine atoms. We present rate constants for the formation and loss pathways of the simplest intermediate in this class: the β-chloroethyl peroxy radical. We also discuss measurements of the rate constants between NO and the $ClRO_2$ formed upon oxidation of ethene, propene, 1-butene, 2-butene, 1,3-butadiene, and isoprene.

Finally, we present results exploring the impact of temperature and humidity on the chemistry of hydroxyl-substituted peroxy radicals ($HORO_2$). In particular, the self reaction of the β-hydroxyethyl peroxy radical was investigated and found to be significantly enhanced by water vapor at cold temperatures. The product branching ratio was also studied and found to shift in favor of radical suppression. Given the prevalence of water vapor throughout the troposphere, altered reactivity of $HORO_2$–H_2O complexes likely plays an important role in atmospheric oxidation mechanisms.

Published Content and Contributions

Wennberg, P.O.; Bates, K.H.; Crounse, J.D.; Dodson, L.G.; McVay, R.C.; Mertens, L.A.; Nguyen, T.B.; Praske, E.; Schwantes, R.H.; Smarte, M.D.; St Clair, J.M.; Teng, A.P.; Zhang, X.; Seinfeld, J.H. "Gas-Phase Reactions of Isoprene and Its Major Oxidation Products," *Chemical Reviews*, **2018**, *118*, 3337–3390, doi: 10.1021/acs.chemrev.7b00439.

M.D.S. wrote the section on oxidation of isoprene by chlorine radicals.

Table of Contents

List of Illustrations and Tables

Chapter 2: Absolute Photoionization Cross Sections of ClO and ClOOCl

Figures

Tables

Chapter 3: Kinetics of Chlorine-Substituted Peroxy Radicals

Figures

Tables

Chapter 4: Water Vapor Dependence of the β-Hydroxyethyl Peroxy Self Reaction

Figures

Appendix B: Kinetics and Spectroscopy of the Acetonyl Peroxy Radical

Figures

Appendix C: Photoionization Cross Sections of Some Atmospheric Molecules

Figures

Tables

Appendix D: Cold Reactor Temperature Measurements

Figures

Tables

This page intentionally left blank.

Chapter 1

Introduction

Human activity has a substantial impact on the atmosphere of Earth. The globally averaged concentration of carbon dioxide, a chemical agent most notorious for its role in climate change, has increased by 40% since the Industrial Revolution.[1] Major cities have also experienced regular episodes of debilitating photochemical smog since that time. Even today, premature deaths associated with particulate matter and ozone are estimated to occur at a rate of 4,000,000 deaths per year.[2] Addressing the issues of global warming and air pollution requires a detailed understanding of the physical, chemical, and radiative properties of the trace constituents of the atmosphere. Scholarly research on these topics has informed major policy achievements such as the Montreal Protocol and various clean air regulations throughout the world. But more work remains to be done.

The field of atmospheric chemistry investigates the photochemical transformations of atmospheric constituents through three complementary approaches: observations, laboratory experiments, and computational modeling. Observations, performed both in the field and remotely, measure the composition of the atmosphere. Laboratory experiments, performed under controlled environments, constrain the parameters that dictate the rates of chemical transformations. Models constructed from computer code implementing these parameters tie the picture together: when simulations of atmospheric composition match observations, an improved understanding of the atmosphere is achieved.

This thesis describes research using the laboratory experiment approach to investigate the kinetic and spectroscopic properties of atmospheric intermediates. Two methodologies are employed: multiplexed synchrotron photoionization mass spectrometry (MPIMS) and cavity ringdown spectroscopy (CRDS). MPIMS is a versatile technique for the study of chemical kinetics and has recently seen increasing application to problems in atmospheric and combustion chemistry. This technique has the unique ability to simultaneously observe many atmospheric intermediates and distinguish them through multiplexed detection of mass-to-charge ratio, kinetic reaction time, and photoionization efficiency.[3,4] CRDS has been applied to the study of atmospheric chemistry for several

decades, although novel variants with ever-lower detection limits continue to be developed. This approach uses an optical cavity formed by highly reflective mirrors to generate long absorption pathlengths capable of detecting atmospheric constituents of very low concentration.[5] Both MPIMS and CRDS are powerful tools for laboratory studies of atmospheric chemistry.

In Chapter 2, we present studies measuring the absolute photoionization cross sections of ClO and ClOOCl using MPIMS. The catalytic cycling of ClO between its monomer and dimer is responsible for a substantial fraction of polar stratospheric ozone loss.[6] However, the rate of this cycling depends on the quantum yields of ClOOCl photolysis, which are known at few wavelengths due to challenges associated with sensitively measuring small changes in ClO and ClOOCl. Photoionization spectroscopy is particularly sensitive toward the detection of halogenated species and may be an ideal technique to determine the first quantum yields of ClOOCl photolysis longwave of 308 nm. We describe experiments that lay the groundwork for this effort by measuring the absolute photoionization cross sections of ClO and ClOOCl. These key spectroscopic parameters are necessary to convert measurements of their ion signals to absolute concentrations.

In Chapters 3 and 4, we present studies measuring the kinetics of organic peroxy radicals that are of relevance to the troposphere using both CRDS and MPIMS. Peroxy radicals are ubiquitous atmospheric intermediates that form in the oxidation of nearly every volatile organic compound.[7] Their diverse fates have the potential to propagate or terminate free radical chemistry in an oxidation mechanism, thereby dictating the extent of pollutant formation. Chlorine radicals serve as an important tropospheric oxidant in marine and coastal regions and react with alkenes to yield chlorine-substituted peroxy radicals; the kinetics of these species have not been the subject of extensive study. Similarly, little is known about the reactivity of organic peroxy radicals under humid conditions, which are prevalent throughout the troposphere. We investigate these topics in this thesis.

The author hopes that the results presented are of use to the atmospheric chemistry community and inspire future studies that improve our understanding of the atmosphere.

(1) Stocker, T. Climate Change 2013: The Physical Science Basis: Working Group I Contribution to the Fifth Assessment Report of the Intergovernmental Panel on Climate Change; Cambridge University Press, 2014.

(2) Anenberg, S. C.; Miller, J.; Minjares, R.; Du, L.; Henze, D. K.; Lacey, F.; Malley, C. S.; Emberson, L.; Franco, V.; Klimont, Z.; et al. Impacts and Mitigation of Excess Diesel-Related NO_x Emissions in 11 Major Vehicle Markets. Nature **2017**, 545 (7655), 467–471. https://doi.org/10.1038/nature22086.

(3) Osborn, D. L.; Zou, P.; Johnsen, H.; Hayden, C. C.; Taatjes, C. A.; Knyazev, V. D.; North, S. W.; Peterka, D. S.; Ahmed, M.; Leone, S. R. The Multiplexed Chemical Kinetic Photoionization Mass Spectrometer: A New Approach to Isomer-Resolved Chemical Kinetics. Review of Scientific Instruments **2008**, 79 (10), 104103. https://doi.org/10.1063/1.3000004.

(4) Taatjes, C. A.; Hansen, N.; Osborn, D. L.; Kohse-Höinghaus, K.; Cool, T. A.; Westmoreland, P. R. "Imaging" Combustion Chemistry via Multiplexed Synchrotron-Photoionization Mass Spectrometry. Phys. Chem. Chem. Phys. **2008**, 10 (1), 20–34. https://doi.org/10.1039/B713460F.

(5) O'Keefe, A.; Deacon, D. A. G. Cavity Ring-down Optical Spectrometer for Absorption Measurements Using Pulsed Laser Sources. Review of Scientific Instruments **1988**, 59 (12), 2544–2551. https://doi.org/10.1063/1.1139895.

(6) Molina, L. T.; Molina, M. J. Production of Chlorine Oxide (Cl2O2) from the Self-Reaction of the Chlorine Oxide (ClO) Radical. J. Phys. Chem. **1987**, 91 (2), 433–436. https://doi.org/10.1021/j100286a035.

(7) Orlando, J. J.; Tyndall, G. S. Laboratory Studies of Organic Peroxy Radical Chemistry: An Overview with Emphasis on Recent Issues of Atmospheric Significance. Chem. Soc. Rev. **2012**, 41 (19), 6294–6317. https://doi.org/10.1039/C2CS35166H.

This page intentionally left blank.

Chapter 2

Absolute Photoionization Cross Sections of ClO and ClOOCl

The absolute photoionization spectra of chlorine monoxide (ClO) and chlorine peroxide (ClOOCl) have been measured from 10.607 to 11.777 eV. ClO and ClOOCl were generated from the reaction of chlorine radicals with ozone at 210 ± 3 K and their parent ions were detected by multiplexed synchrotron photoionization mass spectrometry. The measured time-dependent photoion signals were fit to a chemical kinetic model simulating the absolute concentrations of ClO and ClOOCl. Their photoionization cross sections were determined relative to the cross sections of methyl bromide, which were also measured in this work. For ClO, we measured σ(11.083 eV) = 7.4 ± 1.7 Mb, σ(11.174 eV) = 11.2 ± 2.6 Mb, and σ(11.315 eV) = 22.0 ± 5.0 Mb. For ClOOCl, we measured σ(11.083 eV) = 1.13 ± 0.43 Mb, σ(11.174 eV) = 2.46 ± 0.97 Mb, and σ(11.315 eV) = 10.4 ± 4.1 Mb. The uncertainties represent ± 2 standard errors. Absolute spectra were obtained by scaling a relative spectrum recorded with 9.7 meV resolution and 10 meV steps to match the cross sections determined at individual energies. The photoionization cross sections of ClO derived from our results are at least a factor of three greater than a prior determination. The photoionization cross sections of ClOOCl were measured for the first time in this work. A new explanation is proposed for the formation of the $OClO^+$ daughter ion from the dissociative photoionization of ClOOCl.

2.1 Introduction

Photoionization mass spectrometry (PIMS) has become a common tool for the study of gas-phase photochemistry and chemical kinetics, with increasing application to problems in the fields of combustion and atmospheric chemistry.[1–9] The ability of this technique to quantify the concentration of a detected species requires accurate knowledge of its absolute photoionization cross sections. For many species of interest, such as transient radical intermediates or thermally unstable compounds, experimental measurements of cross sections are difficult due to challenges associated with generating a target species with an independently known concentration. A goal of theoretical studies has been to develop computational methods for the accurate prediction of photoionization cross sections,[10–12] which could potentially alleviate the need for experimental determinations of these values in the future. However, current measurements of absolute cross sections of transient species are limited, and additional data over a diverse range of chemical structures are necessary to accurately benchmark computational methods and promote confidence in using theoretical results to support quantitative experiments.

The atmospheric photochemistry of chlorine peroxide (ClOOCl) is an example system for which our understanding may benefit from the accurate knowledge of absolute photoionization cross sections. Formed under the cold conditions of the winter polar stratosphere, ClOOCl participates in a catalytic mechanism that destroys polar ozone:[13]

$$2 \times [Cl + O_3 \rightarrow ClO + O_2] \quad \text{(R1)}$$

$$ClO + ClO + M \rightarrow ClOOCl + M \quad \text{(R2)}$$

$$ClOOCl + h\nu \rightarrow ClOO + Cl \quad \text{(R3a)}$$

$$ClOO + M \rightarrow Cl + O_2 + M \quad \text{(R4)}$$

$$\textbf{Net:}\ O_3 + O_3 + h\nu \rightarrow O_2 + O_2 + O_2 \quad \text{(R5)}$$

R3a is the rate-limiting step of the mechanism and therefore the photolysis of ClOOCl has been the subject of many studies. Uncertainty over the magnitude of its UV absorption cross sections limits our ability to accurately model polar ozone depletion and the future recovery of the ozone layer. In particular, the value of the cross section at the peak of the UV spectrum (~245 nm) is commonly used to place relative absorption spectra onto an absolute scale.[14–19] Using a molecular beam of ClOOCl and mass-resolved detection, Lien et al. recently measured the cross section at 248.4 nm without the potential of impurity

interference for the first time.[20] However, their value exceeds prior determinations by 15–40%,[21–24] translating into uncertainty on the overall rate of atmospheric ClOOCl photolysis. Uncertainties also exist on the quantum yield of R3a. In competition is an additional photolysis channel that results in a null cycle for ozone loss:

$$\mathrm{ClOOCl} + h\nu \rightarrow \mathrm{ClO} + \mathrm{ClO} \qquad \text{(R3b)}$$

The actinic flux in the polar stratosphere rapidly rises above 300 nm, and therefore most atmospheric ClOOCl photolysis occurs over ~300–450 nm.[25] Laboratory measurements of R3a and R3b quantum yields in this region are difficult due to small ClOOCl cross sections yielding minute Δ[ClO] and Δ[ClOOCl] that are challenging to detect. In fact, there have been no published measurements of these quantum yields longwave of 308 nm, and the most recent NASA Jet Propulsion Laboratory data evaluation recommends wavelength-independent yields above 300 nm of 0.8 and 0.2 for R3a and R3b, respectively.[26] The limited quantum yield data at wavelengths of atmospheric ClOOCl photolysis inhibits our ability to accurately predict the extent of polar ozone depletion from this mechanism.

Molecules with halogen functionality typically have large near-threshold photoionization cross sections, and therefore PIMS may be an ideal technique to constrain uncertainties associated with the R1–R5 mechanism. The ability of PIMS to sensitively measure small Δ[ClO] and Δ[ClOOCl] depends on the magnitude of the ClO and ClOOCl photoionization cross sections. Flesch et al. measured a ClO to ClO^+ cross section of 24 ± 5 Mb at 13.74 eV and used this to place a relative photoionization spectrum from their prior work onto an absolute scale.[27,28] However, their absolute spectrum exhibits an offset of ~5 Mb below the ClO ionization threshold due to higher harmonic light, and introduces uncertainty on the cross sections in the near-threshold region. A ClO to ClO^+ cross section of 15 ± 2 Mb at 11.5 eV has separately been reported,[29] but the details of this determination were never published. To our knowledge, there have been no photoionization cross sections of ClOOCl reported in the literature. Accurate values of near-threshold photoionization cross sections for ClO and ClOOCl are necessary to support PIMS experiments investigating ClOOCl photochemistry. Such measurements may also act as useful benchmarks for theoretical studies involving spectral features over which cross sections are challenging to calculate: the spectrum of ClO exhibits a high density of

resonances from excitation to autoionizing Rydberg states,[30] and the spectrum of ClOOCl has a gradual onset likely due to poor Franck-Condon overlap between the torsional modes of ClOOCl and those of $ClOOCl^+$.

Other photoionization studies of ClO and ClOOCl have focused on measuring their relative photoionization efficiency curves to determine ionization energies (IE). Thorn et al. used PIMS to measure an IE of 10.847 ± 0.016 eV for ClO ($X^3\Sigma^- \leftarrow X^2\Pi_{1/2}$) and 10.885 ± 0.016 eV for ClO ($X^3\Sigma^- \leftarrow X^2\Pi_{3/2}$).[30] These are in excellent agreement with the photoelectron studies of Bulgin et al., who measured 10.83 ± 0.01 eV and 10.87 ± 0.01 eV for the two respective spin-orbit states.[31,32] Schwell et al. used PIMS to measure spectra of both ClO (IE = 10.85 ± 0.05 eV) and ClOOCl (IE = 11.05 ± 0.05 eV).[28] Their resolution was insufficient to resolve the spin-orbit splitting in ClO. Two daughter ions of dissociative ClOOCl photoionization have been observed: a structure with formula ClO_2^+ appearing at 10.95 ± 0.1 eV,[28] and ClO^+ appearing at 11.52 ± 0.025 eV.[33] In a separate PIMS study, Plenge et al. photolyzed ClOOCl at 250 and 308 nm in an attempt to measure the quantum yields of R3a and R3b.[29] They observed no formation of ClO^+ at either wavelength and placed upper bounds on the quantum yield of R3b. However, their results disagree with studies using photofragment translational spectroscopy, which have observed R3b yields in the range of ~0.1–0.2 at the same wavelengths.[34,35] The bounds reported in the PIMS study are ultimately limited by uncertainty on the ClO photoionization cross section assumed.

In the present work, we have measured near-threshold photoionization cross sections of ClO and ClOOCl at 11.083, 11.174, and 11.315 eV. Relative photoionization spectra, collected with greater resolution and smaller step sizes than prior studies, are scaled to the single energy cross sections to yield absolute photoionization spectra. Cross sections are determined through generation of ClO and ClOOCl by pulsed laser photolysis and comparing their observed time-resolved ion signals to concentration profiles predicted by a chemical kinetic model. This method of employing detailed kinetic modeling to determine photoionization cross sections of transient species has been used by our group previously.[36,37] Our results for ClO differ substantially from the only absolute spectrum previously published.[27] To our knowledge, these results represent the first determination of the photoionization cross sections of ClOOCl.

2.2 Experimental Methods

Details of the multiplexed photoionization mass spectrometer (MPIMS) used in these experiments have been described previously.[38,39] A UV excimer laser pulse is propagated along the flow axis of a cylindrical chemical reactor to initiate radical chemistry. The reacting gas mixture is sampled into a vacuum chamber through a pinhole on the side of the reactor. Neutrals are expanded and skimmed to form a molecular beam intersected by quasi-continuous (500 MHz) tunable vacuum ultraviolet (VUV) light from a synchrotron. The resulting cations are extracted into a 50 kHz orthogonal-acceleration time-of-flight mass spectrometer ($m/\Delta m \approx 1200$) and counted by microchannel plates. Every 10 mass spectra are binned to yield time-resolved ion signals with 200 μs spacing. By scanning the frequency of VUV light, multiplexed datasets of ion counts as a function of m/z, reaction time, and photoionization energy are recorded.

Experiments were conducted at the Advanced Light Source of Lawrence Berkeley National Laboratory using VUV radiation from the Chemical Dynamics Beamline. Most experiments used photon energies in the range of 9–12 eV and higher harmonics were removed by a windowless gas filter (~30 Torr of Ar) upstream of the ionization region.[40,41] A monochromator yielded narrow bandwidth radiation that was typically varied over ΔE_{FWHM} = 10–40 meV. The ability to perform measurements over a range of energy resolutions was of central importance to the present work. The spectral lineshape of photons transmitted by the monochromator was measured by scanning over the 8s ← 5p atomic transition of Xe at 12.5752 eV.[42] The broadening of this line is entirely instrument-limited and the spectra were empirically fit to calibrate ΔE_{FWHM} of the VUV light at each slit width (additional details provided in Supplementary Material SM1). The observed position of this line was also used to establish an absolute energy axis.

The low temperature reactor used in these experiments is based on a prototype described previously.[43] The reactor was constructed of two concentric stainless steel tubes. Coolant was flown through the region between the inner tube (ϕ 1/2") and outer tube (ϕ 3/4") to cool the reactant gases flown within the inner tube. A section of the outer tube was cut orthogonal to the flow axis and welded to the inner tube, exposing a small region of the inner tube outer surface to the vacuum chamber. A 300 μm countersunk pinhole was drilled into the inner tube at this location and aligned with the skimmer. This approach

allowed almost all of the inner tube outer surface to be in contact with coolant, while also allowing the process gas to be sampled. The interior surface of the inner tube was coated with a halocarbon wax to mitigate wall loss.

The coolant was dry house nitrogen flown through copper coils immersed in liquid nitrogen. Prior to entering the vacuum chamber, the nitrogen passed through a second set of copper coils wrapped in heating tape. The coolant temperature (T = 181.2 ± 0.7 K) was monitored with a thermocouple and stabilized using feedback from a PID controller to cycle power to the heating tape. A second thermocouple, located within the inner tube ~2" downstream of the pinhole, continuously recorded the *in situ* temperature of the process gas during experiments. The thermal mass of the reactor buffered the process gas from fluctuations in coolant temperature, allowing the measured gas temperature to be stabilized to T = 210.2 ± 0.1 K. The temperature range was greater, however, due to a slight inhomogeneity along the flow axis. A variable length thermocouple probe was translated through the reactor under typical experiment conditions to measure the temperature gradient. The range above the pinhole was found to be less than 6 K over a tube length corresponding to 60 ms of reaction time. We therefore report T = 210 ± 3 K for the low temperature experiments and restricted all kinetic analysis to $t \leq 60$ ms. In the room temperature experiments, the vacuum chamber acted as a buffer from ambient laboratory temperature changes, and therefore only a slow flow of house nitrogen was used without cooling or stabilization. We report T = 300.6 ± 0.9 K for the room temperature experiments from fluctuations in the *in situ* gas temperature recorded across these scans.

The reactant gas mixture was comprised of 4.5% O_2, 0.03–0.11% Cl_2, 220–280 ppm O_3, and 1–9 ppm CH_3Br (photoionization cross section reference gas) in a balance of He. The total pressure in the reactor was maintained at P = 50.00 ± 0.25 Torr. Ozone was generated by flowing oxygen through a commercial ozonizer employing a corona discharge. Most of the O_2/O_3 flow was sent to exhaust while a portion was routed through an absorption cell upstream of the reactant gas mixing region. The ozone concentration was measured using a Hg pen-ray lamp and PMT detector to monitor its 254 nm absorption. I_t was measured during each scan and I_0 was periodically recorded between experiments by turning off the corona discharge. Photochemistry was initiated by an unfocused 351 nm excimer laser pulse (~24 mJ cm^{-2}, 4 Hz) to photolyze Cl_2. Typically, ~0.8% of Cl_2

molecules dissociated to yield $[Cl]_0 \approx 10^{13}$ atoms cm^{-3} (experiments to determine the precise Cl_2 photolysis fraction are described in the next section). The total flow rate within the reactor was set to 1250 and 1500 sccm at 300 and 210 K, respectively. Complete refreshment of the gas sample between subsequent laser pulses was verified by inspection of the pre-photolysis mass spectra. In separate experiments without photochemistry, the photoionization cross sections of CH_3Br were measured in reference to the known cross sections of propene.[44]

The ion signal measured by this instrument for species i at photoionization energy E and reaction time t can be described according to:[45]

$$S_i(E,t) = \Lambda(E) \cdot \sigma_i(E) \cdot \alpha_i \cdot N_i(t) \cdot f_i \quad \text{(Eqn. 1)}$$

$\Lambda(E)$ is a species-independent, instrumental constant for a particular energy and set of experimental conditions, proportional to the VUV photon flux and number of laser shots averaged.[39] $\sigma_i(E)$ is the absolute photoionization cross section. Only partial cross sections to form the parent cation of the neutral were measured in this work, although relative spectra of some daughter ions will be discussed. α_i is the mass discrimination factor specific to the mass of the detected ion and can be empirically described by a power law function: $\alpha_i = m_i^{\beta}$. The value of β was measured for the combinations of temperature (300 and 210 K) and bath gas composition (4.5% and 0% O_2 in He) used in this work. These experiments were similar to those described previously with this instrument and results are presented in the Supplementary Material (SM2).[45] $N_i(t)$ is the time-dependent concentration of the species in the reactor and f_i is the fractional abundance of the detected isotope. Our strategy for determining photoionization cross sections is similar to our prior work and involves the use of a chemical kinetic model to simulate $N_i(t)$ of the target molecule for comparison to its measured $S_i(E,t)$.[36,37] Several instrument effects must be incorporated into simulations of $N_i(t)$: (1) a temporal offset between the predicted and actual firing of the photolysis laser, (2) broadening of the ion signal time-dependence caused by the Maxwell-Boltzmann velocity distribution of sampled species and the finite transit time between exiting the reactor and detection,[46,47] and (3) a spatial gradient in the initial radical concentration along the reactor flow axis due to slight divergence of the propagated UV photolysis beam. Calibrations of these instrument effects were performed

at 300 and 210 K as described in our prior work using NO_2 photolysis and results are presented in the Supplementary Material (SM3).[36]

2.3 Results

2.3.1 Absolute Photoionization Cross Sections of CH_3Br

When measuring absolute photoionization cross sections with the MPIMS instrument, it is necessary to simultaneously detect a reference molecule of known cross section to calibrate $\Lambda(E)$. In our experiments studying ClO and ClOOCl, we chose CH_3Br as the reference molecule for three of its properties: (1) *Inertness*. The rate of CH_3Br oxidation by Cl is negligible under our conditions and will not interfere with ClO formation. (2) *Large* σ_{CH_3Br}. Because the photoionization cross sections of CH_3Br are large over the target energy range, [CH_3Br] can be minimized while still measuring a strong ion signal. This further suppresses possible interference with ClO and ClOOCl chemistry. (3) *High volatility*. The vapor pressure of CH_3Br is high even at 210 K,[48] thereby reducing its potential loss at the walls of the reactor.

We measured the absolute photoionization cross sections of CH_3Br in reference to the known cross sections of propene.[44] A mixture of these gases was flown through the reactor in a He balance without UV photolysis. The unknown cross sections of a compound ("unk") can be determined from the known cross sections of a reference compound ("ref") by taking the ratio of their measured ion signals:[37,45]

$$\sigma_{\mathrm{unk}}(E) = \sigma_{\mathrm{ref}}(E) \cdot \frac{\alpha_{\mathrm{ref}} f_{\mathrm{ref}}}{\alpha_{\mathrm{unk}} f_{\mathrm{unk}}} \cdot \frac{\langle S_{\mathrm{unk}}(E,t)/N_{\mathrm{unk}}(t)\rangle_{\Delta t}}{\langle S_{\mathrm{ref}}(E,t)/N_{\mathrm{ref}}(t)\rangle_{\Delta t'}} \qquad \text{(Eqn. 2)}$$

where the angle brackets $\langle\ \rangle$ denote an average performed over the time window Δt or $\Delta t'$. If two isotopes of the same species are measured, then the precision can be improved by including both in the calculation (assuming there is negligible difference in cross section between the isotopes) and defining $S_i(E,t) = S_{i,1}(E,t) + S_{i,2}(E,t)$ and $\alpha_i f_i = \alpha_{i,1} f_{i,1} + \alpha_{i,2} f_{i,2}$. For measurements of σ_{CH_3Br}, there is no time-dependence due to the lack of photolysis laser. Ion signals are averaged across all times and concentrations are determined from flow rates and gas tank mixing ratios. Both the $CH_3{}^{79}Br$ (m/z = 94) and $CH_3{}^{81}Br$ (m/z = 96) isotopes were included. We typically used the all ^{12}C isotope of

propene (m/z = 42) but occasionally used the isotope with one ^{13}C (m/z = 43) if signal of the former was saturated. The reference σ_{propene} data were linearly interpolated onto the energy points of our spectra.

The measured absolute photoionization spectrum of CH_3Br to CH_3Br^+ is presented in Figure 1. This spectrum is an average of four spectra taken over ΔE_{FWHM} = 7.8–9.9 meV and at 300 and 210 K. No statistically significant difference in the shape or magnitude of the spectrum was observed between the two temperatures. The uncertainties varied at each energy but were typically ±23% at the ±2σ confidence level, limited by uncertainty on the reference σ_{propene} data (±20%).[44] The spectrum exhibits resonances near its onset but is fairly smooth (small $d\sigma/dE$) above 10.86 eV, which is close to the IE of ClO and below the IE of ClOOCl. This implies that when using CH_3Br as a reference molecule, σ_{CH_3Br} is insensitive to the ΔE_{FWHM} used to measure ClO^+ and $ClOOCl^+$ ion signals. To confirm this, we measured σ_{CH_3Br} at 210 K, ΔE_{FWHM} = 9.9, 18.2, 27.2, and 37.9 meV, and three key energies that will be discussed in greater detail below: 11.083, 11.174, and 11.315 eV. The cross sections at each energy were insensitive to resolution and their averages are also plotted in Figure 1. The shape of our σ_{CH_3Br} spectrum agrees extremely well with a prior report, but is ~14% smaller in magnitude.[49] Tabulated cross sections are provided in the Supplementary Material (SM4).

2.3.2 Relative Photoionization Spectra of ClO and ClOOCl

Initial experiments focused on acquiring relative photoionization spectra of ClO and ClOOCl. Following the UV photolysis of Cl_2, nascent Cl atoms reacted with excess O_3 to yield ClO (R1). In the 210 K experiments, ClO then dimerized to form ClOOCl (R2). The shapes of relative spectra, $S_X^{rel}(E)$, were normalized according to:

$$S_X^{rel}(E) \propto \frac{\sum_{\Delta t} S_X(E,t)}{\sum_{\Delta t} S_{CH_3Br}(E,t)} \cdot \sigma_{CH_3Br}(E) \qquad \text{(Eqn. 3)}$$

where X = ClO or ClOOCl. The values of $\sigma_{CH_3Br}(E)$ were determined in separate experiments as described in the previous section, measured over the same energy domain, at the same temperature, and using a similar ΔE_{FWHM} as the corresponding ClO and ClOOCl spectra. By normalizing their ion signals to the simultaneously measured CH_3Br^+ signal, the shapes of the spectra are referenced to the shape of the CH_3Br spectrum, which

itself is referenced to the shape of the literature propene spectrum.[44] We note that tracking relative changes in VUV photon flux across different energies or experiments is not necessary with this approach, although the accuracy is set by the propene spectrum. We summed signals for the ^{35}ClO (m/z = 51) and ^{37}ClO (m/z = 53) isotopes unless the ^{35}ClO peak was saturated, in which case only the ^{37}ClO isotope was used. We also summed signals for the ^{35}ClOO^{35}Cl (m/z = 102) and ^{35}ClOO^{37}Cl (m/z = 104) isotopes. (The least abundant ^{37}ClOO^{37}Cl isotope was not included due to an interfering species from unrelated experiments contributing to signal at the m/z = 106 mass peak. The contaminant was inert and did not interfere with ClO or ClOOCl chemistry.) Analysis of isotope-specific spectra showed no discernable differences at the energy resolutions and step sizes used in this work.

In Figure 2, we present photoionization spectra of ClO and ClOOCl over a broad energy range at 210 K using a step size of 10 meV. The spectrum of ClO at 300 K was also measured and its shape is identical to that of the 210 K spectrum (Supplementary Material SM5). While the $ClOOCl^+$ signal is smooth over this region, the ClO^+ signal exhibits substantial structure that is significant based on the Poisson ion counting statistics and reproducible across repeated scans. These features, which were also observed by Thorn et al.,[30] likely arise from autoionizing transitions to two separate Rydberg series converging to the $a^1\Delta$ and $b^1\Sigma^+$ states of ClO^+. Additional spectra measured over narrow energy ranges with step sizes of 1–2 meV are presented in Figure 3. In particular, the ClO spectrum recorded over 11.122–11.222 eV (Figure 3a) clearly resolves peaks at 11.152 and 11.201 eV and demonstrates that structure in the broad spectrum arises from resonances. Due to time limitations on the use of synchrotron light, we unfortunately could not acquire spectra over the entire near-threshold region with a sufficiently small step size to resolve each resonance and make definitive spectroscopic assignments.

The value of σ_{ClOOCl} at many points in the ClOOCl spectrum is likely to be constant over a wide range of ΔE_{FWHM} due to the gradual and continuous change of $ClOOCl^+$ signal. However, in the ClO spectrum, identifying ideal energies to measure σ_{ClO} is less straightforward. Determining meaningful photoionization cross sections in a spectrum with a high density of resonances is challenging due to the dependence of the measured cross section on energy resolution. Ideally, one wishes to measure a cross section within

the ionization continuum, where $d\sigma/dE$ is small and the result is less sensitive to ΔE_{FWHM}. Cross sections in the continuum are more likely to be transferrable between different instruments attempting to use photoionization ion signal to accurately quantify concentration.

To help identify points in the ClO spectrum to measure σ_{ClO}, we acquired multiple spectra over the narrow energy ranges while varying ΔE_{FWHM}. These spectra are also presented in Figure 3 and were normalized according to Eqn. 3. Occasionally, it was necessary to change [CH_3Br] or [Cl] between scans to prevent saturation of the CH_3Br^+ or ClO^+ signals. In such cases, additional normalization factors were applied so that ion signals of spectra collected over the same energy range could be compared. The most promising results were collected over 11.122–11.222 eV (210 K: Figure 3ab, 300 K: Supplementary Material SM5). As ΔE_{FWHM} increased over 10–40 meV, the peaks at 11.152 and 11.201 eV broaden, in accordance with the broadening lineshape of VUV photons transmitted by the monochromator. However, there is a valley between the resonances where ion signal is independent of ΔE_{FWHM} and contribution to the signal likely stems from solely the ionization continuum. We therefore opted to measure σ_{ClO} and σ_{ClOOCl} at an energy near the middle of this valley: 11.174 eV.

We also sought to measure cross sections near the broad peak of the ClOOCl spectrum. Experiments using photoionization to detect ClOOCl benefit from targeting this region since $ClOOCl^+$ signal is maximized. While σ_{ClO} may be less valid over this range, our method for determining σ_{ClOOCl} does not require an accurate value of σ_{ClO} at the same energy. Spectra collected over 11.243–11.393 eV are presented in Figure 3cd. The $ClOOCl^+$ signal across the peak is insensitive to ΔE_{FWHM}, demonstrating that this feature represents the underlying photoionization process and is not broadened by our energy resolution. An explanation for the observed maximum is discussed in a later section. There is also a narrow set of energies over which the ClO^+ signal is independent of ΔE_{FWHM}. This is somewhat fortuitous since, as the ΔE_{FWHM} = 9.9 meV trace shows, the ClO spectrum is highly structured over this region with several overlapping resonances. Nevertheless, we selected one of these energies to perform an additional measurement of σ_{ClO} and σ_{ClOOCl}: 11.315 eV. We note that while σ_{ClOOCl} should be very reliable at 11.315 eV, σ_{ClO} may deviate outside of ΔE_{FWHM} = 10–40 meV.

Finally, spectra were acquired over 11.013–11.133 eV (Figure 3ef). We once again attempted to identify an energy for which the ClO^+ signal would be independent of resolution. The valley between the large resonances at 11.019 and 11.113 eV appeared promising from the broad spectrum and potentially within the ionization continuum. However, the narrow spectra revealed a weaker resonance in this valley at 11.071 eV. Unfortunately, time limitations only allowed us to acquire the narrow spectra at ΔE_{FWHM} = 9.9 and 18.2 meV. Ion signal immediately adjacent to the weak resonance appeared insensitive to these resolutions, and therefore 11.083 eV was selected as a third energy for σ_{ClO} and σ_{ClOOCl} measurement.

2.3.3 Absolute Photoionization Cross Sections of ClO and ClOOCl

Our strategy for determining photoionization cross sections is similar to our prior work.[36,37] The time-dependent concentrations of ClO and ClOOCl, $N_{\mathrm{ClO}}(t)$ and $N_{\mathrm{ClOOCl}}(t)$, were simulated using a kinetic model for comparison against their observed time-dependent ion signals, $S_{\mathrm{ClO}}(E,t)$ and $S_{\mathrm{ClOOCl}}(E,t)$. With CH_3Br as an inert reference compound, we then used Eqn. 2 to determine σ_{ClO} and σ_{ClOOCl}.

2.3.3.1 Kinetic Model

The kinetic model for simulating $N_{\mathrm{ClO}}(t)$ and $N_{\mathrm{ClOOCl}}(t)$ was constructed from literature rate constants for ClO_x chemistry and is presented in Table 1. Most rate constants were taken from the NASA Jet Propulsion Laboratory data evaluation,[26] with a few exceptions as noted in the table. The chemistry is initiated by 351 nm photolysis of Cl_2 to generate Cl atoms, which reacted with excess O_3 to yield ClO (R1). At 300 K, ClO was mostly inert over our 60 ms observation timescale. At 210 K, a fraction of the ClO dimerized to form ClOOCl (R2). These two reactions govern the majority of the chemistry in the reactor and the observed ClO^+ and $ClOOCl^+$ signals can be reasonably well-described by only including these processes in the model. However, to ensure accuracy, we also included several less important reaction classes:

- *Bimolecular ClO self reactions.* The rate constants for these processes are slow at 300 K (k < 10^{-14} cm^3 $molc^{-1}$ s^{-1}) and have positive temperature dependencies that have been evaluated down to ~254 K.[26] The values are negligible below this temperature and we therefore omit the reactions from our 210 K model. At 300 K,

the sum of the rate constants is comparable to the pseudo bimolecular dimerization rate constant, although both processes are slow and have only a minor impact on the ClO kinetics.

- *Associations and dissociations.* In addition to dimerization, we also included the termolecular associations of Cl and O_2 to form ClOO, and of ClO and OClO to form Cl_2O_3. ClOO is more important at 210 K, although at both temperatures its lifetime is short with respect to dissociation and any Cl briefly sequestered as ClOO will eventually break apart and react with O_3. Cl_2O_3 is only included in the 300 K model (there is no source of OClO in the 210 K model) and has a similarly rapid dissociation; negligible ion signal for Cl_2O_3 was observed in the mass spectra. In contrast, the dissociation of ClOOCl is extremely slow and effectively irreversible at 210 K.
- *Cl reactions with ClO_x species.* The reactions of Cl atoms with ClOOCl, OClO, and ClOO have fast rate constants ($k \approx 10^{-11}$–10^{-10} cm^3 $molc^{-1}$ s^{-1}). However, Cl atoms have short lifetimes in our reactor ($\tau \approx 200$ μs) and have mostly reacted away by the time ClOOCl or OClO accrue to any appreciable concentration. While Cl and ClOO exist on the same timescale, the peak concentration of ClOO is low ($[ClOO]_{max} < 10^{11}$ molc cm^{-3}) and the products of their reaction, two ClO molecules, are the same as if the two Cl atoms had reacted with O_3.

In addition to these chemical processes, we also incorporated first order rate constants to describe heterogeneous loss of ClO and ClOOCl at the walls of the reactor in the 210 K model.

Several reactions were considered but ultimately omitted from the model at both temperatures. The photolysis of CH_3Br is negligible at 351 nm and its reaction rate with Cl atoms is too slow to compete with R1. CH_3Br is effectively an inert spectator under our conditions, which motivated its selection as the reference molecule. Similarly, the recombination of Cl atoms to form Cl_2 is too slow to be important. Since O_3 is in excess, we considered its reactions with various ClO_x species: ClOOCl, OClO, and ClO. However, the pseudo first order rate constants for these processes were negligible ($k < 0.003$ s^{-1}).

The kinetic model is effectively a system of coupled differential rate equations. We integrated the model from a set of initial concentration conditions using homebuilt Python

(v3.6.1) code employing algorithms from the SciPy (v0.19.0) library.[50] The simulated concentrations were convolved with the instrument effects described previously and then scaled to ion signal units. Using the Levenberg-Marquardt algorithm[51,52] to minimize the residual sum of squares between the observed and simulated ion signals for each detected species, the values of specific parameters in the model were optimized. If the concentration of a species was independently known (typically from its stable pre-photolysis concentration), then its scale factor between concentration and ion signal units, $S_i(E,t)/N_i(t)$, could be calculated and fixed in the model. If the concentration of a species was unknown, then its optimum scale factor over time window Δt, $\langle S_i(E,t)/N_i(t)\rangle_{\Delta t}$, could be fit. This allowed for the determination of σ_{ClO} and σ_{ClOOCl}. The various fits performed in this work are described in greater detail below.

2.3.3.2 Initial Radical Concentrations

The initial conditions for model integration were set by the initial concentrations of species calculated from flow rates and gas tank mixing ratios. In the case of O_3, the initial concentration was determined from its absorption at 254 nm measured upstream of the reactor. Determining the initial Cl atom concentration was less straightforward. While the fraction of Cl_2 photolyzed can be estimated from its UV cross section at 351 nm and a measurement of the laser fluence, in practice this approach leads to inaccurate radical concentrations. A seemingly direct determination of laser fluence from the beam shape and energy measured by a power meter can deviate substantially from the effective *in situ* fluence by up to several factors.

Instead, we calibrated the fraction of Cl_2 photolyzed by measuring the depletion of O_3 from R1. To first order, each Cl atom produced will remove one O_3 molecule and therefore the Cl_2 photolysis fraction can be determined from the decrease in O_3 concentration. Deviations from this 1:1 stoichiometry by less important Cl reactions are taken into account by the model. We detected O_3 (IE = 12.52 eV)[53] at its parent ion mass (m/z = 48) by tuning the photoionization energy to 13.0 eV. The ion signal was converted to concentration units using a scale factor calculated from the average pre-photolysis O_3^+ signal and the pre-photolysis O_3 concentration determined by UV absorption. An example time-dependent O_3^+ signal and the corresponding one-parameter fit to optimize the initial Cl atom concentration is shown in Figure 4a. The negative slope in the model arises from

the greater initial Cl concentration, and thus greater O_3 depletion, upstream of the pinhole due to divergence of the photolysis beam as it propagated through the reactor. This photolysis gradient is accurately captured by the model. Because the lifetime of Cl atoms is so short, the modeled O_3^+ signal would approximate a step-function in the absence of instrument effects. For the example shown in Figure 4a, the fitted Cl_2 photolysis fraction at the pinhole was (0.861 ± 0.083)%. The uncertainty represents ±2σ confidence and arises from uncertainties associated with the absolute O_3 concentration, parameters within the kinetic model, and the noise level of the data. The photolysis fraction was calibrated daily and typically around ~0.8%. The initial Cl concentration in scans below the IE of O_3 was determined from the calibrated photolysis fraction and the Cl_2 concentration, which we intentionally varied across different experiments.

2.3.3.3 Wall Loss Rates

Heterogonous loss of ClO and ClOOCl at the walls of the reactor was found to influence their kinetics measured at 210 K. This effect was most noticeable in the $ClOOCl^+$ signals (Figure 4d). Because only a small fraction of ClO dimerizes over our observation timescale, the growth rate of ClOOCl is approximately constant and the model predicts that the $ClOOCl^+$ signal will appear as a line in the absence of any loss. The ClOOCl kinetics shown in Figure 4d demonstrate clear curvature, however, suggesting competition between production and removal mechanisms. While the most obvious loss process would be dissociation, the rate constant is very slow at 210 K and 50 Torr (k = 7.2 x 10^{-5} s^{-1}). No known gas-phase chemical reaction can explain the curvature and we therefore attribute it to wall loss. Heterogeneous removal of peroxides, such as H_2O_2, on the surfaces of reactors is well-established.[36,54–56]

Wall loss rates for ClO and ClOOCl were determined at 210 K by fitting four datasets with different initial radical concentrations of $[Cl]_0$ = (0.9, 1.8, 2.7, 3.6) x 10^{13} atoms cm^{-3}. The ClO^+ and $ClOOCl^+$ signals measured at each radical concentration were fit to the model while floating four parameters: the ClO wall loss rate ($k_{wall,ClO}$), the ClOOCl wall loss rate ($k_{wall,ClOOCl}$), and scale factors to convert each ion signal to concentration units. A weighted average of the fitted rate constants yielded $k_{wall,ClO}$ = 0.26 ± 0.20 s^{-1} and $k_{wall,ClOOCl}$ = 6.6 ± 1.4 s^{-1} (±2σ uncertainties), which were incorporated into the kinetic model (Table 1). The ClO wall loss rate was barely statistically significant but

included nevertheless. The ClOOCl wall loss rate made an appreciable impact on the modeled kinetics and was capable of explaining the curvature in $ClOOCl^+$ signal observed at all radical concentrations. A similar analysis was performed on 300 K datasets but the fitted rates were effectively zero; we therefore omitted wall loss from the 300 K model.

2.3.3.4 Single Energy Cross Sections

The absolute photoionization cross sections of ClO and ClOOCl were measured across 25 experiments with varying initial radical concentrations and ΔE_{FWHM}. The 210 K cross sections of both molecules were measured at the three single energies previously identified: 11.083, 11.174, and 11.315 eV. The 300 K cross sections of ClO were also measured at 11.174 eV. We determined cross sections by fitting the measured ClO^+ and $ClOOCl^+$ signals at each set of conditions to the model presented in Table 1. Two-parameter fits were performed to optimize the scale factors between ion signal and concentration over Δt = 0–60 ms for ClO, $\langle S_{\mathrm{ClO}}(E,t)/N_{\mathrm{ClO}}(t)\rangle_{\Delta t}$, and ClOOCl, $\langle S_{\mathrm{ClOOCl}}(E,t)/N_{\mathrm{ClOOCl}}(t)\rangle_{\Delta t}$. A scale factor for the inert CH_3Br reference was computed using the time-independent CH_3Br^+ signal from the same scan and the known concentration flown through the reactor. With these scale factors, Eqn. 2 was then used to determine the unknown σ_{ClO} and σ_{ClOOCl} in reference to $\sigma_{\mathrm{CH_3Br}}$. The cross sections determined at each set of experimental conditions are presented in Table 2. The final cross sections at each energy, computed as a weighted average across the individual experiments, are reported in Table 3.

Example fits of the model to ClO^+ and $ClOOCl^+$ signals are shown in Figure 4. The ClO kinetics at both temperatures are fairly inert. The slight delay in production of ClO arises from the instrument response function, which is slower than the ClO growth rate from R1. At 300 K, the positive slope in ClO kinetics is not due to sustained chemical production, but rather the photolysis gradient leading to a greater initial concentration of ClO upstream of the pinhole. Both of these instrument effects are well-described by the model (Supplementary Material SM3). (In the absence of a photolysis gradient, the model predicts that the 300 K ClO^+ signal would have a weak negative slope and that decays of the 210 K ClO^+ signals would appear more pronounced.) The ClOOCl kinetics similarly exhibit excellent agreement with the model. The dimerization is quite far from equilibrium at 60 ms and therefore the concavity of the signals does not represent an approach to steady-

state. Instead, the curvature arises from heterogeneous wall loss, as discussed previously. To verify that the presence of CH_3Br did not impact ClO and ClOOCl chemistry, we performed several control experiments without CH_3Br in the reactor. The shapes of the ClO^+ and $ClOOCl^+$ signals measured in these scans were identical to those measured with CH_3Br.

The values of σ_{ClO} and σ_{ClOOCl} at 11.174 and 11.315 eV are plotted as a function of ΔE_{FWHM} in Figure 5. As expected from the relative photoionization spectra collected around these energies, the cross sections are insensitive to resolution over ΔE_{FWHM} = 10–40 meV. Unfortunately, time limitations only allowed us to measure the 11.083 eV cross sections at one resolution. We expect these values are still resolution-independent over at least ΔE_{FWHM} = 10–20 meV, however, due to the constant ion signal at 11.083 eV observed in the relative spectra. At all of the energies, it is likely that the measured σ_{ClOOCl} is independent of ΔE_{FWHM} over a much broader range due to the lack of structure in the ClOOCl spectrum and small $d\sigma/dE$.

In Figure 5a, σ_{ClO} at 11.174 eV is plotted for both the 300 and 210 K experiments. The average σ_{ClO} measured at 300 K is 4.5% greater than the value measured at 210 K. While the error bars in Figure 5 suggest this may be a meaningful difference, we have only included random error in these plots in order to compare data points within the same series. Uncertainties common to each data point in a series were not included so that the independence from ΔE_{FWHM} could be accurately evaluated. The 210 and 300 K measurements were performed on different days and the difference in σ_{ClO} falls within uncertainty associated with daily fluctuations of the Cl_2 photolysis fraction. We therefore do not believe our data demonstrate any statistically significant difference in σ_{ClO} between two temperatures. A complete discussion of the uncertainty analysis is presented in a later section.

2.3.3.5 Absolute Photoionization Spectra

Relative photoionization spectra of ClO and ClOOCl recorded at 210 K over 10.607–11.777 eV (ΔE_{FWHM} = 9.7 and 18.2 meV, 10 meV steps) were scaled to match the cross sections measured at 11.083, 11.174, and 11.315 eV. Each relative spectrum was interpolated onto these energies and the optimal scale factor, minimizing the residual sum of squares between ion signal and cross section, was fitted. The resulting absolute

photoionization spectra are presented in Figure 2. Tabulated data are provided in the Supplementary Material (SM4). The reported values of $\sigma_{\mathrm{ClOOCl}}(E)$ are likely accurate across all energies in the ClOOCl spectrum. However, the reported values of $\sigma_{\mathrm{ClO}}(E)$ may be less reliable outside of the three single energy measurements due to the substantial structure within the ClO spectrum. For example, the cross section at the peak of a resonance will likely have great sensitivity to ΔE_{FWHM}. When using these cross sections to quantitatively assess ClO concentration, we recommend performing experiments at 11.083, 11.174, or 11.315 eV and using an instrument with $\Delta E_{\mathrm{FWHM}} \leq 40$ meV, if possible.

2.3.3.6 Uncertainty Analysis

To evaluate uncertainty on parameters fitted by the kinetic model, we considered two sources of error: random errors associated with the noise level of the data and systematic model errors associated with uncertainty on rate constants and other fixed parameters utilized in the model integration, such as concentrations. To assess random errors, we employed the bootstrap method.[57] Data points in the time-resolved ion signals were randomly sampled with replacement to generate ~1000 random bootstrap datasets of equal size as the original dataset. Each bootstrap dataset was fit to the model and the variance in the distribution of fitted parameters was taken as the variance on that parameter due to random error. To assess model errors, we performed Monte Carlo simulations. Each fixed model parameter was assumed to have normally distributed uncertainty and was randomly sampled to generate ~1000 random sets of fixed model parameters. For most rate constant parameters, we assumed that their uncertainties are uncorrelated. However, for association and dissociation, the uncertainties are correlated since the dissociation rate constant is typically calculated from the association rate constant and K_{eq}. This correlation was taken into account in the simulations. Each set of fixed model parameters was used to fit the original dataset and the variance in the distribution of fitted parameters was taken as the variance on that parameter due to model error. It was assumed that variances associated with random and model errors could be added to represent the total variance on a fitted model parameter.

Bootstrap and Monte Carlo simulations were used to assess parameter uncertainties for each dataset fit to the kinetic model. A typical fit would take ~1 minute on a standard computer. This was chiefly limited by the implementation of the photolysis gradient in the

model, which required that the differential rate equations be integrated 60 times per iteration of the fit (additional details provided in Supplementary Material SM3). Because ~2000 fits were performed for each of the 25 single energy cross section experiments conducted in this work, we parallelized the calculations using computational resources from the Extreme Science and Engineering Discovery Environment (XSEDE) on the Comet cluster at the San Diego Supercomputer Center.[58]

To identify the dominant sources of uncertainty in σ_{ClO} and σ_{ClOOCl}, we partitioned errors stemming from the terms in Eqn. 2 into four categories: (1) *Random error* associated with the noise level of the ClO^+ or $ClOOCl^+$ signal (determined by bootstrap simulations) and the CH_3Br^+ signal. (2) *Model error* predominantly arising from uncertainties in rate constants and the initial radical concentration (determined by Monte Carlo simulations). (3) *Mass discrimination error* arising from the ratio of the mass discrimination factors and uncertainty in the mass-dependent ion collection efficiency of the instrument. (4) *Reference cross section error* associated with uncertainty in the values of $\sigma_{\mathrm{CH_3Br}}$ measured in this work. The relative standard errors from each of these categories can be added in quadrature to give the total relative standard error on a cross section. An error budget for σ_{ClO} and σ_{ClOOCl} measured at each energy is presented in Table 3.

For σ_{ClO}, the greatest source of uncertainty is the value of the reference cross section, $\sigma_{\mathrm{CH_3Br}}$. The uncertainty on $\sigma_{\mathrm{CH_3Br}}$ is almost entirely set by uncertainty on the cross section of the reference molecule used in those experiments, propene. The literature $\sigma_{\mathrm{propene}}$ are estimated to be accurate to ±20% at the ±2σ level of confidence.[44] Because the shapes of the ClO and ClOOCl spectra have been normalized to the shape of the literature propene spectrum, the reported σ_{ClO} and σ_{ClOOCl} can be scaled by the ratio $(\sigma_{new}/\sigma_{old})_{\mathrm{propene}}$ at each energy should more accurate propene cross sections become available in the future, and the uncertainty would decrease accordingly. Error from the kinetic model plays only a minor role in the overall uncertainty of σ_{ClO} since the ClO kinetics are fairly inert at both temperatures. The minor amount of model error is mostly attributed to uncertainty on the initial radical concentration.

In contrast, the greatest source of uncertainty on σ_{ClOOCl} comes from the kinetic model. Specifically, the value of σ_{ClOOCl} is highly sensitive to the value of the dimerization rate constant, k_2, which is accurate to ±30% at the ±2σ level of confidence. There has

unfortunately been no direct measurement of k_2 at the specific conditions of this experiment: 50 Torr, 210 K, and a bath gas of He. The determination of a literature value for k_2 and an evaluation of its consistency with our data are presented in the next section. We note that error stemming from the ratio of the mass discrimination factors is substantially smaller for σ_{ClOOCl} than for σ_{ClO}, due to the close masses of ClOOCl and the CH_3Br reference.

2.4 Discussion

2.4.1 ClO Photoionization

Photoionization cross sections of ClO to ClO^+ have been reported previously and can be compared to the results of the present study. Flesch et al. used pulsed VUV light and time-of-flight detection to measure a value of 27.5 ± 5 Mb at 13.74 eV.[27,59] ClO was generated from the photolysis of OClO at 359.5 nm under collision-free conditions and its cross section determined in reference to that of the O coproduct. ClO formed in this approach is known to be vibrationally excited,[60] and the authors applied an empirical correction to estimate the cross section of ClO (v = 0) as 24 ± 5 Mb at 13.74 eV. This value was then used to place a relative spectrum collected in a prior study by the same group onto an absolute scale.[28] (A cross section of 21.3 ± 3 Mb at 13.41 eV was also measured but not used to scale the spectrum.[27]) Their absolute spectrum was not tabulated and the data is noisy in the near-threshold region, as it was recorded up to 20 eV. Nevertheless, it is clear that the magnitude of their cross sections differs substantially from the values presented in our work: Flesch et al. report values less than 10 Mb for all energies below 12 eV, while we measure cross sections as high as 30–35 Mb (Figure 2a) over the same region.

One key difference between the studies is our use of an Ar gas filter upstream of the ionization region to filter higher harmonic light from the synchrotron. The relative spectrum used by Flesch et al. was also collected with a synchrotron light source, but without use of a harmonic filter.[27,28] The result is positive ClO^+ signal recorded at energies below the ionization threshold of ClO. After scaling to the cross section at 13.74 eV, which was not measured using a synchrotron and unaffected by higher harmonics, their reported

absolute spectrum has a 5 Mb offset below threshold. Since the impact of higher harmonic light on the relative spectrum is unlikely to be a constant factor, this approach could distort cross sections at energies besides 13.74 eV, although Flesch et al. note that attenuation should only occur below 12 eV due to the reflectivity of the VUV optics employed.[27] Below 12 eV, correction for higher harmonic light would result in even smaller near-threshold cross sections in their study, further increasing the disagreement with our work.

To investigate the large discrepancy in magnitude, we considered possible systematic errors that may influence our ClO cross sections. The reaction of Cl with O_3 (R1) has been observed to produce significant population in excited ClO vibrational states up to v = 6 and could reach as high as v = 17 from the reaction exothermicity.[61–64] If ClO (v > 0) photoionization substantially contributes to our observed ClO^+ signal, then it would cause the cross sections of thermally equilibrated ClO to be overestimated. (At equilibrium, 98.2% and 99.7% of ClO is in v = 0 at 300 K and 210 K, respectively.) However, unlike the collision-free experiments of Flesch et al.,[27] ClO undergoes numerous thermalizing collisions in our 50 Torr experiments and the spectrum arises from integrating the ClO^+ signal over 0 to 60 ms after initial photolysis. To impact our results, ClO (v > 0) would need to persist for many milliseconds. Matsumi et al. measured state-resolved kinetics of ClO produced from R1 and observed that vibrational equilibrium was established within ~800 μs at 2 Torr of N_2.[63] Our experiments were conducted in a partial pressure of 2.25 Torr of O_2, which is expected to have a similar quenching efficiency as that of N_2. The remaining 47.75 Torr in our reactor is predominantly He, which serves to further reduce the lifetime of ClO (v > 0). It is likely that ClO has thermalized after only a few hundred microseconds in our experiment and thus our ClO^+ spectrum represents photoionization of an equilibrium distribution of ClO vibrational states.

Other potential complications from excited ClO could arise from non-stoichiometric conversion of Cl to ClO due to the following reactions:[65]

$$ClO\ (v > 2) + Cl \rightarrow Cl_2 + O \qquad \text{(R6)}$$

$$ClO + O \rightarrow O_2 + Cl \qquad \text{(R7)}$$

This would lead to a decreased ClO yield than that predicted by our kinetic model. Modeling the extent of this chemistry is unfortunately not possible since the rate constant of R6 is unknown. Evidence for these reactions has been reported in studies where Cl is

in excess and O_3 is the limiting reactant to R1.[65,66] The lifetime of Cl atoms is relatively long under such conditions and there may be substantial opportunity for R6 to occur prior to quenching of ClO (v > 2). Burkholder et al. quantitatively explored this effect by varying the ratio of $[O_3]_0/[Cl]_0$ at ~0.3 Torr and found that non-stoichiometric conversion of the limiting reactant to ClO could be minimized if this ratio was kept above ~5.[65] In our experiments, this ratio is $[O_3]_0/[Cl]_0 \approx 25$ and our pressure is much greater, leading to faster deactivation of ClO (v > 2) and further suppression of R6. Neglecting this chemistry from our model should have negligible impact on the cross sections we determine. We note that if [ClO] were overpredicted, then the true cross sections would be even greater, and therefore this could not explain the discrepancy between our results and those of Flesch et al.[27]

A possible contribution to the disagreement in cross section magnitude could arise from differences in energy resolution. Due to the great density of resonances in the near-threshold region, we made a considerable effort to calibrate our resolution and measure cross sections at energies where ion signal was constant over ΔE_{FWHM} = 10–40 meV. The relative near-threshold spectrum collected by Schwell et al. does not show resonances,[28] suggesting that our spectrum may have better resolution. However, in their spectrum collected from threshold to 20 eV (scaled by Flesch et al. to acquire an absolute spectrum[27]), Schwell et al. tentatively assigned a broad peak at ~14.0 eV as an autoionizing resonance. This feature would arise from a different Rydberg series than those we observe. It is possible that this peak is much narrower than could be resolved by Schwell et al. or is a dense series of resonances appearing as one band. Calculations on the electronic states of the cation predict that ClO^+ ($c^1\Sigma^-$) falls ~14.1 eV above neutral ClO ($X^2\Pi$),[67] and therefore resonances converging to this ionic state may exist around 13.74 eV. The energy resolution in the study of Flesch et al. was not reported. If 13.74 eV falls on a resonance, then the cross section measured in their study could have been inadvertently underestimated due to instrument broadening. Higher resolution spectra around ~14 eV are necessary to address this hypothesis. Differences in resolution thus could partially – though not completely – resolve the discrepancy between their study and our work. A definitive explanation for the differences, which are at least a factor of ~3, remains unknown.

Figure 6 expands the spectrum near the appearance of ClO^+ signal at 210 K. Steps in the spectrum agree very well with the IEs of ClO reported in the photoelectron spectroscopy studies of Bulgin et al.: 10.83 ± 0.01 eV for ClO ($X^3\Sigma^- \leftarrow X^2\Pi_{1/2}$, $v = 0$) and 10.87 ± 0.01 eV for ClO ($X^3\Sigma^- \leftarrow X^2\Pi_{3/2}$, $v = 0$).[31] The latter IE was reported as 10.95 eV in a subsequent paper from the same group,[32] although Thorn et al. explained this as a typographical error that has unfortunately propagated into data compilations.[30] The inset of Figure 6 expands another step in signal at lower energy. The location of this step agrees well with the predicted position of the ClO ($X^3\Sigma^- \leftarrow X^2\Pi_{3/2}$, $v = 1$) hot band IE as 10.766 eV, assuming ω_e = 853.8 cm^{-1} and $\omega_e x_e$ = 5.5 cm^{-1} for ClO ($X^2\Pi_{3/2}$).[68] While the equilibrium population of ClO ($X^2\Pi_{3/2}$, $v = 1$) is estimated to decrease by 82% from 300 to 210 K, our 300 K ClO^+ spectrum was averaged less and is too noisy over this energy range to make a quantitative comparison.

Bulgin et al. determined $\omega_e = 1040 \pm 30$ cm^{-1} for ClO^+ ($X^3\Sigma^-$) from spacing between the $v' = 0$–3 bands in their photoelectron spectrum,[31,32] and we overlay these steps on our photoionization spectrum in Figure 2a. The spacing between these states agrees well with a more recent measurement of ω_e and $\omega_e x_e$ for ClO^+ ($X^3\Sigma^-$) determined over $v' = 8$–16.[69] As our spectrum clearly shows, assessing the vibrational structure of the cation with photoionization spectroscopy is not tractable due to the many resonances obscuring the underlying vibrational steps. Thorn et al. also used synchrotron PIMS to record a relative ClO^+ spectrum over a comparable energy range and similarly observed many resonances in the near-threshold region.[30] While their energy resolution and step size were slightly broader, the general shape of their spectrum and the approximate locations of resonances agree exceptionally well with the present work.

The two resonances near 11.174 eV are well-resolved in our spectra collected with a step size of 1–2 meV at 210 K (Figure 3a) and 300 K (Supplementary Material SM5). The FWHMs of these peaks agree reasonably well with the calibrated ΔE_{FWHM} of the VUV light, indicating that broadening of the resonances is mostly instrument-limited. However, at our narrowest energy resolution of 9.9 meV, we find the resonances are slightly broader with widths of ~14 meV. This suggests that we may be partially resolving their rotational contours. To explore this possibility, we performed rough simulations of the rotational lines within a resonance using PGOPHER (v10.1.182).[70] The resonances in the near-

threshold region likely arise from two separate Rydberg series converging to the $a^1\Delta$ and $b^1\Sigma^+$ states of ClO^+. We performed a simulation for each, approximating the upper state rotational constant based on the equilibrium bond length of the cation state calculated previously with CASSCF/MRCI.[67] Intensities were set by the rotational distribution of ground state ClO. The calculated rotational lines were convolved with a 9.9 meV FWHM Lorentzian lineshape and the resulting contours have FWHMs of ~12–13 meV, in good agreement with the observed values.

Overall, the present work has demonstrated the importance of a judicious choice of photoionization energy and a well-calibrated energy resolution when using PIMS to accurately assess ClO concentration. While measurements at energies within solely the ionization continuum would have the least sensitivity to resolution and be the most reliable, the near-threshold spectrum of ClO to ClO^+ has a high density of resonances and avoiding them can be arduous. We have measured photoionization cross sections at three energies (11.083, 11.174, 11.315 eV) where ion signal is independent of resolution over ΔE_{FWHM} = 10–40 meV. These cross sections were used to scale relative spectra to absolute cross sections over 10.607–11.777 eV, although we note values outside of the three single energies may be less reliable. We have the greatest confidence in the cross section measured at 11.174 eV, which is located in the valley between a pair of well-resolved resonances (Figure 3a). However, even this energy could lead to systematic error if the VUV bandwidth is too broad and intensity from the resonances begins to influence the effective cross section. Both narrow resolution and precise energy control are necessary to ensure accuracy.

2.4.2 ClOOCl Photoionization

The greatest source of uncertainty in our photoionization cross sections of ClOOCl to $ClOOCl^+$ arises from uncertainty in the rate constant for ClO dimerization, k_2. Since this reaction is a termolecular association, it is essential that the value of k_2 used in the kinetic model correspond to our experimental conditions of P = 50 Torr and M = He. While k_2 has been measured extensively over conditions relevant to the polar stratosphere, there have been few studies conducted in He. The value of k_2 used in our model was derived using the fall-off curve parameters from the NASA Jet Propulsion Laboratory data

evaluation (JPL 2015).[26] The JPL 2015 parameters correspond to a N_2 bath gas and were used without adjustment except for the low pressure limit rate constant at 300 K (k_{0,N_2}^{300}), which was scaled by the ratio $k_{0,He}^{300}/k_{0,N_2}^{300}$ = 0.51 measured by Nickolaisen et al.[71] Scaling the low pressure limit rate constant is a common method to correct for different quenching efficiencies of bath gases. The combined JPL 2015 / Nickolaisen method gives k_2 = (7.1 ± 2.1) x 10^{-14} cm^3 $molc^{-1}$ s^{-1} (±30%, ±2σ) at 50 Torr and 210 K in He.

To assess the validity of this rate constant, we reanalyzed low temperature ClO and ClOOCl kinetics at 11.315 eV while floating k_2 as an additional fit parameter. Because the radical concentration is independently determined and fixed in our model, the fitted value of k_2 is sensitive to the observed rates of pseudo bimolecular ClO decay and ClOOCl growth. Optimization across four different initial radical concentrations yields k_2 = (7.7 ± 1.1) x 10^{-14} cm^3 $molc^{-1}$ s^{-1}, with uncertainty determined from bootstrap and Monte Carlo simulations comparable to those performed in the cross section analysis described above. The fitted value is in excellent agreement with the value from the JPL 2015 / Nickolaisen method. However, our experiment was not designed to determine k_2 (our observation timescale is less than one half-life for dimerization). Despite the smaller stated uncertainty from our fit, we opted to fix k_2 at the value of JPL 2015 / Nickolaisen in the cross section analysis. The uncertainty reported by JPL 2015 is typically conservative and represents the confidence in a rate constant after evaluating the range of values that have been reported across the literature.[26] We therefore believe that the rate constant and uncertainty determined by the JPL 2015 / Nickolaisen method best represents the present accuracy of k_2. If a more accurate value of k_2 under these conditions is established in the future, then our data could be reanalyzed to yield more accurate ClOOCl photoionization cross sections.

We also estimated a value for k_2 from the results of Trolier et al., who have published the only pressure fall-off curves with He as the bath gas.[72] Their curves exhibited a positive intercept in the zero-pressure limit, which were later explained by Nickolaisen et al. as an undercorrection for third body quenching by Cl_2.[71] Our Cl_2 concentrations are at least ~30 times smaller than those used by Trolier et al. and Cl_2 collisions have a negligible contribution to our dimerization kinetics. We estimated k_2 using the fitted fall-off parameters of Trolier et al. that include an intercept term, but then dropping the intercept

term from the calculation. The result gives k_2 = 3.9 x 10^{-14} cm^3 $molc^{-1}$ s^{-1}. This disagrees with the value of k_2 fitted from our data and was therefore not used in our analysis of the cross section.

Our measurements have determined the first absolute cross sections for the photoionization of ClOOCl to $ClOOCl^+$. The relative spectrum has been measured previously in the synchrotron PIMS study of Schwell et al., who reported the spectrum from threshold to 20 eV and an IE of 11.05 ± 0.05 eV.[28] Determining the IE of ClOOCl from the $ClOOCl^+$ signal is not straightforward due to the gradual rise of signal likely caused by poor Franck-Condon overlap between the torsional modes of ClOOCl and those of $ClOOCl^+$. Nevertheless, we have estimated the IE from our data to be 10.95 ± 0.10 eV (Figure 7), in good agreement with the prior study. Future experiments using photoelectron spectroscopy could help more definitively establish this value.

The shape of the ClOOCl spectrum measured by Schwell et al. exhibits differences from our spectrum. The maximum in $ClOOCl^+$ signal we observed at ~11.3 eV (Figure 2b) is not seen by Schwell et al., who instead recorded a continuously increasing signal over 11.0–11.5 eV.[28] The reason for this discrepancy is not immediately apparent. Schwell et al. argued that at least one other Cl_2O_2 isomer, either ClOClO or $ClClO_2$, was formed in their experiment. If this species ionizes to its parent cation, then the shape of the m/z = 102, 104, and 106 signals would not solely represent ionization to $ClOOCl^+$, potentially creating the discrepancy. However, their method for generating ClOOCl was very similar to our approach: low temperature dimerization of ClO, formed from the reaction of Cl atoms with excess O_3. The main difference is that their experiment produced Cl atoms from a microwave discharge of Cl_2 and our experiment used pulsed laser photolysis, although we do not expect this to significantly alter the ensuing chemistry. Multiplexed photoionization mass spectrometry can potentially resolve isomers at the same m/z through differences in their photoionization efficiency curves or reaction kinetics.[38,39] Unfortunately, because the spectra of the isomers are not independently known and their formation kinetics from ClO dimerization would be identical, we could not experimentally evaluate the isomer ratio in this work. Many experimental and theoretical studies have established that ClOOCl is the dominant product of ClO dimerization.[23,73–77] In particular, Birk et al. measured the rotational spectrum of Cl_2O_2 produced from the ClO self reaction

at T < 240 K.[73] On the basis of their observed nuclear spin statistics and structure analysis, they determined Cl_2O_2 must possess identical Cl atoms in a peroxide configuration, inconsistent with the ClOClO or $ClClO_2$ structures. We therefore believe our measured ion signals correspond to photoionization of solely the ClOOCl isomer. The reason for the discrepancy between our $ClOOCl^+$ spectrum and the prior work remains unclear.

The decrease in $ClOOCl^+$ signal above ~11.3 eV can be explained in terms of mass peaks observed at m/z = 67 and 69. These ion signals have identical kinetics and photoionization efficiency curves, with masses and an intensity ratio consistent with the isotopologues of ClO_2^+. The kinetics of the ClO_2^+ signal are also identical to the kinetics of $ClOOCl^+$ (Supplementary Material SM5), providing strong evidence that the observed ClO_2^+ signal arises from dissociative ionization of ClOOCl. As shown in Figure 7, the decrease in $ClOOCl^+$ signal above ~11.3 eV is correlated with the steep rise in ClO_2^+ signal around the same energy. It is likely that the total photoionization cross sections of ClOOCl monotonically increase with energy, but the yields shift to favor dissociative ionization, resulting in a decrease of the partial cross section to form $ClOOCl^+$. Alternative explanations for the ClO_2^+ signal are the ionization of neutral OClO or ClOO in the reactor. However, we rule these out for several reasons: the concentrations of OClO and ClOO predicted by the kinetic model are negligible over the observation timescale, the ClO_2^+ signal is only present under conditions where there is appreciable ClOOCl formation, and the IEs of OClO (10.35 eV) and ClOO (11.39 eV) are inconsistent with the measured spectrum.[53]

Dissociative ionization has also been observed by Schwell et al., who reported a ClO_2^+ appearance energy (AE) of 10.95 ± 0.1 eV.[28] Similar to the IE of ClOOCl, determining a precise AE of ClO_2^+ is challenging due to the gradual onset of signal. We report a larger AE of 11.15 ± 0.10 eV with conservative uncertainty bounds, although examination of the threshold region indicates 10.95 eV is still reasonable (Figure 7). An AE of 11.34 ± 0.05 eV has been reported by Plenge et al. but this value is inconsistent with our data.[29] Schwell et al. and Plenge et al. argue that the structure of the daughter ion is $OClO^+$, formed from dissociative ionization of ClOClO or $ClClO_2$. However, as discussed above, we believe that ClOOCl is the sole isomer that forms under our conditions. If the

prior studies indeed have other Cl_2O_2 isomers, then this could explain the discrepancy between the reported AEs of ClO_2^+ and our spectrum.

We propose that the daughter ion in our experiment also has the structure $OClO^+$, but is produced from dissociative photoionization of the ClOOCl isomer. Figure 8 presents an energy diagram for ClOOCl ionization constructed from energies determined in this experiment and taken from the literature.[53] The energy required to generate the $ClOO^+$ structure exceeds the AE of ClO_2^+ by more than 1 eV. On the other hand, the energy required to generate $OClO^+$ matches the observed AE within our uncertainty. This suggests that rearrangement and dissociation of $ClOOCl^+$ to yield $OClO^+$ is nearly barrierless and that hot $ClOOCl^+$ produced with at least ~0.2–0.3 eV of internal energy may undergo this process. Additional studies on the dynamics and energetics of $ClOOCl^+$ would be useful to address this hypothesis.

A second daughter ion of ClOOCl photoionization, ClO^+, has been previously observed with an AE of 11.52 ± 0.025 eV.[33] However, in our 210 K experiments, only a small fraction of the ClO dimerizes over the observation timescale and [ClO] is in excess over [ClOOCl]. We believe that our ClO^+ spectrum represents almost exclusively the photoionization of ClO with only a minor contribution from dissociative ClOOCl ionization. This is consistent with the shape of the ClO^+ spectrum at 210 K being indistinguishable from the shape of the ClO^+ spectrum at 300 K, where the ClOOCl yield is negligible. Agreement of the spectra holds across all energies, particularly those above 11.52 eV (Supplementary Material SM5). We note that the single energy cross sections determined in this work were measured at energies below 11.52 eV; therefore, the ClO^+ signals in those experiments represent solely photoionization of ClO.

2.5 Conclusions

The absolute photoionization cross sections of ClO have been measured and are found to be at least a factor of three greater than a prior report,[27] although the shape of the measured spectrum agrees exceptionally well with a separate study.[30] The accuracy of the cross sections is predominantly limited by the accuracy of the reference methyl bromide cross sections, which have been determined in reference to those of propene. A more accurate measurement of methyl bromide or propene cross sections would reduce

uncertainty on the cross sections determined in this work. The near-threshold spectrum of ClO exhibits a great density of autoionizing resonances and therefore the reported cross sections are most reliable at the three single energy measurements of 11.083, 11.174, and 11.315 eV, where we verified independence over ΔE_{FWHM} = 10–40 meV. The cross section at 11.174 eV appears particularly reliable and within the ionization continuum. Nevertheless, we emphasize that narrow energy resolution and precise energy control are necessary when using photoionization spectroscopy to accurately determine ClO concentration.

The absolute photoionization cross sections of ClOOCl were measured for the first time in this work. Their accuracy is limited by the accuracy of the dimerization rate constant; an improved measurement of this rate constant at our experimental conditions (210 K, 50 Torr, He bath gas) would reduce the uncertainty of these results. The reported ClOOCl cross sections are likely reliable at all energies in the absolute spectrum and across a broad range of ΔE_{FWHM} due to the continuous nature of the spectrum and lack of resonances. The measured $ClOOCl^+$ signal decreases below 11.3 eV, in disagreement with a previously reported relative spectrum.[28] We attribute this decrease to dissociative ionization and hypothesize that rearrangement and dissociation of $ClOOCl^+$ to yield $OClO^+$ is a nearly barrierless process. Additional studies on the dynamics and energetics of $ClOOCl^+$ are recommended.

The results of this work enable absolute concentrations of ClO and ClOOCl to be quantified by photoionization mass spectrometry. The near-threshold cross sections of ClO are fairly large and may allow for the sensitive detection of small changes in ClO concentration. Future experiments may benefit from using photoionization mass spectrometry to constrain persistent uncertainties associated with the mechanism of catalytic ozone depletion in the polar stratosphere.

2.6 Figures

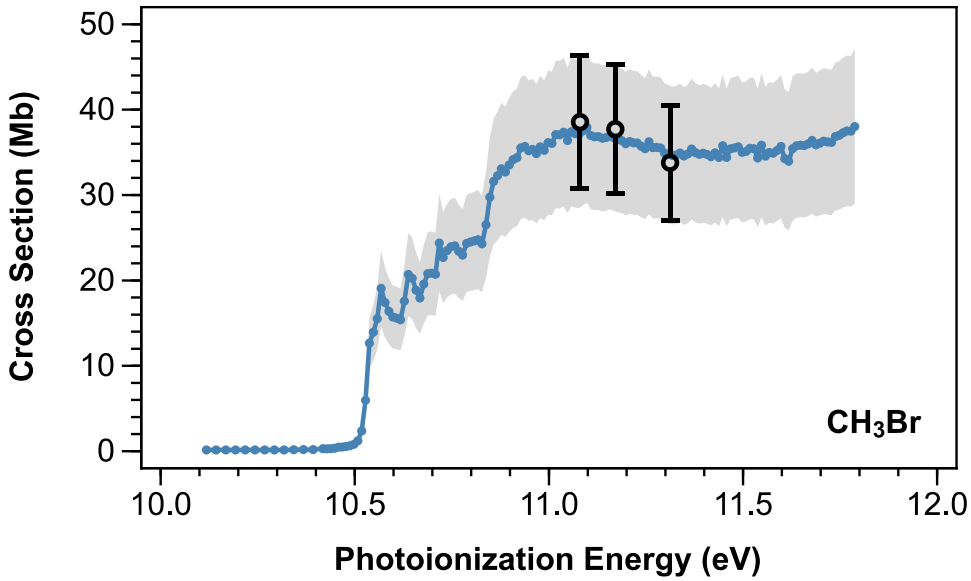

Figure 1: Absolute photoionization cross sections of CH_3Br. The spectrum (blue trace) is an average of four spectra recorded over ΔE_{FWHM} = 7.8–9.9 meV and at 300 and 210 K with a step size of 10 meV. The gray brand represents ±2σ confidence in the value of σ_{CH_3Br} at each energy. Uncertainties are typically ±23% and limited by systematic uncertainties associated with the cross sections of the propene reference. The single energy cross sections (black circles) were measured at 11.083, 11.174, and 11.315 eV at 210 K and averaged over ΔE_{FWHM} = 9.9, 18.2, 27.2, and 37.9 meV. All data is provided in the Supplementary Material (SM4).

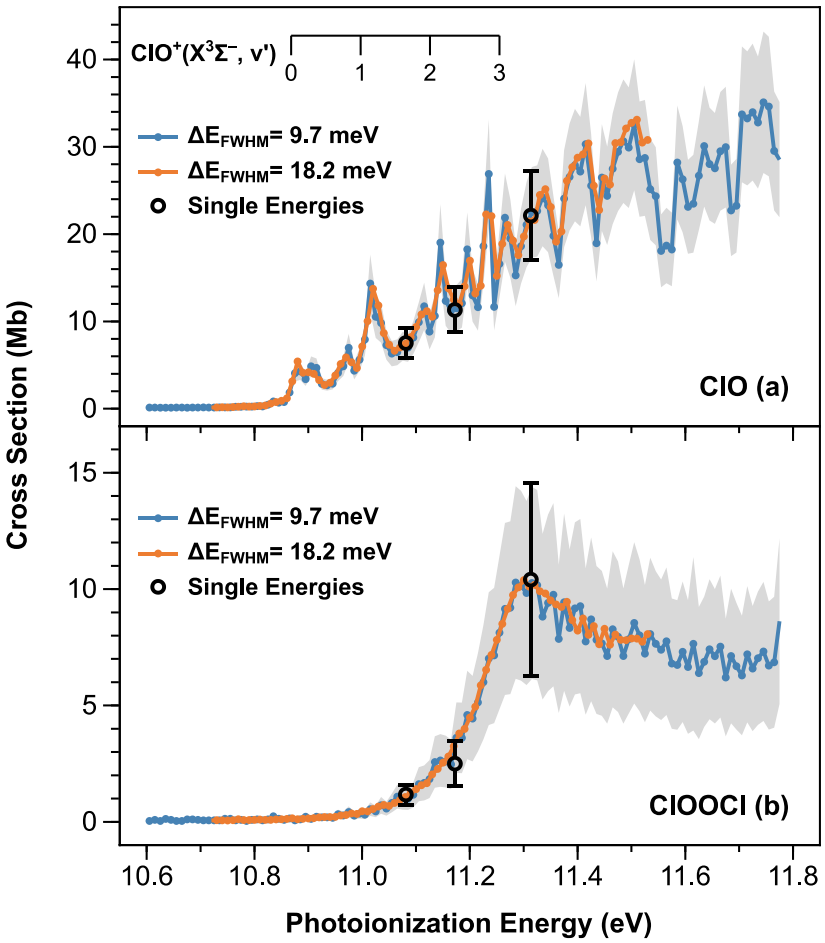

Figure 2: Absolute photoionization spectra of ClO and ClOOCl obtained by scaling relative spectra (blue and orange traces) to the single energy cross sections (black circles) measured at 11.083, 11.174, and 11.315 eV. Spectra were recorded at 210 K with a step size of 10 meV. The gray brands represent ±2σ confidence in the values of σ_{ClO} and σ_{ClOOCl} at each energy in the ΔE_{FWHM} = 9.7 meV spectrum. All data is provided in Table 3 and the Supplementary Material (SM4). **(a)** ClO cross sections. Vibrational steps ($X^3\Sigma^-$, $v' \leftarrow X^2\Pi_{3/2}$, v = 0) measured in the photoelectron spectroscopy study of Bulgin et al. are overlaid for reference.[31] Uncertainties on σ_{ClO} are typically ±23% and limited by systematic uncertainties associated with the cross sections of the CH_3Br reference. **(b)** ClOOCl cross sections. Uncertainties on σ_{ClOOCl} are typically ±39% and limited by systematic uncertainties associated with the cross sections of the CH_3Br reference and the value of the ClO dimerization rate constant at these conditions.

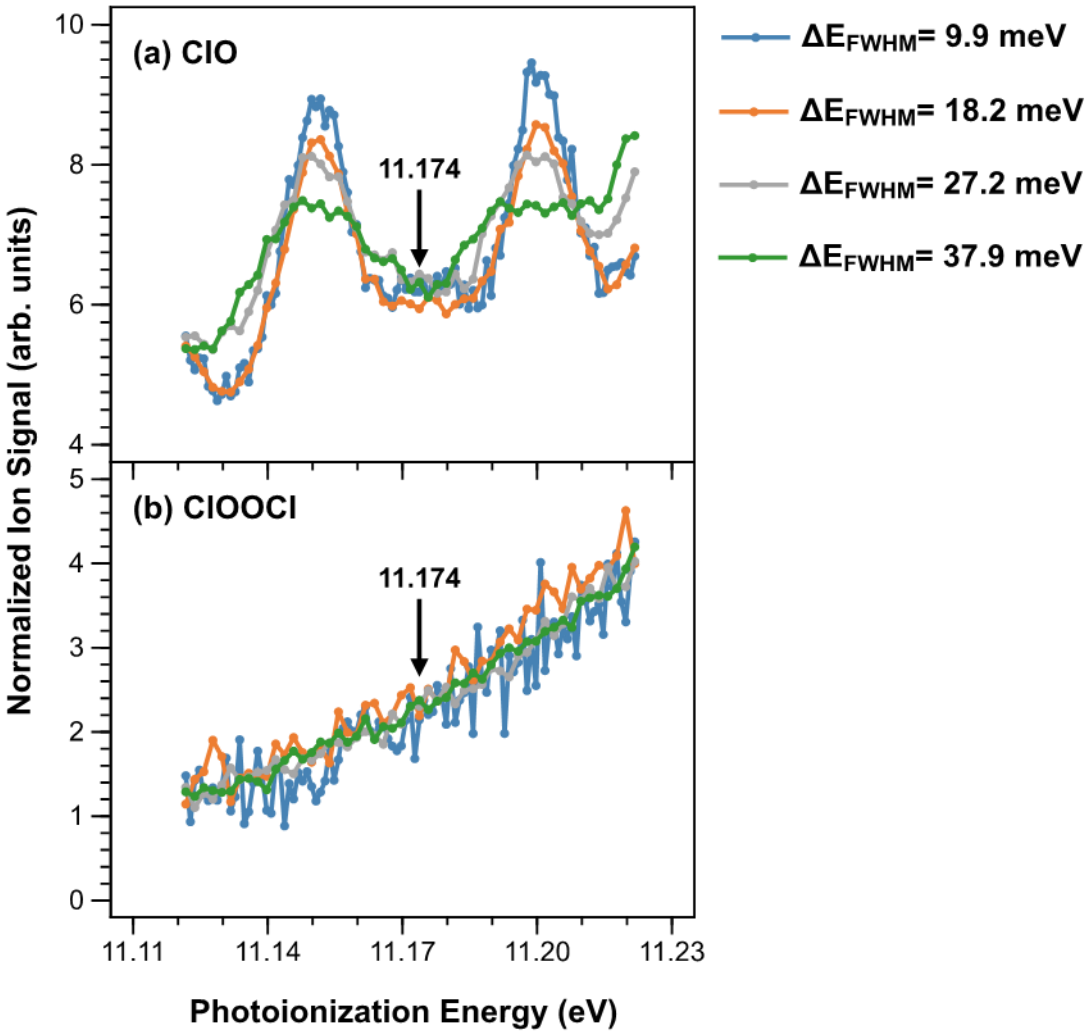

(Figure 3 continued on next page)

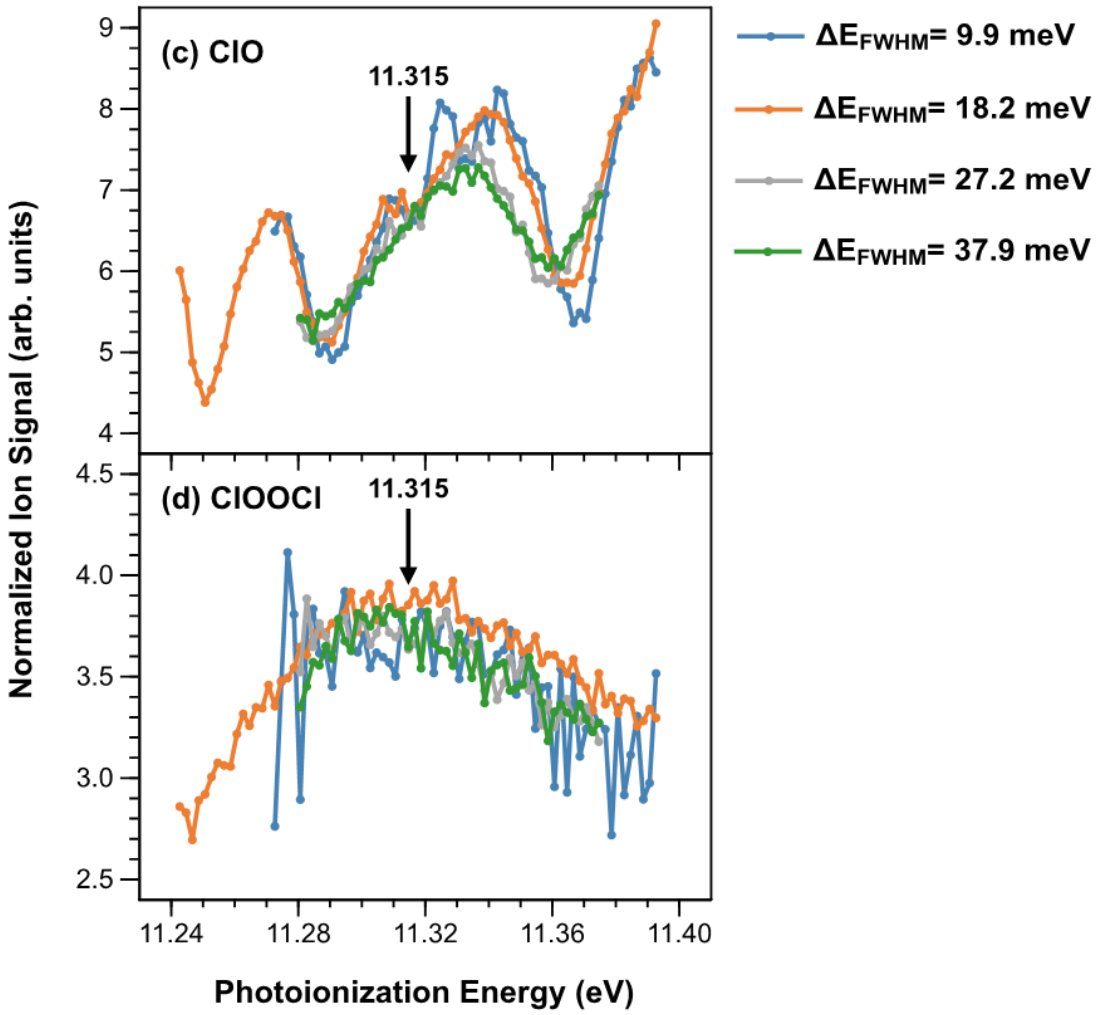

(Figure 3 continued on next page)

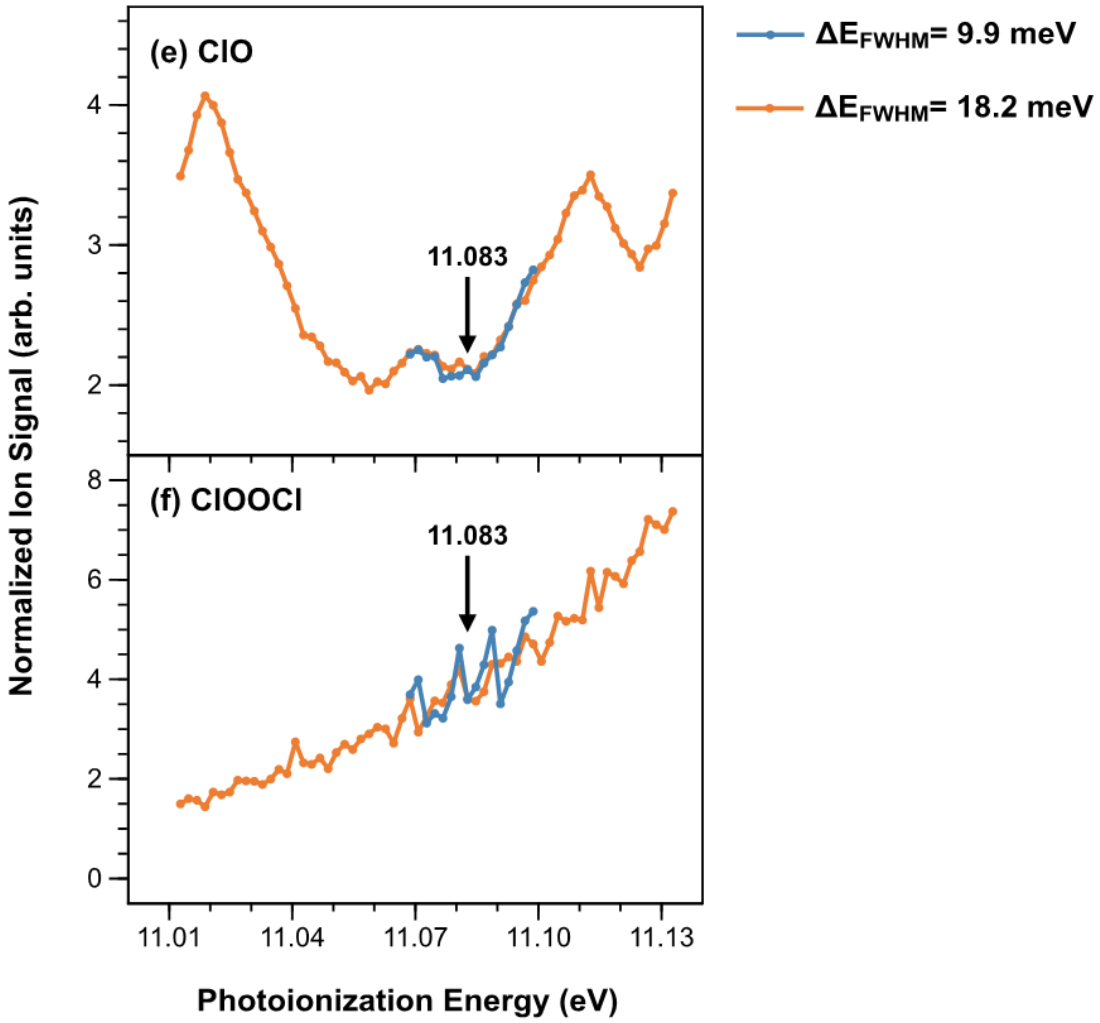

Figure 3: Relative photoionization spectra of ClO and ClOOCl acquired at 210 K with a 1–2 meV step size and ΔE_{FWHM} = 9.9, 18.2, 27.2, and 37.9 meV. The single energies used for measurements of absolute cross sections are labeled. Spectra for ClO at 300 K are provided in the Supplementary Material (SM5). **(a)** ClO and **(b)** ClOOCl recorded over 11.122–11.222 eV. **(c)** ClO and **(d)** ClOOCl recorded over 11.243–11.393 eV. **(e)** ClO and **(f)** ClOOCl recorded over 11.013–11.133 eV.

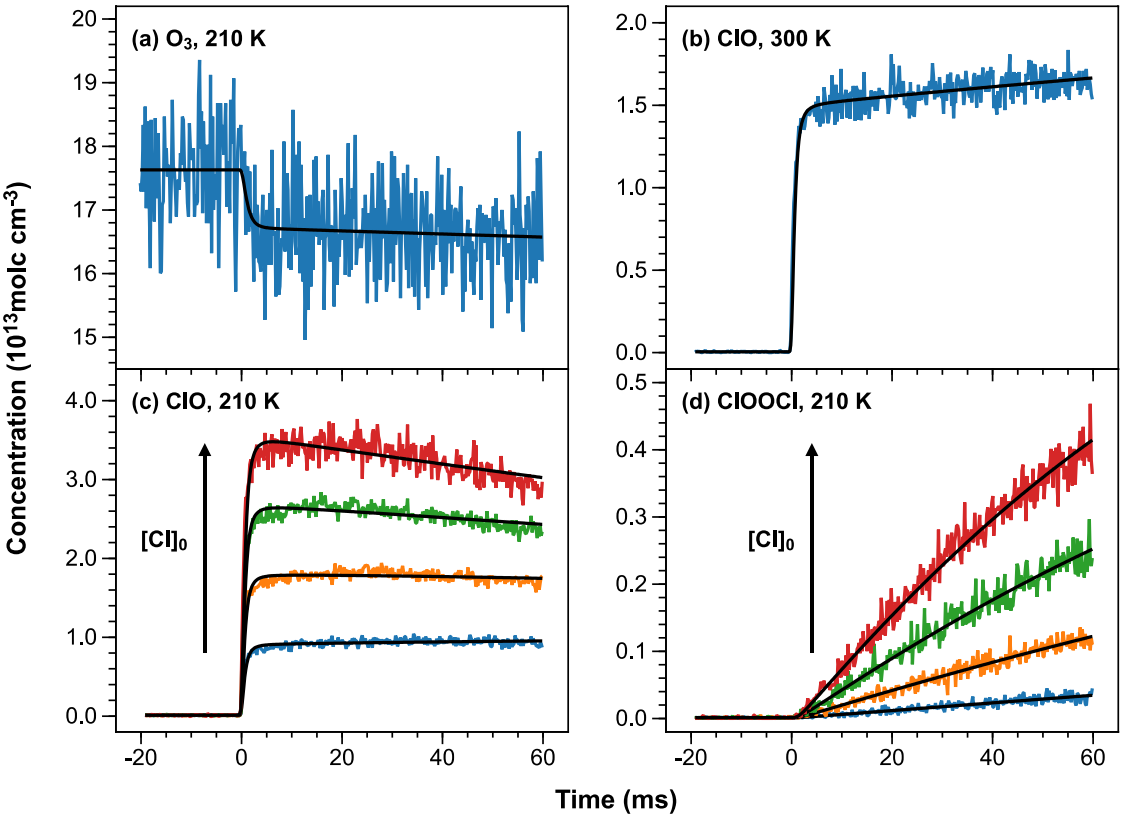

Figure 4: Representative kinetics traces and fits for key species detected in this work. Time-resolved ion signals have been scaled to absolute concentration units. The fits to the kinetic model (black lines) include convolution with instrument effects. **(a)** O_3 at 210 K and 13.0 eV. The fitted depletion corresponds to a Cl_2 photolysis fraction of (0.861 ± 0.083)% (±2σ confidence). **(b)** ClO at 300 K and 11.174 eV in an experiment conducted with $[Cl]_0$ = 1.5 x 10^{13} atoms cm^{-3}. **(c)** ClO and **(d)** ClOOCl at 210 K and 11.315 eV in experiments conducted with $[Cl]_0$ = 0.9 (blue), 1.8 (orange), 2.7 (green), and 3.6 (red) atoms cm^{-3}.

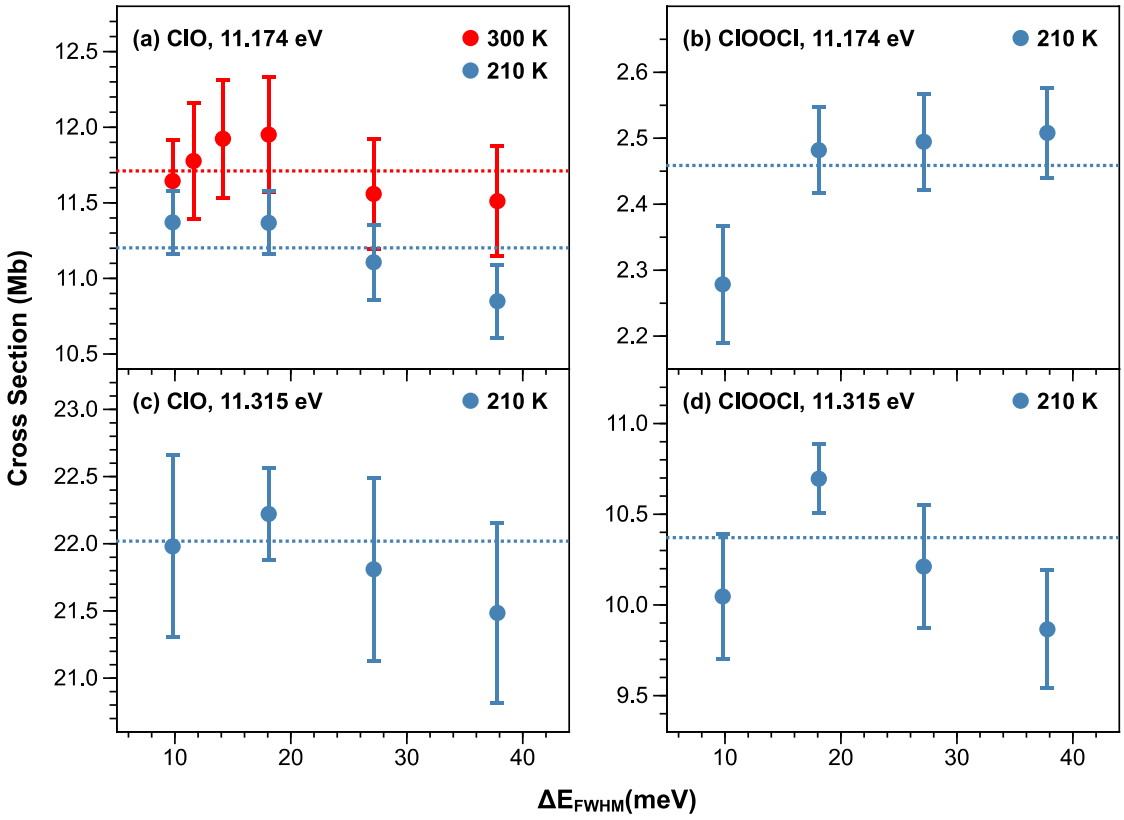

Figure 5: The measured photoionization cross sections of ClO and ClOOCl plotted as a function of energy resolution. Each point represents a weighted average across all cross sections measured at a particular ΔE_{FWHM}. The dashed lines represent a weighted average across all cross sections measured at the specified photoionization energy. To evaluate the independence of cross section from ΔE_{FWHM}, we have only included ±2σ random error in the uncertainty bars. Systematic errors that would adjust each point in a series by the same factor were not included. **(a)** σ_{ClO}(11.174 eV) at 300 (red) and 210 (blue) K. **(b)** σ_{ClOOCl}(11.174 eV) at 210 K. **(c)** σ_{ClO}(11.315 eV) at 210 K. **(d)** σ_{ClOOCl}(11.315 eV) at 210 K.

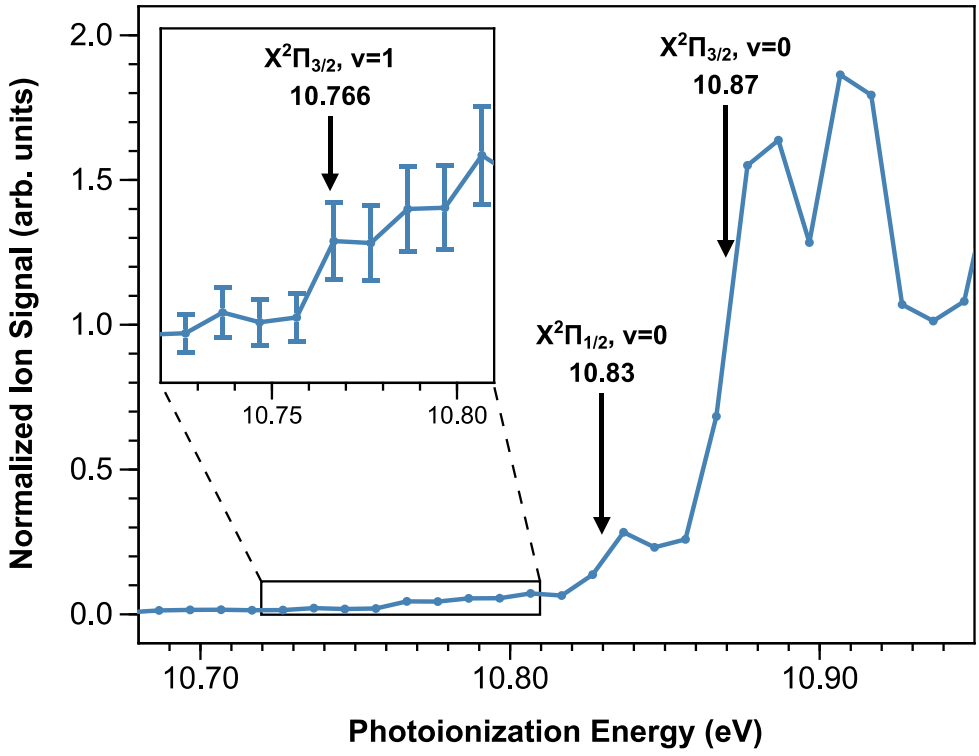

Figure 6: Relative photoionization spectrum of ClO in the threshold region, recorded with ΔE_{FWHM} = 9.7 meV and 10 meV steps at 210 K. The IEs of ClO ($X^2\Pi_{1/2}$, v = 0) and ClO ($X^2\Pi_{3/2}$, v = 0) measured in the photoelectron spectroscopy study of Bulgin et al. are overlaid and consistent with steps in signal observed in our photoionization spectrum.[31] The inset presents an expanded view of a step in signal at lower energy. Inset data points include ±2σ uncertainty bars associated with random error from the ion counting. While small, the step is statistically significant and its position is consistent with the predicted ClO ($X^2\Pi_{3/2}$, v = 1) hot band IE, assuming ω_e = 853.8 cm^{-1} and $\omega_e x_e$ = 5.5 cm^{-1} for ClO ($X^2\Pi_{3/2}$).[68]

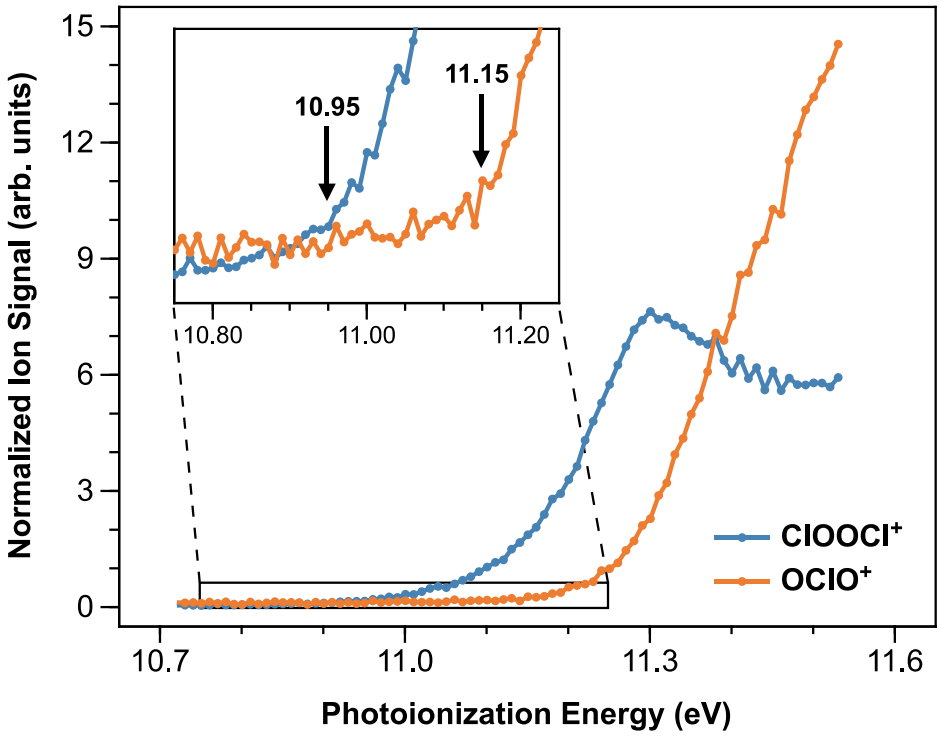

Figure 7: Relative spectra of the parent ($ClOOCl^+$) and daughter ($OClO^+$) ion signals produced from the photoionization of ClOOCl, recorded with ΔE_{FWHM} = 18.2 meV and 10 meV steps at 210 K. The inset presents an expanded view of the threshold region. The IE of ClOOCl and the AE of $OClO^+$ are estimated to be 10.95 ± 0.10 eV and 11.15 ± 0.10 eV, respectively. The uncertainty bounds are conservative due to the gradual onset of signal.

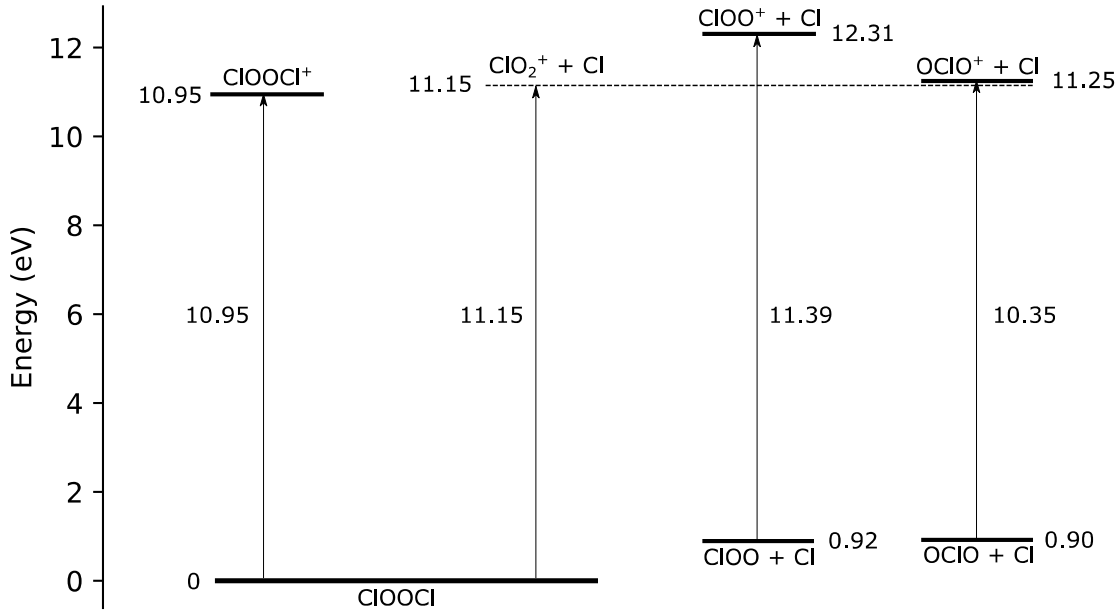

Figure 8: Energy diagram of ClOOCl photoionization. The IE of ClOOCl and the AE of ClO_2^+ were taken from this work. Other energies were derived from the Active Thermochemical Tables (ATcT v1.122d).[53] Dissociative ionization to form $ClOO^+$ is inconsistent with the observed AE of ClO_2^+. Formation of $OClO^+$ is energetically accessible within the uncertainty.

2.7 Tables

Table I. Kinetic model used to simulate the time-dependent concentrations of ClO, ClOOCl, and O_3. Pressure-dependent rate constants were determined for 50 Torr of He. All rate constants have units of cm^3 $molc^{-1}$ s^{-1} and were taken from the NASA Jet Propulsion Laboratory data evaluation (JPL 2015) unless otherwise noted.[26] Uncertainties are ±2σ.

Reaction	k (300 K)	k (210 K)	Notes
Initiation:			
$Cl + O_3 \rightarrow ClO + O_2$	$(1.2 \pm 0.4) \times 10^{-11}$	$(8.9 \pm 4.1) \times 10^{-12}$	(R1)
Associations / Dissociations:			[a]
$ClO + ClO + M \rightarrow ClOOCl + M$	$(1.4 \pm 0.4) \times 10^{-14}$	$(7.1 \pm 2.1) \times 10^{-14}$	(R2) [b]
$ClOOCl + M \rightarrow ClO + ClO + M$	$2.9 \pm 2.5\ s^{-1}$	$(7.2 \pm 7.6) \times 10^{-5}\ s^{-1}$	
$Cl + O_2 + M \rightarrow ClOO + M$	$(1.4 \pm 0.3) \times 10^{-15}$	$(5.9 \pm 1.2) \times 10^{-15}$	[c]
$ClOO + M \rightarrow Cl + O_2 + M$	$(5.1 \pm 7.3) \times 10^{5}\ s^{-1}$	$(6.0 \pm 11.5) \times 10^{4}\ s^{-1}$	(R4)
$ClO + OClO + M \rightarrow Cl_2O_3 + M$	$(4.3 \pm 0.9) \times 10^{-14}$	------	[d]
$Cl_2O_3 + M \rightarrow ClO + OClO + M$	$(1.2 \pm 0.6) \times 10^{3}\ s^{-1}$	------	
Bimolecular ClO Self Reactions:			
$ClO + ClO \rightarrow Cl + OClO$	$(3.6 \pm 3.7) \times 10^{-15}$	------	
$ClO + ClO \rightarrow Cl + ClOO$	$(8.5 \pm 8.8) \times 10^{-15}$	------	
$ClO + ClO \rightarrow Cl_2 + O_2$	$(5.0 \pm 5.1) \times 10^{-15}$	------	
Cl Reactions with ClO_x:			
$Cl + ClOO \rightarrow Cl_2 + O_2$	$(2.3 \pm 4.6) \times 10^{-10}$	$(2.3 \pm 7.6) \times 10^{-10}$	
$Cl + ClOO \rightarrow ClO + ClO$	$(1.2 \pm 2.4) \times 10^{-11}$	$(1.2 \pm 4.0) \times 10^{-11}$	
$Cl + ClOOCl \rightarrow Cl_2 + ClOO$	$(9.4 \pm 3.8) \times 10^{-11}$	$(1.0 \pm 0.8) \times 10^{-10}$	[e]
$Cl + OClO \rightarrow ClO + ClO$	$(5.8 \pm 3.0) \times 10^{-11}$	------	
Wall Loss:			
$ClO \rightarrow$ wall	------	$0.26 \pm 0.20\ s^{-1}$	This Work
$ClOOCl \rightarrow$ wall	------	$6.6 \pm 1.4\ s^{-1}$	This Work

[a] Association and dissociation rate constants are pseudo bimolecular and pseudo first order, respectively. Dissociation rate constants are calculated from the corresponding association rate constant and K_{eq} from JPL 2015. Their uncertainties are therefore correlated.

[b] Determined in He using JPL 2015 and data from Nickolaisen et al.[71] See discussion in text.

[c] Determined in He using data from Baer et al.[78]

[d] Determined using low-pressure parameters in He from Green et al.[79] and high-pressure parameters from Burkholder et al.[80]

[e] JPL 2015 evaluated 217–298 K. Extrapolated to 210 K due to minor temperature-dependence.

Table II. Summary of initial conditions and results of single energy cross section experiments. Pressure was 50.00 ± 0.25 Torr with a bath of 4.5% O_2 and a balance of He. [O_3] was measured by UV absorption at 254 nm and is accurate to ±5%. [Cl] was calculated from the calibrated Cl_2 photolysis fraction. Uncertainties represent ±2σ confidence.

	T (K)	Energy (eV)	ΔE_{FWHM} (meV)	[Cl] (10^{13} atoms cm^{-3})	[Cl_2] (10^{14} molc cm^{-3})	[O_3] (10^{14} molc cm^{-3})	[CH_3Br] (10^{12} molc cm^{-3})	σ_{ClO} (Mb)	σ_{ClOOCl} (Mb)
1	300.6 ± 0.9	11.174	9.9	1.49 ± 0.12	9.30	3.68	6.90	11.6 ± 3.1	-----
2	300.6 ± 0.9	11.174	9.9	1.49 ± 0.12	9.31	3.65	3.15	11.7 ± 3.1	-----
3	300.6 ± 0.9	11.174	11.7	1.49 ± 0.12	9.31	3.65	3.15	11.8 ± 3.1	-----
4	300.6 ± 0.9	11.174	14.2	1.49 ± 0.12	9.31	3.66	3.15	11.9 ± 3.1	-----
5	300.6 ± 0.9	11.174	18.2	1.49 ± 0.12	9.31	3.66	3.15	11.9 ± 3.1	-----
6 [a]	300.6 ± 0.9	11.174	18.2	1.49 ± 0.12	9.32	3.65	-----	-----	-----
7	300.6 ± 0.9	11.174	27.2	1.24 ± 0.10	7.76	3.56	3.15	11.6 ± 3.0	-----
8	300.6 ± 0.9	11.174	37.9	0.83 ± 0.07	5.19	3.51	2.15	11.5 ± 3.0	-----
9 [b]	210 ± 3	11.174	9.9	1.14 ± 0.11	6.62	4.08	21.5	11.7 ± 2.7	-----
10	210 ± 3	11.174	9.9	2.28 ± 0.22	13.2	4.06	21.5	11.4 ± 2.6	2.35 ± 0.96
11	210 ± 3	11.174	9.9	4.55 ± 0.44	26.4	4.08	21.5	11.0 ± 2.6	2.24 ± 0.83
12	210 ± 3	11.174	18.2	1.85 ± 0.18	10.8	4.09	3.80	12.0 ± 2.8	2.43 ± 1.01
13 [a]	210 ± 3	11.174	18.2	1.85 ± 0.18	10.8	4.10	-----	-----	-----
14	210 ± 3	11.174	18.2	2.28 ± 0.22	13.2	4.49	5.35	11.3 ± 2.6	2.72 ± 1.09
15	210 ± 3	11.174	18.2	4.54 ± 0.44	26.4	4.28	5.35	10.9 ± 2.5	2.44 ± 0.92
16	210 ± 3	11.174	27.2	2.28 ± 0.22	13.2	4.19	2.41	11.0 ± 2.5	2.52 ± 1.01
17	210 ± 3	11.174	27.2	2.28 ± 0.22	13.2	4.10	2.41	11.2 ± 2.6	2.48 ± 0.98
18	210 ± 3	11.174	37.9	2.28 ± 0.22	13.2	4.13	2.41	10.8 ± 2.5	2.54 ± 1.08
19	210 ± 3	11.174	37.9	2.28 ± 0.22	13.2	4.10	2.41	10.9 ± 2.5	2.48 ± 1.01
20	210 ± 3	11.315	9.9	3.58 ± 0.34	26.4	4.25	21.6	22.0 ± 5.1	10.0 ± 3.9
21	210 ± 3	11.315	18.2	0.90 ± 0.09	6.63	4.24	7.73	23.6 ± 5.5	11.5 ± 5.0
22	210 ± 3	11.315	18.2	1.79 ± 0.17	13.2	4.26	7.73	22.8 ± 5.3	11.1 ± 4.5
23	210 ± 3	11.315	18.2	2.69 ± 0.26	19.8	4.21	7.73	22.4 ± 5.2	10.6 ± 4.3
24	210 ± 3	11.315	18.2	3.58 ± 0.34	26.4	4.30	7.73	20.6 ± 4.7	10.2 ± 3.9
25	210 ± 3	11.315	27.2	2.69 ± 0.26	19.8	4.52	3.46	21.8 ± 5.0	10.2 ± 4.0
26 [a]	210 ± 3	11.315	27.2	2.69 ± 0.26	19.8	4.42	-----	-----	-----

27	210 ± 3	11.315	37.9	2.69 ± 0.26	19.8	4.43	3.11	21.5 ± 5.0	9.9 ± 3.9
28	210 ± 3	11.083	18.2	3.58 ± 0.34	26.4	4.45	4.16	7.4 ± 1.7	1.13 ± 0.43

[(a)] Experiment to verify independence of ClO and ClOOCl kinetics from the presence of CH_3Br.

[(b)] The $ClOOCl^+$ signal was too noisy (insufficient averaging) to determine σ_{ClOOCl}.

Table III. Absolute photoionization cross sections of ClO and ClOOCl. Cross sections were computed as a weighted average across all experiments performed at each single energy. A budget of the error sources is also presented (categories are defined in the text). The relative errors from each category can be added in quadrature to give the total relative error on a cross section. The fraction of the total error arising from each category is given in parentheses. Uncertainties represent ±2σ confidence.

T (K)	Energy (eV)	σ_{ClO} (Mb)	Random Error	Model Error	Mass Discrimination Error	Reference Cross Section Error	Total Error
300.6 ± 0.9	11.174	11.7 ± 3.1	±1.2% (< 1%)	±8.2% (10%)	±9.0% (12%)	±23% (78%)	±26% (100%)
210 ± 3	11.083	7.4 ± 1.7	±3.1% (2%)	±9.1% (15%)	±5.9% (6%)	±20% (77%)	±23% (100%)
210 ± 3	11.174	11.2 ± 2.6	±1.0% (< 1%)	±9.5% (17%)	±5.8% (6%)	±20% (77%)	±23% (100%)
210 ± 3	11.315	22.0 ± 5.0	±1.2% (< 1%)	±9.3% (17%)	±5.7% (6%)	±20% (77%)	±23% (100%)

T (K)	Energy (eV)	σ_{ClOOCl} (Mb)	Random Error	Model Error	Mass Discrimination Error	Reference Cross Section Error	Total Error
210 ± 3	11.083	1.13 ± 0.43	±3.6% (1%)	±32% (70%)	±0.7% (< 1%)	±20% (29%)	±38% (100%)
210 ± 3	11.174	2.46 ± 0.97	±1.5% (< 1%)	±34% (74%)	±0.7% (< 1%)	±20% (26%)	±40% (100%)
210 ± 3	11.315	10.4 ± 4.1	±1.3% (< 1%)	±35% (75%)	±0.7% (< 1%)	±20% (25%)	±40% (100%)

2.8 References

(1) Eskola, A. J.; Timonen, R. S. Kinetics of the Reactions of Vinyl Radicals with Molecular Oxygen and Chlorine at Temperatures 200–362 K. *Phys. Chem. Chem. Phys.* **2003**, *5* (12), 2557–2561. https://doi.org/10.1039/B302894A.

(2) Mysak, E. R.; Wilson, K. R.; Jimenez-Cruz, M.; Ahmed, M.; Baer, T. Synchrotron Radiation Based Aerosol Time-of-Flight Mass Spectrometry for Organic Constituents. *Anal. Chem.* **2005**, *77* (18), 5953–5960. https://doi.org/10.1021/ac050440e.

(3) Hansen, N.; Klippenstein, S. J.; Miller, J. A.; Wang, J.; Cool, T. A.; Law, M. E.; Westmoreland, P. R.; Kasper, T.; Kohse-Höinghaus, K. Identification of C5Hx Isomers in Fuel-Rich Flames by Photoionization Mass Spectrometry and Electronic Structure Calculations. *J. Phys. Chem. A* **2006**, *110* (13), 4376–4388. https://doi.org/10.1021/jp0569685.

(4) Cool, T. A.; Wang, J.; Hansen, N.; Westmoreland, P. R.; Dryer, F. L.; Zhao, Z.; Kazakov, A.; Kasper, T.; Kohse-Höinghaus, K. Photoionization Mass Spectrometry and Modeling Studies of the Chemistry of Fuel-Rich Dimethyl Ether Flames. *Proceedings of the Combustion Institute* **2007**, *31* (1), 285–293. https://doi.org/10.1016/j.proci.2006.08.044.

(5) Taatjes, C. A.; Meloni, G.; Selby, T. M.; Trevitt, A. J.; Osborn, D. L.; Percival, C. J.; Shallcross, D. E. Direct Observation of the Gas-Phase Criegee Intermediate (CH2OO). *J. Am. Chem. Soc.* **2008**, *130* (36), 11883–11885. https://doi.org/10.1021/ja804165q.

(6) Gaie-Levrel, F.; Gutlé, C.; Jochims, H.-W.; Rühl, E.; Schwell, M. Photoionization of Atmospheric Aerosol Constituents and Precursors in the 7−15 EV Energy Region: Experimental and Theoretical Study. *J. Phys. Chem. A* **2008**, *112* (23), 5138–5151. https://doi.org/10.1021/jp7119334.

(7) Welz, O.; Zádor, J.; Savee, J. D.; Ng, M. Y.; Meloni, G.; Fernandes, R. X.; Sheps, L.; Simmons, B. A.; Lee, T. S.; Osborn, D. L.; et al. Low-Temperature Combustion Chemistry of Biofuels: Pathways in the Initial Low-Temperature (550 K–750 K) Oxidation Chemistry of Isopentanol. *Phys. Chem. Chem. Phys.* **2012**, *14* (9), 3112–3127. https://doi.org/10.1039/C2CP23248K.

(8) Felsmann, D.; Moshammer, K.; Krüger, J.; Lackner, A.; Brockhinke, A.; Kasper, T.; Bierkandt, T.; Akyildiz, E.; Hansen, N.; Lucassen, A.; et al. Electron Ionization, Photoionization and Photoelectron/Photoion Coincidence Spectroscopy in Mass-Spectrometric Investigations of a Low-Pressure Ethylene/Oxygen Flame. *Proceedings of the Combustion Institute* **2015**, *35* (1), 779–786. https://doi.org/10.1016/j.proci.2014.05.151.

(9) Savee, J. D.; Papajak, E.; Rotavera, B.; Huang, H.; Eskola, A. J.; Welz, O.; Sheps, L.; Taatjes, C. A.; Zádor, J.; Osborn, D. L. Direct Observation and Kinetics of a Hydroperoxyalkyl Radical (QOOH). *Science* **2015**, *347* (6222), 643–646. https://doi.org/10.1126/science.aaa1495.

(10) Melania Oana, C.; Krylov, A. I. Dyson Orbitals for Ionization from the Ground and Electronically Excited States within Equation-of-Motion Coupled-Cluster

Formalism: Theory, Implementation, and Examples. *J. Chem. Phys.* **2007**, *127* (23), 234106. https://doi.org/10.1063/1.2805393.

(11) Gozem, S.; Gunina, A. O.; Ichino, T.; Osborn, D. L.; Stanton, J. F.; Krylov, A. I. Photoelectron Wave Function in Photoionization: Plane Wave or Coulomb Wave? *J. Phys. Chem. Lett.* **2015**, *6* (22), 4532–4540. https://doi.org/10.1021/acs.jpclett.5b01891.

(12) Matsuzaki, R.; Yabushita, S. Optimization of Complex Slater-Type Functions with Analytic Derivative Methods for Describing Photoionization Differential Cross Sections. *Journal of Computational Chemistry* **2017**, *38* (12), 910–925. https://doi.org/10.1002/jcc.24766.

(13) Molina, L. T.; Molina, M. J. Production of Chlorine Oxide (Cl2O2) from the Self-Reaction of the Chlorine Oxide (ClO) Radical. *J. Phys. Chem.* **1987**, *91* (2), 433–436. https://doi.org/10.1021/j100286a035.

(14) Permien, T.; Vogt, R.; Schindler, R. N. Mechanisms of Gas Phase-Liquid Phase Chemical Transformations. Air Pollution Report 17, RA Cox, Ed. *Environmental Research Program of the CEC, Brussels* **1988**.

(15) Vogt, R.; Schindler, R. N. Photochemical Investigations on the Atmospheric Chlorine Reservoir Compounds. *Air Pollution Report* **1990**, *34*, 167–171.

(16) Huder, K. J.; DeMore, W. B. Absorption Cross Sections of the ClO Dimer. *J. Phys. Chem.* **1995**, *99* (12), 3905–3908. https://doi.org/10.1021/j100012a007.

(17) McKeachie, J. R.; Appel, M. F.; Kirchner, U.; Schindler, R. N.; Benter, Th. Observation of a Heterogeneous Source of OClO from the Reaction of ClO Radicals on Ice. *J. Phys. Chem. B* **2004**, *108* (43), 16786–16797. https://doi.org/10.1021/jp049314p.

(18) Pope, F. D.; Hansen, J. C.; Bayes, K. D.; Friedl, R. R.; Sander, S. P. Ultraviolet Absorption Spectrum of Chlorine Peroxide, ClOOCl. *J. Phys. Chem. A* **2007**, *111* (20), 4322–4332. https://doi.org/10.1021/jp067660w.

(19) Hobe, M. von; Stroh, F.; Beckers, H.; Benter, T.; Willner, H. The UV/Vis Absorption Spectrum of Matrix-Isolated Dichlorine Peroxide, ClOOCl. *Phys. Chem. Chem. Phys.* **2009**, *11* (10), 1571–1580. https://doi.org/10.1039/B814373K.

(20) Lien, C.-Y.; Lin, W.-Y.; Chen, H.-Y.; Huang, W.-T.; Jin, B.; Chen, I.-C.; Lin, J. J. Photodissociation Cross Sections of ClOOCl at 248.4 and 266 Nm. *J. Chem. Phys.* **2009**, *131* (17), 174301. https://doi.org/10.1063/1.3257682.

(21) Cox, R. A.; Hayman, G. D. The Stability and Photochemistry of Dimers of the ClO Radical and Implications for Antarctic Ozone Depletion. *Nature* **1988**, *332* (6167), 796. https://doi.org/10.1038/332796a0.

(22) Burkholder, J. B.; Orlando, J. J.; Howard, C. J. Ultraviolet Absorption Cross Sections of Chlorine Oxide (Cl2O2) between 210 and 410 Nm. *J. Phys. Chem.* **1990**, *94* (2), 687–695. https://doi.org/10.1021/j100365a033.

(23) DeMore, W. B.; Tschuikow-Roux, E. Ultraviolet Spectrum and Chemical Reactivity of the Chlorine Monoxide Dimer. *J. Phys. Chem.* **1990**, *94* (15), 5856–5860. https://doi.org/10.1021/j100378a046.

(24) Papanastasiou, D. K.; Papadimitriou, V. C.; Fahey, D. W.; Burkholder, J. B. UV Absorption Spectrum of the ClO Dimer (Cl2O2) between 200 and 420 Nm. *J. Phys. Chem. A* **2009**, *113* (49), 13711–13726. https://doi.org/10.1021/jp9065345.

(25) Young, I. a. K.; Jones, R. L.; Pope, F. D. The UV and Visible Spectra of Chlorine Peroxide: Constraining the Atmospheric Photolysis Rate. *Geophysical Research Letters* **2014**, *41* (5), 1781–1788. https://doi.org/10.1002/2013GL058626.

(26) Burkholder, J. B.; Sander, S. P.; Abbatt, J. P. D.; Barker, J. R.; Huie, R. E.; Kolb, C. E.; Kurylo, M. J.; Orkin, V. L.; Wilmouth, D. M.; Wine, P. H. *Chemical Kinetics and Photochemical Data for Use in Atmospheric Studies: Evaluation Number 18*; Pasadena, CA: Jet Propulsion Laboratory, National Aeronautics and Space …, 2015.

(27) Flesch, R.; Schürmann, M. C.; Plenge, J.; Hunnekuhl, M.; Meiss, H.; Bischof, M.; Rühl, E. Absolute Photoionization Cross Sections of the Primary Photofragments of Chlorine Dioxide and Dichlorine Monoxide. *Phys. Chem. Chem. Phys.* **1999**, *1* (24), 5423–5428. https://doi.org/10.1039/A905259C.

(28) Schwell, M.; Jochims, H.-W.; Wassermann, B.; Rockland, U.; Flesch, R.; Rühl, E. Ionization Energies of ClO and Cl2O2. *J. Phys. Chem.* **1996**, *100* (24), 10070–10075. https://doi.org/10.1021/jp9602585.

(29) Plenge, J.; Flesch, R.; Kühl, S.; Vogel, B.; Müller, R.; Stroh, F.; Rühl, E. Ultraviolet Photolysis of the ClO Dimer. *J. Phys. Chem. A* **2004**, *108* (22), 4859–4863. https://doi.org/10.1021/jp049690+.

(30) Thorn, R. P.; Stief, L. J.; Kuo, S.-C.; Klemm, R. B. Ionization Energy of Cl2O and ClO, Appearance Energy of ClO+ (Cl2O), and Heat of Formation of Cl2O. *J. Phys. Chem.* **1996**, *100* (33), 14178–14183. https://doi.org/10.1021/jp961262j.

(31) Bulgin, D. K.; Dyke, J. M.; Jonathan, N.; Morris, A. An Accurate Determination of the First Ionization Potential of the ClO(X2Π i) Radical Using Photoelectron Spectroscopy. *Molecular Physics* **1976**, *32* (5), 1487–1489. https://doi.org/10.1080/00268977600102841.

(32) Bulgin, D. K.; Dyke, J. M.; Jonathan, N.; Morris, A. Vacuum Ultraviolet Photoelectron Spectroscopy of Transient Species. Part 9.—ClO(X2Πi) Radical. *J. Chem. Soc., Faraday Trans. 2* **1979**, *75* (0), 456–465. https://doi.org/10.1039/F29797500456.

(33) Plenge, J.; Kühl, S.; Vogel, B.; Müller, R.; Stroh, F.; von Hobe, M.; Flesch, R.; Rühl, E. Bond Strength of Chlorine Peroxide. *J. Phys. Chem. A* **2005**, *109* (30), 6730–6734. https://doi.org/10.1021/jp044142h.

(34) Moore, T. A.; Okumura, M.; Seale, J. W.; Minton, T. K. UV Photolysis of ClOOCl. *J. Phys. Chem. A* **1999**, *103* (12), 1691–1695. https://doi.org/10.1021/jp984410+.

(35) Huang, W.-T.; F Chen, A.; Chen, I.-C.; Tsai, C.-H.; Jr-Min Lin, J. Photodissociation Dynamics of ClOOCl at 248.4 and 308.4 Nm. *Physical Chemistry Chemical Physics* **2011**, *13* (18), 8195–8203. https://doi.org/10.1039/C0CP02453H.

(36) Dodson, L. G.; Shen, L.; Savee, J. D.; Eddingsaas, N. C.; Welz, O.; Taatjes, C. A.; Osborn, D. L.; Sander, S. P.; Okumura, M. VUV Photoionization Cross Sections of HO_2, H_2O_2, and H_2CO. *The Journal of Physical Chemistry A* **2015**, *119* (8), 1279–1291. https://doi.org/10.1021/jp508942a.

(37) Dodson, L. G.; Savee, J. D.; Gozem, S.; Shen, L.; Krylov, A. I.; Taatjes, C. A.; Osborn, D. L.; Okumura, M. Vacuum Ultraviolet Photoionization Cross Section of the Hydroxyl Radical. *J. Chem. Phys.* **2018**, *148* (18), 184302. https://doi.org/10.1063/1.5024249.

(38) Taatjes, C. A.; Hansen, N.; Osborn, D. L.; Kohse-Höinghaus, K.; Cool, T. A.; Westmoreland, P. R. "Imaging" Combustion Chemistry via Multiplexed

Synchrotron-Photoionization Mass Spectrometry. *Phys. Chem. Chem. Phys.* **2008**, *10* (1), 20–34. https://doi.org/10.1039/B713460F.

(39) Osborn, D. L.; Zou, P.; Johnsen, H.; Hayden, C. C.; Taatjes, C. A.; Knyazev, V. D.; North, S. W.; Peterka, D. S.; Ahmed, M.; Leone, S. R. The Multiplexed Chemical Kinetic Photoionization Mass Spectrometer: A New Approach to Isomer-Resolved Chemical Kinetics. *Review of Scientific Instruments* **2008**, *79* (10), 104103. https://doi.org/10.1063/1.3000004.

(40) Suits, A. G.; Heimann, P.; Yang, X.; Evans, M.; Hsu, C.; Lu, K.; Lee, Y. T.; Kung, A. H. A Differentially Pumped Harmonic Filter on the Chemical Dynamics Beamline at the Advanced Light Source. *Review of Scientific Instruments* **1995**, *66* (10), 4841–4844. https://doi.org/10.1063/1.1146161.

(41) Heimann, P. A.; Koike, M.; Hsu, C. W.; Blank, D.; Yang, X. M.; Suits, A. G.; Lee, Y. T.; Evans, M.; Ng, C. Y.; Flaim, C.; et al. Performance of the Vacuum Ultraviolet High-Resolution and High-Flux Beamline for Chemical Dynamics Studies at the Advanced Light Source. *Review of Scientific Instruments* **1997**, *68* (5), 1945–1951. https://doi.org/10.1063/1.1148082.

(42) Beutler, H. Über Absorptionsserien von Argon, Krypton und Xenon zu Termen zwischen den beiden Ionisierungsgrenzen2P32/0und2P12/0. *Z. Physik* **1935**, *93* (3), 177–196. https://doi.org/10.1007/BF01365116.

(43) L. Dodson. Thesis, California Institute of Technology, 2016.

(44) Person, J. C.; Nicole, P. P. *ANL Radiological Physics Division Annual Report*; ANL-7760; 1970; p 97.

(45) Savee, J. D.; Soorkia, S.; Welz, O.; Selby, T. M.; Taatjes, C. A.; Osborn, D. L. Absolute Photoionization Cross-Section of the Propargyl Radical. *J. Chem. Phys.* **2012**, *136* (13), 134307. https://doi.org/10.1063/1.3698282.

(46) Taatjes, C. A. How Does the Molecular Velocity Distribution Affect Kinetics Measurements by Time-Resolved Mass Spectrometry? *International Journal of Chemical Kinetics* **2007**, *39* (10), 565–570. https://doi.org/10.1002/kin.20262.

(47) Welz, O.; Savee, J. D.; Osborn, D. L.; Vasu, S. S.; Percival, C. J.; Shallcross, D. E.; Taatjes, C. A. Direct Kinetic Measurements of Criegee Intermediate (CH2OO) Formed by Reaction of CH2I with O2. *Science* **2012**, *335* (6065), 204–207. https://doi.org/10.1126/science.1213229.

(48) Beersmans, J.; Jungers, J. C. Synthèse et Étude des Chlorure, Bromure et Iodure de Deutérométhyle. *Bulletin des Sociétés Chimiques Belges* **1947**, *56* (5–8), 238–250. https://doi.org/10.1002/bscb.19470560506.

(49) Person, J. C.; Nicole, P. P. Isotope Effects in the Photoionization Yields and in the Absorption Cross Sections for Methanol, Ethanol, Methyl Bromide, and Ethyl Bromide. *J. Chem. Phys.* **1971**, *55* (7), 3390–3397. https://doi.org/10.1063/1.1676590.

(50) Oliphant, T. E. Python for Scientific Computing. *Computing in Science Engineering* **2007**, *9* (3), 10–20. https://doi.org/10.1109/MCSE.2007.58.

(51) Levenberg, K. A Method for the Solution of Certain Non-Linear Problems in Least Squares. *Quart. Appl. Math.* **1944**, *2* (2), 164–168. https://doi.org/10.1090/qam/10666.

(52) Marquardt, D. An Algorithm for Least-Squares Estimation of Nonlinear Parameters. *Journal of the Society for Industrial and Applied Mathematics* **1963**, *11* (2), 431–441. https://doi.org/10.1137/0111030.
(53) Ruscic, B.; Bross, D. H. ATcT.anl.gov.
(54) Pradhan, M.; Kalberer, M.; Griffiths, P. T.; Braban, C. F.; Pope, F. D.; Cox, R. A.; Lambert, R. M. Uptake of Gaseous Hydrogen Peroxide by Submicrometer Titanium Dioxide Aerosol as a Function of Relative Humidity. *Environ. Sci. Technol.* **2010**, *44* (4), 1360–1365. https://doi.org/10.1021/es902916f.
(55) Pradhan, M.; Kyriakou, G.; Archibald, A. T.; Papageorgiou, A. C.; Kalberer, M.; Lambert, R. M. Heterogeneous Uptake of Gaseous Hydrogen Peroxide by Gobi and Saharan Dust Aerosols: A Potential Missing Sink for H_2O_2 in the Troposphere. *Atmospheric Chemistry and Physics* **2010**, *10* (15), 7127–7136. https://doi.org/10.5194/acp-10-7127-2010.
(56) Zhao, Y.; Chen, Z.; Shen, X.; Zhang, X. Kinetics and Mechanisms of Heterogeneous Reaction of Gaseous Hydrogen Peroxide on Mineral Oxide Particles. *Environ. Sci. Technol.* **2011**, *45* (8), 3317–3324. https://doi.org/10.1021/es104107c.
(57) Efron, B. Bootstrap Methods: Another Look at the Jackknife. *Ann. Statist.* **1979**, *7* (1), 1–26. https://doi.org/10.1214/aos/1176344552.
(58) Towns, J.; Cockerill, T.; Dahan, M.; Foster, I.; Gaither, K.; Grimshaw, A.; Hazlewood, V.; Lathrop, S.; Lifka, D.; Peterson, G. D.; et al. XSEDE: Accelerating Scientific Discovery. *Computing in Science Engineering* **2014**, *16* (5), 62–74. https://doi.org/10.1109/MCSE.2014.80.
(59) Flesch, R.; Schürmann, M. C.; Hunnekuhl, M.; Meiss, H.; Plenge, J.; Rühl, E. A Pump-Probe Photoionization Mass Spectrometer Utilizing Tunable Extreme Ultraviolet Laser-Produced-Plasma Radiation. *Review of Scientific Instruments* **2000**, *71* (3), 1319–1324. https://doi.org/10.1063/1.1150457.
(60) Furlan, A.; Scheld, H. A.; Huber, J. R. The Photodissociation Dynamics of OClO between 306 and 370 Nm: Fragment Translational Energy Release and Recoil Anisotropy. *J. Chem. Phys.* **1997**, *106* (16), 6538–6547. https://doi.org/10.1063/1.473652.
(61) McGrath, W. D.; Norrish, R. G. W. The Study of Energy Transfer and Energy Distributions in Fast Chemical Reactions by Flash Photolysis and Kinetic Spectroscopy. *zpch* **1958**, *15* (1–6), 245. https://doi.org/10.1524/zpch.1958.15.1-6.245.
(62) McGrath W. D.; Norrish Ronald George Wreyford. Studies of the Reactions of Excited Oxygen Atoms and Molecules Produced in the Flash Photolysis of Ozone. *Proceedings of the Royal Society of London. Series A. Mathematical and Physical Sciences* **1960**, *254* (1278), 317–326. https://doi.org/10.1098/rspa.1960.0022.
(63) Matsumi, Y.; Nomura, S.; Kawasaki, M.; Imamura, T. Vibrational Distribution of ClO Radicals Produced in the Reaction Cl + O3 → ClO + O2. *J. Phys. Chem.* **1996**, *100* (1), 176–179. https://doi.org/10.1021/jp9518872.
(64) Baumgärtel, S.; Delmdahl, R. F.; Gericke, K.-H.; Tribukait, A. Reaction Dynamics of Cl OClO O. *Eur. Phys. J. D* **1998**, *4* (2), 199–205. https://doi.org/10.1007/s100530050200.
(65) Burkholder, J. B.; Hammer, P. D.; Howard, C. J.; Goldman, A. Infrared Line Intensity Measurements in the v = 0–1 Band of the ClO Radical. *Journal of*

Geophysical Research: Atmospheres **1989**, *94* (D2), 2225–2234. https://doi.org/10.1029/JD094iD02p02225.

(66) Lang, V. I.; Sander, S. P.; Friedl, R. R. Absolute Infrared Band Strength Measurement of the ClO Radical by Fourier Transform Infrared Spectroscopy. *Journal of Molecular Spectroscopy* **1988**, *132* (1), 89–103. https://doi.org/10.1016/0022-2852(88)90061-6.

(67) LANE, I. C.; ORR-EWING, A. J. A CASSCF/MRCI Study of the Low-Lying Rydberg States of CIO. *Molecular Physics* **2000**, *98* (12), 793–806. https://doi.org/10.1080/00268970009483350.

(68) Klaus P. Huber; Gerhard H. Herzberg. *"Constants of Diatomic Molecules" in NIST Chemistry WebBook, NIST Standard Reference Database Number 69, Eds. P.J. Linstrom and W.G. Mallard*; National Institute of Standards and Technology, Gaithersburg MD, 20899.

(69) Daniel Freeman, C.; Grubb, M. P.; Lane, I. C.; North, S. W. Vibrational State-Selected Photodissociation of ClO+. *Chemical Physics* **2012**, *408*, 43–49. https://doi.org/10.1016/j.chemphys.2012.09.016.

(70) Western, C. M. PGOPHER: A Program for Simulating Rotational, Vibrational and Electronic Spectra. *Journal of Quantitative Spectroscopy and Radiative Transfer* **2017**, *186*, 221–242. https://doi.org/10.1016/j.jqsrt.2016.04.010.

(71) Nickolaisen, S. L.; Friedl, R. R.; Sander, S. P. Kinetics and Mechanism of the Chlorine Oxide ClO + ClO Reaction: Pressure and Temperature Dependences of the Bimolecular and Termolecular Channels and Thermal Decomposition of Chlorine Peroxide. *J. Phys. Chem.* **1994**, *98* (1), 155–169. https://doi.org/10.1021/j100052a027.

(72) Trolier, M.; Mauldin, R. L.; Ravishankara, A. R. Rate Coefficient for the Termolecular Channel of the Self-Reaction of Chlorine Monoxide. *J. Phys. Chem.* **1990**, *94* (12), 4896–4907. https://doi.org/10.1021/j100375a027.

(73) Birk, M.; Friedl, R. R.; Cohen, E. A.; Pickett, H. M.; Sander, S. P. The Rotational Spectrum and Structure of Chlorine Peroxide. *J. Chem. Phys.* **1989**, *91* (11), 6588–6597. https://doi.org/10.1063/1.457377.

(74) Slanina, Z.; Uhlik, F. An Estimation of Dimerization Energetics of the CIO Radical. *Chemical Physics Letters* **1991**, *182* (1), 51–56. https://doi.org/10.1016/0009-2614(91)80102-4.

(75) Stanton, J. F.; Rittby, C. M. L.; Bartlett, R. J.; Toohey, D. W. Low-Lying Isomers of the Chlorine Oxide Dimer: A Theoretical Study. *J. Phys. Chem.* **1991**, *95* (6), 2107–2110. https://doi.org/10.1021/j100159a004.

(76) Lee, T. J.; Rohlfing, C. M.; Rice, J. E. An Extensive Ab Initio Study of the Structures, Vibrational Spectra, Quadratic Force Fields, and Relative Energetics of Three Isomers of Cl2O2. *J. Chem. Phys.* **1992**, *97* (9), 6593–6605. https://doi.org/10.1063/1.463663.

(77) Golden, D. M. Reaction ClO + ClO → Products: Modeling and Parameterization for Use in Atmospheric Models. *International Journal of Chemical Kinetics* **2003**, *35* (5), 206–211. https://doi.org/10.1002/kin.10120.

(78) Baer, S.; Hippler, H.; Rahn, R.; Siefke, M.; Seitzinger, N.; Troe, J. Thermodynamic and Kinetic Properties of the Reaction Cl+O2+M=ClOO+M in the Range 160–300

K and 1–1000 Bar. *J. Chem. Phys.* **1991**, *95* (9), 6463–6470. https://doi.org/10.1063/1.461543.

(79) Green, T. J.; Islam, M.; Guest, P.; Hickson, K.; Canosa-Mas, C. E.; Wayne, R. P. A Discharge-Flow Study of Cl2O3. *Phys. Chem. Chem. Phys.* **2003**, *5* (24), 5409–5418. https://doi.org/10.1039/B311005B.

(80) Burkholder, J. B.; Mauldin, R. L.; Yokelson, R. J.; Solomon, S.; Ravishankara, A. R. Kinetic, Thermochemical, and Spectroscopic Study of Chlorine Oxide (Cl2O3). *J. Phys. Chem.* **1993**, *97* (29), 7597–7605. https://doi.org/10.1021/j100131a032.

2.9 Supplementary Material

2.9.SM1 Energy Resolution Calibration

The lineshape of vacuum ultraviolet (VUV) photons transmitted by the monochromator was measured by scanning over the 8s ← 5p transition of Xe at 12.5752 eV.[1] The broadening of this resonance is entirely instrument-limited. The spectra were measured at the four slit widths most commonly used in these experiments of 45, 250, 425, and 600 μm and found to have ΔE_{FWHM} of 9.9, 18.2, 27.2, and 37.9 meV, respectively. However, it was observed that no single lineshape function could satisfactorily describe the transmitted photons at each slit width. Instead, it was necessary to change the lineshape function to properly fit each spectrum. Figure S1a shows the spectra and their corresponding fits. (The ionization continuum was fit empirically with a linear or quadratic baseline and has been subtracted for clarity.) At 45 μm, the spectrum was best described by a Lorentzian lineshape (fits with a Voigt returned a negligible Gaussian component). At 250 and 425 μm, the spectra were best described by a Gaussian lineshape (fits with a Voigt returned a negligible Lorentzian component). At 600 μm, the lineshape was neither Lorentzian nor Gaussian, and was instead fit with a piecewise linear function.

Despite the difference in lineshapes, the trend in ΔE_{FWHM} as a function of slit width was found to be approximately linear (Figure S1b). For experiments conducted at 45, 250, 425, or 600 μm, we used the value of ΔE_{FWHM} specifically fit from the spectrum acquired at that slit width, and note that the vast majority of experiments were conducted at one of those slit widths. However, for experiments conducted at a different slit width, we used the linear relationship to estimate ΔE_{FWHM}.

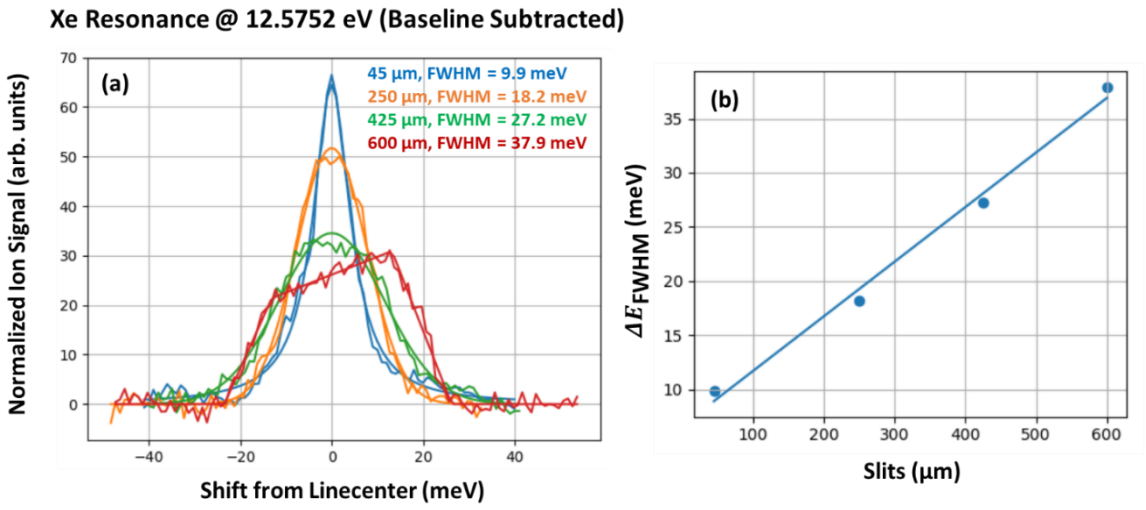

Figure S1: (a) Spectra of Xe acquired over the resonance at 12.5752 eV. The fits are overlaid. The ionization continuum was fit as a linear or quadratic baseline and has been subtracted for clarity. The intensities of the peaks have been normalized to have an area of unity. The spectrum at 45 µm was fit with a Lorentzian, the spectra at 250 and 425 µm were fit with a Gaussian, and the spectrum at 600 µm was fit with a piecewise linear function. **(b)** The fitted ΔE_{FWHM} as a function of slit width. The linear function was used to estimate ΔE_{FWHM} for experiments conducted at slit widths for which a Xe spectrum was not measured.

2.9.SM2 Mass Discrimination Factor Calibration

The ion detection efficiency of a photoionization mass spectrometer is typically mass-dependent when sampling from a molecular beam. To calibrate the mass discrimination, we have followed an approach outlined previously for this instrument.[2] The mass discrimination factor is empirically described as a power law function: $\alpha_i = m_i^{\beta}$. To determine the optimum value of β, we measured the photoionization signals at 18 eV of a mixture of H_2, Ar, Kr and Xe (multiple isotopes of Kr and Xe can be detected), which encompasses a broad range of masses including all species detected in this study. The photoionization signal of these species can be described according to Eqn. 1 in the main text. Rearranging this equation gives:[2]

$$S_i^{\mathrm{adj}} \equiv \frac{S_i}{\sigma_i \cdot N_i \cdot f_i} = \Lambda \cdot \alpha_i = \Lambda \cdot m_i^{\beta} \qquad \text{(Eqn. 1)}$$

where the energy-dependence has been removed since these experiments are conducted solely at 18 eV, and the time-dependence has been removed since the photolysis laser is not fired. The gas tank used as the source of H_2, Ar, Kr, and Xe contains mixing ratios of each species that have been well-calibrated and thus the accuracy of N_i is very good. Similarly, accurate values of σ_i are known for each species at 18 eV.[3,4] With sufficient averaging to acquire good statistics on S_i, the value of S_i^{adj} can calculated with minimal uncertainty. Two-parameter, weighted fits of S_i^{adj} as a function of m_i allow the optimum value of β to be determined. Uncertainty on β is determined by the bootstrap resampling method, as described in the main text.

The value of β has been observed to vary as a function of temperature, pressure, and bath gas composition within the reactor. We therefore performed calibrations at the four combinations of temperature (300 and 210 K) and bath gas composition (4.5% and 0% O_2 in He) used in this work. Each experiment was conducted at 50 Torr. The resulting S_i^{adj} as a function m_i are plotted in Figure S2, where the S_i^{adj} have been normalized by the fitted value of Λ so that the difference of the fitted β between each series can be visualized. For the dataset collected at 210 K and 4.5% O_2, the O_2^+ signal at m/z = 32 was very strong, creating a baseline in the mass spectrum and attenuating signals for a range of masses above this peak. This effect precluded use of ^{40}Ar in the fit, but appeared to have subsided by the ^{80}Kr mass peak. For the dataset collected at 300 K and 4.5% O_2, the effect was more pronounced due to the greater flux of VUV photons from the synchrotron on that day. Even with the monochromator slit width nominally set to 0 μm, the saturated O_2^+ signal led to a baseline and signal attenuation that ranged up to the Xe isotope masses. We therefore could not fit this dataset. However, as evidenced by the 210 K datasets, the addition of 4.5% O_2 to the bath gas appears to alter β to only a minor extent that is within our uncertainty. We therefore assumed that the value of β at 300 K and 4.5% O_2 was the same as that at 300 K and 0% O_2. The calibrated values of β used in this work are tabulated in Table SI.

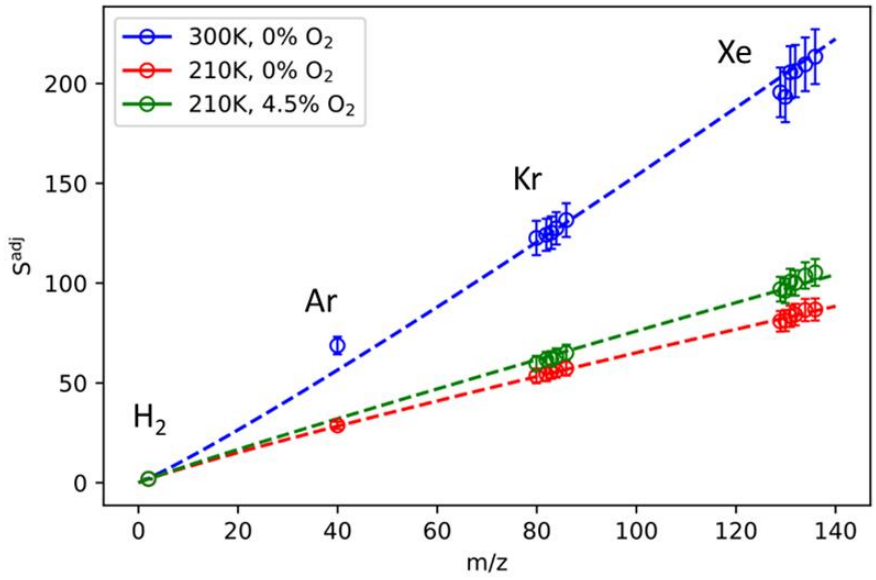

Figure S2: Fits of $S_i^{\text{adj}} = \Lambda \cdot m_i^{\beta}$ at each set of experimental conditions. The 300 K and 4.5% O_2 dataset is omitted for reasons discussed in the text. Each dataset and corresponding fit have been normalized by the fitted value of Λ, so that differences in β can be assessed.

Table SI: Summary of calibrated values of β used to calculate the mass discrimination factors ($\alpha_i = m_i^{\beta}$). Pressure is 50 Torr with a balance of He. Uncertainties represent ±2σ confidence.

T (K)	O_2 Fraction	β
300.6 ± 0.9	0%	1.09 ± 0.14
300.6 ± 0.9	4.5%	1.09 ± 0.14
210 ± 3	0%	0.907 ± 0.017
210 ± 3	4.5%	0.940 ± 0.095

2.9.SM3 Modeling and Calibration of Instrument Effects

In this section, we describe with greater detail the instrument effects referenced in the main text. The treatment of each effect in the kinetic model and the experiments used for calibration are discussed. Our approach is similar to methodology outlined previously.[5,6]

2.9.SM3.1 Photolysis Gradient

The fluence of the unfocused photolysis beam diverges slightly as it propagates through the reactor tube. This creates a spatial gradient in the photolysis fraction, and thus also the initial radical concentration. Because ion signal measured at later reaction times arises from sampling a gas parcel that was photolyzed upstream of the pinhole, the gradient is also temporal and impacts the measured kinetics. The ion signal measured at each time point is generated by chemistry that has propagated from a different initial radical concentration ($[X]$) than other time points. The gradient in $[X]$ can be described through:

$$[X](t) = \phi \cdot \{1 - \exp[-\sigma_{\mathrm{UV}} \cdot F(t)]\} \cdot [Y] \approx \phi \cdot \sigma_{\mathrm{UV}} \cdot F(t) \cdot [Y] \quad (2)$$

where $[Y]$ is the radical precursor concentration, σ_{UV} is the photolysis cross section, ϕ is the quantum yield to produce X, and $F(t)$ is the laser fluence. We note that $[X](t)$ does not correspond to the radical concentration, but rather the *initial* radical concentration of the gas parcel sampled at reaction time t. The linear approximation assumes that the fraction of precursor photolyzed is small (~0.8% in the present work). We define $[X]_0$ and F_0 as the initial radical concentration and laser fluence at pinhole, respectively. Then by differentiating Eqn. 2, we obtain:

$$\frac{1}{[X]_0}\frac{d[X]}{dt} = \frac{1}{F_0}\frac{dF}{dt} \equiv B \quad (3)$$

B represents the fractional change in radical density and fluence per unit time, relative to the pinhole. If we assume the fluence changes linearly along the reactor tube, then B is a constant.

To incorporate the effect of the photolysis gradient on the modeled kinetics, we partitioned the time axis into 1 ms intervals. The initial radical concentration for each time interval was determined by integrating Eqn. 3:

$$[X](t) = [X]_0(1 + B \cdot t) \quad (4)$$

and evaluating at the interval midpoint. To simulate the concentration profile of each species i arising from the chemistry in the model (N_i^{chem}), the system of differential rate equations was integrated in steps. For $t < 0$, each $N_i^{\text{chem}}(t)$ was set to its pre-photolysis concentration. For the 0-1 ms interval, the model was integrated over 0-1 ms, and the result appended to $N_i^{\text{chem}}(t)$. For the 1-2 ms interval, the model was integrated over 0-2 ms, and the 1-2 ms portion was appended to $N_i^{\text{chem}}(t)$. For the 2-3 ms interval, the model was integrated over 0-3 ms, and the 2-3 ms portion was appended to $N_i^{\text{chem}}(t)$. This process was repeated out to 60 ms.

One consequence of this approach is that discontinuities are created at the edges of each time interval. However, because the photolysis gradient is small, the initial radical concentration is similar between adjacent intervals and the discontinuities are imperceptible after convolution with the temporal instrument response function described in the next subsection.

2.9.SM3.2 Temporal Instrument Response

Species sampled from the molecular beam have a distribution of velocities that has been shown to approximate a Maxwell-Boltzmann distribution.[7] The distribution is mass-dependent, with species of greater mass having a broader velocity distribution than those of smaller mass. Due to the finite transit time between exiting the pinhole and detection, ion signal recorded at time t arises from neutrals sampled from the reactor at a distribution of times less than t. In practical terms, changes in the ion signal intensity measured for a species appear slower than true concentration changes of that species within the reactor.

This effect must be integrated into our model in order to accurately compare concentration profiles to time-resolved ion signals and determine cross sections. For a species exiting the reactor at time 0, its distribution of arrival times (t') at the detector is proportional to $h_i(t')$:[5]

$$h_i(t') = \frac{\exp\left(A_{m_i}/t'^2\right)}{t'^4} \tag{5}$$

where $t' > 0$ (species cannot be detected before they exit the reactor) and $A_{m_i} = A \cdot m_i$. A is a negative, mass-independent instrument constant describing the temporal response. Larger absolute values of A indicate a broader distribution of detection times (slower

response) than smaller absolute values of A. After integrating the chemical kinetic model to determine $N_i^{\text{chem}}(t)$, we convolve each profile with the instrument response according to:

$$N_i(t) = \frac{\int_{-\infty}^{t} N_i^{\text{chem}}(s)\, h_i(t-s) ds}{\int_{-\infty}^{t} h_i(t-s)\, ds} \quad (6)$$

where $N_i(t)$ is the simulated concentration profile for comparison to the time-resolved ion signal. The denominator in Eqn. 6 acts as a normalization factor. $N_i(t)$ is effectively a weighted average of the concentration within the reactor across all times less than t, with the weighting set by the distribution of arrival times.

2.9.SM3.3 Photolysis Offset

This effect is a simple offset (t_0) between the predicted and actual firing of the photolysis laser. Concentration profiles are simulated assuming photolysis occurs at t = 0. After these profiles are convolved with the temporal instrument response (Eqn. 3), the model time axis is shifted by t_0 such that photolysis occurs at t = t_0, in proper correspondence with the data time axis.

2.9.SM3.4 Calibration Experiments

The instrument parameters A, B, and t_0 require calibration in order to simulate $N_i(t)$ for ClO and ClOOCl. We determined these instrument constants at 300 and 210 K by 351 nm photolysis of a sample of NO_2 diluted in He:

$$NO_2 + h\nu \rightarrow NO + O \quad (R1)$$

The O atoms react with the excess NO_2 precursor according to:

$$O + NO_2 \rightarrow NO + O_2 \quad (R2)$$

$$O + NO_2 + M \rightarrow NO_3 + M \quad (R3)$$

At the total pressure of 50 Torr and both temperatures, R2 substantially dominates over R3. The total rate constant for the O + NO_2 reaction is 1.0 x 10^{-11} and 1.5 x 10^{-11} cm^3 $molc^{-1}$ s^{-1} at 300 and 210 K, respectively.[8] With the [NO_2] used in these experiments, this leads to an O atom lifetime of τ < 90 μs. Since the data points are binned to 200 μs spacing, the concentration profile of the NO produced from R1 and R2 should appear as a step-function in the absence of any instrument effects, with the step occurring at t = 0. Deviations of the measured NO^+ signal from a step-function act as a probe of the instrument parameters.

The NO^+ signals measured at 300 and 210 K are presented in Figure S3. As expected, the signal rises gradually after photolysis, rather than exhibiting a discrete step, due to the temporal instrument response. After the initial fast rise, the signal has a slower, linear rise due to the photolysis gradient. We first determined B from a linear regression over 20–60 ms. By the definition given in Eqn. 3, B is equal to the fitted slope divided by the fitted intercept. We neglected the first 20 ms to avoid any bias from the initial rise of signal. Over 20–60 ms, the change in signal due to the photolysis gradient is much slower than the instrument response.

We next determined A and t_0. A simple kinetic model was constructed describing the [NO] as a step function. B was fixed at the value determined from the linear regression. Initially, we performed three-parameter fits, simultaneously floating A, t_0, and the NO signal after the step ($S_{\mathrm{NO},\infty}$). However, due to the strong correlation between A and t_0, fits would typically terminate at a local minimum close to the initial guess. In order to find the global minimum across this parameter space, we performed a series of two-parameter fits, in which t_0 was fixed and stepped through an array with 0.01 ms spacing, while A and $S_{\mathrm{NO},\infty}$ were floated. The A and t_0 that led to a global minimum in the residual sum of squares were taken as the instrument parameters. Overlaid on the traces in Figure S3 are the simulated signals from the step-function model implementing the optimized values of A, B, and t_0.

The values of A and t_0 determined at the two temperatures were similar. However, the value of B at 210 K was found to be ~4 times greater than the value at 300 K. This is not due to a difference in the photolysis gradient at the two temperatures, but rather an artifact that arises from the dimerization of NO_2 at cold temperatures. While the rate constant for NO_2 dimerization is not known at 210 K, extrapolation of available data suggests that dimerization has a half-life of order ~100 ms at our conditions.[9] This is sufficiently long that fresh NO_2 dimerizes as it flows through the reactor, leading to a spatial gradient in [NO_2]. Since the [NO] produced upon photolysis is proportional to [NO_2], this yields an additional gradient in initial radical concentration on top of that generated by divergence of the photolysis beam. To explore this effect, we conducted experiments by flowing different [NO_2] through the reactor. Because the dimerization is pseudo bimolecular, changing [NO_2] should result in a different dimerization half-life, and

thus different kinetics. The NO^+ signals measured in these experiments are presented in Figure S4. Despite having approximately the same signal level immediately after photolysis, the shapes of the traces diverge at longer times, reflecting the different rates of NO_2 dimerization.

This effect does not impact our experiments studying ClO and ClOOCl because the radical precursor, Cl_2, is stable at 210 K. The gradient in initial radical concentration in those experiments arises solely from divergence of the photolysis beam. The studies at 300 and 210 K were conducted using the same alignment of the beam through the reactor tube and the rate of divergence does not depend on temperature. We therefore assumed in our 210 K model of ClO and ClOOCl kinetics that the value of B was the same as the value determined from 300 K NO_2 photolysis. We note that the values of A and t_0 determined from 210 K NO_2 photolysis were not impacted by NO_2 dimerization since the value of B used in those fits encompassed both gradients (Figure S3b).

The final values of A, B, and t_0 determined from the NO_2 photolysis experiments and used to model ClO and ClOOCl kinetics are presented in Table SII. The instrument response was slightly slower at 210 K than at 300 K, although only to a minor extent.

Table SII: Values of temporal response (A), photolysis gradient (B), and photolysis offset (t_0) instrument parameters used to model ClO and ClOOCl concentration profiles.

T (K)	A (ms^2 amu^{-1})	B (ms^{-1})	t_0 (ms)
300.6 ± 0.9	-0.0306	0.00271	-0.60
210 ± 3	-0.0377	0.00271	-0.63

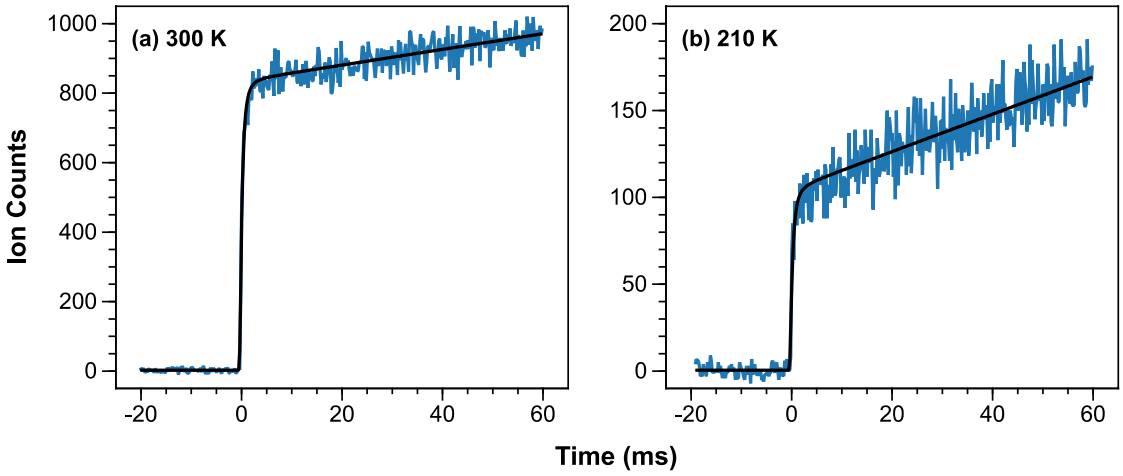

Figure S3: NO^+ signals (blue) recorded in experiments photolyzing NO_2. The step-function model implementing optimized values of the instrument parameters is overlaid (black). **(a)** 300 K, 10.0 eV, and $[NO_2] = 3.74 \times 10^{15}$ molc cm^{-3}. The fitted value of B = 0.00271 ms^{-1} corresponds to an initial radical concentration gradient arising from solely divergence of the photolysis beam. **(b)** 210 K, 10.1 eV, and $[NO_2] = 7.67 \times 10^{14}$ molc cm^{-3}. The fitted value of B = 0.0103 ms^{-1} corresponds to an initial radical concentration gradient arising from divergence of the photolysis beam and a gradient in the NO_2 precursor concentration.

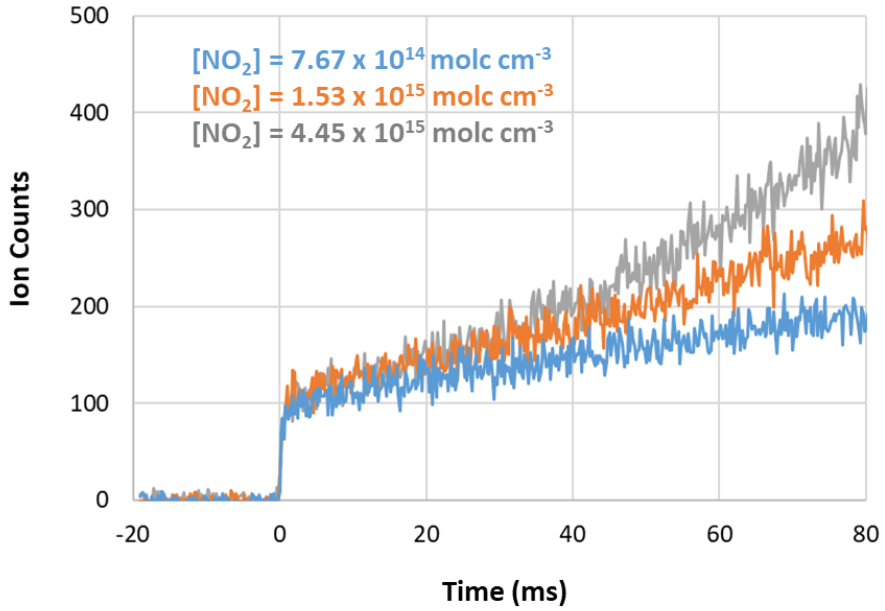

Figure S4: NO^+ signals recorded at 210 K and 10.1 eV in experiments photolyzing different concentrations of NO_2.

2.9.SM4 Tabulated Cross Sections

Table SIII: Single energy cross sections of CH_3Br. The value at 300 K is an average across measurements performed with ΔE_{FWHM} = 9.9, 11.7, 14.2, 18.2, 27.2, and 37.9 meV. The values at 210 K are an average across measurements performed with E_{FWHM} = 9.9, 18.2, 27.2, and 37.9 meV and are plotted in Figure 1 of the main text. Uncertainties represent ±2σ confidence.

T (K)	Energy (eV)	σ_{CH_3Br} (Mb)
300.6 ± 0.9	11.174	36.9 ± 8.5
210 ± 3	11.083	38.4 ± 7.8
210 ± 3	11.174	37.6 ± 7.6
210 ± 3	11.315	33.7 ± 6.8

Table SIV: Absolute photoionization cross sections of CH_3Br. These values are an average of four spectra recorded over ΔE_{FWHM} = 7.8–9.9 meV and at 300 and 210 K. The data are plotted in Figure 1 of the main text. Uncertainties represent ±2σ confidence.

Energy (eV)	σ_{CH_3Br} (Mb)	Energy (eV)	σ_{CH_3Br} (Mb)	Energy (eV)	σ_{CH_3Br} (Mb)
10.121	0.007 ± 0.010	10.801	24.4 ± 5.7	11.301	34.8 ± 8.1
10.146	0	10.811	24.5 ± 5.8	11.311	34.6 ± 8.1
10.171	0.003 ± 0.007	10.821	24.6 ± 5.8	11.321	34.5 ± 8.1
10.196	0.007 ± 0.010	10.831	24.2 ± 5.7	11.331	34.6 ± 8.1
10.221	0	10.841	26.4 ± 6.2	11.341	34.8 ± 8.1
10.246	0.006 ± 0.008	10.851	29.6 ± 7.0	11.351	34.4 ± 8.1
10.271	0.006 ± 0.009	10.861	31.5 ± 7.4	11.361	34.7 ± 8.1
10.296	0.015 ± 0.014	10.871	32.1 ± 7.5	11.371	35.3 ± 8.3
10.321	0.007 ± 0.008	10.881	33.0 ± 7.7	11.381	34.8 ± 8.2
10.346	0.037 ± 0.022	10.891	32.6 ± 7.7	11.391	34.6 ± 8.1
10.371	0.058 ± 0.028	10.901	33.4 ± 7.8	11.401	34.8 ± 8.1
10.396	0.057 ± 0.028	10.911	34.0 ± 8.0	11.411	34.6 ± 8.1

10.421	0.15 ± 0.05	10.921	34.3 ± 8.0	11.421	34.4 ± 8.0
10.431	0.15 ± 0.05	10.931	35.4 ± 8.3	11.431	34.8 ± 8.2
10.441	0.16 ± 0.06	10.941	35.6 ± 8.4	11.441	34.3 ± 8.0
10.451	0.21 ± 0.07	10.951	35.1 ± 8.2	11.451	35.6 ± 8.4
10.461	0.32 ± 0.09	10.961	35.2 ± 8.3	11.461	34.3 ± 8.0
10.471	0.35 ± 0.10	10.971	34.7 ± 8.2	11.471	35.3 ± 8.3
10.481	0.42 ± 0.12	10.981	35.5 ± 8.3	11.481	35.4 ± 8.3
10.491	0.51 ± 0.14	10.991	35.1 ± 8.2	11.491	35.5 ± 8.3
10.501	0.67 ± 0.18	11.001	36.0 ± 8.4	11.501	34.9 ± 8.2
10.511	1.07 ± 0.27	11.011	35.9 ± 8.4	11.511	35.0 ± 8.2
10.521	2.24 ± 0.55	11.021	37.0 ± 8.7	11.521	35.3 ± 8.3
10.531	5.8 ± 1.4	11.031	36.9 ± 8.6	11.531	35.3 ± 8.3
10.541	12.5 ± 3.0	11.041	37.2 ± 8.7	11.541	34.2 ± 8.1
10.551	13.8 ± 3.3	11.051	36.3 ± 8.5	11.551	35.7 ± 8.4
10.561	15.4 ± 3.7	11.061	37.3 ± 8.7	11.561	34.4 ± 8.1
10.571	18.9 ± 4.5	11.071	37.1 ± 8.7	11.571	34.8 ± 8.2
10.581	17.3 ± 4.1	11.081	37.0 ± 8.7	11.581	34.8 ± 8.2
10.591	16.2 ± 3.9	11.091	37.4 ± 8.8	11.591	35.1 ± 8.3
10.601	15.6 ± 3.7	11.101	37.8 ± 8.8	11.601	35.5 ± 8.4
10.611	15.5 ± 3.7	11.111	36.8 ± 8.6	11.611	34.1 ± 8.1
10.621	15.3 ± 3.6	11.121	36.7 ± 8.6	11.621	33.8 ± 8.1
10.631	17.4 ± 4.1	11.131	36.7 ± 8.6	11.631	35.3 ± 8.5
10.641	20.6 ± 4.9	11.141	36.5 ± 8.5	11.641	35.6 ± 8.5
10.651	20.1 ± 4.8	11.151	36.6 ± 8.6	11.651	35.7 ± 8.4
10.661	18.7 ± 4.4	11.161	36.8 ± 8.6	11.661	35.7 ± 8.4
10.671	17.8 ± 4.2	11.171	36.6 ± 8.6	11.671	35.8 ± 8.5
10.681	19.4 ± 4.6	11.181	36.4 ± 8.5	11.681	36.3 ± 8.6
10.691	20.6 ± 4.9	11.191	36.2 ± 8.5	11.691	35.8 ± 8.4
10.701	20.7 ± 4.9	11.201	35.9 ± 8.4	11.701	35.9 ± 8.5
10.711	20.6 ± 4.9	11.211	36.1 ± 8.5	11.711	36.2 ± 8.5
10.721	24.3 ± 5.7	11.221	36.0 ± 8.4	11.721	36.1 ± 8.5
10.731	22.5 ± 5.3	11.231	36.0 ± 8.4	11.731	36.0 ± 8.5
10.741	23.4 ± 5.5	11.241	35.6 ± 8.3	11.741	36.7 ± 8.7
10.751	23.8 ± 5.6	11.251	35.3 ± 8.3	11.751	36.9 ± 8.7
10.761	23.9 ± 5.6	11.261	36.1 ± 8.5	11.761	37.2 ± 8.8
10.771	23.3 ± 5.5	11.271	35.4 ± 8.3	11.771	37.4 ± 8.8
10.781	22.8 ± 5.4	11.281	35.4 ± 8.3	11.781	37.3 ± 8.8
10.791	24.2 ± 5.7	11.291	35.4 ± 8.3	11.791	37.9 ± 9.1

Table SV: Absolute photoionization cross sections of ClO. These values are obtained by scaling a relative spectrum recorded with ΔE_{FWHM} = 9.7 meV at 210 K to the single energy cross sections reported in Table 3 of the main text. The data are plotted in Figure 2a of the main text. Uncertainties represent ±2σ confidence.

Energy (eV)	σ_{ClO} **(Mb)**	**Energy (eV)**	σ_{ClO} **(Mb)**	**Energy (eV)**	σ_{ClO} **(Mb)**
10.417	0.003 ± 0.005	10.877	3.95 ± 0.93	11.337	24.1 ± 5.6
10.427	0	10.887	4.17 ± 0.98	11.347	23.2 ± 5.4
10.437	0.002 ± 0.005	10.897	3.27 ± 0.78	11.357	19.7 ± 4.6
10.447	0	10.907	4.8 ± 1.1	11.367	16.4 ± 3.8
10.457	0.005 ± 0.007	10.917	4.6 ± 1.1	11.377	24.0 ± 5.6
10.467	0.003 ± 0.005	10.927	2.7 ± 0.6	11.387	26.4 ± 6.1
10.477	0.005 ± 0.007	10.937	2.6 ± 0.6	11.397	27.8 ± 6.4
10.487	0.002 ± 0.005	10.947	2.8 ± 0.7	11.407	27.0 ± 6.3
10.497	0	10.957	4.0 ± 0.9	11.417	30.2 ± 7.0
10.507	0.004 ± 0.006	10.967	4.7 ± 1.1	11.427	25.4 ± 5.9
10.517	0.005 ± 0.007	10.977	6.9 ± 1.6	11.437	18.8 ± 4.4
10.527	0.005 ± 0.008	10.987	4.2 ± 1.0	11.447	26.4 ± 6.1
10.537	0.009 ± 0.009	10.997	5.5 ± 1.3	11.457	24.3 ± 5.6
10.547	0.012 ± 0.011	11.007	7.8 ± 1.8	11.467	27.4 ± 6.3
10.557	0.009 ± 0.009	11.017	14.2 ± 3.3	11.477	29.3 ± 6.8
10.567	0.019 ± 0.014	11.027	10.4 ± 2.4	11.487	30.5 ± 7.1
10.577	0.007 ± 0.008	11.037	9.7 ± 2.3	11.497	29.8 ± 6.9
10.587	0.012 ± 0.011	11.047	7.2 ± 1.7	11.507	32.4 ± 7.5
10.597	0.005 ± 0.007	11.057	6.2 ± 1.5	11.517	28.5 ± 6.6
10.607	0.014 ± 0.012	11.067	6.4 ± 1.5	11.527	28.6 ± 6.6
10.617	0.014 ± 0.012	11.077	7.0 ± 1.6	11.537	25.0 ± 5.8
10.627	0.009 ± 0.010	11.087	6.9 ± 1.6	11.547	24.2 ± 5.6
10.637	0.009 ± 0.009	11.097	8.0 ± 1.9	11.557	18.0 ± 4.2
10.647	0.009 ± 0.010	11.107	9.8 ± 2.3	11.567	18.6 ± 4.3
10.657	0.017 ± 0.013	11.117	11.6 ± 2.7	11.577	18.1 ± 4.2
10.667	0.027 ± 0.017	11.127	8.7 ± 2.0	11.587	28.1 ± 6.5
10.677	0.007 ± 0.008	11.137	10.5 ± 2.4	11.597	26.2 ± 6.1
10.687	0.024 ± 0.016	11.147	18.9 ± 4.4	11.607	23.0 ± 5.4
10.697	0.028 ± 0.018	11.157	12.2 ± 2.8	11.617	23.4 ± 5.6
10.707	0.030 ± 0.018	11.167	11.1 ± 2.6	11.627	26.6 ± 6.2

10.717	0.026 ± 0.017	11.177	11.4 ± 2.7	11.637	30.0 ± 6.9
10.727	0.027 ± 0.017	11.187	12.0 ± 2.8	11.647	27.9 ± 6.5
10.737	0.045 ± 0.023	11.197	18.1 ± 4.2	11.657	27.4 ± 6.3
10.747	0.037 ± 0.021	11.207	12.9 ± 3.0	11.667	29.4 ± 6.8
10.757	0.041 ± 0.022	11.217	11.5 ± 2.7	11.677	29.9 ± 6.9
10.767	0.10 ± 0.04	11.227	18.5 ± 4.3	11.687	22.6 ± 5.2
10.777	0.10 ± 0.04	11.237	26.8 ± 6.2	11.697	23.1 ± 5.4
10.787	0.13 ± 0.05	11.247	11.6 ± 2.7	11.707	33.6 ± 7.8
10.797	0.13 ± 0.05	11.257	16.5 ± 3.8	11.717	33.1 ± 7.7
10.807	0.17 ± 0.06	11.267	21.8 ± 5.0	11.727	33.9 ± 7.8
10.817	0.16 ± 0.05	11.277	19.4 ± 4.5	11.737	32.7 ± 7.6
10.827	0.34 ± 0.10	11.287	15.2 ± 3.5	11.747	35.0 ± 8.1
10.837	0.71 ± 0.18	11.297	18.5 ± 4.3	11.757	34.5 ± 8.0
10.847	0.58 ± 0.15	11.307	21.0 ± 4.9	11.767	29.4 ± 6.8
10.857	0.65 ± 0.17	11.317	22.4 ± 5.2	11.777	28.4 ± 6.6
10.867	1.74 ± 0.42	11.327	22.5 ± 5.2		

Table SVI: Absolute photoionization cross sections of ClO. These values are obtained by scaling a relative spectrum recorded with ΔE_{FWHM} = 18.2 meV at 210 K to the single energy cross sections reported in Table 3 of the main text. The data are plotted in Figure 2a of the main text. Uncertainties represent ±2σ confidence.

Energy (eV)	σ_{ClO} **(Mb)**	**Energy (eV)**	σ_{ClO} **(Mb)**	**Energy (eV)**	σ_{ClO} **(Mb)**
10.722	0.021 ± 0.015	11.002	7.0 ± 1.6	11.282	19.1 ± 4.4
10.732	0.032 ± 0.019	11.012	9.9 ± 2.3	11.292	17.5 ± 4.0
10.742	0.053 ± 0.026	11.022	13.6 ± 3.2	11.302	19.6 ± 4.5
10.752	0.047 ± 0.023	11.032	11.7 ± 2.7	11.312	21.3 ± 4.9
10.762	0.081 ± 0.033	11.042	8.6 ± 2.0	11.322	21.5 ± 5.0
10.772	0.11 ± 0.04	11.052	7.2 ± 1.7	11.332	24.4 ± 5.6
10.782	0.16 ± 0.05	11.062	6.5 ± 1.5	11.342	25.0 ± 5.8
10.792	0.13 ± 0.04	11.072	6.9 ± 1.6	11.352	23.0 ± 5.3
10.802	0.15 ± 0.05	11.082	7.3 ± 1.7	11.362	19.0 ± 4.4
10.812	0.20 ± 0.06	11.092	8.1 ± 1.9	11.372	20.2 ± 4.7
10.822	0.26 ± 0.08	11.102	9.3 ± 2.1	11.382	26.0 ± 6.0

10.832	0.48 ± 0.13	11.112	10.7 ± 2.5	11.392	27.6 ± 6.4
10.842	0.65 ± 0.17	11.122	11.1 ± 2.6	11.402	28.6 ± 6.6
10.852	0.79 ± 0.20	11.132	10.4 ± 2.4	11.412	29.0 ± 6.7
10.862	1.07 ± 0.26	11.142	13.5 ± 3.1	11.422	30.3 ± 7.0
10.872	3.02 ± 0.71	11.152	16.3 ± 3.8	11.432	25.4 ± 5.9
10.882	5.3 ± 1.2	11.162	13.7 ± 3.2	11.442	22.7 ± 5.2
10.892	4.0 ± 0.9	11.172	12.4 ± 2.9	11.452	26.3 ± 6.1
10.902	4.1 ± 1.0	11.182	11.9 ± 2.8	11.462	25.6 ± 5.9
10.912	3.9 ± 0.9	11.192	13.9 ± 3.2	11.472	30.3 ± 7.0
10.922	3.2 ± 0.7	11.202	16.8 ± 3.9	11.482	30.4 ± 7.0
10.932	2.6 ± 0.6	11.212	13.1 ± 3.0	11.492	32.0 ± 7.4
10.942	2.9 ± 0.7	11.222	14.0 ± 3.2	11.502	32.6 ± 7.5
10.952	3.7 ± 0.9	11.232	22.2 ± 5.1	11.512	33.0 ± 7.6
10.962	5.0 ± 1.2	11.242	22.0 ± 5.1	11.522	30.4 ± 7.0
10.972	5.8 ± 1.3	11.252	15.1 ± 3.5	11.532	30.7 ± 7.1
10.982	5.2 ± 1.2	11.262	18.8 ± 4.3		
10.992	4.5 ± 1.1	11.272	20.9 ± 4.8		

Table SVII: Absolute photoionization cross sections of ClOOCl. These values are obtained by scaling a relative spectrum recorded with ΔE_{FWHM} = 9.7 meV at 210 K to the single energy cross sections reported in Table 3 of the main text. The data are plotted in Figure 2b of the main text. Uncertainties represent ±2σ confidence.

Energy (eV)	σ_{ClOOCl} **(Mb)**	**Energy (eV)**	σ_{ClOOCl} **(Mb)**	**Energy (eV)**	σ_{ClOOCl} **(Mb)**
10.417	0.024 ± 0.049	10.877	0.02 ± 0.04	11.337	8.8 ± 3.6
10.427	0	10.887	0.07 ± 0.08	11.347	9.4 ± 3.8
10.437	0	10.897	0.18 ± 0.14	11.357	9.7 ± 3.9
10.447	0.039 ± 0.058	10.907	0.09 ± 0.09	11.367	7.8 ± 3.2
10.457	0.024 ± 0.048	10.917	0.18 ± 0.15	11.377	9.4 ± 3.8
10.467	0	10.927	0.15 ± 0.13	11.387	8.3 ± 3.4
10.477	0.023 ± 0.046	10.937	0.15 ± 0.13	11.397	9.1 ± 3.7
10.487	0.043 ± 0.063	10.947	0.13 ± 0.12	11.407	9.2 ± 3.7
10.497	0.042 ± 0.062	10.957	0.29 ± 0.20	11.417	7.7 ± 3.1
10.507	0	10.967	0.23 ± 0.17	11.427	8.7 ± 3.5

10.517	0.023 ± 0.047	10.977	0.38 ± 0.24	11.437	7.8 ± 3.2
10.527	0.024 ± 0.050	10.987	0.23 ± 0.17	11.447	7.6 ± 3.1
10.537	0.021 ± 0.043	10.997	0.31 ± 0.21	11.457	7.1 ± 2.9
10.547	0.022 ± 0.044	11.007	0.27 ± 0.19	11.467	8.2 ± 3.4
10.557	0.021 ± 0.043	11.017	0.50 ± 0.29	11.477	7.9 ± 3.2
10.567	0	11.027	0.41 ± 0.25	11.487	7.1 ± 2.9
10.577	0.021 ± 0.043	11.037	0.67 ± 0.36	11.497	7.8 ± 3.2
10.587	0	11.047	0.53 ± 0.30	11.507	8.5 ± 3.5
10.597	0	11.057	0.77 ± 0.40	11.517	8.0 ± 3.3
10.607	0	11.067	1.04 ± 0.51	11.527	7.2 ± 2.9
10.617	0.044 ± 0.064	11.077	0.96 ± 0.48	11.537	8.0 ± 3.3
10.627	0	11.087	0.95 ± 0.48	11.547	7.6 ± 3.1
10.637	0.083 ± 0.090	11.097	1.12 ± 0.55	11.557	7.4 ± 3.0
10.647	0.043 ± 0.064	11.107	1.58 ± 0.73	11.567	7.7 ± 3.2
10.657	0	11.117	1.63 ± 0.75	11.577	6.8 ± 2.8
10.667	0	11.127	1.80 ± 0.82	11.587	6.7 ± 2.8
10.677	0.066 ± 0.081	11.137	2.5 ± 1.1	11.597	7.3 ± 3.0
10.687	0.065 ± 0.080	11.147	2.6 ± 1.1	11.607	6.6 ± 2.9
10.697	0.044 ± 0.064	11.157	2.5 ± 1.1	11.617	7.6 ± 3.7
10.707	0.022 ± 0.044	11.167	2.4 ± 1.1	11.627	6.4 ± 2.8
10.717	0.022 ± 0.045	11.177	3.6 ± 1.5	11.637	6.8 ± 2.8
10.727	0.021 ± 0.043	11.187	3.6 ± 1.5	11.647	7.4 ± 3.0
10.737	0.022 ± 0.044	11.197	4.6 ± 1.9	11.657	7.1 ± 2.9
10.747	0.090 ± 0.096	11.207	4.4 ± 1.8	11.667	7.5 ± 3.0
10.757	0.088 ± 0.094	11.217	5.1 ± 2.1	11.677	6.2 ± 2.5
10.767	0.022 ± 0.045	11.227	6.0 ± 2.5	11.687	7.1 ± 2.9
10.777	0.044 ± 0.064	11.237	7.0 ± 2.9	11.697	6.6 ± 2.7
10.787	0	11.247	7.1 ± 2.9	11.707	6.2 ± 2.6
10.797	0.042 ± 0.062	11.257	8.1 ± 3.3	11.717	7.2 ± 2.9
10.807	0.064 ± 0.079	11.267	9.1 ± 3.7	11.727	6.5 ± 2.7
10.817	0.022 ± 0.044	11.277	9.2 ± 3.7	11.737	7.0 ± 2.9
10.827	0.064 ± 0.077	11.287	10.2 ± 4.1	11.747	7.3 ± 3.0
10.837	0.20 ± 0.15	11.297	10.1 ± 4.1	11.757	6.7 ± 2.8
10.847	0.09 ± 0.10	11.307	9.8 ± 4.0	11.767	6.8 ± 2.8
10.857	0.04 ± 0.06	11.317	10.2 ± 4.1	11.777	8.6 ± 3.6
10.867	0.11 ± 0.10	11.327	10.1 ± 4.1		

Table SVIII: Absolute photoionization cross sections of ClOOCl. These values are obtained by scaling a relative spectrum recorded with ΔE_{FWHM} = 18.2 meV at 210 K to the single energy cross sections reported in Table 3 of the main text. The data are plotted in Figure 2b of the main text. Uncertainties represent ±2σ confidence.

Energy (eV)	σ_{ClOOCl} **(Mb)**	**Energy (eV)**	σ_{ClOOCl} **(Mb)**	**Energy (eV)**	σ_{ClOOCl} **(Mb)**
10.722	0.020 ± 0.022	11.002	0.41 ± 0.18	11.282	9.7 ± 3.8
10.732	0.030 ± 0.027	11.012	0.41 ± 0.18	11.292	10.0 ± 3.9
10.742	0.026 ± 0.025	11.022	0.51 ± 0.22	11.302	10.3 ± 4.1
10.752	0.020 ± 0.021	11.032	0.62 ± 0.26	11.312	10.1 ± 4.0
10.762	0.029 ± 0.026	11.042	0.69 ± 0.29	11.322	10.1 ± 4.0
10.772	0.073 ± 0.048	11.052	0.65 ± 0.27	11.332	9.9 ± 3.9
10.782	0.034 ± 0.029	11.062	0.77 ± 0.32	11.342	9.8 ± 3.8
10.792	0.034 ± 0.029	11.072	0.90 ± 0.37	11.352	9.5 ± 3.7
10.802	0.041 ± 0.032	11.082	1.03 ± 0.42	11.362	9.3 ± 3.7
10.812	0.058 ± 0.041	11.092	1.21 ± 0.49	11.372	9.2 ± 3.6
10.822	0.042 ± 0.032	11.102	1.36 ± 0.55	11.382	9.4 ± 3.7
10.832	0.046 ± 0.034	11.112	1.53 ± 0.62	11.392	8.6 ± 3.4
10.842	0.067 ± 0.044	11.122	1.62 ± 0.65	11.402	8.2 ± 3.2
10.852	0.073 ± 0.046	11.132	2.00 ± 0.80	11.412	8.7 ± 3.4
10.862	0.083 ± 0.050	11.142	2.23 ± 0.89	11.422	8.0 ± 3.1
10.872	0.11 ± 0.06	11.152	2.50 ± 1.00	11.432	8.4 ± 3.3
10.882	0.07 ± 0.05	11.162	2.8 ± 1.1	11.442	7.6 ± 3.0
10.892	0.09 ± 0.05	11.172	3.2 ± 1.3	11.452	8.3 ± 3.2
10.902	0.11 ± 0.06	11.182	3.8 ± 1.5	11.462	7.6 ± 3.0
10.912	0.12 ± 0.06	11.192	3.9 ± 1.6	11.472	8.0 ± 3.2
10.922	0.15 ± 0.08	11.202	4.4 ± 1.8	11.482	7.8 ± 3.1
10.932	0.17 ± 0.08	11.212	4.9 ± 1.9	11.492	7.8 ± 3.1
10.942	0.16 ± 0.08	11.222	5.8 ± 2.3	11.502	7.8 ± 3.1
10.952	0.17 ± 0.09	11.232	6.5 ± 2.6	11.512	7.8 ± 3.1
10.962	0.23 ± 0.11	11.242	7.1 ± 2.8	11.522	7.7 ± 3.0
10.972	0.25 ± 0.12	11.252	7.8 ± 3.1	11.532	8.0 ± 3.2
10.982	0.32 ± 0.14	11.262	8.5 ± 3.3		
10.992	0.30 ± 0.14	11.272	9.1 ± 3.6		

2.9.SM5 Additional Spectra and Kinetics

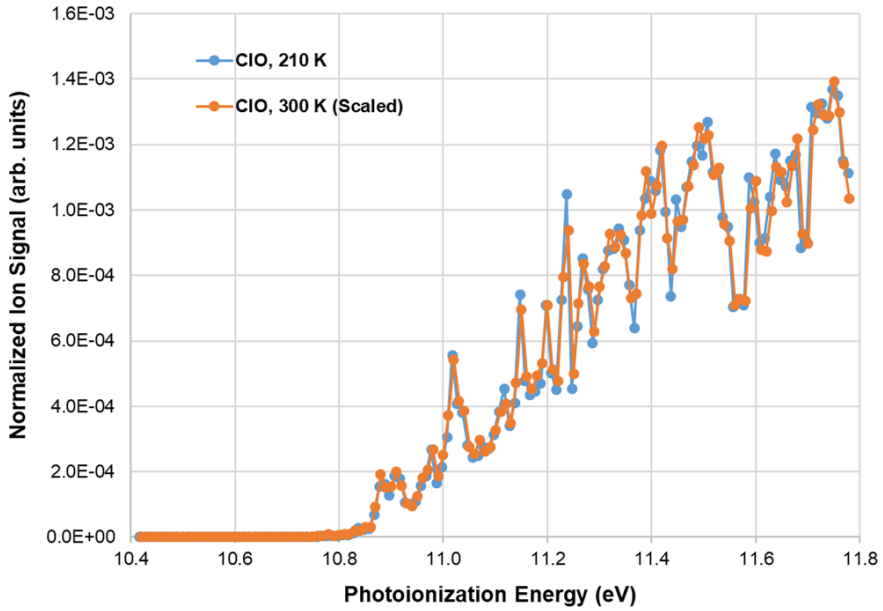

Figure S5: Relative photoionization spectra of ClO acquired in experiments conducted at 300 K (ΔE_{FWHM} = 7.9 meV) and 210 K (ΔE_{FWHM} = 9.7 meV). The 300 K spectrum was arbitrarily scaled to compare its shape to the 210 K spectrum.

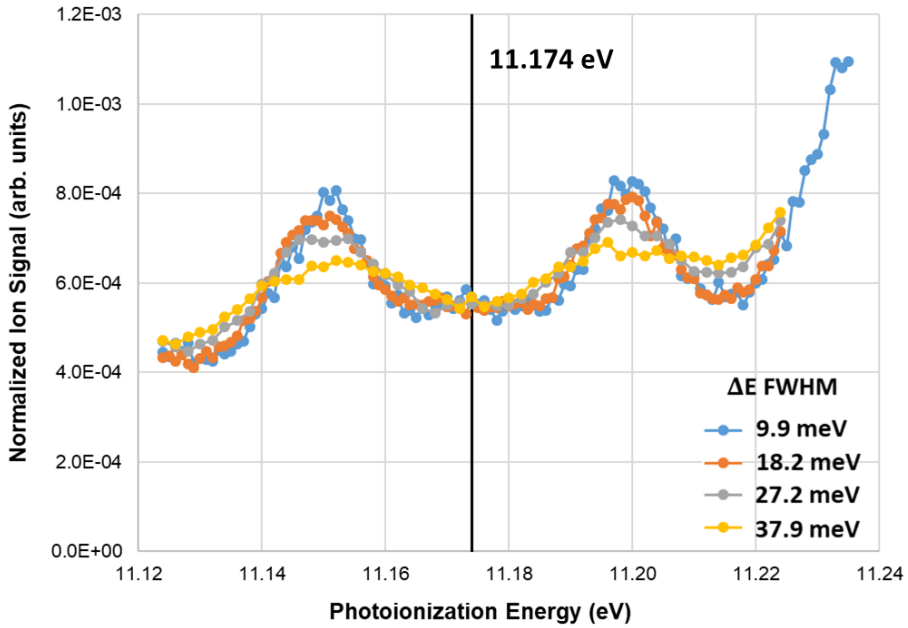

Figure S6: Relative photoionization spectra of ClO acquired at 300 K with a 1–2 meV step size and ΔE_{FWHM} = 9.9, 18.2, 27.2, and 37.9 meV. The single energy used for measurement of an absolute cross section is labeled. The spectra were normalized such that their intensities could be compared, according to the procedure described in the main text for the narrow energy range spectra at 210 K. This figure is the same as Figure 3a in the main text, but at 300 K.

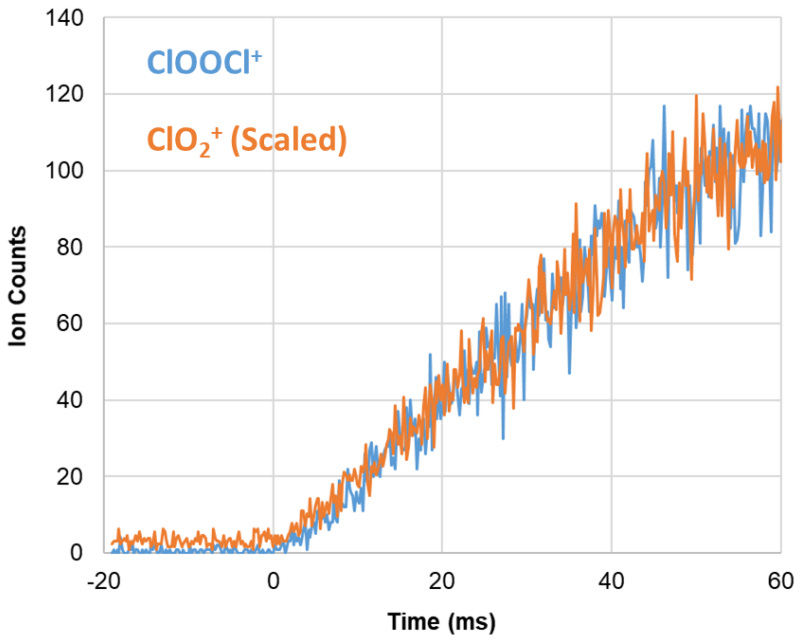

Figure S7: $ClOOCl^+$ and ClO_2^+ kinetics, obtained by integrating their time-resolved signals across all energies in a photoionization energy scan over 10.7–11.5 eV (10 meV steps, ΔE_{FWHM} = 18.2 meV). The ClO_2^+ signal was arbitrarily scaled for comparison to $ClOOCl^+$. The agreement of the kinetics supports the theory that ClO_2^+ arises from dissociative ionization of ClOOCl.

2.9.SM6 Supplementary Material References

(1) Beutler, H. Über Absorptionsserien von Argon, Krypton und Xenon zu Termen zwischen den beiden Ionisierungsgrenzen2P32/0und2P12/0. *Z. Physik* **1935**, *93* (3), 177–196. https://doi.org/10.1007/BF01365116.

(2) Savee, J. D.; Soorkia, S.; Welz, O.; Selby, T. M.; Taatjes, C. A.; Osborn, D. L. Absolute Photoionization Cross-Section of the Propargyl Radical. *J. Chem. Phys.* **2012**, *136* (13), 134307. https://doi.org/10.1063/1.3698282.

(3) Samson, J. A. R.; Stolte, W. C. Precision Measurements of the Total Photoionization Cross-Sections of He, Ne, Ar, Kr, and Xe. *Journal of Electron Spectroscopy and Related Phenomena* **2002**, *123* (2), 265–276. https://doi.org/10.1016/S0368-2048(02)00026-9.

(4) Chung, Y. M.; Lee, E. -M.; Masuoka, T.; Samson, J. A. R. Dissociative Photoionization of H2 from 18 to 124 EV. *J. Chem. Phys.* **1993**, *99* (2), 885–889. https://doi.org/10.1063/1.465352.

(5) Welz, O.; Savee, J. D.; Osborn, D. L.; Vasu, S. S.; Percival, C. J.; Shallcross, D. E.; Taatjes, C. A. Direct Kinetic Measurements of Criegee Intermediate (CH2OO) Formed by Reaction of CH2I with O2. *Science* **2012**, *335* (6065), 204–207. https://doi.org/10.1126/science.1213229.

(6) Dodson, L. G.; Shen, L.; Savee, J. D.; Eddingsaas, N. C.; Welz, O.; Taatjes, C. A.; Osborn, D. L.; Sander, S. P.; Okumura, M. VUV Photoionization Cross Sections of HO2, H2O2, and H2CO. *J. Phys. Chem. A* **2015**, *119* (8), 1279–1291. https://doi.org/10.1021/jp508942a.

(7) Taatjes, C. A. How Does the Molecular Velocity Distribution Affect Kinetics Measurements by Time-Resolved Mass Spectrometry? *International Journal of Chemical Kinetics* **2007**, *39* (10), 565–570. https://doi.org/10.1002/kin.20262.

(8) Burkholder, J. B.; Sander, S. P.; Abbatt, J. P. D.; Barker, J. R.; Huie, R. E.; Kolb, C. E.; Kurylo, M. J.; Orkin, V. L.; Wilmouth, D. M.; Wine, P. H. *Chemical Kinetics and Photochemical Data for Use in Atmospheric Studies: Evaluation Number 18*; Pasadena, CA: Jet Propulsion Laboratory, National Aeronautics and Space …, 2015.

(9) Borrell, P.; Cobos, C. J.; Luther, K. Falloff Curve and Specific Rate Constants for the Reaction Nitrogen Dioxide + Nitrogen Dioxide .Dblarw. Nitrogen Oxide (N2O4). *J. Phys. Chem.* **1988**, *92* (15), 4377–4384. https://doi.org/10.1021/j100326a027.

This page intentionally left blank.

Chapter 3

Kinetics of Chlorine-Substituted Peroxy Radicals

Organic peroxy radicals are ubiquitous intermediates in atmospheric chemistry. Their competing fates can terminate or propagate free radical chemistry in an oxidation mechanism. Atomic chlorine is a minor tropospheric oxidant, found in marine and coastal regions, which reacts with volatile alkenes to yield chlorine-substituted peroxy radicals ($ClRO_2$). The kinetics of these species have not been the subject of prior systematic study. In this chapter, we investigated the kinetics of $ClRO_2$ radicals using pulsed cavity ringdown spectroscopy to probe their $\tilde{A} \leftarrow \tilde{X}$ transition in the near-IR. Unlike the more commonly studied $\tilde{B} \leftarrow \tilde{X}$ transition, the $\tilde{A} \leftarrow \tilde{X}$ transition of peroxy radicals is between two bound electronic states and yields detailed absorption spectra that vary with molecular structure. Of particular importance is that absorption by HO_2, a byproduct of almost all organic peroxy radical chemistry, is well isolated. We first present measurements of the association rate constant of β-chloroethyl radicals with O_2 to form β-chloroethyl peroxy (β-CEP). The methodology outlined serves as a generalized approach for measurements of association rate constants to form peroxy radicals. We next present studies of the self and cross reactions of β-CEP and HO_2. The cross reaction rate constant was found to be substantially slower than a prior indirect determination and the branching ratio of the β-CEP self reaction was found to differ from the results of stable product studies. In support of this work, the absolute absorption cross section of β-CEP at 7352.48 cm^{-1} was also determined. Finally, we present rate constant measurements for the reactions between NO and the peroxy radicals formed in the Cl-initiated oxidation of ethene, propene, 1-butene, 2-butene, 1,3-butadiene, and isoprene. The rate constants are compared to the results of a prior study using chemical ionization mass spectrometry. Good agreement is observed for the peroxy radicals derived from ethene, propene, and 1-butene oxidation, but slower rate constants are measured for those derived from 2-butene, 1,3-butadiene, and isoprene. For the isoprene oxidation system, we assigned a peak in the peroxy radical spectrum at 7652 cm^{-1} as the 3° 1-Cl, 2-OO $ClRO_2$ isomer. The absorption feature was used to measure the isomer-specific rate constant for the reaction of this species with NO.

3.1 Introduction

Volatile alkenes comprise the largest class of non-methane hydrocarbons emitted into the atmosphere with an emission rate exceeding ~750 Tg $year^{-1}$.[1] Atmospheric oxidants (e.g. OH, NO_3, Cl) preferentially react with an alkene through addition to one end of the electron rich double bond, followed by rapid addition of ambient O_2 to yield a β-substituted (or δ-substituted for a conjugated alkene) peroxy radical (RO_2). The competing fates of RO_2 species govern chemistry throughout the lower atmosphere. Reaction with NO produces O_3, an EPA criteria air pollutant and greenhouse gas, while reaction with HO_2 tends to produce highly oxygenated species susceptible to further oxidation and aerosol formation. Functionalization has been shown to adjust the rates of RO_2 reactions occurring under low NO_x conditions by more than an order of magnitude.[2]

On a global scale, atomic chlorine is a minor tropospheric oxidant due to its average number density of less than 10^3 atoms cm^{-3}.[3] However, concentrations as high as ~10^5 atoms cm^{-3} have been estimated for the marine boundary layer.[4] Cl reacts more quickly with volatile organic compounds (VOCs) than other oxidants causing Cl oxidation to be important at even this low radical concentration. Unique products from Cl oxidation of alkenes have been observed in an urban coastal region of southeast Texas.[5] Interestingly, high concentrations of Cl precursors have also been detected in Boulder, Colorado suggesting Cl chemistry may play a role in mid-continental urban regions.[6] In addition to their atmospheric significance, Cl radicals react similarly to the more atmospherically prevalent OH radicals but form intermediates that lack intramolecular hydrogen bonding. Comparing the reactivity of Cl and OH substituted RO_2 radicals may provide insight into the influence of hydrogen bonding on RO_2 fates.

3.1.1 Low NO_x Oxidation of Ethene

Ethene (C_2H_4) is the simplest alkene and acts a prototypical molecule for studying their reactivity. Oxidation by Cl produces the β-chloroethyl radical, which rapidly associates with O_2 to form the β-chloroethyl peroxy radical (β-CEP, $ClCH_2CH_2O_2$):

$$Cl + CH_2CH_2 + M \rightarrow ClCH_2CH_2 + M \quad (R1)$$

$$ClCH_2CH_2 + O_2 + M \rightarrow ClCH_2CH_2O_2 + M \quad (R2)$$

where M denotes an inert third body (typically N_2 or O_2 or in the atmosphere). The

dominant fate of β-CEP in low NO_x regions of the atmosphere is reaction with HO_2:

$$ClCH_2CH_2O_2 + HO_2 \rightarrow ClCH_2CH_2OOH + O_2 \quad (R3)$$

to form an organic hydroperoxide. To a lesser extent, β-CEP also reacts with other organic peroxy radicals. The simplest is the self reaction:

$$ClCH_2CH_2O_2 + ClCH_2CH_2O_2 \rightarrow ClCH_2CH_2O + ClCH_2CH_2O + O_2 \quad (R4a)$$

$$\rightarrow ClCH_2CH_2OH + ClCH_2CHO + O_2 \quad (R4b)$$

which has radical propagating (R4a) and radical terminating (R4b) channels. A third channel to form an organic peroxide exists but is thought to be insignificant for the smaller C_2 RO_2 radicals. Understanding RO_2 self and cross reactions is important when interpreting the results of laboratory experiments, where high radical densities are often necessary for sufficient signal-to-noise but complicate measurements of an atmospheric reaction.

The alkoxy radicals (RO) formed from R4a act as an indirect source of HO_2 that can either undergo R3 or self react:

$$ClCH_2CH_2O + O_2 \rightarrow ClCH_2CHO + HO_2 \quad (R5)$$

$$HO_2 + HO_2 \rightarrow H_2O_2 + O_2 \quad (R6)$$

Laboratory measurements of R3 and R4 are therefore complicated by R5 which links the two processes. One would ideally wish to measure the rate constant k_3 under pseudo first order conditions by probing the β-CEP decay in the presence of excess HO_2. This ensures that β-CEP reacts quantitatively with HO_2 and that complication by R4 is insignificant. Achieving such experimental conditions is difficult, however, due to a common radical source needed to simultaneously generate the RO_2 and HO_2 radicals. As HO_2 is raised to pseudo first order conditions, RO_2 decreases and reaches undetectable levels depending on experimental sensitivity. Only one study has measured rate constants for RO_2 + HO_2 reactions using this approach although their concentration of RO_2 was typically as high as 10–25% that of HO_2.[7] Other studies have determined these rate constants by kinetic modeling of the full system under non-pseudo first order conditions, but this approach suffers from uncertainties in the RO_2 self reaction rate constant and branching ratio.

Studies of self reactions conducted by probing solely the RO_2 decay report an observed depletion rate constant for RO_2 loss by both the self reaction and secondary HO_2 ($k_{4,\mathrm{obs}}$). $k_{4,\mathrm{obs}}$ is then reduced to the true self reaction rate constant (k_4) using the

branching fraction for the radical propagating channel ($\alpha = k_{4a}/k_4$). This key parameter is typically determined in product studies by quantifying the aldehyde (common to both channels) and alcohol (unique to the radical terminating channel) products. The approach works well for molecules like ethyl peroxy, where the self reaction rate is substantially slower than the rate of reaction with HO_2. Each HO_2 molecule produced by the self reaction can then be assumed to react with RO_2 and a straightforward relationship exists between $k_{4,obs}$, k_4, and α: $k_{4,obs} = k_4(1 + \alpha)$. The situation is more complex for functionalized peroxy radicals with fast self reaction rates, such as β-CEP. HO_2 is formed rapidly and acquires sufficient concentrations for R6 to become competitive with R3. There is no longer a direct relationship between $k_{4,obs}$, k_4, and α therefore detailed kinetic modeling is required to elucidate the true self reaction rate constant.

Prior kinetic investigations of β-CEP utilized UV absorption spectroscopy to probe the RO_2 $\tilde{B} \leftarrow \tilde{X}$ transition and measured room temperature $k_{4,obs}$ ranging 3.57–6.0 x 10^{-12} cm^3 $molc^{-1}$ s^{-1}.[8–10] FTIR spectroscopy of the alcohol and aldehyde products was used in two studies to infer room temperature α values of 0.57 and 0.69.[11,12] Determining k_4 from these data alone is not possible due to the fast $k_{4,obs}$, disagreement between the reported values of α, and lack of precise measurements of k_3. The UV kinetic measurements are also complicated by many species within the mechanism absorbing in this spectral region: $ClCH_2CH_2O_2$, $ClCH_2CH_2OOH$, $ClCH_2CHO$, HO_2, and H_2O_2.

In the first part of this chapter, we present measurements of k_2. The rate constants of R + O_2 reactions for functionalized R groups have not been the subject of extensive study due to the great atmospheric abundance of O_2 leading to a rapid association rate. However, there is an increasingly evident need to understand the factors controlling these rate constants, particularly for functional groups and conditions relevant to combustion.[13] The impact of chlorine functionality is explored in this work.

In the second part of this chapter, we present simultaneous measurements of k_3, k_4, and α determined by monitoring the time-resolved near-infrared (near-IR) absorption of β-CEP and HO_2 at varying initial radical ratios $[HO_2]_0/[ClCH_2CH_2O_2]_0$. This approach utilizes detailed kinetic fitting to create a self-consistent model of the low NO_x β-CEP chemistry and overcomes the need of prior methods for an analytical relationship between k_{obs} and α. By varying the initial radical ratio, we optimize the sensitivity of our

measurements to specific rate constants and reduce correlations associated with simultaneously fitting several parameters. This approach has previously been used to study analogous reactions of the ethyl peroxy radical.[14] We choose to probe β-CEP and HO_2 through the forbidden RO_2 $\tilde{A} \leftarrow \tilde{X}$ transition in the near-IR, which has seen increasing use in kinetic studies of peroxy radicals.[15–17] Absorption features in this region exhibit greater isolation than in the UV, thereby minimizing interferences on the peroxy radical measurements. The results of our work provide insight into the effect of chlorine functionalization on the low NO_x reactivity of organic peroxy radicals.

3.1.2 High NO_x Oxidation of Alkenes

The dominant fate of β-CEP in high NO_x regions of the atmosphere is reaction with nitric oxide (NO):

$$ClCH_2CH_2O_2 + NO \rightarrow ClCH_2CH_2O + NO_2 \quad \text{(R7a)}$$

$$ClCH_2CH_2O_2 + NO + M \rightarrow ClCH_2CH_2ONO_2 + M \quad \text{(R7b)}$$

For a simple C_2 structure like β-CEP, the RO radicals produced from R7a will react with O_2 to form HO_2 (R5). Nascent HO_2 reacts with the excess NO to recycle oxidant:

$$HO_2 + NO \rightarrow OH + NO_2 \quad \text{(R8)}$$

For structures with larger carbon backbones, the RO radicals have additional fates: isomerization and/or decomposition. While the mechanism varies with structure, these processes typically yield a carbon-centered radical that will associate with O_2 to form a second generation RO_2. Reaction with O_2 has been predicted to be more important than decomposition for RO radicals containing β-chloro functionality.[18]

Laboratory measurements of RO_2 + NO rate constants are typically conducted with excess precursor VOC (to ensure rapid conversion of oxidant to RO_2 radicals) and excess NO (to ensure pseudo first order conditions). Kinetic measurements using absorption spectroscopy to detect the target RO_2 radical can be complicated by absorption interferences from second generation RO_2. In addition to RO isomerization and decomposition, the OH from R8 can yield secondary RO_2 by oxidation of the excess VOC to form hydroxyl-substituted RO_2 ($HORO_2$). In their study of chlorine-substituted RO_2 ($ClRO_2$) + NO rate constants, Patchen et al. avoided this complication by detecting $ClRO_2$ using chemical ionization mass spectrometry (CIMS), rather than absorption

spectroscopy.[19] Since the $ClRO_2$ radicals have different masses than the corresponding $HORO_2$ (or other secondary RO_2), the measured decays arose solely from the $ClRO_2$ + NO reaction. However, since all of the $ClRO_2$ isomers formed from the Cl-initiated oxidation of a VOC precursor have the same mass, no differences in chemical structure could be assessed with their technique. The measured rate constant was effectively an average across all $ClRO_2$ isomers produced, weighted by the yields of each isomer and their sensitivities for detection by CIMS.

In the third part of this chapter, we present measurements of $ClRO_2$ + NO rate constants across a range of $ClRO_2$ structures derived from the chlorine-initiated oxidation of ethene (k_7), propene, 1-butene, 2-butene, 1,3-butadiene, and isoprene. For the precursors with more than two carbons atoms, various $ClRO_2$ isomers form upon oxidation. We detected $ClRO_2$ in the near-IR by probing their forbidden $\tilde{A} \leftarrow \tilde{X}$ transition. Unlike the $\tilde{B}$ state, the $\tilde{A}$ state of RO_2 radicals is bound, leading to detailed absorption spectra that vary with chemical structure.[20] This transition therefore has the potential to differentiate RO_2 isomers in a complex oxidation system as well as discriminate first generation RO_2 from later generation RO_2 formed by radical recycling. We evaluate the practicalities of such measurements in this work. Furthermore, it is commonly assumed that RO_2 + NO reactions proceed with approximately the same rate constant ($k \approx 9 \times 10^{-12}$ cm^3 $molc^{-1}$ s^{-1}), with little sensitivity to structure. Possible evidence for a difference in rate constant between $ClRO_2$ isomers derived from the same VOC precursor is discussed.

A schematic summary of the oxidations and peroxy radical reactions studied in this work is presented in Figure 1. For β-CEP, we have measured k_2, k_3, k_4, α, and k_7. For larger alkene precursors, we have measured $ClRO_2$ + NO rate constants.

3.2 Experimental Methods

3.2.1 Pulsed Cavity Ringdown Spectrometer

The spectroscopy of organic peroxy radicals in the near-IR has been investigated extensively and reviewed by the Miller group.[20] While the $\tilde{A} \leftarrow \tilde{X}$ transition produces detailed absorption spectra, it is forbidden with small cross sections ($\sigma \sim 10^{-21}$–10^{-20} cm^2).[21] Cavity enhanced methods are therefore often necessary to detect the RO_2 radicals. Cavity

ringdown spectroscopy (CRDS) is a popular approach in which the probe light beam becomes resonant with an optical cavity formed by two highly reflective mirrors to generate long effective pathlengths.[22] With each pass, the intracavity power drops as a small fraction of photons are lost at the mirrors or absorbed/scattered by the analyte gas. A detector positioned behind one of the mirrors records the exponential decay of light intensity leaking out of the cavity (a "ringdown"). By comparing the lifetime of photons within the resonator both with and without the analyte gas present, the absorption can be deduced.

The near-IR spectrometer used in this work for pulsed CRDS absorption measurements has been described previously.[23,24] A schematic of the instrument is presented in Figure 2. Tunable visible radiation from a Nd:YAG (Continuum NY61) pumped dye laser (Lambda Physik FL3002) was focused into a 2 m long stainless steel Herriott cell filled with ~10 atm of hydrogen.[25] After nine passes, the stimulated Raman scattering was filtered for the second sequential Stokes shift in the near-IR spectral region. The beam was injected into a 50 cm long optical cavity formed by two highly reflective mirrors (R ~ 99.99%). Transmitted radiation was focused onto an InGaAs photodetector (ThorLabs PDA10CS, 17 MHz bandwidth) and the ringdown signals were digitized by a 14-bit transient digitizer (GaGe CompuScope 4327). By using multiple ringdown mirrors and laser dyes, the spectrometer is capable of performing pulsed near-IR CRDS over 7000–9000 cm^{-1} with a 0.2 cm^{-1} linewidth (set by the dye laser) and a ~1 mJ pulse energy. The typical noise-equivalent absorption (NEA) coefficient for this system is ~1.5 x 10^{-8} cm^{-1} $Hz^{-1/2}$. In practical terms, assuming an absorption pathlength of 10 cm, a cross section of $\sigma \approx 10^{-21}$–10^{-20} cm^2, and $N = 100$ averages (5 Hz), this corresponds to a minimum detectable concentration of $[RO_2]_{min} \sim 10^{11}$–$10^{12}$ molc cm^{-3}.

An excimer laser (Lambda Physik LPF220, 5 Hz, 351 nm) initiated radical chemistry through photolysis of Cl_2. The UV beam was expanded (~6 mJ cm^{-2} fluence in the reactor) and propagated orthogonal to the axis of the optical cavity through two quartz windows mounted on the sides of the ringdown cell. A digital delay generator synchronized the firing of the Nd:YAG and excimer laser pulses and established a time axis for kinetic measurements. Ringdowns were acquired both with and without excimer laser photolysis to elucidate the absorption induced by radical chemistry.

Reactant gases were flown through the ringdown cell in the region enclosed by the photolysis windows. The ringdown mirrors were protected by a purge of N_2 set at 10% of the total flow. The pressure was set to 300 Torr and experiments were conducted at room temperature (T ≈ 296 K). Specific concentrations in the reactor were varied to optimize conditions for measurement of different rate constants. Typically, our radical precursor was set to $[Cl_2] \approx 5 \times 10^{16}$ molc cm^{-3} and yielded $[Cl]_0 \approx 2 \times 10^{14}$ atoms cm^{-3} upon photolysis (~0.2%). The VOC precursor was set to great excess at ~10^{16}–10^{17} molc cm^{-3} to ensure that the Cl + VOC oxidation step was never rate-limiting to the measured $ClRO_2$ kinetics. Ethene, propene, 1-butene, 2-butene, and 1,3-butadiene were diluted from pure tanks into custom tanks of ~5–20% in N_2. The vapor from liquid methanol and isoprene was used to prepare tanks of these species at ~5% in N_2. For experiments measuring k_2, the $[O_2]$ was kept low and varied around ~10^{16} molc cm^{-3} (< 1%) to ensure the pseudo first order association rates were slow enough to measure (the bath gas was almost entirely N_2). For experiments measuring $ClRO_2$ + NO rate constants, O_2 was raised to ~5% to ensure that formation of $ClRO_2$ was effectively instantaneous relative to its decay (~95% N_2). [NO] was kept at least an order of magnitude in excess of $[Cl]_0$ and varied within ~10^{15}–10^{16} molc cm^{-3}. For experiments measuring k_3, k_4, and α, O_2 was raised to ~75% to minimize the impact of secondary chemistry that will be discussed in a later section (~25% N_2). The total flow rate was maintained at ~4250 sccm to set the residence time in the flow cell at ~160 ms and ensure complete refreshment of the gases between adjacent photolysis pulses.

3.2.2 Calibration of the Initial Radical Concentration

To calibrate $[Cl]_0$, we conducted experiments oxidizing methanol:

$$Cl + CH_3OH \rightarrow HCl + CH_2OH \quad \text{(R9)}$$

$$CH_2OH + O_2 \rightarrow HCHO + HO_2 \quad \text{(R10)}$$

The conditions of these experiments were such that each Cl atom yielded one HO_2 radical. Loss of nascent HO_2 was exclusively through its self reaction to form H_2O_2 (R6). Since the rate constant k_6 is well-known,[26] the bimolecular decay constant of HO_2 absorption can be used to determine the initial HO_2 concentration and $[Cl]_0$.

The absorption of HO_2 was monitored near the peak of its $\tilde{A} \leftarrow \tilde{X}$ origin Q-branch band at 7041.64 cm^{-1}.[27] However, the H_2O_2 product also has absorption in this region

arising from a vibrational overtone band.[28] Spectra of HO_2 and H_2O_2 measured in this work are presented in Figure 3. The spectra measured with a 10 μs delay between the probe and photolysis pulses was recorded before the self reaction has occurred to any appreciable extent, and thus represents solely HO_2. The spectrum measured with a 35 ms delay was recorded after many half-lives of the self reaction, and represents solely H_2O_2.

Since the rate of HO_2 decay is linked to the rate of H_2O_2 production, integration of their rate laws shows that the absorption at 7041.64 cm^{-1} can be modeled according to:

$$A(t) = \frac{A_0 - A_\infty}{1 + 2k_6[HO_2]_0 t} + A_\infty \qquad \text{(Eqn. 1)}$$

The measured time-resolved absorption, collected over 0–10 ms with 0.1 ms steps, undergoes a three-parameter fit to Eqn. 1 to determine the initial HO_2 absorption before the self reaction (A_0), the H_2O_2 absorption after completion of the self reaction (A_∞), and the bimolecular decay constant of HO_2 ($k_6[HO_2]_0$). Dividing the last parameter by the known value of k_6 gives $[HO_2]_0$, which we assume to be equal to $[Cl]_0$. An example absorption signal and fit yielding $[Cl]_0$ = 1.66 x 10^{14} molc cm^{-3} is shown in Figure 4.

Each day, we performed calibrations of the $[Cl]_0$ yielded from Cl_2 photolysis. In the event that $[Cl_2]$ was changed from the concentration used in the calibration scan, we assumed that the Cl_2 photolysis fraction was constant to determine $[Cl]_0$ in the other scan. The calibration was generally performed at the beginning and end of experiments to ensure that $[Cl]_0$ had not drifted to any significant extent.

3.3 Results & Discussion

3.3.1 Formation Rate Constant of β-Chloroethyl Peroxy

The rate constant k_2 for the association of the β-chloroethyl radical with O_2 to form β-CEP (R2) was determined by measuring pseudo first order growth rates of β-CEP at varying $[O_2]$. We probed β-CEP absorption on the peak of the $\tilde{A} \leftarrow \tilde{X}$ origin band of the C-C-O-O gauche, Cl-C-C-O trans (GT) conformer at 7352.48 cm^{-1}.[29] A spectrum of this broad, rotationally-unresolved band is presented in Figure 5.

β-chloroethyl radicals were generated by the Cl-initiated oxidation of ethene (R1). The concentration of ethene was set to 9.0 x 10^{16} molc cm^{-3} and yielded a short Cl radical

lifetime of τ_{Cl+R} < 0.2 μs. This ensured that R1 was never rate-limiting to the measured growth rate of β-CEP. The [O_2] was varied over (1–6) x 10^{16} molc cm^{-3} and yielded β-CEP growth rates of k_P = (2–18) x 10^4 s^{-1} (τ_{ClR+O_2} = 5–50 μs). Such fast rates were necessary to prevent self reactions of β-chloroethyl radicals, due to the large radical concentrations employed in this work. For our conditions, we estimated a worst-case half-life of $\tau_{ClR+ClR}$ ≈ 500 μs. Association with O_2 was therefore always at least an order of magnitude faster than the self reaction, and we assumed all β-chloroethyl radicals formed β-CEP.

One issue with such fast association rates is that traditional kinetic analysis using CRDS requires that the absorption/concentration of the analyte species be unchanging during a ringdown event. If the concentration changes with a time constant comparable to the photon lifetime, then the decay of light intensity will no longer be exponential due to a different fraction of photons being absorbed with each pass through the cavity. Typical vacuum ringdown time constants were on the order of ~15–30 μs in this work, and therefore our RO_2 formation time constants of $\tau_{ClR+O_2} \leq$ 50 μs clearly violated this requirement.

Thankfully, Brown et al. have shown that one can effectively fit the non-exponential behavior of a ringdown signal to extract meaningful kinetic information when a reaction occurs on the same timescale as the photon lifetime.[30] With their technique, called Simultaneous Kinetics and Ringdown (SKaR), they show that rate constants can be measured by fitting the ratio of a ringdown signal obtained with the target absorber present (when the UV laser is fired) to a ringdown signal obtained without the target absorber present (when the UV laser is not fired). For pseudo first order production of β-CEP, the absorption evolves according to:

$$A(t) = A_\infty(1 - e^{-k_P t}) \qquad \text{(Eqn. 2)}$$

where A_∞ is the absorption after all β-CEP has formed and $k_P = k_2[O_2]$ is the pseudo first order rate constant. The dominant loss process of β-CEP under these conditions is its self reaction (R4). However, R4 is slow relative to R2 and negligible loss of β-CEP was observed over the measurement timescale; omitting R4 from the absorption model did not impact the results. For a first order growth process, Brown et al. showed that the ratio of the ringdown signals $R(t)$ evolves according to:[30]

$$R(t) = \exp\left[-\left(\frac{c}{d}\right)\left(\frac{A_\infty}{k_P}\right)[k_P t - (1 - e^{-k_P t})]\right] \quad \text{(Eqn. 3)}$$

where c is the speed of light and d is the length of the optical cavity, which is typically longer than the absorption pathlength. Eqn. 3 assumes that the scalar intensities of the ringdown signals acquired with and without photolysis are equal and therefore cancel to unity upon taking the ratio. In practice, there are slight differences in intensity associated with shot-to-shot fluctuations in near-IR power, although it is straightforward to scale $R(t)$ such that $R(0) = 1$. Alternatively, an additional scalar parameter can be added to Eqn. 3 to account for the difference in intensity.

The original SKaR paper assumes that the delay between the photolysis and probe pulses is zero;[30] we take a slightly different approach in this work. At each [O_2], we measured the ratio of ringdown signals at ~100 delay times between the firing of the photolysis and probe laser pulses. Each ratio was shifted by its delay time onto a uniform kinetic time axis for which photolysis occurs at $t = 0$. In Appendix A of this thesis, we show that ringdown ratios acquired with different delay times differ by only a constant scale factor after they are shifted onto a uniform time axis. We therefore constructed $R(t)$ at each [O_2] according to the following procedure: (1) ordering the ratios by ascending delay time; (2) setting $R(t)$ equal to the ratio with the earliest delay time; (3) computing the optimal scale factor (least squares minimization) between $R(t)$ and the ratio with the next earliest delay time, over the time domain for which they overlap; (4) multiplying the ratio with the next earliest delay time by this scale factor and appending the result to $R(t)$; (5) repeating this procedure from step 3 for each successive delay time until all of the data has been incorporated into $R(t)$. In the original SKaR approach with the delay between the lasers fixed at zero, the signal-to-noise of $R(t)$ degrades substantially at later reaction times due to the decay of the ringdown signals. Fits of kinetic parameters are biased toward earlier reaction times. In this modified approach, high signal-to-noise can be maintained throughout the entire $R(t)$ trace. Full details are provided in Appendix A.

An example $R(t)$ trace recorded at [O_2] = 2.2 x 10^{16} molc cm^{-3} is shown in Figure 6. The corresponding two-parameter fit to Eqn. 3 is overlaid and yielded k_P = 7.0 x 10^4 s^{-1}. Fits were performed at each [O_2] and the resulting bimolecular plot (k_P vs [O_2]) is presented in Figure 7. The slope of this line yielded k_2 = 2.9 x 10^{-12} cm^3 $molc^{-1}$ s^{-1} at 300

Torr and 296 K. A small, positive intercept was observed from the linear fit and had magnitude consistent with the background [O_2] expected in the reactor from the base pressure and atmospheric mixing ratio of O_2. To verify that the measured k_2 was in the high-pressure limit, we repeated the experiment at lower pressure. The resulting rate constant was k_2 = 2.8 x 10^{-12} cm^3 $molc^{-1}$ s^{-1} at 200 Torr, indistinguishable from the value of k_2 at 300 Torr.

To validate our result, we also used this technique to measure the known association rate constant between ethyl radicals and O_2 to form ethyl peroxy. Ethyl radicals were generated from the Cl-initiated oxidation of ethane. We probed ethyl peroxy absorption at the peak of the $\tilde{A} \leftarrow \tilde{X}$ origin band of the C-C-O-O trans (T) conformer at 7366 cm^{-1}, and at the peak of the $\tilde{A} \leftarrow \tilde{X}$ origin band of the C-C-O-O gauche (G) conformer at 7596 cm^{-1}.[31] The rate constants measured from experiments conducted at each frequency were (6.9 and 6.3) x 10^{-12} cm^3 $molc^{-1}$ s^{-1}, respectively. The bimolecular plots are presented in Figure 8. The data were noisier than the β-CEP experiments due to the smaller peak absorption cross sections of ethyl peroxy than that of β-CEP. Nevertheless, the rate constants agree well with the evaluated ethyl + O_2 association rate constant at 300 Torr of (7.3 ± 1.5) x 10^{-12} cm^3 $molc^{-1}$ s^{-1},[32] promoting confidence in the ability of our technique to accurately measure rate constants in this reaction class.

The high-pressure limit formation rate constant of β-CEP measured in this work is ~2.5 times slower than the evaluated high-pressure limit formation rate constant of unsubstituted ethyl peroxy.[32] The reason is not immediately apparent, but suggests that β-chloro substitution of the ethyl radical deactivates its association with O_2. In the β position, chlorine is expected to exert an inductive electron-withdrawing effect to destabilize both the alkyl and peroxy radicals. Due to the proximity of the radical center to the substituent, it is likely that the β-chloroethyl radical is destabilized to a greater extent than β-CEP (relative to their unsubstituted counterparts). This would increase the peroxy radical energy well depth thereby decreasing the association rate constant, in agreement with the observed trend between ethyl peroxy and β-CEP. Additional studies on the formation rate constants of β-substituted organic peroxy radicals across substituents with a range of inductive strengths would help address this hypothesis.

3.3.2 Low NO_x Kinetics of β-Chloroethyl Peroxy

The dominant fate of β-CEP in low NO_x regions of the atmosphere is its reaction with HO_2 (R3). As discussed in the Introduction, measuring the decay of β-CEP under pseudo first order excess of HO_2 is generally not possible due to a common radical source necessary to simultaneously generate the two peroxy radicals; increasing HO_2 comes at the expense of β-CEP absorption signal. Our experiments measuring k_3 have initial $[\beta\text{-CEP}]_0$ and $[HO_2]_0$ that are of similar orders of magnitude. Under these conditions, the self reactions of β-CEP (R4) and HO_2 (R6) are both competitive with the cross reaction (R3) we wish to study. While the value of k_6 is well-established, the value of k_4 and its branching fraction α are much less certain. Kinetic studies usually only measure $k_{4,\text{obs}}$,[8–10] which depends on initial radical concentration and cannot generally be transferred across different experiments. Further complications arise from the radical propagating channel of the self reaction (R4a) acting as a secondary, continuous source of HO_2 through R5.

Our strategy follows methodology described previously for studying the ethyl peroxy + HO_2 reaction.[14] The time-resolved absorption signals of β-CEP and HO_2 were measured across a range of ratios of their initial radical concentrations ($[HO_2]_0/[\beta\text{-CEP}]_0$). The unknown parameters k_3, k_4, and α are constants independent of $[HO_2]_0/[\beta\text{-CEP}]_0$; by optimizing the parameters across a range of these ratios, we minimize uncertainties introduced by secondary chemistry and reduce correlation between their fitted values. The hydrocarbons in the reactant gas mixture were ethene, for the generation of β-CEP (R1 and R2), and methanol, for the generation of HO_2 (R9 and R10). Since the hydrocarbons and O_2 are in great excess, the initial radical ratio is given by:

$$\frac{[HO_2]_0}{[\beta\text{-CEP}]_0} = \left(\frac{k_9}{k_1}\right) \cdot \left(\frac{[CH_3OH]}{[C_2H_4]}\right) \qquad \text{(Eqn. 4)}$$

and can be adjusted by varying the $[CH_3OH]/[C_2H_4]$ precursor ratio. Parameters k_4 and α were typically optimized in scans where $[HO_2]_0 = 0$ and R4 dominated the chemistry. k_3 was typically optimized in scans where $[HO_2]_0 > 0$ and R3 was promoted. A schematic summary of our strategy is presented in Figure 9.

3.3.2.1 Calibrations

Unlike the pseudo first order kinetics of the reactions studied in sections 3.3.1 and 3.3.3, the reactions and conditions in these experiments led to β-CEP and HO_2 kinetics that

were concentration-dependent. It was therefore necessary to establish calibrations for each species to convert its absorption signal to absolute concentration. Unfortunately, absorption cross sections for the $\tilde{A} \leftarrow \tilde{X}$ transitions of these peroxy radicals are unknown.

HO_2 kinetics were probed at the same frequency used in the $[Cl]_0$ calibration experiments described in section 3.2.2: the peak of the $\tilde{A} \leftarrow \tilde{X}$ origin Q-branch band at 7041.64 cm^{-1} (Figure 3). The experiment was also used to derive a calibration factor between HO_2 concentration and absorption at this frequency (S_{HO_2}). By fitting the self reaction kinetics of HO_2 produced from the oxidation of methanol to Eqn. 1 (Figure 4), we determined the initial absorption signal A_0 (due to solely HO_2) and $[HO_2]_0$. It is then straightforward to calculate: $S_{HO_2} = A_0/[HO_2]_0$ = 4.15 x 10^{-19} cm^3 $molc^{-1}$. Since H_2O_2 has weak absorption at this frequency, we must also determine its calibration factor ($S_{H_2O_2}$) for inclusion in our analysis. The absorption after the completion of the self reaction is a fitted parameter A_∞ (due to solely H_2O_2). From the stoichiometry of R6, $[H_2O_2]_\infty = [HO_2]_0/2$. It is then straightforward to calculate: $S_{H_2O_2} = A_\infty/[H_2O_2]_\infty$ = 7.91 x 10^{-20} cm^3 $molc^{-1}$.

An additional calibration of HO_2 was performed to verify that the measured absorption signal was linearly proportional to concentration. A known issue with pulsed CRDS is that a systematic nonlinearity can exist between these quantities when the probe laser linewidth is of comparable magnitude to, or greater than, the linewidth of the absorption feature.[33] The ringdown signal is no longer strictly exponential in this scenario, but rather a weighted sum of exponentials that decay at different rates set by the overlap of the spectral intensity distribution of the laser and the absorber. Since greater absorption leads to a faster decay rate and less contribution to the signal, fitting the multiexponential ringdown to a single exponential function will bias the result toward slower decay rates and thus underpredict absorption. The extent of the bias has been shown to increase with the ratio of the laser linewidth to the absorption linewidth, and with the ratio of the absorption magnitude to vacuum cavity loss;[34] the latter is responsible for the nonlinearity between measured absorption and concentration. Unfortunately, the linewidth of the HO_2 absorption peak probed in this work (Figure 3b) appears to be comparable to, and likely broadened by, our laser linewidth (~0.2 cm^{-1}). To check for nonlinearity, we conducted experiments oxidizing methanol and measuring the absorption of HO_2 at 7041.64 cm^{-1} while varying $[Cl_2]$ to linearly change $[HO_2]$. We used a 10 μs delay time, which allowed

for the complete conversion of Cl radicals to HO_2 but minimized HO_2 lost by R6. A plot of HO_2 absorption vs $[Cl_2]$ is shown in Figure 10a and is linear over the range of absorption magnitudes measured in this work. This indicates that linewidth effects do not appreciably bias our results and that the linear calibration factor S_{HO_2} determined above is valid.

β-CEP kinetics were probed at the same frequency used in the formation rate constant measurements described in section 3.3.1: the peak of the $\tilde{A} \leftarrow \tilde{X}$ origin band of the GT conformer at 7352.48 cm^{-1}. Unlike HO_2, the β-CEP absorption band has a broad linewidth (~50 cm^{-1}) much greater than that of our probe laser and there is no concern about nonlinearity between measured absorption and concentration. Nevertheless, we performed a similar experiment to determine the β-CEP calibration factor ($S_{\beta\text{-CEP}}$): ethene was oxidized and the β-CEP absorption measured at 7352.48 cm^{-1} with a 10 μs delay time while varying $[Cl_2]$ to linearly change [β-CEP]. The β-CEP absorption was plotted as a function of $[Cl]_0$, where the latter was calculated from the calibrated Cl_2 photolysis fraction (section 3.2.2). At a 10 μs delay, [β-CEP] = $[Cl]_0$, and therefore the slope of the best-fit line gives $S_{\beta\text{-CEP}}$. The data is presented in Figure 10b and yielded $S_{\beta\text{-CEP}}$ = 2.94 x 10^{-19} cm^3 $molc^{-1}$. This value can also be used to determine an absorption cross section since our probe laser linewidth is much narrower than that of the absorption band. Assuming an absorption pathlength of 11.5 cm (the length of the cavity axis illuminated by the photolysis beam), we attain σ = 2.56 x 10^{-20} cm^2 for β-CEP at 7352.48 cm^{-1}. Cross sections of this magnitude are typical for the $\tilde{A} \leftarrow \tilde{X}$ transition of organic peroxy radicals.[21]

With the calibration factors of HO_2, H_2O_2, and β-CEP established, the time-resolved absorption signals could be modeled according to:

$$A(t, 7042\ cm^{-1}) = S_{HO_2} \cdot [HO_2](t) + S_{H_2O_2} \cdot [H_2O_2](t) + \gamma \cdot S_{\beta\text{-CEP}} \cdot [\beta\text{-CEP}](t) \quad \text{(Eqn. 5)}$$

$$A(t, 7352\ cm^{-1}) = S_{\beta\text{-CEP}} \cdot [\beta\text{-CEP}](t) \quad \text{(Eqn. 6)}$$

where the time-resolved concentrations were determined from the kinetic model described in the next section. We remind that S_{HO_2} and $S_{H_2O_2}$ correspond to 7041.64 cm^{-1}, while $S_{\beta\text{-CEP}}$ corresponds to 7352.48 cm^{-1}. The $\gamma \cdot S_{\beta\text{-CEP}} \cdot [\beta\text{-CEP}](t)$ term in Eqn. 5 takes into account that the β-CEP spectrum exhibits weak absorption at the frequency used to probe HO_2. The constant γ in this term is equal to the ratio of the cross section of β-CEP at

7041.64 cm^{-1} to that at 7352.48 cm^{-1}. We determined γ in experiments oxidizing ethene, taking the ratio of absorption at 7041.64 cm^{-1} to that at 7352.48 cm^{-1} and averaging this ratio over 0–10 μs. Over this time domain, secondary HO_2 from R4a and R5 has not yet been produced, and absorption at both frequencies is due to solely β-CEP. Figure 11 outlines the analysis used to determine γ. The measured value of γ = 0.0300 is quite small and reflects that absorption at 7041.64 cm^{-1} arises almost exclusively from HO_2 and H_2O_2. These species did not exhibit absorption at 7352.48 cm^{-1} and therefore Eqn. 6 only includes a term for β-CEP.

A minor offset correction was applied to datasets before fitting them to Eqns. 5 and 6. The offset arises from the fact that both the methanol and ethene precursors absorb at 7041.64 cm^{-1} and 7352.48 cm^{-1}. After their oxidation by Cl, a small, negative absorption signal is created at each frequency due to the reduction in $[CH_3OH]$ and $[C_2H_4]$ relative to their pre-photolysis concentrations. This absorption effectively appears as an offset since R1 and R9 are so rapid (τ_{Cl+R} < 2 μs). To calibrate this effect, we conducted experiments measuring the cavity loss at each frequency while varying $[CH_3OH]$ and $[C_2H_4]$ in the absence of photolysis. The results are presented in Figure 12 and the slopes are equal to their calibration factors. The $[CH_3OH]$ and $[C_2H_4]$ depleted by oxidation are calculated from $[Cl]_0$ and Eqn. 4, and then multiplied by their respective calibration factors to determine the absorption offset. The offset corrections were typically small (less than 0.5 ppm) and did not appreciably impact the fits, although they were included nevertheless.

Finally, we considered several other effects that could impact the concentration-dependent peroxy radical kinetics measured in this work: (1) the nonuniformity of the radical distribution along the cavity axis due to the spatial inhomogeneity of the photolysis beam, (2) diffusion of radicals along concentration gradients within the flow reactor, and (3) an effective time-dependent decrease in the absorption pathlength as the sample is pumped out and replaced by fresh gas. Experiments conducted to calibrate these effects showed they would have negligible impact on our results over the longest time domain used in these studies of 0–10 ms; we therefore omitted them from our model.

3.3.2.2 Kinetic Model and Fits

Experiments measuring k_3, k_4, and α were conducted across 13 initial radical concentration ratios ranging $[HO_2]_0/[\beta\text{-CEP}]_0$ = 0–12. At each ratio, we measured a pair of time-resolved absorption signals at 7041.64 cm^{-1} and 7352.48 cm^{-1}. Each signal was recorded over 0–10 ms with 0.1 ms spacing. A summary of the initial conditions across these experiments is presented in Table I.

A chemical kinetic model constructed from literature rate constants was used to describe the chemistry initiated upon photolysis. A summary of this model is presented in Table II. The network of reactions was expressed as a system of coupled differential rate equations. Integration of this system from a set of initial conditions allowed for the determination of $[HO_2](t)$, $[H_2O_2](t)$, and $[\beta\text{-CEP}](t)$. The concentrations could then be compared to the measured absorption signals for a particular $[HO_2]_0/[\beta\text{-CEP}]_0$ through Eqns. 5 and 6.

In addition to the reactions that have been previously discussed, the model also included a side reaction between the alkoxy and peroxy radicals to produce stable products:

$$ClCH_2CH_2O + ClCH_2CH_2O_2 \rightarrow ClCH_2CH_2OOH + ClCH_2CHO \qquad (R11)$$

R5 and R11 represent the possible fates of the alkoxy radical and neither k_5 nor k_{11} is known; in the model, we assume they have the same values as the analogous reactions of ethyl peroxy and ethyl alkoxy. R11 rarely occurs in the atmosphere but can occur in laboratory studies with high radical concentrations. In this study, we used a large $[O_2]$ = 7.44 x 10^{18} molc cm^{-3} (~75%) to greatly promote R5 over R11 and ensure that every alkoxy instantaneously yielded HO_2. The alkoxy radical lifetime (τ_{ClRO} < 15 μs) was very short compared to the peroxy radical chemistry such that our model had little sensitivity to the precise values of k_5 and k_{11}; as long as the true values are of the same order of magnitude as the assumed values, they introduce negligible uncertainty to our results. The large $[O_2]$ also caused our results to be insensitive to k_2 and k_{10} as these reactions are effectively instantaneous. Similarly, the large hydrocarbon precursor concentrations caused R1 and R9 to occur instantaneously.

The procedure used to fit the datasets and determine k_3, k_4, and α is adapted from the study of Noell et al., who measured similar rate constants for ethyl peroxy.[14] Simultaneously optimizing k_3, k_4, and α for a pair of signals typically yielded nonphysical

values due to the high degree of correlation between the parameters and the fact that the kinetics at an individual $[HO_2]_0/[\beta\text{-CEP}]_0$ were generally only sensitive to a subset of the parameters. To overcome this correlation and determine physically accurate rate constants, we typically limited optimization of each parameter to only those datasets for which the kinetics were actually sensitive to the parameter value. Furthermore, we noticed that when $[HO_2]_0$ and $[\beta\text{-CEP}]_0$ were fixed at the values calculated from $[Cl]_0$ and Eqn. 4, the modeled absorption signals disagreed substantially from the measured absorption signals close to $t = 0$. This is perhaps not surprising, since the ratio $k_9/k_1 = 0.85 \pm 0.46$ in Eqn. 4 is highly uncertain (±54% error, assuming the evaluated values of k_1 and k_9 are uncorrelated).[32] As discussed previously, R1, R2, R9, and R10 are effectively instantaneous in these experiments. We therefore omitted these reactions when fitting to the kinetic model and assumed the chemistry began directly from HO_2 and β-CEP at $t = 0$. $[HO_2]_0$ and $[\beta\text{-CEP}]_0$ were optimized in each fit as floated parameters.

Following the procedure of Noell et al.,[14] we fit the datasets iteratively until convergence in k_3, k_4, and α was achieved:

1. Initially, each dataset for which $[HO_2]_0/[\beta\text{-CEP}]_0 > 1$ underwent a fit with all five parameters floated: k_3, k_4, α, $[HO_2]_0$, and $[\beta\text{-CEP}]_0$. The initial guesses of k_3, k_4, and α were derived from previous studies in the literature that will be discussed in greater detail below.
2. Next, we performed three-parameter fits to each dataset for which $[HO_2]_0/[\beta\text{-CEP}]_0 = 0$, floating k_4, α, and $[\beta\text{-CEP}]_0$. Under these conditions, R4 dominates the chemistry. We minimized the following cost function for each dataset:

$$\chi^2(k_4, \alpha, [\beta\text{-CEP}]_0) = \sum_j \left(\frac{A^{7042}_{expt,j} - A^{7042}_{model,j}}{\delta A^{7042}_{expt,j}} \right)^2 + \sum_j \left(\frac{A^{7352}_{expt,j} - A^{7352}_{model,j}}{\delta A^{7352}_{expt,j}} \right)^2 \quad \text{(Eqn. 7)}$$

where A_{expt} is the measured absorption, δA_{expt} is its uncertainty, A_{model} is the modeled absorption calculated from the output of the integrated kinetic model and Eqns. 5 or 6, and j indexes the time points. $[HO_2]_0$ was fixed at zero and k_3 was fixed at the average of its optimized values across all scans in the previous iteration. Similarly, the initial guesses for k_4 and α were their average optimized values from the previous iteration.

3. We then performed three-parameter fits to each dataset for which $[HO_2]_0/[\beta\text{-CEP}]_0 > 0$, floating k_3, $[HO_2]_0$, and $[\beta\text{-CEP}]_0$. Under these conditions, R3 was promoted. We minimized the following cost function for each dataset:

$$\chi^2(k_3, [HO_2]_0, [\beta\text{-CEP}]_0) = \sum_j \left(\frac{A_{expt,j}^{7042} - A_{model,j}^{7042}}{\delta A_{expt,j}^{7042}} \right)^2 + \sum_j \left(\frac{A_{expt,j}^{7352} - A_{model,j}^{7352}}{\delta A_{expt,j}^{7352}} \right)^2 \quad \text{(Eqn. 8)}$$

   k_4 and α were fixed at the average of their optimized values across all scans in the previous iteration. Similarly, the initial guess for k_3 was fixed at its average optimized value from the previous iteration.

4. Steps 2 and 3 were continuously repeated until the values of k_3, k_4, and α had negligible change between successive iterations.

With this procedure, we converged to optimum values of k_3 = (3.4 ± 1.0) x 10^{-12} cm^3 $molc^{-1}$ s^{-1}, k_4 = (4.9 ± 0.9) x 10^{-12} cm^3 $molc^{-1}$ s^{-1}, and α = 0.46 ± 0.09. The uncertainties were estimated from how the quality of the fits degraded as the parameters were perturbed from their optimum values.

In Figure 13, we present the absorption signals acquired at three different values of $[HO_2]_0/[\beta\text{-CEP}]_0$. The integrated kinetic model using optimized values of k_3, k_4, and α is overlaid, after conversion to absorption units by Eqns. 5 and 6. At $[HO_2]_0/[\beta\text{-CEP}]_0 = 0$, the loss of β-CEP is dominated by R4. HO_2 rapidly grows due to the radical propagating channel R4a, and decays at longer times due to both R3 and R6. At $[HO_2]_0/[\beta\text{-CEP}]_0$ = 0.155, β-CEP loss is mostly due to R4, but R3 now becomes competitive. The growth of HO_2 signal from R4a is still evident, but minor in comparison to the initial HO_2 yielded by methanol oxidation. At $[HO_2]_0/[\beta\text{-CEP}]_0 = 2.52$, β-CEP loss is dominated by R3. No evidence of HO_2 production can be observed and its loss is dominated by R6. In all of these cases, the model adequately describes the observed kinetics. Due to the millisecond lifetimes of the peroxy radicals, the use of SKaR in the data analysis was not necessary.

k_3, k_4, and α have been measured previously; the literature values differ greatly from the optimum values determined in this work. α was measured twice in FTIR studies that quantified the stable end products of ethene oxidation. From the ratio of the chloroacetaldehyde (common to R4a and R4b) and 2-chloroethanol (unique to R4b) concentrations, the two studies separately measured α = 0.57 and 0.69.[11,12] k_4 has never

been directly measured; kinetic studies have only reported $k_{4,obs}$,[8–10] which is an effective rate constant for β-CEP loss by both R4 and R3 due to secondary HO_2. As discussed previously, $k_{4,obs}$ is generally not transferrable between experiments using flash photolysis to generate β-CEP. No straightforward relationship between $k_{4,obs}$ and α exists since k_3 and k_4 are of similar order of magnitude. However, the study of Chakir et al. is an exception: using modulated photolysis of the Cl_2 precursor, they generated a steady-state distribution of β-CEP and detected the radical through its $\tilde{B} \leftarrow \tilde{X}$ transition in the UV.[10] Under such conditions, mathematical relationships can be established between k_3, k_4, $k_{4,obs}$, and α. Chakir et al. measured $k_{4,obs}$ = 4.5 x 10^{-12} cm^3 $molc^{-1}$ s^{-1} and used the values of α from the product studies to calculate k_3 and k_4; the full details are provided in their work. Wallington et al. detected the β-chloroethyl hydroperoxide product of R3 and constrained k_3 = (4–20) x 10^{-12} cm^3 $molc^{-1}$ s^{-1}, although we did not consider this value further due to the broad range.

A literature kinetic model was constructed for comparison to our datasets. In the literature model, we set α = 0.63 (the average of the two end product studies).[11,12] We then used this α with the results of Chakir et al.[10] to determine k_3 = 13.5 x 10^{-12} cm^3 $molc^{-1}$ s^{-1} and k_4 = 2.8 x 10^{-12} cm^3 $molc^{-1}$ s^{-1}. In Figure 14, the literature model integrated with these parameters is overlaid on datasets acquired at two different values of $[HO_2]_0/[\beta\text{-CEP}]_0$. At $[HO_2]_0/[\beta\text{-CEP}]_0$ = 0.155, β-CEP is in excess of HO_2 and therefore the loss of HO_2 is dominated by R3. While our data exhibits initial growth of HO_2 (R4a), the literature model predicts that HO_2 would disappear almost immediately due to the fast value of k_3. At $[HO_2]_0/[\beta\text{-CEP}]_0$ = 2.52, HO_2 is in excess of β-CEP and now the loss of β-CEP is dominated by R3. Under these conditions, the literature model predicts β-CEP would disappear almost immediately while our data shows β-CEP persists with a half-life of several milliseconds. These comparisons demonstrate that the literature value of k_3, which is ~4 times faster than the value we determined, is wholly inconsistent with our data.

The reason for the discrepancy in k_3 is not readily apparent. The study of Chakir et al. did not directly measure k_3 but rather inferred the value from their measured $k_{4,obs}$ and α from the product studies.[10] In order for their derived k_3 to match our results, it would be necessary to assume α = 0.13, inconsistent with both of the product studies[11,12] and the value optimized in our work. One key difference between our study and that of Chakir et

al. is the wavelength region used to probe β-CEP: we used the $\tilde{A} \leftarrow \tilde{X}$ transition in the near-IR while Chakir et al. used the $\tilde{B} \leftarrow \tilde{X}$ transition in the UV. While our data collected at 7041.64 cm^{-1} was complicated by the presence of multiple absorbers, nearly every radical and product in the oxidation mechanism has a UV absorption band (β-CEP, $ClCH_2CH_2OOH$, $ClCH_2CHO$, HO_2, and H_2O_2). It is possible that the study of Chakir et al. did not properly partition the contribution of each species to the measured absorption, although this explanation is entirely speculative.

Values of the $RO_2 + HO_2$ rate constants for unsubstituted ethyl peroxy (6.9 x 10^{-12} cm^3 $molc^{-1}$ s^{-1}) and β-hydroxyethyl peroxy (β-HEP, 13 x 10^{-12} cm^3 $molc^{-1}$ s^{-1}) have been evaluated.[35] Comparing to our β-CEP value of k_3 = 3.4 x 10^{-12} cm^3 $molc^{-1}$ s^{-1}, it appears that β-hydroxy and β-chloro substitution have opposite effects on the reaction rate. As both substituents are inductive electron-withdrawing groups, it was initially expected that they would alter the rate constant in the same manner. However, β-HEP possesses intramolecular hydrogen bonding that may outweigh the inductive effects by placing the peroxy radical into a favorable geometry for reaction with HO_2 along the triplet surface. An empirical relationship between the $RO_2 + HO_2$ rate constant and the energy of the singly occupied molecular orbital (SOMO) of the RO_2 radical was derived by King and Thompson,[36] but the predicted rate constants of β-CEP (9.01 x 10^{-12} cm^3 $molc^{-1}$ s^{-1}) and β-HEP (9.16 x 10^{-12} cm^3 $molc^{-1}$ s^{-1}) disagree with the values measured experimentally.

The value of α determined by our work is smaller than the value determined by both of the stable product studies.[11,12] Interestingly, a similar discrepancy exists for α in the self reaction of ethyl peroxy. The accepted value, determined in experiments that measured the ratio of the acetaldehyde and ethanol products, is α = 0.60.[32] However, Noell et al. measured a much smaller value of α = 0.28.[14] Their approach was similar to our work and effectively determined α by comparing the growth of HO_2 relative to the loss of RO_2. While the discrepancy is greater for ethyl peroxy than for β-CEP, it is interesting that studies determining α from the radical kinetics consistently measure smaller values than those determined by stable product studies. This trend warrants additional study and may indicate a deficient understanding of the self reaction mechanism.

3.3.3 Reaction of Chlorine-Substituted Peroxy Radicals with NO

The rate constant for the reaction between peroxy radicals and NO (R7 for β-CEP) was determined by measuring the pseudo first order decay of peroxy radical absorption under conditions of excess NO. Peroxy radicals were probed via their $\tilde{A} \leftarrow \tilde{X}$ transition in the near-IR. Since our radical densities were ~10^{14} molc cm^{-3}, we kept [NO] at least an order of magnitude greater and varied the concentration over (2–6) x 10^{15} molc cm^{-3}. This leads to peroxy radical lifetimes of $\tau_{RO_2+NO} \approx$ 15–60 μs assuming a typical RO_2 + NO rate constant of k = 9 x 10^{-12} cm^3 molc^{-1} s^{-1}. As these time constants are of comparable magnitude as vacuum cavity ringdown times, our analysis again required the use of SKaR.

We typically measured RO_2 absorption decays at multiple frequencies in the RO_2 radical spectrum derived from the chlorine-initiated oxidation of a hydrocarbon precursor. Measurements were performed with ~8 different [NO] and we recorded ringdowns across ~100 delay times at each concentration. The ringdown ratio function, $R(t)$, was constructed using the procedure described in section 3.3.1 and Appendix A. For the pseudo first order decay of an RO_2 radical, the absorption was modeled according to:

$$A(t) = A_0 e^{-k't} + A_\infty \qquad \text{(Eqn. 9)}$$

with corresponding ringdown ratio function:[30]

$$R(t) = \exp\left[-\left(\frac{c}{d}\right)\left[\frac{A_0}{k'}\left(1 - e^{-k't}\right) + A_\infty t\right]\right] \qquad \text{(Eqn. 10)}$$

where k' is the pseudo first order decay constant and c and d have been defined previously. A_0 represents the initial RO_2 absorption. The conditions of these experiments were such that formation of the RO_2 radical was complete within a few microseconds. To ensure that the formation kinetics did not perturb the results, we typically fit $R(t)$ over t > 5 μs. Even though formation chemistry may cause A_0 to not perfectly correspond to $[RO_2]_0$, the fitted k' is unaffected since the decay rate is independent of $[RO_2]$. A_∞ is an empirical baseline absorption offset; its inclusion improved the quality of fits to Eqn. 10. Nevertheless, the fitted value of A_∞ was typically less than 5% of A_0 and fixing A_∞ = 0 yielded negligible difference in k'. As discussed previously, $R(0)$ was typically not unity due to fluctuations in the probe beam intensity, although the data could be scaled to $R(0)$ = 1 without any impact on the fitted value of k'.

Typical ringdown ratio data and their fits to Eqn. 10 are presented in Figure 15. The examples correspond to the absorption decay measured at 7448 cm^{-1} in the spectrum of RO_2 radicals produced from the Cl-initiated oxidation of 1,3-butadiene. We observe that data collected at smaller [NO] (smaller k') exhibit a greater decrease in $R(t)$ relative to pre-photolysis. This is consistent with the limiting behavior of Eqn. 10 as $t \to \infty$, assuming $A_\infty \approx 0$. From the fitted k', we constructed bimolecular plots (k' vs [NO]) whose slopes yielded the RO_2 + NO rate constant.

In the next subsections, we present RO_2 + NO rate constant results for the peroxy radicals formed in the Cl-initiated oxidation of ethene, propene, 1-butene, 2-butene, 1,3-butadiene, and isoprene. The RO_2 radicals were typically chlorine-substituted, although oxidation by chlorine can occur with small yield through abstraction of hydrogen atoms bonded to sp^3 hybridized carbons. Therefore, with the exception of ethene and 1,3-butadiene, our absorption spectra likely have a minor contribution from RO_2 radicals with only alkyl and/or allylic functionality. The SKaR approach was utilized to determine rate constants in each oxidation system and some additional analyses are presented for 2-butene and isoprene. Throughout, we compare our results to those of Patchen et al., who performed similar experiments measuring the pseudo-first order decays of chlorine-substituted peroxy radicals via CIMS detection.[19] A summary of our results is presented in Table III.

3.3.3.1 Ethene

Oxidation of ethene by Cl yields solely the β-CEP radical (R1, R2). We measured absorption decays in the presence of NO at two frequencies in the β-CEP spectrum: the peaks of the $\tilde{A} \leftarrow \tilde{X}$ origin bands of the GT (7352 cm^{-1}) and GG (7521 cm^{-1}) conformers.[29] The rate constants measured at each frequency were essentially identical: k_7 = (10.6 ± 1.4 and 11.0 ± 1.4) x 10^{-12} cm^3 $molc^{-1}$ s^{-1}, respectively. This is consistent with only one peroxy radical forming upon initial oxidation by Cl. Figure 16 presents a near-IR spectrum of β-CEP and the bimolecular plots at each probe frequency. While the two absorption peaks correspond to different conformers, their interconversion is rapid and it is unlikely that any conformer-dependent reactivity can be assessed.

Patchen et al. measured a rate constant of k_7 = (9.7 ± 1.2) x 10^{-12} cm^3 $molc^{-1}$ s^{-1} that is slightly slower, but within our uncertainty range.[19] One advantage of their CIMS

approach is that $ClRO_2$ radicals are detected at a unique mass, and therefore their signals have no interference from other peroxy radicals that may be in the reactor. In our experiments, interpretation of absorption decays could be complicated by the formation of second-generation, hydroxyl-substituted peroxy radicals, $HORO_2$. HO_2 produced from R5 reacts with NO to yield OH (R8). OH radicals then oxidize ethene to form β-HEP. The near-IR spectrum of β-HEP has been measured previously and its most intense absorption peak, centered at 7381 cm^{-1},[37] is indeed close to the β-CEP band we probed at 7352 cm^{-1}. However, the formation of β-HEP is rate-limited by the β-CEP + NO reaction, and this rate is comparable to the loss rate of β-HEP through the β-HEP + NO reaction. Therefore, the steady-state concentration of β-HEP is small and likely has only minor contribution to the absorption signals we measured. Furthermore, if β-HEP absorption were important, then its presence would systematically decrease the apparent value of k_7. We measured a value of k_7 that is slightly faster than that measured by Patchen et al., suggesting secondary $HORO_2$ did not impact our results.

3.3.3.2 Propene

Oxidation of propene by Cl yields three different RO_2 radicals: 1,2-chloropropyl, 2,1-chloropropyl, and allyl peroxy. We measured absorption decays in the presence of NO at three frequencies in the resulting spectrum: 7384, 7462, and 7587 cm^{-1}. The RO_2 + NO rate constants measured at each frequency were essentially identical: (10.3 ± 1.4, 10.0 ± 1.4, and 10.0 ± 1.4) x 10^{-12} cm^3 $molc^{-1}$ s^{-1}, respectively. Figure 17 presents a near-IR spectrum of the peroxy radical mixture and the bimolecular plots at each probe frequency.

Definitive assignments of the absorption bands in the near-IR spectrum arising from the Cl-initiated oxidation of propene are not firmly established. However, the near-IR spectrum of pure allyl peroxy has been measured previously.[38] The strongest peak in the allyl peroxy spectrum, centered at 7605 cm^{-1}, is close to the band we probed at 7587 cm^{-1}. It is likely that this band has contribution from allyl peroxy, but not exclusively, due to the mismatch between the center frequencies. Indeed, the yield of allyl peroxy from oxidation of propene by Cl is estimated to be only ~10% at 300 Torr.[39] The peaks in our spectrum centered at 7384 and 7462 cm^{-1} are likely dominated by the 1,2-chloropropyl and 2,1-chloropropyl peroxy radical isomers. While allyl peroxy exhibits a broad absorption band over these frequencies, it is less intense than its band at 7605 cm^{-1}.[38] Since our spectrum

shows the opposite intensity distribution (greater signal at 7384 cm^{-1} than at 7587 cm^{-1}), it is unlikely that allyl peroxy contributes substantially to absorption at 7384 or 7462 cm^{-1}.

Patchen et al. measured a rate constant of (10.2 ± 1.2) x 10^{-12} cm^3 $molc^{-1}$ s^{-1} for $ClRO_2$ radicals formed upon propene oxidation.[19] Eberhard et al. measured (10.5 ± 1.8) x 10^{-12} cm^3 $molc^{-1}$ s^{-1} for allyl peroxy.[40] These values are in excellent agreement with the results of the present work. If allyl peroxy and the chloropropyl peroxy isomers had different rate constants for reaction with NO, then it is possible we would have obtained a different result at 7587 cm^{-1} than at 7384 and 7462 cm^{-1}.

The OH generated from the alkoxy radical reactions with O_2 and R8 will oxidize propene to yield the 1,2-hydroxypropyl and 2,1-hydroxypropyl peroxy radicals as second generation $HORO_2$. The near-IR spectrum of the less abundant 2,1-hydroxypropyl isomer has been measured and exhibits absorption intensity over the frequencies probed in this work.[41] However, as argued in the previous subsection, the steady-state concentrations of secondary $HORO_2$ radicals is small and they are unlikely to have appreciable contribution to the measured absorption signals. The agreement between our rate constants and prior studies reflects this.

3.3.3.3 1-Butene

Oxidation of 1-butene by Cl yields a mixture of chlorobutyl (1- or 2-addition), allylic (3-abstraction), and alkyl (4-abstraction) peroxy radicals. The 1,2-chlorobutyl and 2,1-chlorobutyl peroxy radical isomers are expected to dominate. Figure 18 presents a near-IR spectrum of the peroxy radical mixture and the bimolecular plots for the RO_2 + NO rate constant measurements conducted at each probe frequency. Due to the complexity of the resulting near-IR spectrum (many peroxy radicals and conformers), assignments of the absorption bands have not been established.

We measured absorption decays in the presence of NO at three frequencies in the resulting spectrum: 7346, 7422, and 7508 cm^{-1}. The RO_2 + NO rate constants measured at each frequency were essentially identical: (8.8 ± 1.2, 8.7 ± 1.2, and 8.5 ± 1.2) x 10^{-12} cm^3 $molc^{-1}$ s^{-1}, respectively. Patchen et al. measured a rate constant of (9.6 ± 1.0) x 10^{-12} cm^3 molc-^{1} s^{-1} for the $ClRO_2$ radicals formed upon 1-butene oxidation.[19] Our values are slightly slower, but still in excellent agreement.

3.3.3.4 2-Butene

Oxidation of 2-butene (cis/trans mixture) by Cl yields only one $ClRO_2$ isomer: 2,3-chlorobutyl peroxy. Several unsubstituted, allylic peroxy radicals can also form through hydrogen abstractions, but their yields are likely minor. We measured absorption decays in the presence of NO at the center of three peaks in the resulting spectrum: 7364, 7473, and 7600 cm^{-1}. The rate constants measured at each frequency were not identical for this system: (4.0 ± 0.6, 5.4 ± 0.8, and 5.8 ± 0.8) x 10^{-12} cm^3 $molc^{-1}$ s^{-1}, respectively. Figure 19 presents a near-IR spectrum of 2,3-chlorobutyl peroxy (and possibly the minor allylic peroxy radicals) and the bimolecular plots at each frequency.

2-Butene oxidation was the only system for which we observed a difference in rate constant across measurements conducted at multiple frequencies: the rate constants measured at 7473 and 7600 cm^{-1} agree, but the rate constant measured at 7364 cm^{-1} is ~20–30% slower. We also note that the bimolecular plot at 7364 cm^{-1} exhibits a large, positive offset that cannot be readily explained. While the values could reflect a difference in rate constant between 2,3-chlorobutyl peroxy and the allylic peroxy radicals, this seems unlikely since the yields of the latter are expected to be small. Furthermore, our results at each frequency are ~40–60% slower than the rate constant of (9.8 ± 1.2) x 10^{-12} cm^3 $molc^{-1}$ s^{-1} for 2,3-chlorobutyl peroxy measured by Patchen et al.[19] The fact that none of our measurements match their result suggests another factor may be at play.

We explored the possibility that second generation peroxy radicals formed from the alkoxy radical chemistry yielded sustained absorption signal, which would lead to an apparent slowing of the decay rate that is frequency-dependent. The fates of the 2,3-chlorobutyl alkoxy radical product of the $ClRO_2$ + NO reaction are summarized in Figure 20a. Reaction with O_2 yields HO_2, which forms OH through R8. OH will then oxidize 2-butene to form 2,3-hydroxybutyl peroxy. The near-IR spectrum of this species is unknown. Nevertheless, it is unlikely that this radical contributes substantially to the measured absorption signal for reasons discussed previously. If second generation $HORO_2$ were important, then we would have also measured slower rate constants for the peroxy radicals formed upon oxidation of ethene, propene, and 1-butene. Our results for those species were in excellent agreement with those of Patchen et al.,[19] suggesting $HORO_2$ is not the cause of the slower absorption decays in 2-butene oxidation.

Two possible decomposition channels exist for 2,3-chlorobutyl alkoxy that eventually yield α-chloroethyl peroxy (α-CEP) and methyl peroxy (Figure 20a). The near-IR spectrum of pure methyl peroxy is known and characterized by three bands over this region centered at 7383, 7488, and 7610 cm^{-1}.[42,43] Coincidentally, these frequencies fall on the three major absorption bands in the 2,3-chlorobutyl peroxy spectrum, centered at 7364, 7473, and 7600 cm^{-1}. The intensity distributions are opposite, however, with the methyl peroxy bands becoming less intense as frequency increases while the 2,3-chlorobutyl peroxy bands become more intense. Interestingly, the values of the measured rate constants also appear correlated to these intensity distributions. The slowest rate constant was measured at 7383 cm^{-1}, where the methyl peroxy spectrum is the most intense and the 2,3-chlorobutyl peroxy spectrum is the least intense. This supports a hypothesis that second generation methyl peroxy absorption can explain the slower decay rates, as we would expect the bias to be greatest where methyl peroxy absorption is strong and 2,3-chlorobutyl peroxy absorption is weak. Figure 20b presents a near-IR spectrum of the reactive mixture collected with a 100 μs delay time using our lowest [NO] = 1.95 x 10^{15} molc cm^{-3}. While the spectrum is still dominated by 2,3-chlorobutyl peroxy, we see a small, sharp peak appear at 7383 cm^{-1}. The position of this peak exactly matches the frequency of the sharp Q-branch transition of the $\tilde{A} \leftarrow \tilde{X}$ methyl peroxy origin band,[43] suggesting that methyl peroxy indeed contributes to our absorption signals.

The spectrum of the other decomposition product, α-CEP, has not been reported previously and was therefore measured in this work. The results are summarized in Figure 21. Chloroethane was oxidized by Cl through hydrogen abstraction to generate α-CEP and β-CEP with yields of 82% and 18%, respectively (Figure 21a).[44] To remove the contribution of β-CEP from the composite spectrum, we conducted separate experiments oxidizing ethene to yield β-CEP with 100% yield. Spectra measured in these two experiments were obtained using the same initial $[Cl]_0$, in the absence of NO, and at a 10 μs delay (before RO_2 self and cross reactions occur). This ensured that the spectra were obtained with the same total peroxy radical concentration. We could then scale the 100% β-CEP spectrum (from ethene) by 0.18 and subtract it from the composite 18% β-CEP spectrum (from chloroethane) to obtain a spectrum of solely α-CEP (Figure 21b). Despite constituting only 18% of the peroxy radical yield, β-CEP was responsible for most of the

absorption signal in the composite spectrum. The pure α-CEP spectrum over 7300–7700 cm^{-1} appears fairly weak and featureless.

In an attempt to disentangle the second generation peroxy radical absorption (methyl peroxy and α-CEP) from the first generation 2,3-chlorobutyl peroxy absorption, we measured spectra from 2-butene oxidation over a series of delay times ranging 3–300 μs. We used the lowest [NO] = 1.95 x 10^{15} molc cm^{-3} in these experiments, where the pseudo first order decay rates are slow enough that the use of SKaR is less important. The resulting spectra were fit as a linear combination of the pure 2,3-chlorobutyl peroxy, α-CEP, and methyl peroxy spectra. (Since the methyl peroxy spectrum in the prior reports was not tabulated,[42,43] we also conducted experiments to measure its pure spectrum through the Cl-initiated oxidation of methane. Our spectrum was in good agreement with the prior reports but noisier, due to slow rate constants for Cl + CH_4 and CH_3 + O_2 and background absorption of the methane precursor.) In Figure 20c, the amplitudes of the peroxy radical signals from the fits are plotted as a function of reaction time. The amplitude of 2,3-chlorobutyl peroxy was fit to Eqn. 9 and yielded k' = 1.1 x 10^4 s^{-1}. Dividing this by [NO] yields an estimate for the $ClRO_2$ + NO rate constant as 5.6 x 10^{-12} cm^3 $molc^{-1}$ s^{-1}. Surprisingly, this is similar to the values measured without taking into account secondary peroxy radicals (Figure 19). It is possible that our fits do not accurately capture the contribution of α-CEP due to the lack of distinct features and noise level in its pure spectrum. Indeed, the fitted amplitude of α-CEP in Figure 20c suspiciously begins above zero and is fairly time-independent, whereas the kinetics of the 2,3-chlorobutyl and methyl peroxy amplitudes follow expected behavior. It is also possible that the value of k' was biased to slower values in the analysis, since SKaR cannot be utilized with spectra. Unfortunately, our efforts did not reach a satisfying conclusion, although we still believe that second generation peroxy radical absorption is responsible the slower, frequency-dependent rate constants measured for the 2,3-chlorobutyl peroxy + NO reaction.

3.3.3.5 1,3-Butadiene

Oxidation of 1,3-butadiene by Cl yields solely chlorine-substituted peroxy radicals. The distribution is likely dominated by allylic $ClRO_2$ from terminal Cl-addition, with only minor contribution by $ClRO_2$ from internal Cl-addition. We measured absorption decays in the presence of NO at two frequencies in the resulting spectrum: 7448 and 7592 cm^{-1}.

The RO_2 + NO rate constants measured at each frequency were essentially identical: (7.5 ± 1.0 and 7.2 ± 1.0) x 10^{-12} cm^3 $molc^{-1}$ s^{-1}, respectively. Figure 22 presents a near-IR spectrum of the peroxy radical mixture and the bimolecular plots at each probe frequency.

The rate constants we measured are ~40% slower than the value determined by Patchen et al. of (11.8 ± 1.0) x 10^{-12} cm^3 $molc^{-1}$ s^{-1}. Nevertheless, our value is similar to typical rate constants of RO_2 + NO reactions. It is possible that our measured decay rates appear artificially slow due to second generation peroxy radicals sustaining the absorption signal, as we expect to be the case in our measurements of 2-butene oxidation. Indeed, the 1-Cl 2-OO $ClRO_2$ isomer from 1,3-butadiene oxidation, which is the most stable and expected to have the greatest yield, forms an alkoxy radical that can decompose to form β-CEP. From measurements described earlier in this chapter, we know that β-CEP has strong absorption signal over this region. We measured a series of time-dependent spectra of 1,3-butadiene oxidation in the presence of NO and found no evidence for the formation of β-CEP absorption peaks at later delay times. Therefore, we did not further explore the possibility of secondary peroxy radical interference.

3.3.3.6 Isoprene

Isoprene is the most emitted non-methane hydrocarbon (NMHC) at a rate of ~500 Tg $year^{-1}$; a substantial flux of carbon proceeds through its oxidative pathways.[45] The oxidation of isoprene by Cl has been discussed in a recent review.[46] Addition of Cl to isoprene can yield eight distinct $ClRO_2$ isomers (including stereoisomers), although only the six isomers resulting from addition to the terminal carbons are expected to be important.[47] Abstraction of hydrogen yields an additional unsubstituted peroxy radical with ~15% yield.[48] We measured absorption decays in the presence of NO at four frequencies in the resulting spectrum: 7452, 7534, 7652, and 7709 cm^{-1}. The RO_2 + NO rate constants measured at each frequency were essentially identical: (5.9 ± 0.8, 6.2 ± 0.8, 6.4 ± 0.8, and 6.4 ± 0.8) x 10^{-12} cm^3 $molc^{-1}$ s^{-1}, respectively. Figure 23 presents a near-IR spectrum of peroxy radical mixture and the bimolecular plots at each frequency.

Once again, we observed disagreement with the results of Patchen et al.[19] The rate constants we measured are ~50% slower than their value of (11.5 ± 1.1) x 10^{-12} cm^3 $molc^{-1}$ s^{-1}. Due to the many first generation peroxy radicals in the mixture, we did not evaluate the entire suite of second generation peroxy radicals that could arise from alkoxy radical

decomposition (or isomerization) and contribute to absorption, as we did with 2-butene oxidation. We also did not evaluate second generation $HORO_2$ due to their negligible impact in the studies of ethene, propene, and 1-butene and for the other reasons discussed previously. However, we did consider one possible second generation peroxy radical: chloromethyl peroxy. The 1-Cl, 2-OO and 4-Cl, 3-OO isomers are expected to comprise ~50% of the first generation $ClRO_2$ yield from isoprene oxidation[49] and their corresponding alkoxy radicals can decompose to form chloromethyl radicals, with methyl vinyl ketone and methacrolein as the respective coproducts. Therefore, second generation chloromethyl peroxy may be produced with sufficient yield to sustain absorption and slow the apparent decay rates.

To investigate this possibility, we measured spectra from isoprene oxidation over a series of delay times ranging 5–500 μs (shown in Figure 24a). We used the lowest [NO] = 1.98×10^{15} molc cm^{-3} in these experiments, where the pseudo first order decay rates are slow enough that the use of SKaR is less important. Similar to the analysis described for 2-butene oxidation, we fit these spectra as a linear combination of a pure chloromethyl peroxy spectrum (obtained from the Cl-initiated oxidation of chloromethane) and a spectrum of the mixture of peroxy radicals formed immediately upon isoprene oxidation (obtained in the absence of NO at a delay time of 10 μs, before any self and cross reactions could occur). The time-dependent amplitude of the isoprene peroxy radical spectrum was fit to Eqn. 9 and yielded an estimated RO_2 + NO rate constant of 5.0×10^{-12} cm^3 $molc^{-1}$ s^{-1}. Surprisingly, this value is slightly slower than the those obtained in the single frequency measurements, although the uncertainty may be great due to the use of only one [NO]. The amplitude of the pure chloromethyl peroxy spectrum was essentially zero at all delay times, suggesting that second generation chloromethyl peroxy cannot explain the slow rate constants. The lack of chloromethyl peroxy yield is consistent with a study predicting that the chloroalkenyl alkoxy radicals formed in Cl-initiated oxidation of isoprene are more likely to react with O_2 than decompose when compared to the analogous alkoxy radicals formed in the OH-initiated oxidation of isoprene.[18]

Inspection of the time-dependent spectra collected in the presence of NO (Figure 24a) revealed an interesting observation: the sharp peak centered at 7652 cm^{-1} decays much faster than the rest of the spectrum, and has essentially disappeared by ~100 μs. The

remaining broad, featureless absorption decays at a much slower rate and does not disappear until closer to ~500 μs. To help identify the peroxy radical responsible for the peak, we measured a series of spectra over delay times ranging 10 μs – 35 ms in the absence of NO (shown in Figure 24b), where absorption decays are due to peroxy radical self and cross reactions. Under these conditions, the peak at 7652 cm^{-1} exhibits the opposite behavior, persisting much longer than other features in the spectrum. Indeed, the inversion in intensity of the peaks at 7452 and 7534 cm^{-1} between 10 μs and 1.5 ms strongly suggests isomer-dependent reactivity. 3° peroxy radicals are known to self and cross react with other peroxy radicals quite slowly.[50] Previously, Glover and Miller used this fact to distinguish *t*-butyl peroxy (3°) from isobutyl peroxy (1°) in the near-IR spectrum of peroxy radicals formed upon isobutane oxidation.[51] Following the same reasoning, we assign the peak at 7652 cm^{-1} as the 1-Cl, 2-OO $ClRO_2$ isomer, which is the only 3° peroxy radical that forms upon isoprene oxidation. The structure of this species is shown in Figure 24.

We attempted to separate the RO_2 + NO kinetics of the 3° 1-Cl, 2-OO peroxy radical from other peroxy radicals contributing to the spectrum, whether they be first or second generation. To achieve this, we assumed that absorption at 7685 cm^{-1}, positioned immediately off of the sharp peak and within the broad absorption band, is approximately equal to the sum of all peroxy radical absorption except 1-Cl, 2-OO at 7652 cm^{-1}, the peak center. (In other words, we are assuming that the spectrum of the peroxy radical mixture without 1-Cl, 2-OO would be flat between 7652 and 7685 cm^{-1}.) The difference in signal between 7652 cm^{-1} (peak center) and 7685 cm^{-1} (immediately off the peak) is then equal to absorption solely by 1-Cl, 2-OO. In Figure 25, we plot the difference in absorption between these two frequencies observed in the time-dependent spectra collected with [NO] = 1.98 x 10^{15} molc cm^{-3}. The pseudo first order absorption decay is fit to Eqn. 9 and yields an RO_2 + NO rate constant of 10.8 x 10^{-12} cm^3 $molc^{-1}$ s^{-1} for the 3° 1-Cl, 2-OO peroxy radical isomer, in good agreement with the value determined by Patchen et al.[18] While we have now successfully measured the rate constant of an individual peroxy radical isomer generated by isoprene oxidation, the interpretation of our results for the other isomers is less clear. The slower rate constants determined by the single frequency analysis could reflect isomer-dependent reactivity in the RO_2 + NO reaction, since fitting a superposition of decay rates will be biased toward the slower decay rates. Alternatively, unidentified

second generation peroxy radicals could be sustaining the absorption signal and artificially slowing the apparent decay rates. Unfortunately, the results of the present study cannot definitively distinguish between these two possibilities.

3.4 Conclusions

In this chapter, we have described experiments using pulsed cavity ringdown spectroscopy to study the kinetics of chlorine-substituted peroxy radicals through their forbidden $\tilde{A} \leftarrow \tilde{X}$ transition in the near-IR. Cl radicals are a minor tropospheric oxidant but can add an additional spark to VOC oxidation cycles, particularly in coastal, urban regions. Oxidation of alkenes by Cl yields chlorine-substituted peroxy radicals. The kinetics of these species have not been the subject of prior systematic study. Previous measurements have focused on the β-chloroethyl peroxy radical (β-CEP), formed in the oxidation of ethene, and studied its kinetics through the $\tilde{B} \leftarrow \tilde{X}$ transition in the UV.[8–10] While this transition offers large cross sections, it is broad and dissociative, leading to absorption bands that lack any identifying structure. Since many functional groups exhibit UV absorption, distinguishing RO_2 radicals from other species in the oxidation mechanism is not straightforward. In contrast, the $\tilde{A} \leftarrow \tilde{X}$ transition is between two bound states, and yields detailed RO_2 spectra that vary with molecular structure.

The first part of the chapter presented measurements of the rate constant for the association of β-chloroethyl radicals with O_2 to yield β-CEP. The high-pressure limit rate constant was found to be ~2.5 times slower than the evaluated association rate constant to form unsubstituted ethyl peroxy.[32] This was rationalized as the β-chloro functional group inducing an electron-withdrawing effect that destabilizes the β-chloroethyl radical to a greater extent than β-CEP, due to the proximity of the group to the radical center. Additional studies over a range of substituents would help address this hypothesis. The methodology outlined here may act as a generalized approach to measuring association rate constants to form peroxy radicals.

The second part of the chapter presented a direct measurement of the rate constant between β-CEP and HO_2, which represents the dominant fate of β-CEP in low NO_x regions of the atmosphere. The resulting rate constant was found to be substantially slower than a

value determined indirectly by a prior study using the $\tilde{B} \leftarrow \tilde{X}$ transition.[10] However, comparison of a model constructed from the prior rate constants to the absorption signals measured in this work demonstrated that a fast β-CEP + HO_2 rate constant is wholly inconsistent with our data (Figure 14). Our rate constant was also found to be slower than those for the analogous reactions of unsubstituted ethyl peroxy and β-hydroxyethyl peroxy (β-HEP). We hypothesized that substitution by a β electron-withdrawing group will in general deactivate the RO_2 + HO_2 reaction. However, intramolecular hydrogen bonding in β-HEP could outweigh the inductive effect by placing the molecule into a favorable geometry for reaction with HO_2 along the triplet surface.

We also measured the rate constant and branching ratio of the β-CEP self reaction in the second part of the chapter. Self reactions are relatively unimportant in the atmosphere, but can become important in laboratory studies where high radical densities are often necessary to achieve sufficient signal-to-noise. The branching ratio (α) to the radical propagating channel of the β-CEP self reaction was found to be smaller than values measured in stable product studies.[11,12] This discrepancy has also been observed in a study of the ethyl peroxy self reaction,[14] in which the value of α was determined by comparing the growth of HO_2 relative to the loss of RO_2 (similar to our approach) and found to be smaller than the accepted value from stable product studies.[32] This trend warrants additional study and may indicate a deficient understanding of the mechanism for peroxy radical self reactions.

Finally, in the last part of the chapter we presented rate constant measurements for the reactions between NO and the peroxy radicals formed in the Cl-initiated oxidation of ethene, propene, 1-butene, 2-butene, 1,3-butadiene, and isoprene. Experiments were performed by probing absorption decays at several discrete frequencies in the peroxy radical spectrum across a range of [NO] under pseudo first order conditions. The rate constants determined in experiments with ethene, propene, and 1-butene as the alkene precursors agreed well with the results of Patchen et al.,[19] who performed similar measurements detecting peroxy radicals with chemical ionization mass spectrometry (CIMS). The rate constants determined using 2-butene, 1,3-butadiene, and isoprene as the precursors were substantially slower than the results of Patchen et al. For 2-butene and isoprene, we measured time-dependent spectra at a single [NO] to investigate if the slower

absorption decays were caused by second generation peroxy radicals from the alkoxy radical chemistry leading to artificially sustained absorption signals. The results of those experiments were unfortunately inconclusive and in the case of isoprene, we could not definitively distinguish between isomer-dependent reactivity or second generation peroxy radical absorption. At any rate, the agreement between the literature values and our results for ethene, propene, and 1-butene suggests the slower decay rates are not caused by second generation $HORO_2$ radicals, which form in each oxidation system. For isoprene oxidation, we conducted separate experiments to assign the sharp feature at 7652 cm^{-1} in the near-IR spectrum as the 3° 1-Cl, 2-OO $ClRO_2$ isomer. We elucidated its time-dependent absorption signal and measured an isomer-specific rate constant for reaction with NO that is in good agreement with the results of the CIMS study.[19]

Overall, our experiments have demonstrated that cavity ringdown spectroscopy can be a powerful technique in the study of organic peroxy radical kinetics through detection of the RO_2 $\tilde{A} \leftarrow \tilde{X}$ transition in the near-IR. Nevertheless, while studies in the near-IR reduce the number of interfering absorbers relative to studies conducted in the UV, complications are still introduced in oxidation systems containing many distinct organic peroxy radicals (such as isomers) due to their overlapping absorption bands.

3.5 Figures

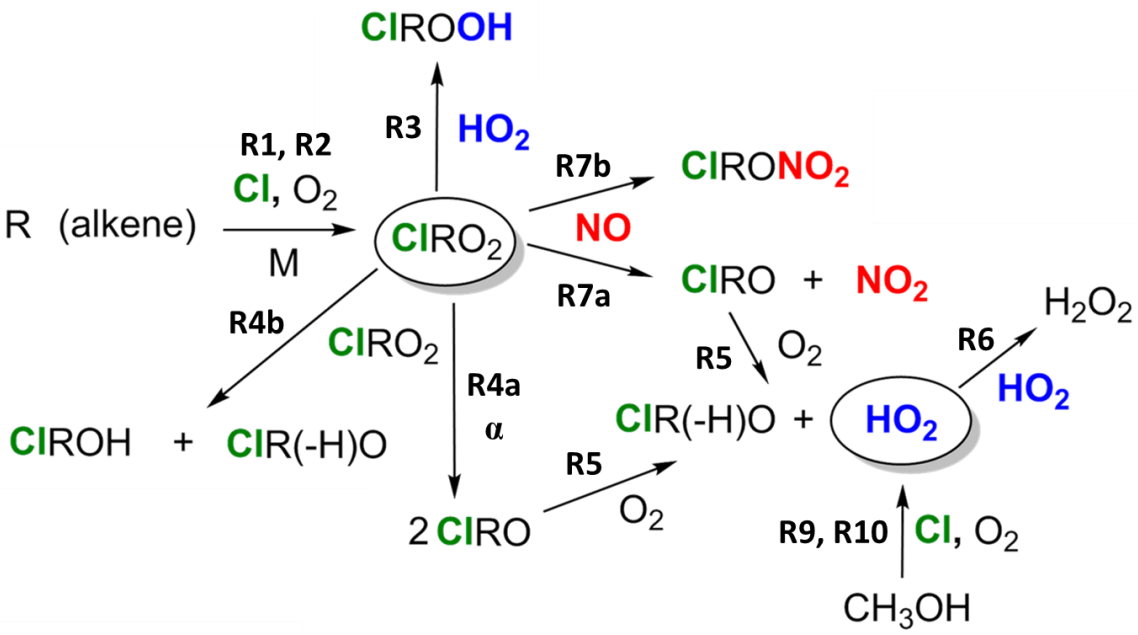

Figure 1: Schematic summary of the oxidations and peroxy radical reactions studied in this chapter. The circled species are detected through the $\tilde{A} \leftarrow \tilde{X}$ transition of RO_2 radicals in the near-IR. The reaction numbers correspond to the values in the text, assuming the oxidized alkene is ethene. The schematic does not show alternative alkoxy radical reactions (isomerization / decomposition) nor other products of the $ClRO_2$ + HO_2 reaction, which are possible for larger alkene precursors. We have measured k_2, k_3, k_4, α, and k_7 for β-CEP derived from Cl-initiated oxidation of ethene. The $ClRO_2$ + NO rate constants of $ClRO_2$ derived from Cl-initiated oxidation of propene, 1-butene, 2-butene, 1,3-butadiene, and isoprene have also been measured.

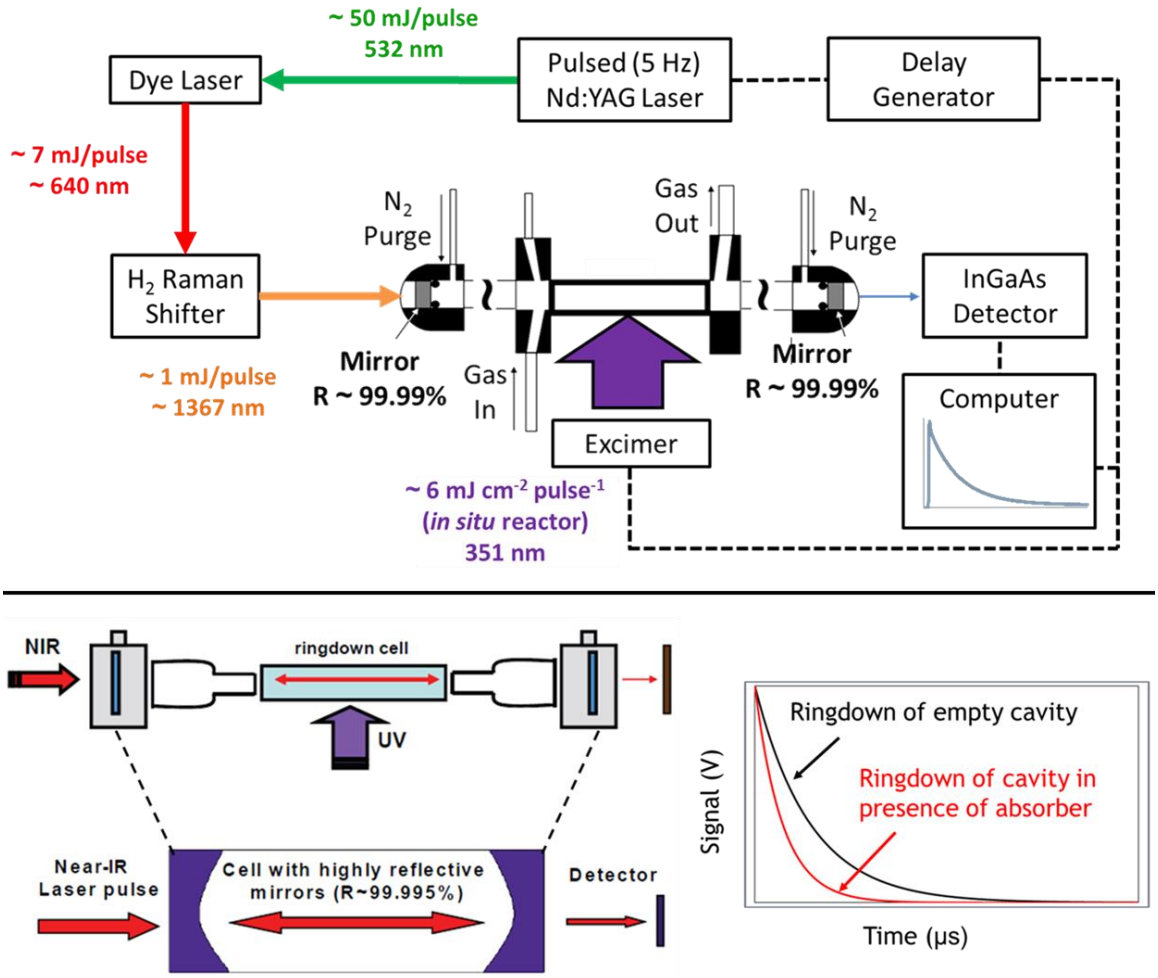

Figure 2: Schematic of the pulsed near-IR cavity ringdown spectrometer used to study peroxy radical kinetics. **(top)** Summary of key instrumentation. The second harmonic of a Nd:YAG laser is used to pump a dye laser. Tunable, visible radiation is focused into a 9-pass Herriot cell filled with ~10 atm of H_2 acting as Raman laser. The outputted radiation is longpass filtered to transmit the second sequential Stokes shift in the near-IR for cavity ringdown absorption measurements. The near-IR pulse becomes resonant with an optical cavity enclosing a chemical reactor. The decay of intracavity power is measured by an InGaAs detector. A digital delay generator synchronizes firing of the probe and photolysis lasers to establish a time axis for kinetic measurements. **(bottom)** Expanded view of the ringdown cavity. The difference in photon lifetime between the presence and absence of a photolysis pulse determines the absorption induced by radical chemistry.

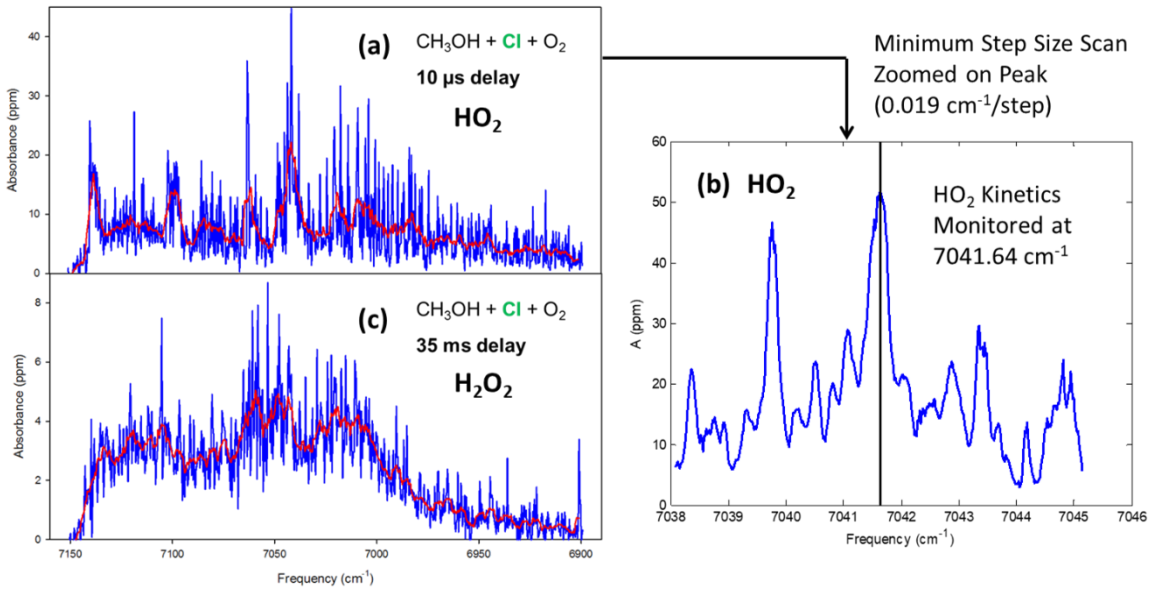

Figure 3: Near-IR spectra recorded over the $\tilde{A} \leftarrow \tilde{X}$ origin Q-branch region of HO_2 following the oxidation of methanol. The red lines represent a running average over adjacent frequencies. **(a)** Spectrum recorded over 6900–7150 cm^{-1} with a 10 μs delay between photolysis and probe pulses. The HO_2 self reaction has occurred to a negligible extent and the spectrum represents solely HO_2. **(b)** Spectrum recorded with a 10 μs delay zoomed over a narrower frequency range of 7038–7045 cm^{-1} with 0.019 cm^{-1} steps. Time-resolved HO_2 absorption was monitored at the peak of signal at 7041.64 cm^{-1}. **(c)** Spectrum recorded over 6900–7150 cm^{-1} with a 35 ms delay. The HO_2 self reaction has completed and the spectrum represents solely H_2O_2.

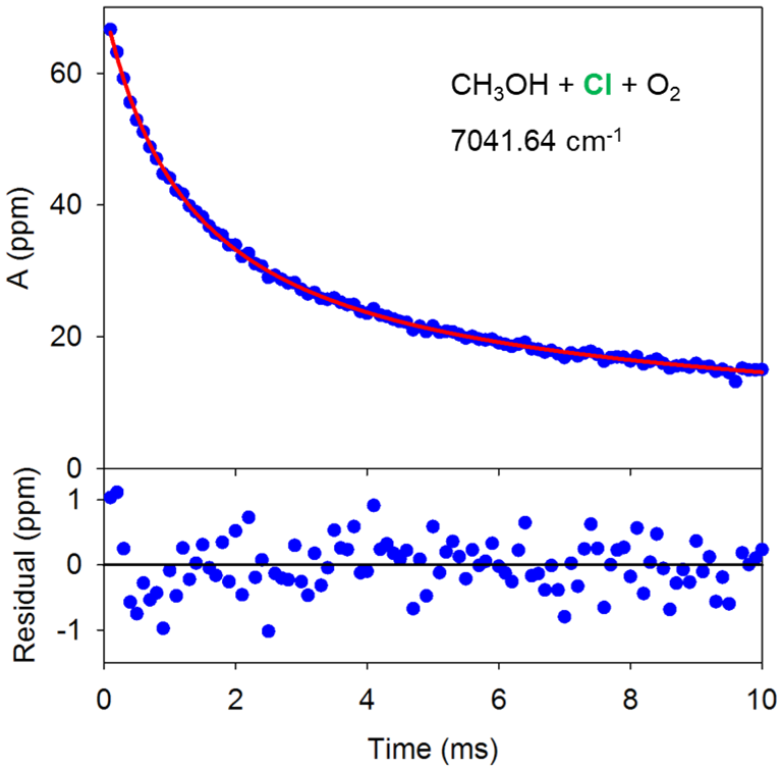

Figure 4: Example HO_2 self reaction kinetics recorded over 0-10 ms with 0.1 steps. Time-resolved absorption was monitored at 7041.64 cm^{-1}. A three-parameter fit to Eqn. 1 is overlaid in red. From the optimized parameters, we determined $[Cl]_0$ = 1.66 x 10^{14} atoms cm^{-3}, S_{HO_2} = 4.15 x 10^{-19} cm^3 $molc^{-1}$, and $S_{H_2O_2}$ = 7.91 x 10^{-20} cm^3 $molc^{-1}$.

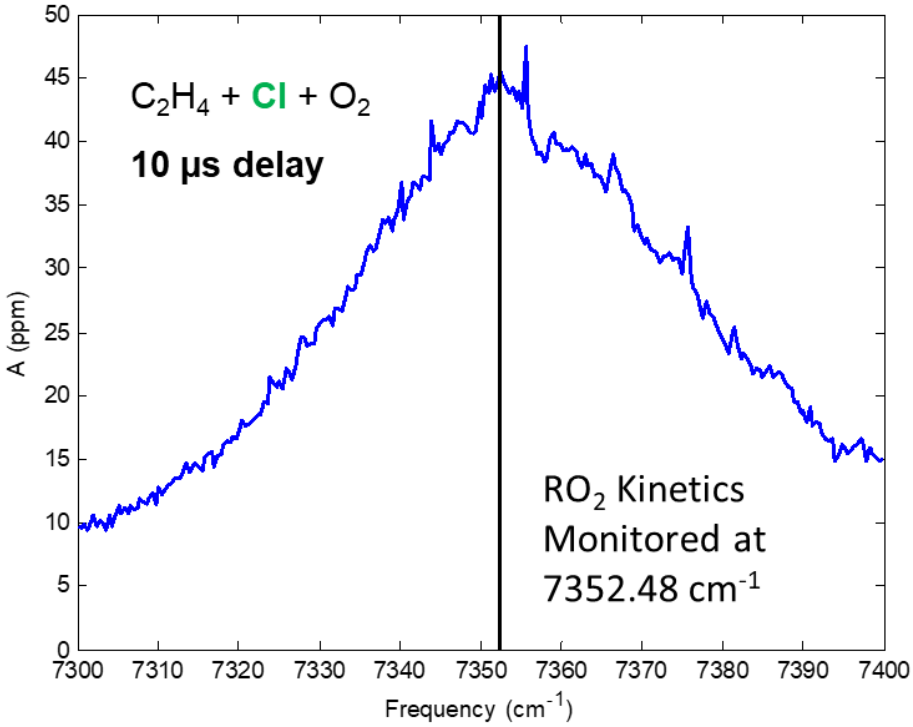

Figure 5: Spectrum of the $\tilde{A} \leftarrow \tilde{X}$ origin band of the C-C-O-O gauche, Cl-C-C-O trans (GT) conformer of β-CEP, generated by the Cl-initiated oxidation of ethene. Most β-CEP kinetics were measured by probing absorption at the peak of this band at 7352.48 cm^{-1}.

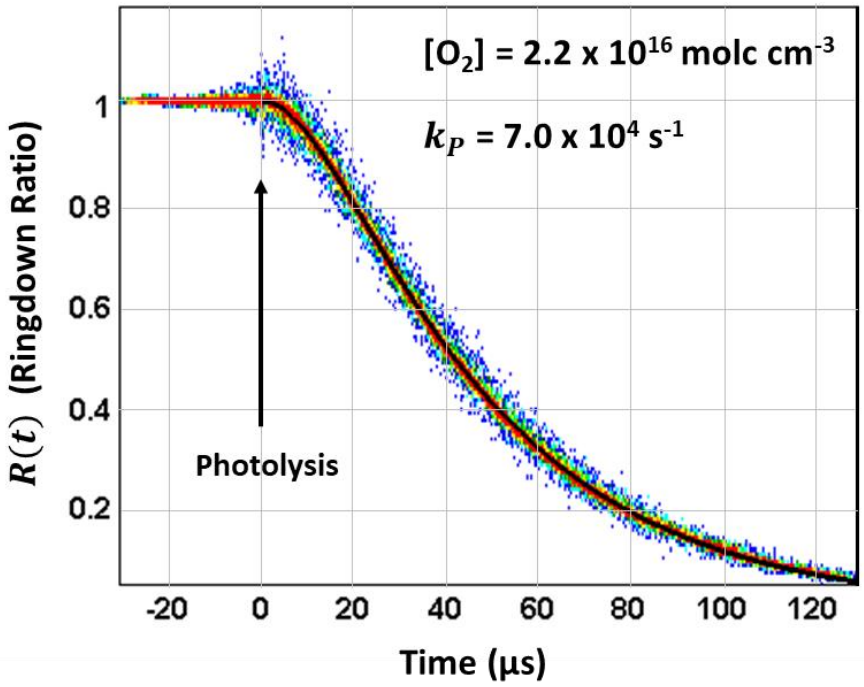

Figure 6: Typical ringdown ratio dataset $R(t)$ constructed as described in the text for experiments measuring the formation rate constant of β-CEP. Pixels of hotter colors correspond to greater data point density than pixels of cooler colors. This signal was recorded for $[O_2]$ = 2.2 x 10^{16} molc cm^{-3} and the two-parameter fit to Eqn. 3 (overlaid as a black curve) yielded a pseudo first order formation rate constant of k_P = 7.0 x 10^4 s^{-1}.

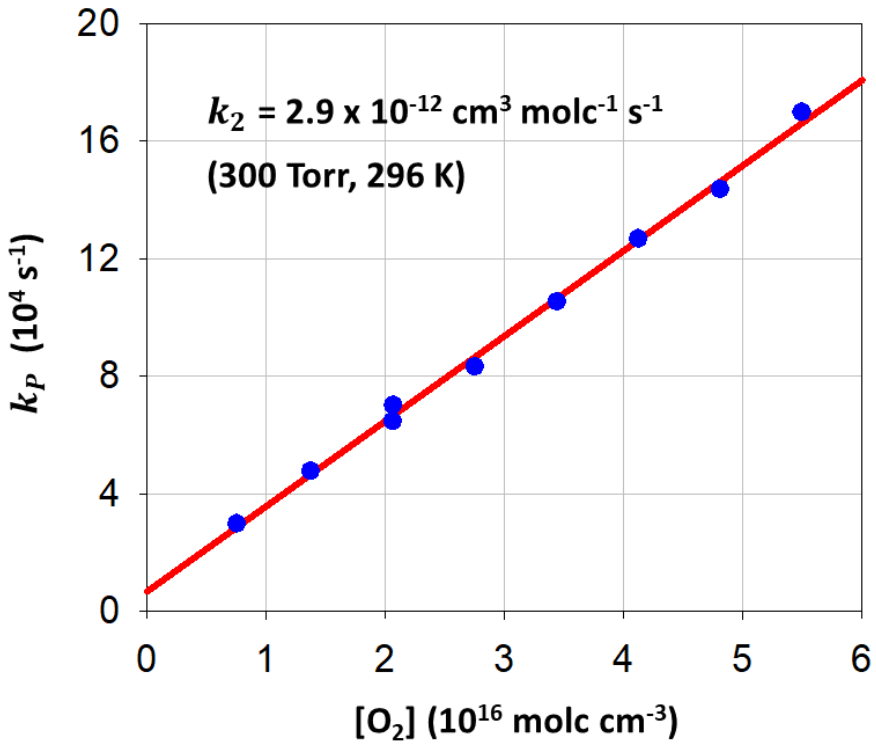

Figure 7: Bimolecular plot (k_P vs [O_2]) for experiments measuring the formation rate constant of β-CEP. The slope of the line gives the rate constant for the association of β-chloroethyl radicals with O_2: k_2 = 2.9 x 10^{-12} cm^3 $molc^{-1}$ s^{-1} at 300 Torr and 296 K. Separate experiments confirmed that this value is in the high-pressure limit. The magnitude of the small, positive intercept is consistent with the background [O_2] expected in the reactor from the base pressure and atmospheric mixing ratio of O_2.

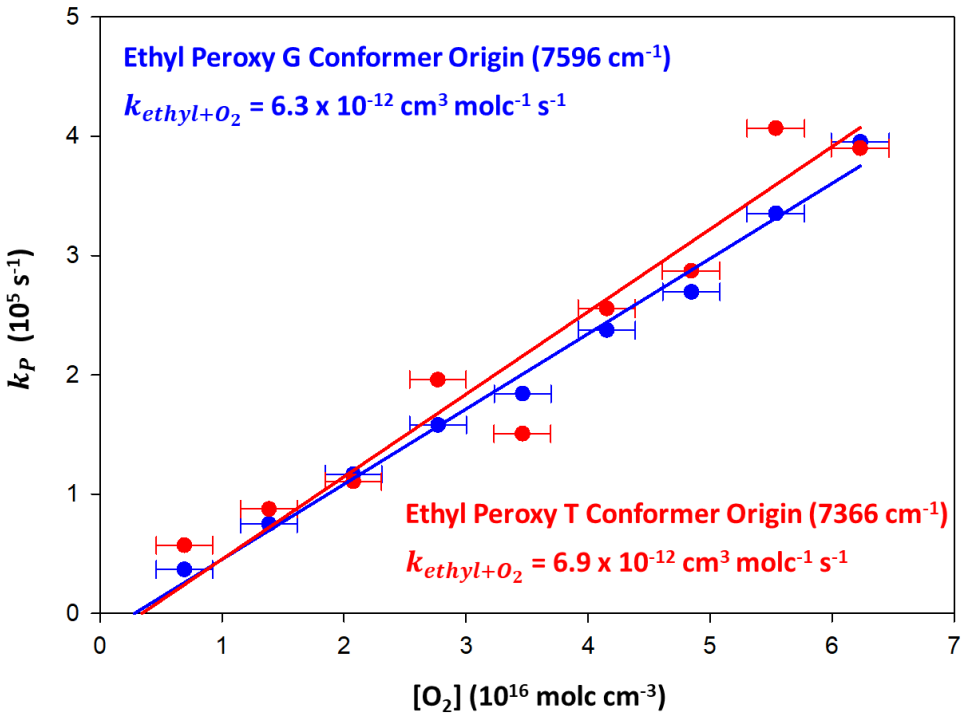

Figure 8: Bimolecular plots (k_P vs [O_2]) for experiments measuring the formation rate constant of ethyl peroxy at 300 Torr and 296 K. Ethyl peroxy was probed at the peaks of its $\tilde{A} \leftarrow \tilde{X}$ origin bands of the trans (7366 cm^{-1}, T) and gauche (7596 cm^{-1}, G) C-C-O-O conformers. The data is noisier than that of β-CEP due to smaller absorption cross sections, but the results agree with the evaluated value of the ethyl + O_2 rate constant at 300 Torr of (7.3 ± 1.5) x 10^{-12} cm^3 $molc^{-1}$ s^{-1}.[32]

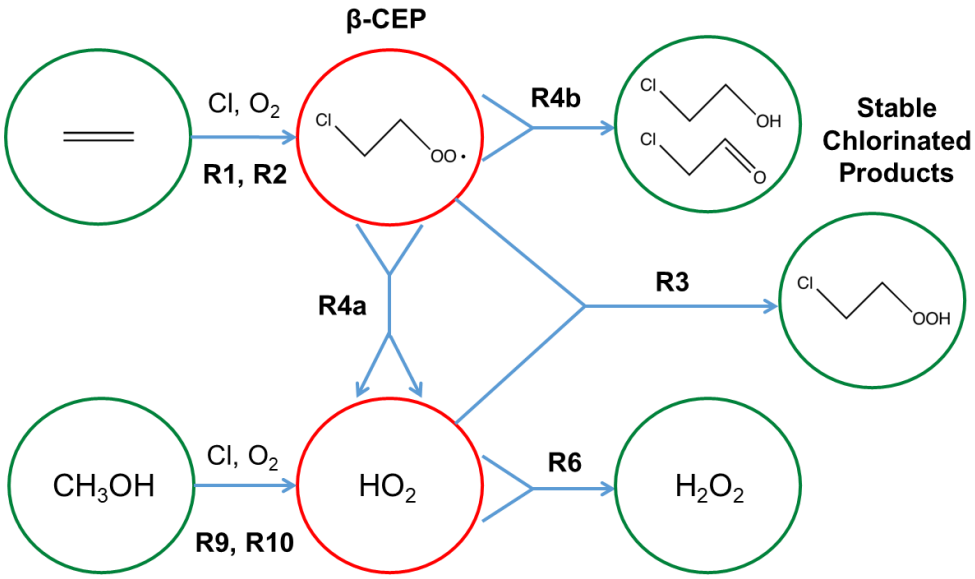

Figure 9: Schematic of key reactions involved in the study of β-CEP and HO_2 self and cross reaction rate constants. The peroxy radicals circled in red are detected in this work. The reaction numbers correspond to the values in the text. By changing the hydrocarbon precursor ratio $[CH_3OH]/[C_2H_4]$, the ratio of initial radical concentrations $[HO_2]_0/[\beta\text{-CEP}]_0$ is also varied as well as the rates of R3, R4, and R6. The unknown parameters k_3, k_4, and α are constants and we reduce correlation in their fitted values by optimizing across a range of $[HO_2]_0/[\beta\text{-CEP}]_0$.

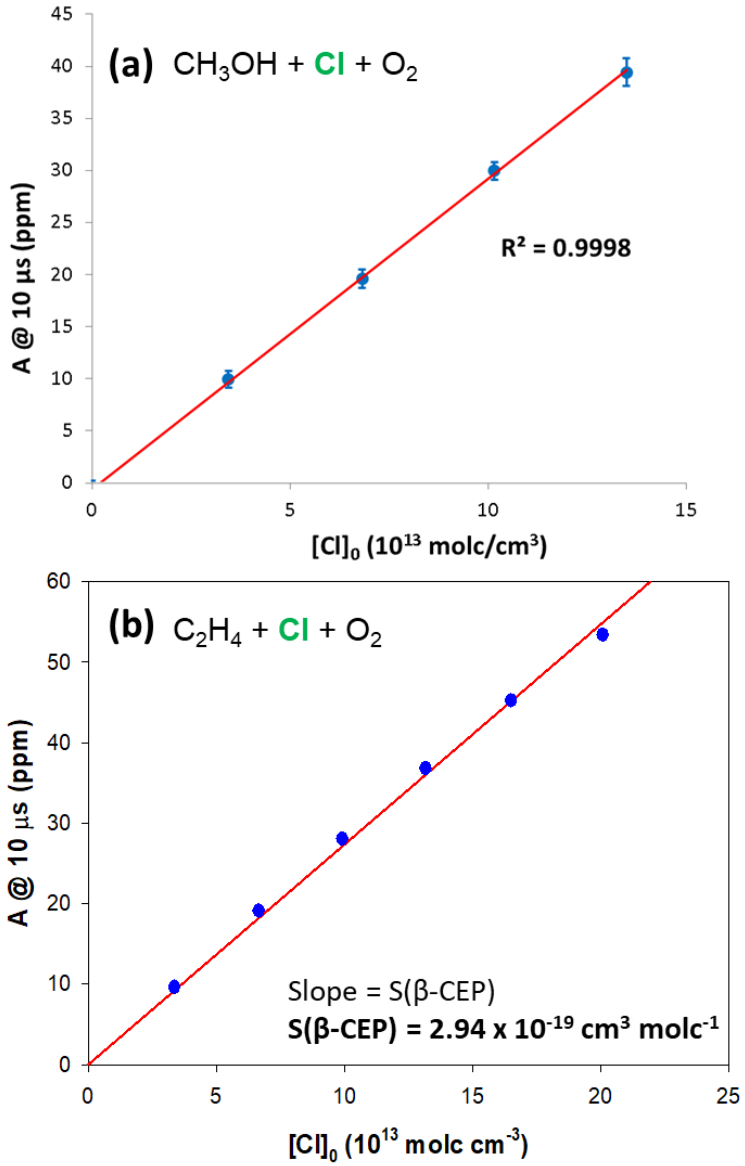

Figure 10: (a) HO_2 absorption at 7041.64 cm^{-1} probed 10 µs after the initiation of radical chemistry. At this delay time, $[HO_2] = [Cl]_0$ ($[Cl]_0$ is directly proportional to $[Cl_2]$). The linear relationship between absorption and concentration ($R^2 = 0.9998$) demonstrates that probe laser linewidth effects associated with pulsed CRDS did not impact our results. **(b)** β-CEP absorption at 7352.48 cm^{-1} probed 10 µs after the initiation of radical chemistry. At this delay time, $[\beta\text{-CEP}] = [Cl]_0$. The slope of the line gives $S_{\beta\text{-CEP}} = 2.94 \times 10^{-19}$ cm^3 $molc^{-1}$ and $\sigma = 2.56 \times 10^{-20}$ cm^2 at 7352.48 cm^{-1}.

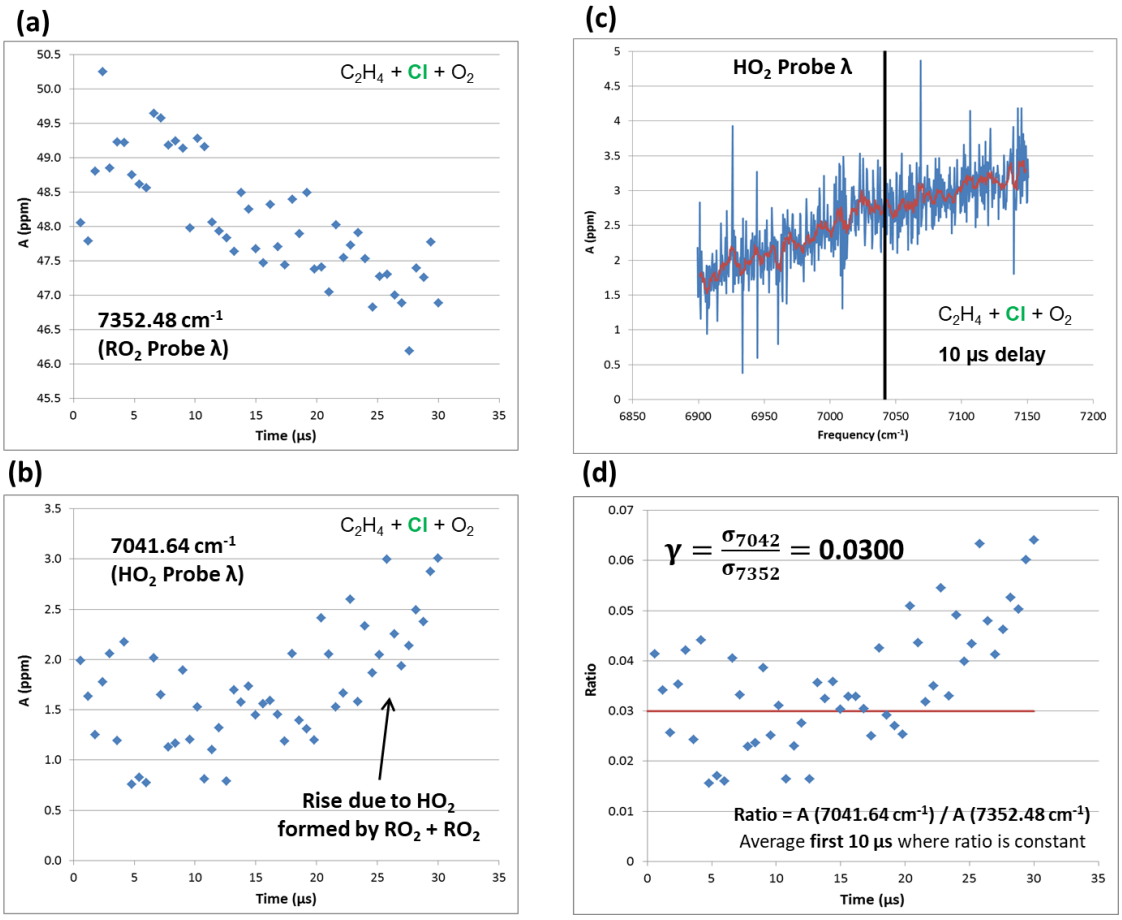

Figure 11: Results of experiments used to determine γ, the ratio of the β-CEP absorption cross section at 7041.64 cm^{-1} to that at 7352.48 cm^{-1}. Ethene was oxidized in the absence of methanol. **(a)** β-CEP absorption at 7352.48 cm^{-1} measured over 0–30 μs with 0.6 μs spacing. The decay after ~10 μs is due to the β-CEP self reaction. **(b)** β-CEP absorption at 7041.64 cm^{-1} measured over 0–30 μs with 0.6 μs spacing. The rise around ~20 μs is due to the production of secondary HO_2, which absorbs strongly at this frequency. **(c)** Spectrum recorded 10 μs after the oxidation of ethene over the frequency used to probe HO_2. The shape of the spectrum represents β-CEP and differs greatly from the pure HO_2 spectrum shown in Figures 3. **(d)** Ratio of the signals presented in (a) and (b). The ratio is approximately constant out to ~20 μs, reflecting that solely β-CEP is absorbing and secondary HO_2 has not yet formed. We averaged this ratio over 0–10 μs to determine $\gamma = 0.0300$.

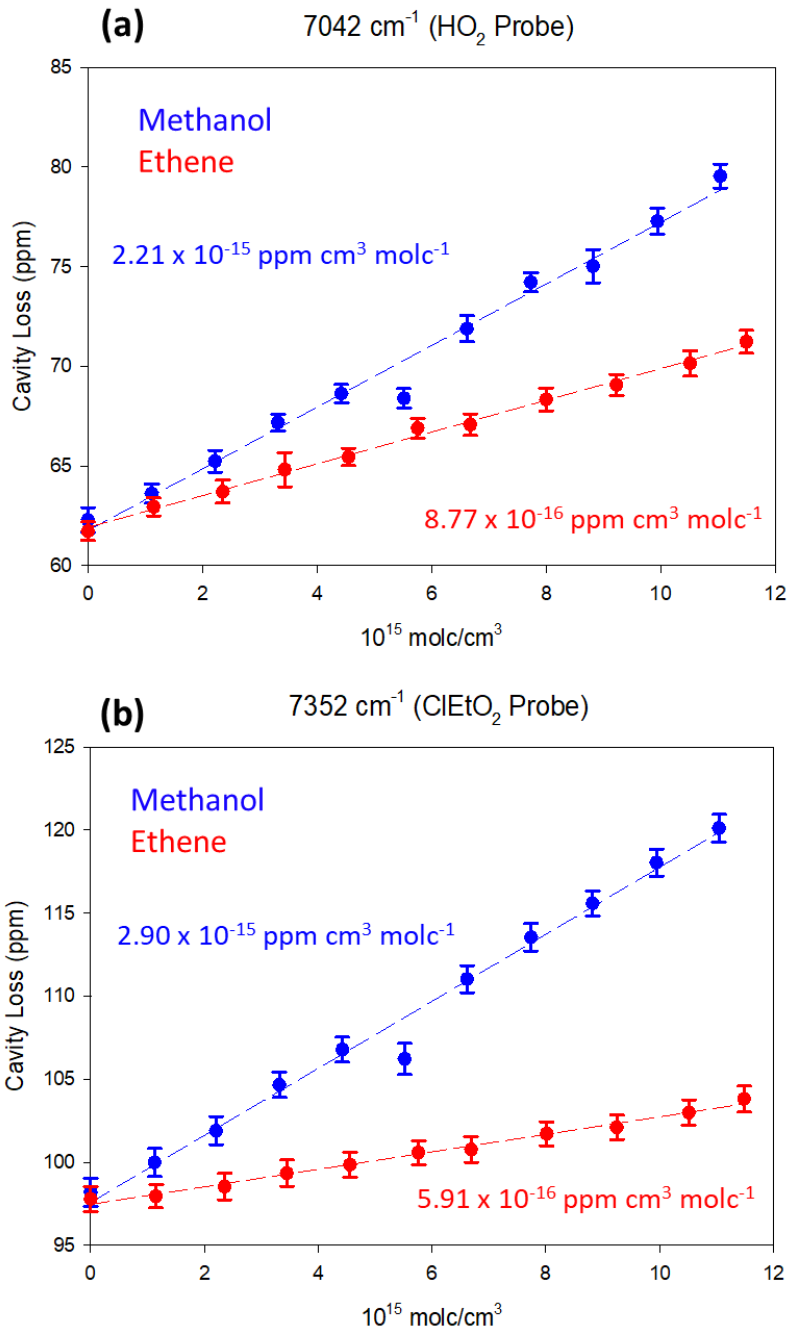

Figure 12: Results of experiments conducted without photolysis to determine the calibration factors for methanol (blue) and ethene (red) at **(a)** 7041.64 cm^{-1} and **(b)** 7352.48 cm^{-1}. The slopes of the fitted lines were used to correct datasets for the absorption offset created by the depletion of the methanol and ethene precursors in experiments with photolysis. Offset were typically small and less than 0.5 ppm.

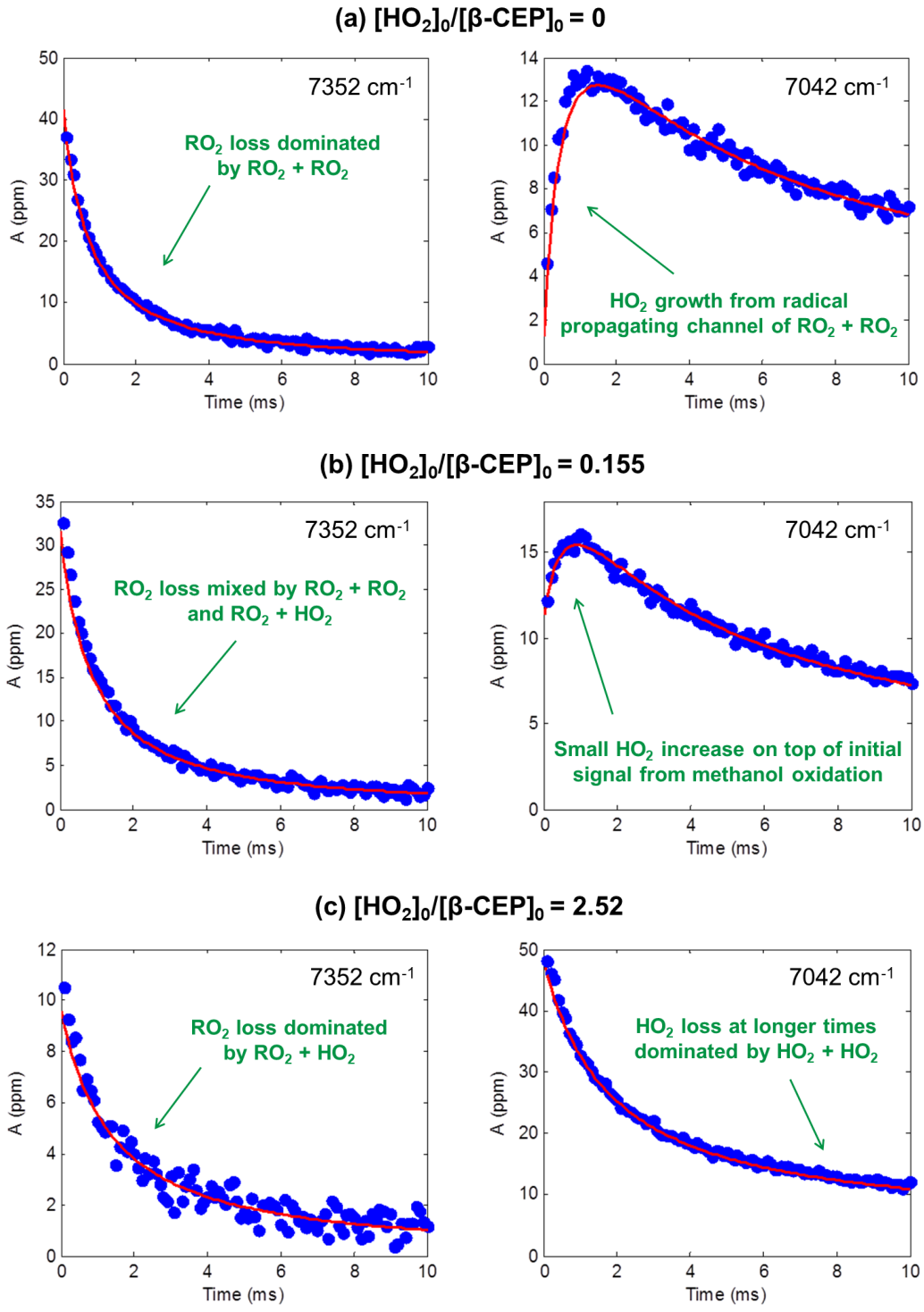

Figure 13: Absorption signals recorded at 7352.48 cm^{-1} and 7041.64 cm^{-1} reflecting β-CEP and HO_2 kinetics, respectively. The data points (blue) were recorded over 0–10 ms with 0.1 ms spacing. Modeled absorption signals are overlaid (red) and were simulated using the optimized values of k_3 = 3.4 x 10^{-12} cm^3 $molc^{-1}$ s^{-1}, k_4 = 4.9 x 10^{-12} cm^3 $molc^{-1}$ s^{-1}, and α = 0.46 determined in this work. $[HO_2]_0/[\beta\text{-CEP}]_0$ was determined using Eqn. 4. **(a)** $[HO_2]_0/[\beta\text{-CEP}]_0 = 0$. **(b)** $[HO_2]_0/[\beta\text{-CEP}]_0 = 0.155$. **(c)** $[HO_2]_0/[\beta\text{-CEP}]_0 = 2.52$.

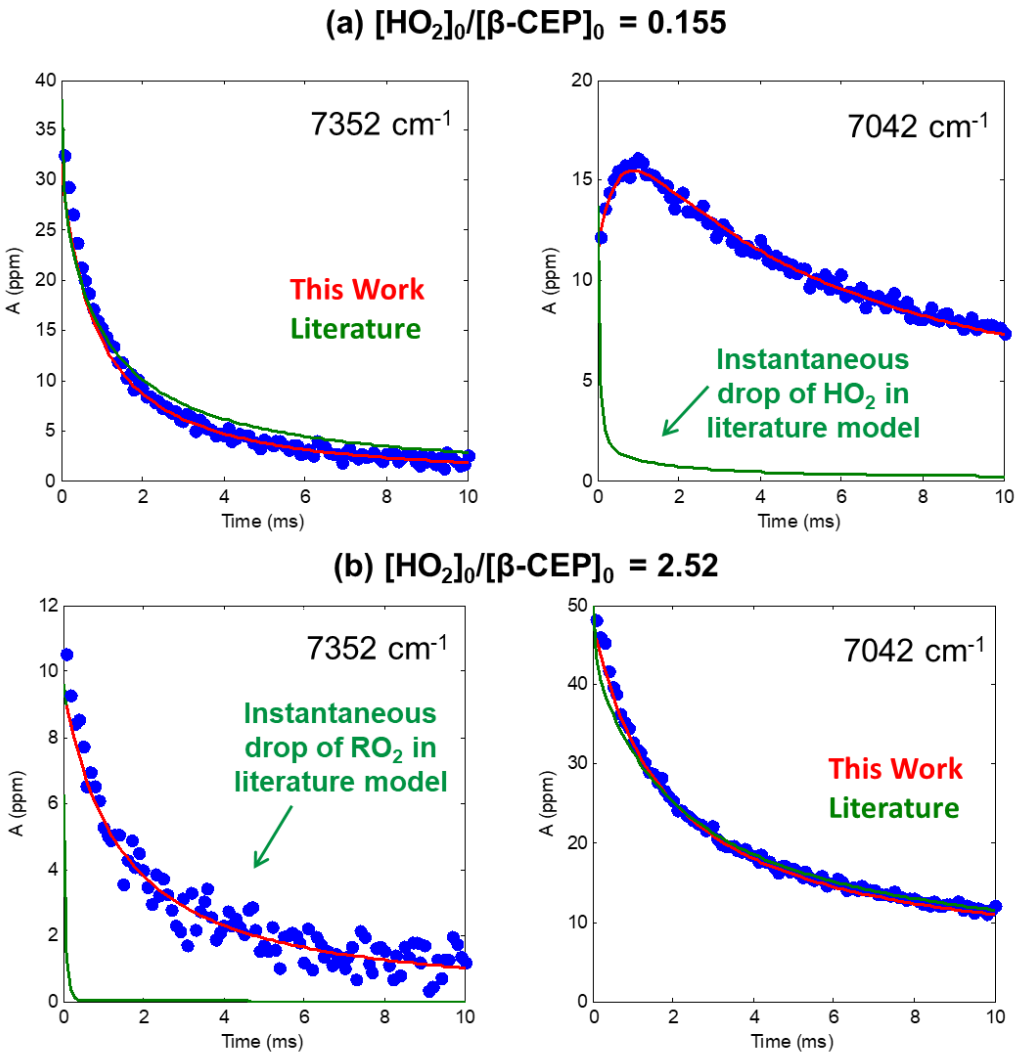

Figure 14: Comparison of the literature model (k_3 = 13.5 x 10^{-12} cm^3 $molc^{-1}$ s^{-1}, k_4 = 2.8 x 10^{-12} cm^3 $molc^{-1}$ s^{-1}, and α = 0.63) to absorption signals measured in this work. **(a)** $[HO_2]_0/[\beta\text{-CEP}]_0$ = 0.155 and **(b)** $[HO_2]_0/[\beta\text{-CEP}]_0$ = 2.52. In both cases, the literature model predicts that the less abundant peroxy radical is removed instantaneously by R3, in disagreement with our data. The literature value of k_3 appears to be too fast.

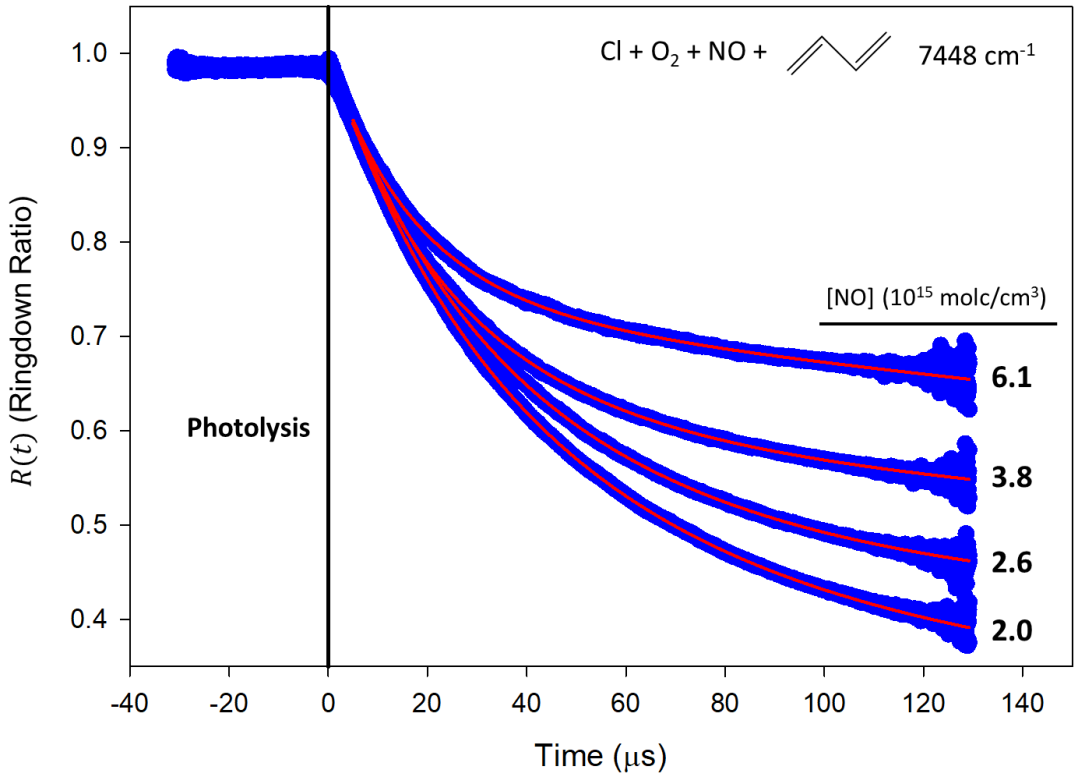

Figure 15: Typical ringdown ratio data (blue) in the RO_2 + NO rate constant experiments and the corresponding fits (red) to Eqn. 10 used to determine k'. The example datasets correspond to absorption measured at 7448 cm^{-1} in the spectrum of RO_2 radicals produced from the Cl-initiated oxidation of 1,3-butadiene. Traces were acquired with [NO] = (2.0, 2.6, 3.8, 6.1) x 10^{15} molc cm^{-3} and yielded k' = (1.4, 1.8, 2.7, 4.6) x 10^4 s^{-1}, respectively.

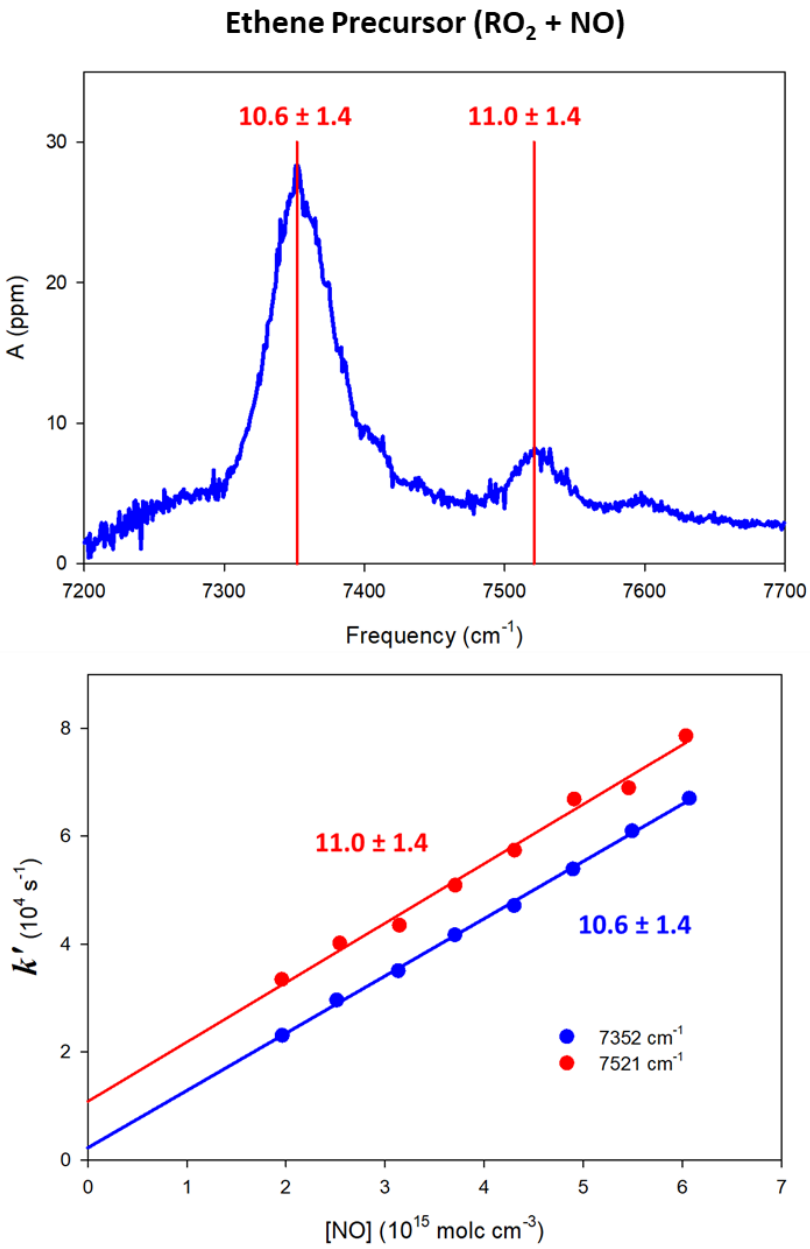

Figure 16: Kinetics of β-CEP + NO. Numbers labeled on the plots correspond to the measured value of k_7 and have units of 10^{-12} cm^3 $molc^{-1}$ s^{-1}. **(top)** Near-IR spectrum of β-CEP (10 μs delay, [NO] = 0). The vertical lines are located at the frequencies used to probe absorption decays. **(bottom)** Bimolecular plots (k' vs [NO]) measured at each frequency. The value of k_7 was determined from the slope of the fitted line. The 7521 cm^{-1} data is offset by 1 x 10^4 s^{-1}.

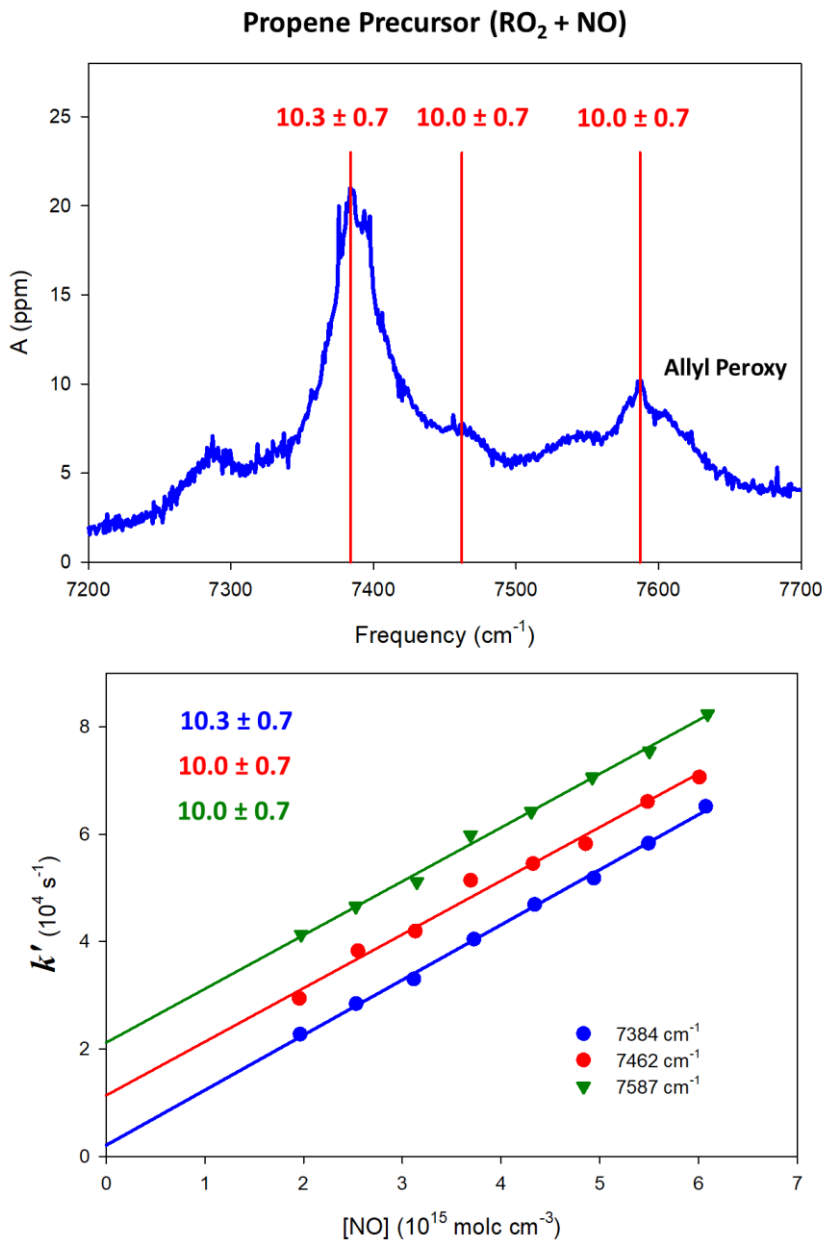

Figure 17: Kinetics of the reaction between NO and the peroxy radicals formed upon Cl-initiated oxidation of propene. Numbers labeled on the plots correspond to the measured rate constants and have units of 10^{-12} cm^3 $molc^{-1}$ s^{-1}. **(top)** Near-IR spectrum of the peroxy radical mixture (10 μs delay, [NO] = 0). The vertical lines are located at the frequencies used to probe absorption decays. The absorption at 7587 cm^{-1} likely has contribution from ally peroxy. **(bottom)** Bimolecular plots (k' vs [NO]) measured at each frequency. The rate constants were determined from the slopes of the fitted lines. The 7462 and 7587 cm^{-1} data are offset by (1 and 2) x 10^4 s^{-1}, respectively.

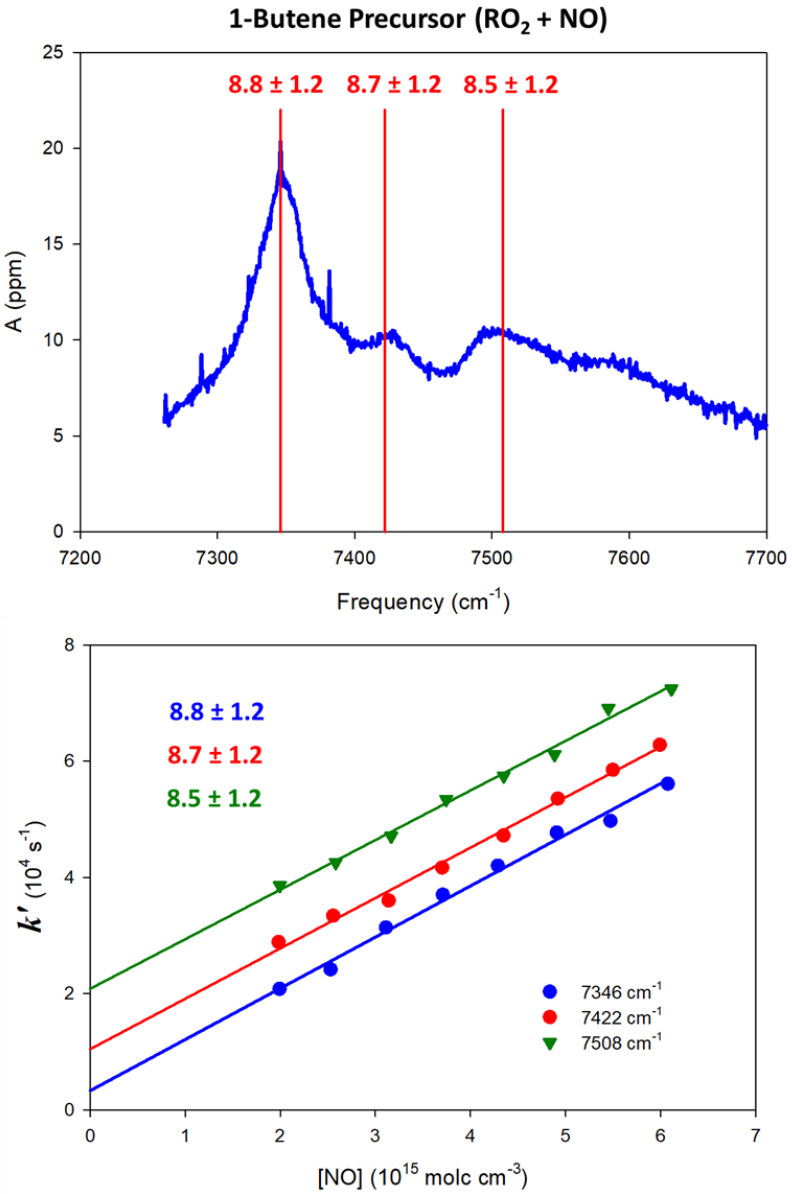

Figure 18: Kinetics of the reaction between NO and the peroxy radicals formed upon Cl-initiated oxidation of 1-butene. Numbers labeled on the plots correspond to the measured rate constants and have units of 10^{-12} cm^3 $molc^{-1}$ s^{-1}. **(top)** Near-IR spectrum of the peroxy radical mixture (10 μs delay, [NO] = 0). The vertical lines are located at the frequencies used to probe absorption decays. **(bottom)** Bimolecular plots (k' vs [NO]) measured at each frequency. The rate constants were determined from the slopes of the fitted lines. The 7422 and 7508 cm^{-1} data are offset by (1 and 2) x 10^4 s^{-1}, respectively.

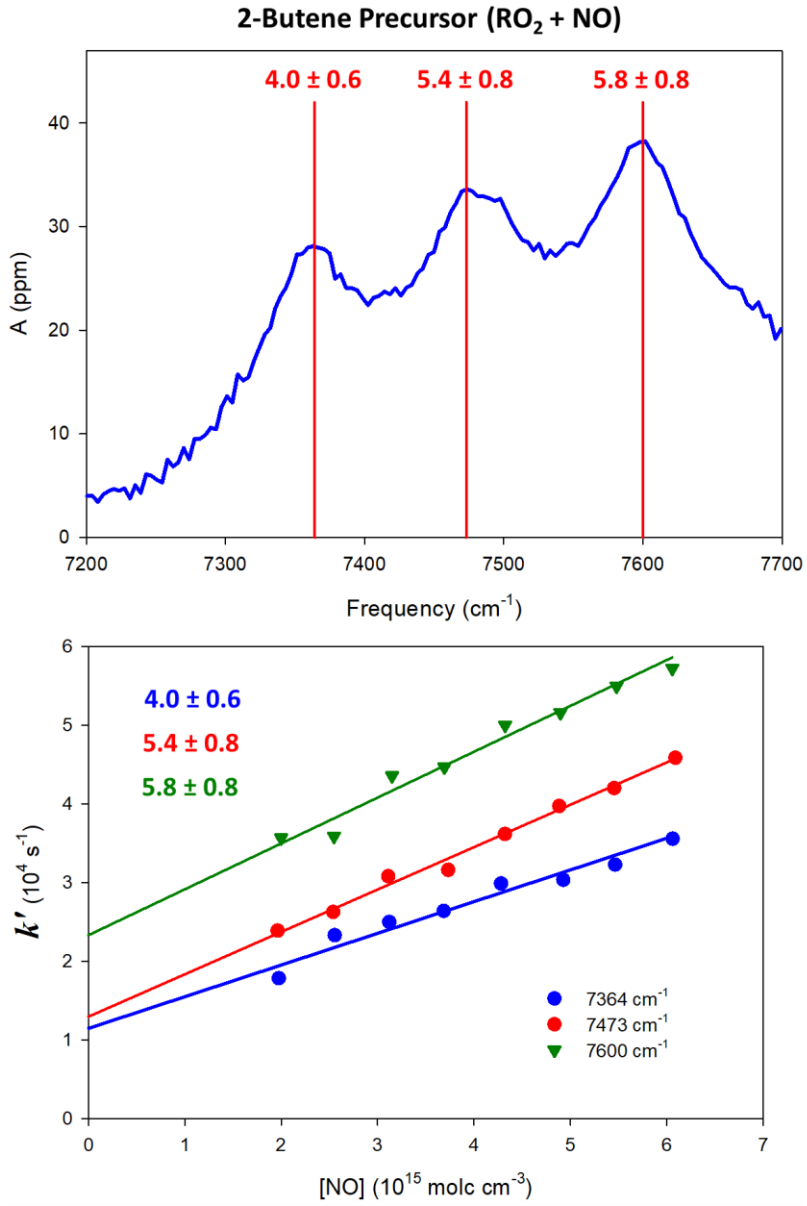

Figure 19: Kinetics of NO + 2,3-chlorobutyl peroxy (and minor contribution from unsubstituted, allylic peroxy radicals). Numbers labeled on the plots correspond to the measured rate constants and have units of 10^{-12} cm^3 $molc^{-1}$ s^{-1}. **(top)** Near-IR spectrum of 2,3-chlorobutyl peroxy (10 μs delay, [NO] = 0). The vertical lines are located at the frequencies used to probe absorption decays. **(bottom)** Bimolecular plots (k' vs [NO]) measured at each frequency. The rate constants were determined from the slopes of the fitted lines. The 7473 and 7600 cm^{-1} data are offset by (1 and 2) x 10^4 s^{-1}, respectively. The 7364 cm^{-1} data has no offset; the reason for the large, positive intercept is unknown but may be due to secondary peroxy radicals formed in the alkoxy radical chemistry.

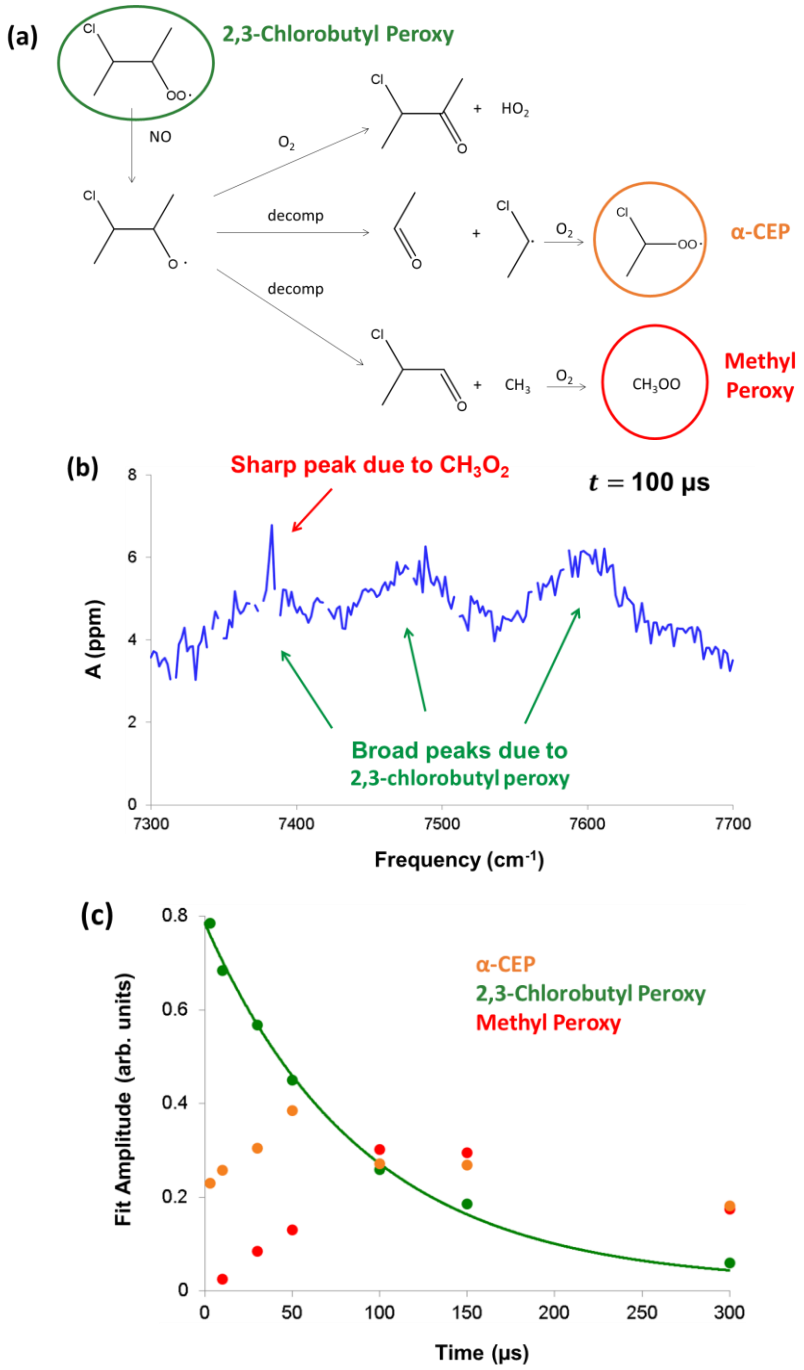

Figure 20: (a) Possible fates of the alkoxy radical formed in the 2,3-chlorobutyl peroxy + NO reaction (nitrate pathway not shown). The peroxy radicals are circled and may contribute to the measured absorption. **(b)** Spectrum of the reacting mixture at a delay time of 100 µs and [NO] = 1.95 x 10^{15} molc cm^{-3}. The peaks mostly resemble 2,3-chlorobutyl peroxy although there is some evidence of methyl peroxy. **(c)** Results of fitting the reactive spectra at various delay times and [NO] = 1.95 x 10^{15} molc cm^{-3} to reference spectra of pure 2,3-chlorobutyl peroxy, α-CEP, and methyl peroxy. The amplitudes can be compared within a series but not between series. The fit of the 2,3-chlorobutyl peroxy amplitude decay to Eqn. 9 is given as a solid line and yielded k' = 1.1 x 10^{4} s^{-1}.

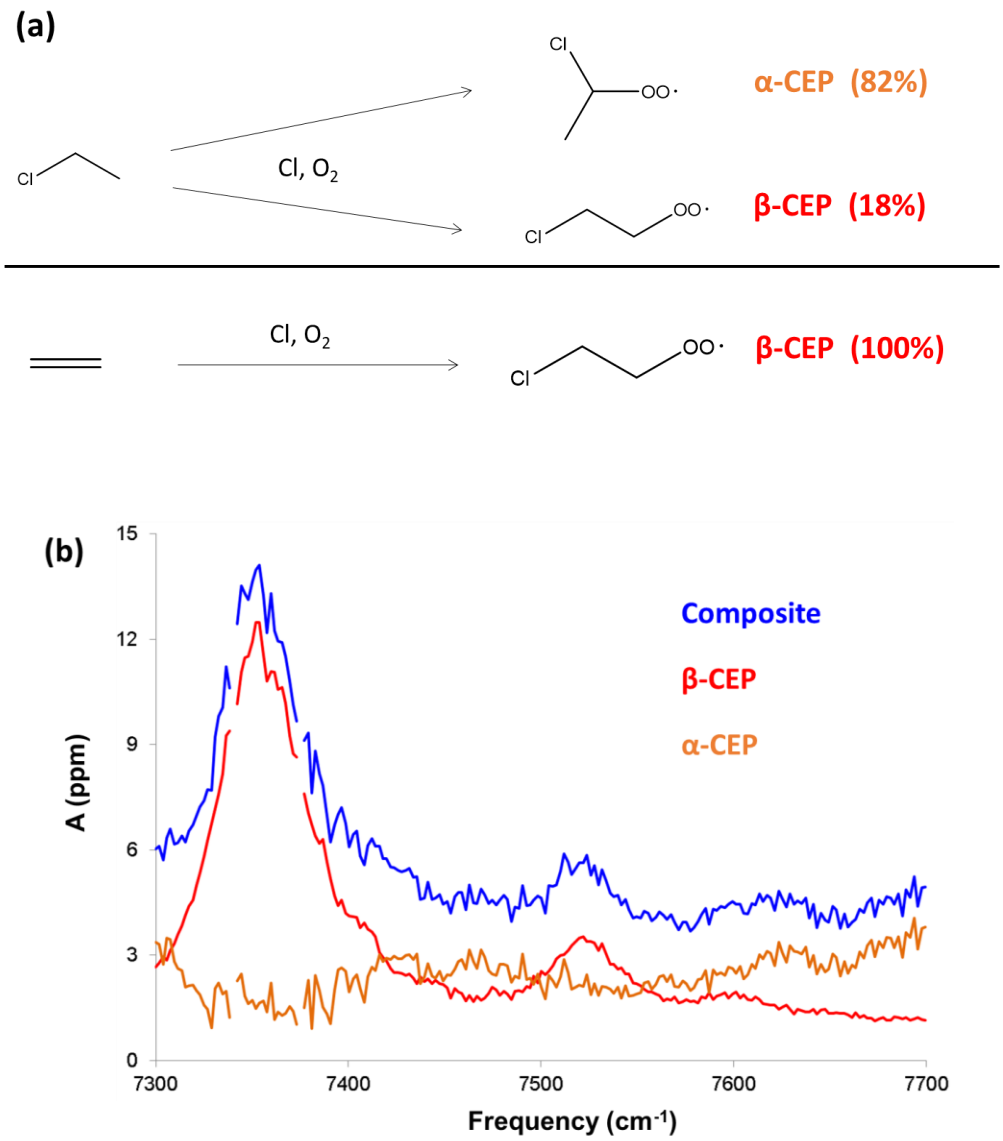

Figure 21: Summary of experiments used to determine the near-IR spectrum of α-CEP. **(a)** Oxidation of chloroethane generates α-CEP and β-CEP with yields of 82% and 18%, respectively. Oxidation of ethene yields β-CEP with 100% yield. **(b)** The composite spectrum of α-CEP and β-CEP from chloroethane oxidation (blue) and the spectrum of pure β-CEP from ethene oxidation, scaled by 0.18 (red). The spectra were recorded under conditions where the total peroxy radical concentration was the same. Therefore, by scaling the pure β-CEP spectrum by 0.18 and subtracting it from the composite spectrum, we obtain the spectrum of solely α-CEP (orange).

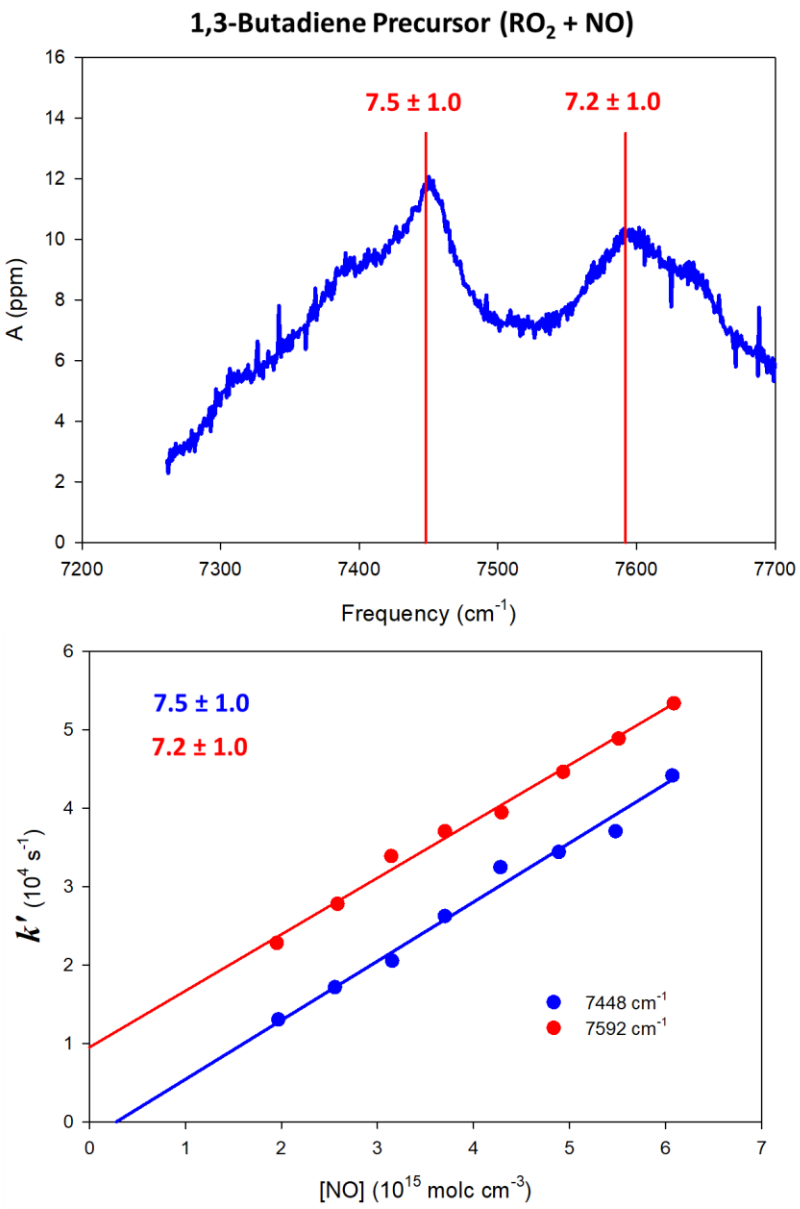

Figure 22: Kinetics of the reaction between NO and the chlorine-substituted peroxy radicals formed upon oxidation of 1,3-butadiene. Numbers labeled on the plots correspond to the measured rate constants and have units of 10^{-12} cm^3 $molc^{-1}$ s^{-1}. **(top)** Near-IR spectrum of the peroxy radical mixture (10 µs delay, [NO] = 0). The vertical lines are located at the frequencies used to probe absorption decays. **(bottom)** Bimolecular plots (k' vs [NO]) measured at each frequency. The rate constants were determined from the slopes of the fitted lines. The 7592 cm^{-1} data are offset by 1 x 10^4 s^{-1}.

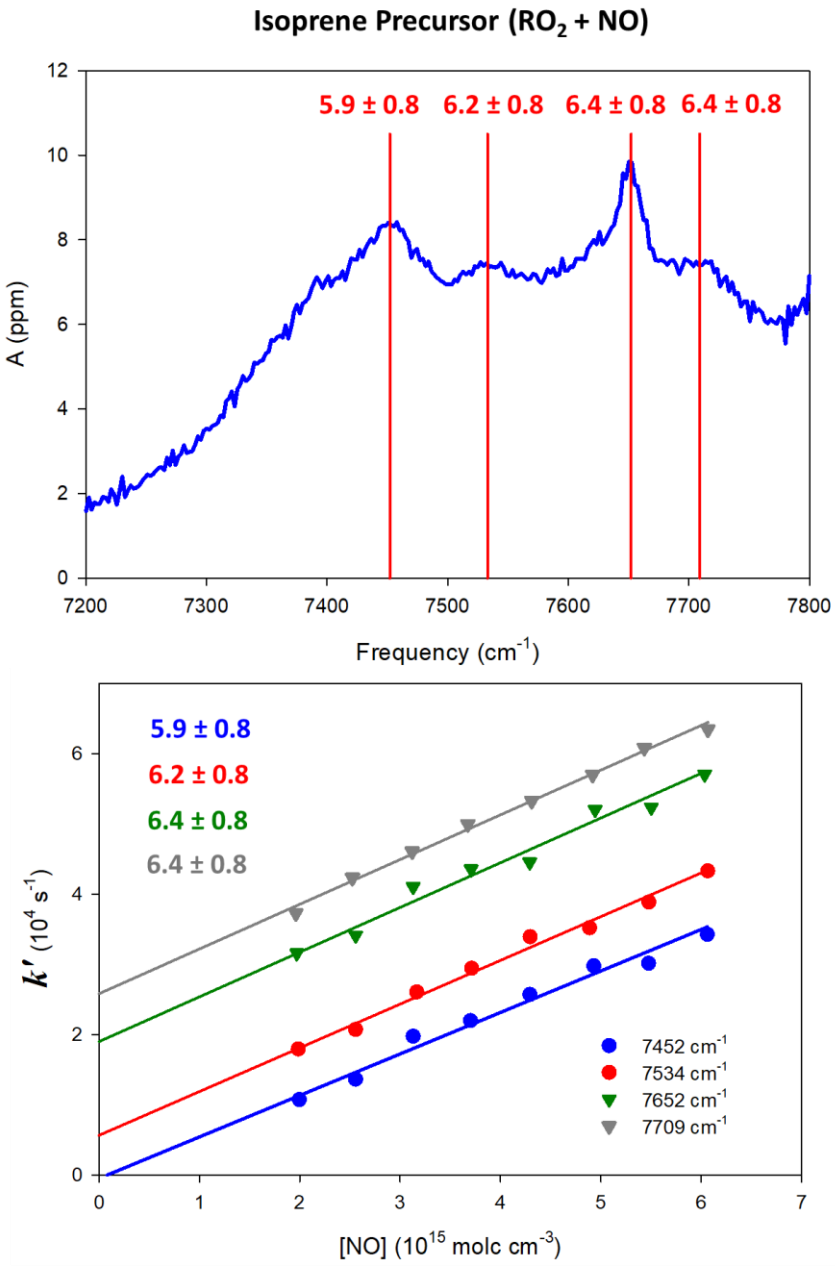

Figure 23: Kinetics of the reaction between NO and the peroxy radicals formed upon Cl-initiated oxidation of isoprene. Numbers labeled on the plots correspond to the measured rate constants and have units of 10^{-12} cm^3 $molc^{-1}$ s^{-1}. **(top)** Near-IR spectrum of the peroxy radical mixture (10 µs delay, [NO] = 0). The vertical lines are located at the frequencies used to probe absorption decays. **(bottom)** Bimolecular plots (k' vs [NO]) measured at each frequency. The rate constants were determined from the slopes of the fitted lines. The 7534, 7652, and 7709 cm^{-1} data are offset by (1, 2, and 3) x 10^4 s^{-1}, respectively.

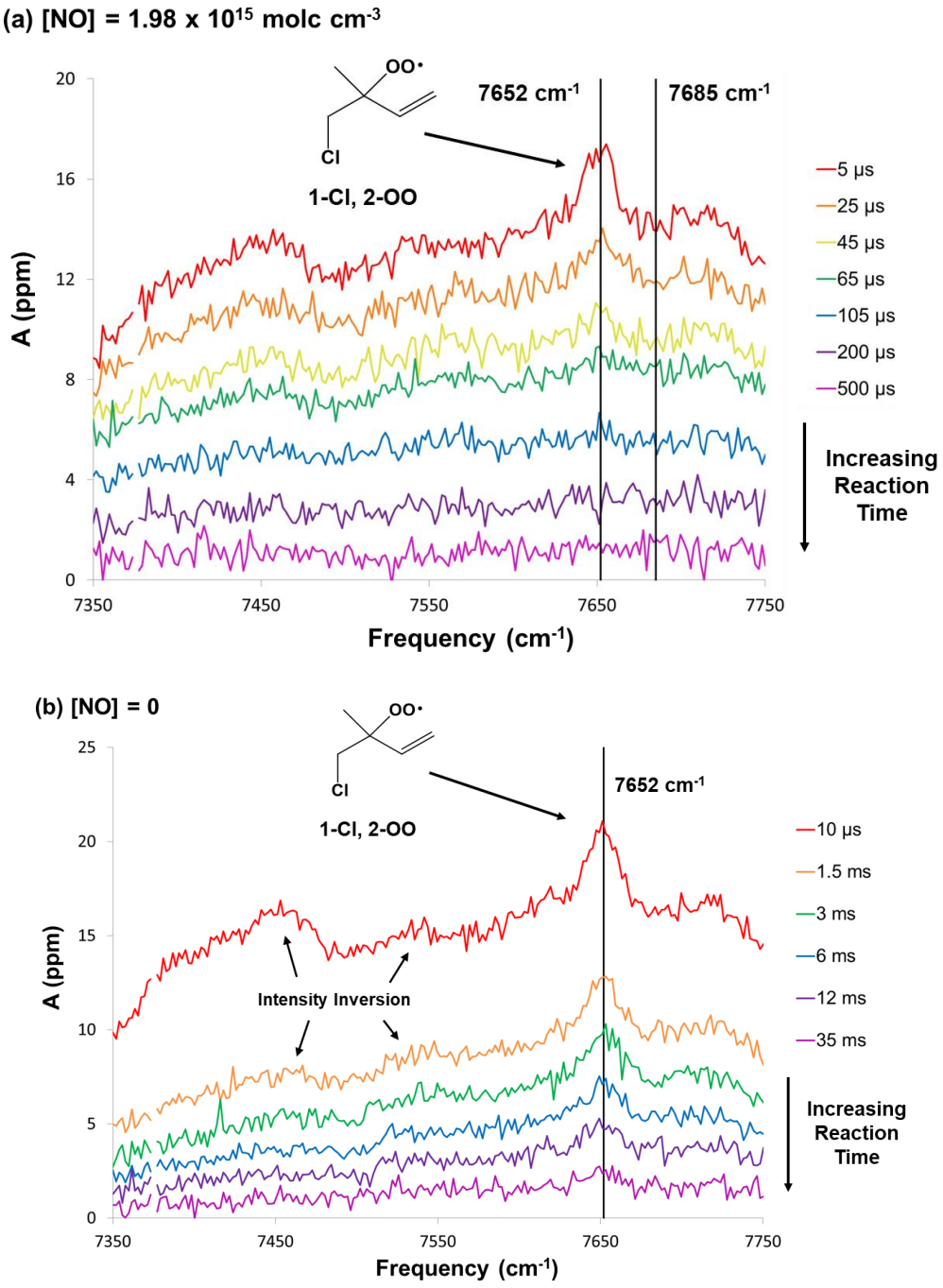

Figure 24: Spectra of Cl-initiated oxidation of isoprene at various delay times. The peak at 7652 cm^{-1} is labeled and assigned as absorption from the 1-Cl, 2-OO $ClRO_2$ isomer. **(a)** [NO] = 1.98 x 10^{15} molc cm^{-3}. The 1-Cl, 2-OO peak decays faster than the remaining broad, featureless absorption. The difference in signal between 7652 and 7685 cm^{-1} is used to approximate absorption by solely the 1-Cl, 2-OO isomer. **(b)** [NO] = 0. Chemistry is dominated by peroxy radical self and cross reactions. The inversion in intensity of the peaks at 7452 and 7534 cm^{-1} between 10 µs and 1.5 ms strongly suggests isomer-dependent reactivity. We assigned the long-lived peak at 7652 cm^{-1} as the 1-Cl, 2-OO isomer on the basis that 3° peroxy radicals react with other peroxy radicals slowly.

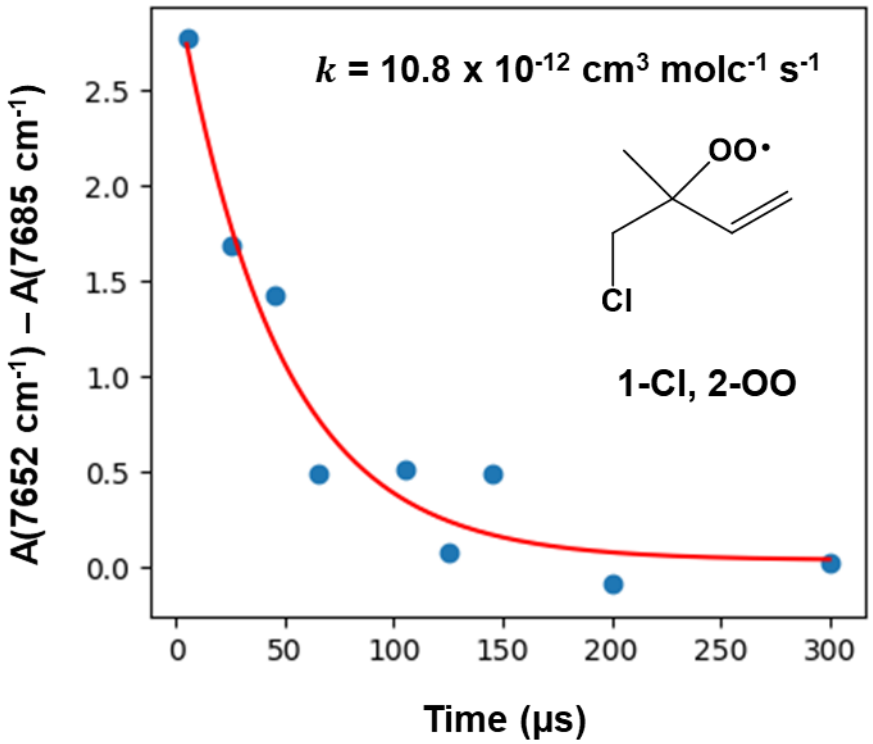

Figure 25: Time-dependent absorption of the 1-Cl, 2-OO $ClRO_2$ isomer generated by the Cl-initiated oxidation of isoprene. Absorption by solely the 1-Cl, 2-OO isomer was calculated as the difference in signal between 7652 and 7685 cm^{-1} in the spectra presented in Figure 24a. Data was collected at the lowest [NO] = 1.98 x 10^{15} molc cm^{-3}, where the use of SKaR is less important. The absorption decay was fit to Eqn. 9 and yielded $k' =$ 2.14 x 10^4 s^{-1}. The corresponding $ClRO_2$ + NO rate constant is 10.8 x 10^{-12} cm^3 molc^{-1} s^{-1}. This value likely has large uncertainty due to the use of only one [NO], but is consistent with the value of (11.5 ± 1.1) x 10^{-12} cm^3 molc^{-1} s^{-1} measured in the CIMS studies of Patchen et al.[19]

3.6 Tables

Table I. Summary of initial conditions for experiments used to determine k_3, k_4, and α. All experiments were conducted at P = 300 Torr and room temperature (T ≈ 296 K). The bath gas was comprised of O_2 ($[O_2]$ = 7.44 x 10^{18} molc cm^{-3}, ~75%) and N_2 ($[N_2]$ = 2.29 x 10^{18} molc cm^{-3}, ~25%). At each set of conditions, the time-resolved absorption was measured at both 7041.64 cm^{-1} and 7352.48 cm^{-1} unless otherwise noted.

	$[Cl_2]$ (10^{16} molc cm^{-3})	**(b) $[Cl]_0$ (10^{14} atoms cm^{-3})**	**$[C_2H_4]$ (10^{15} molc cm^{-3})**	**$[CH_3OH]$ (10^{15} molc cm^{-3})**	**(c) $\frac{[HO_2]_0}{[\beta\text{-CEP}]_0}$**
1 (a)	5.65	1.66	0	7.40	-----
2	5.65	1.65	10.1	0	0
3	5.65	1.61	10.0	0	0
4	5.65	1.61	9.51	0.370	0.0329
5	5.65	1.62	9.00	0.741	0.0696
6	5.65	1.62	8.04	1.48	0.155
7	5.65	1.61	6.98	2.22	0.269
8	5.65	1.62	6.01	2.96	0.417
9	5.65	1.64	5.02	3.71	0.625
10	5.65	1.62	3.92	4.45	0.961
11	5.65	1.62	3.01	5.19	1.46
12	5.65	1.63	1.99	5.92	2.52
13	5.65	1.62	0.995	6.67	5.67
14	5.65	1.61	0.491	7.04	12.1
15 (a)	5.65	1.61	0	7.41	-----

(a) Radical calibration scans performed at the beginning and end of experiments. $[Cl]_0$ was determined from the analysis in section 3.2.2. Data was only collected at 7041.64 cm^{-1}.

(b) For each scan, the relative power of the photolysis laser was tracked by a power meter positioned behind the exit window of the reactor. $[Cl]_0$ was calculated by interpolating between the power and $[Cl]_0$ measured in the radical calibration scans. The excimer power and $[Cl]_0$ were essentially constant, dropping by only ~3% across the experiments.

(c) Ratio of the initial radical concentrations calculated by Eqn. 4. As discussed in the text, the fitted values of $[HO_2]_0$ and $[\beta\text{-CEP}]_0$ deviated from the values calculated by Eqn. 4 and $[Cl]_0$, and we therefore floated these parameters when optimizing rate constants. The table is sorted by this column for clarity although the data were collected in random order.

Table II. Kinetic model used to simulate the time-dependent concentrations of β-CEP, HO_2, and H_2O_2 in experiments measuring k_3, k_4, and α. Rate constants were determined at 300 Torr and room temperature (T ≈ 296 K). The pseudo bimolecular rate coefficient is given for termolecular associations. Units are cm^3 $molc^{-1}$ s^{-1} and were taken from the NASA Jet Propulsion Laboratory data evaluation unless otherwise noted.[32]

Reaction	k	Notes
Initiation:		[a]
$Cl + CH_2CH_2 + M \rightarrow ClCH_2CH_2 + M$	6.5×10^{-11}	R1
$ClCH_2CH_2 + O_2 + M \rightarrow ClCH_2CH_2O_2 + M$	2.9×10^{-12}	R2 [b]
$Cl + CH_3OH \rightarrow HCl + CH_2OH$	5.5×10^{-11}	R9
$CH_2OH + O_2 \rightarrow HCHO + HO_2$	9.1×10^{-12}	R10
RO_2 Self and Cross Reactions:		
$ClCH_2CH_2O_2 + HO_2 \rightarrow ClCH_2CH_2OOH + O_2$	3.4×10^{-12}	R3 [b]
$2\ ClCH_2CH_2O_2 \rightarrow 2\ ClCH_2CH_2O + O_2$	2.2×10^{-12}	R4a [b],[c]
$2\ ClCH_2CH_2O_2 \rightarrow ClCH_2CH_2OH + ClCH_2CHO + O_2$	2.7×10^{-12}	R4b [b],[c]
$2\ HO_2 \rightarrow H_2O_2 + O_2$	2.05×10^{-12}	R6 [d]
RO Reactions:		[e]
$ClCH_2CH_2O + O_2 \rightarrow ClCH_2CHO + HO_2$	1.0×10^{-14}	R5
$ClCH_2CH_2O + ClCH_2CH_2O_2 \rightarrow ClCH_2CH_2OOH + ClCH_2CHO$	1.5×10^{-11}	R11 [f]

[a] Initiation reactions are provided for reference only. As discussed in the text, these reactions were omitted when fitting to the model since they are effectively instantaneous due to the large oxygen and hydrocarbon precursor concentrations. The chemistry was assumed to start directly from β-CEP and HO_2.

[b] Determined in this work.

[c] Calculated from the optimized k_4 and α: $k_{4a} = \alpha k_4$ and $k_{4b} = (1 - \alpha)k_4$.

[d] Taken from the IUPAC data evaluation,[35] which contains terms that depend on $[N_2]$ and $[O_2]$.

[e] Rate constants for the alkoxy radical reactions are unknown; we used values for the analogous reactions of ethyl alkoxy. Due to the large $[O_2]$, R5 was effectively instantaneous and dominated over R11. The model was therefore insensitive to the precise values of k_5 and k_{11}.

[f] Taken from Noell et al.[14]

Table III. Rate constants of the RO_2 + NO reaction for peroxy radicals derived from the Cl-initiated oxidation of alkenes, measured at 300 Torr and room temperature (T ≈ 296 K). The tabulated value is an average across the single frequency SKaR measurements unless otherwise noted. The measured absorption signals mostly represented chlorine-substituted peroxy radicals, although unsubstituted peroxy radicals could be present to a minor extent in the oxidations of propene, 1-butene, 2-butene, and isoprene. Results of the CIMS study of Patchen et al. are provided for comparison.[19] Units are 10^{-12} cm^3 $molc^{-1}$ s^{-1} and the statistical uncertainties are ±2σ.

Alkene Precursor	This Work	Patchen et al.[19]
Ethene	[(a)] 10.8 ± 1.4	9.7 ± 1.2
Propene	10.1 ± 1.4	10.2 ± 1.2
1-Butene	8.7 ± 1.2	9.6 ± 1.0
2-Butene	[(b)] 4.0 ± 0.6, [(c)] 5.6 ± 0.8, [(d)] 5.6	9.8 ± 1.2
1,3-Butadiene	7.4 ± 1.0	11.8 ± 1.0
Isoprene	6.2 ± 0.8, [(e)] 5.0, [(f)] 10.8	11.5 ± 1.1

[(a)] Rate constant is k_7 in the text.

[(b)] Measured at 7364 cm^{-1}. Not averaged with 7473 and 7600 cm^{-1} due to statistically significant difference.

[(c)] Average of measurements at 7473 and 7600 cm^{-1}. Not averaged with 7364 cm^{-1} due to statistically significant difference.

[(d)] Result of fitting the time-dependent spectra at the lowest [NO] as a linear combination of pure 2,3-chlorobutyl peroxy, α-CEP, and methyl peroxy spectra. See details in text.

[(e)] Result of fitting the time-dependent spectra at the lowest [NO] as a linear combination of a pure chloromethyl peroxy spectrum and a spectrum of the mixture of peroxy radicals formed immediately upon isoprene oxidation. See details in text.

[(f)] Result of fitting the absorption decay of solely the 3° 1-Cl, 2-OO $ClRO_2$ isomer at the lowest [NO]. See details in text.

3.7 References

(1) Ehhalt, D. H. Global Aspects of Atmospheric Chemistry; Zellner, R., Baumgärtel, H., Grünbein, W., Hensel, F., Eds.; Steinkopff; Springer: Darmstadt; New York, 1999; pp 40–47.

(2) Orlando, J. J.; Tyndall, G. S. Laboratory Studies of Organic Peroxy Radical Chemistry: An Overview with Emphasis on Recent Issues of Atmospheric Significance. *Chemical Society Reviews* **2012**, *41* (19), 6294–6317. https://doi.org/10.1039/C2CS35166H.

(3) Rudolph, J.; Koppmann, R.; Plass-Dülmer, Ch. The Budgets of Ethane and Tetrachloroethene: Is There Evidence for an Impact of Reactions with Chlorine Atoms in the Troposphere? *Atmospheric Environment* **1996**, *30* (10–11), 1887–1894. http://dx.doi.org/10.1016/1352-2310(95)00385-1.

(4) Singh, H. B.; Gregory, G. L.; Anderson, B.; Browell, E.; Sachse, G. W.; Davis, D. D.; Crawford, J.; Bradshaw, J. D.; Talbot, R.; Blake, D. R.; et al. Low Ozone in the Marine Boundary Layer of the Tropical Pacific Ocean: Photochemical Loss, Chlorine Atoms, and Entrainment. *Journal of Geophysical Research: Atmospheres* **1996**, *101* (D1), 1907–1917. https://doi.org/10.1029/95JD01028.

(5) Riemer, DanielD.; Apel, EricC.; Orlando, JohnJ.; Tyndall, GeoffreyS.; Brune, WilliamH.; Williams, EricJ.; Lonneman, WilliamA.; Neece, JamesD. Unique Isoprene Oxidation Products Demonstrate Chlorine Atom Chemistry Occurs in the Houston, Texas Urban Area. *Journal of Atmospheric Chemistry* **2008**, *61* (3), 227–242. https://doi.org/10.1007/s10874-009-9134-5.

(6) Thornton, J. A.; Kercher, J. P.; Riedel, T. P.; Wagner, N. L.; Cozic, J.; Holloway, J. S.; Dubé, W. P.; Wolfe, G. M.; Quinn, P. K.; Middlebrook, A. M.; et al. A Large Atomic Chlorine Source Inferred from Mid-Continental Reactive Nitrogen Chemistry. *Nature* **2010**, *464* (7286), 271–274.

(7) Boyd, A. A.; Flaud, P.-M.; Daugey, N.; Lesclaux, R. Rate Constants for RO2 + HO2 Reactions Measured under a Large Excess of HO2. *The Journal of Physical Chemistry A* **2003**, *107* (6), 818–821. https://doi.org/10.1021/jp026581r.

(8) Dagaut, P.; Wallington, T. J.; Kurylo, M. J. A Flash Photolysis Investigation of the UV Absorption Spectrum and Self-Reaction Kinetics of CH2ClCH2O2 Radicals in the Gas Phase. *Chemical Physics Letters* **1988**, *146* (6), 589–595. http://dx.doi.org/10.1016/0009-2614(88)87507-9.

(9) Maricq, M. M.; Shi, J.; Szente, J. J.; Rimai, L.; Kaiser, E. W. Evidence for the Three-Center Elimination of Hydrogen Chloride from 1-Chloroethoxy. *The Journal of Physical Chemistry* **1993**, *97* (38), 9686–9694. https://doi.org/10.1021/j100140a027.

(10) Chakir, A.; Brion, J.; Ganne, J. P.; Daumont, D. Study of ClCH2CH2O2 Using Modulated Photolysis: Ultra-Violet Spectrum and Self-Reaction Kinetics. *Physical Chemistry Chemical Physics* **2003**, *5* (12), 2573–2580. https://doi.org/10.1039/B301621H.

(11) Yarwood, G.; Peng, N.; Niki, H. FTIR Spectroscopic Study of the Cl- and Br-Atom Initiated Oxidation of Ethene. *International Journal of Chemical Kinetics* **1992**, *24* (4), 369–383. https://doi.org/10.1002/kin.550240406.

(12) Wallington, T. J.; Andino, J. M.; Japar, S. M. FTIR Product Study of the Self-Reaction of CH2ClCH2O2 Radicals in Air at 295 K. *Chemical Physics Letters* **1990**, *165* (2–3), 189–194. http://dx.doi.org/10.1016/0009-2614(90)85427-E.

(13) Zádor, J.; Fernandes, R. X.; Georgievskii, Y.; Meloni, G.; Taatjes, C. A.; Miller, J. A. The Reaction of Hydroxyethyl Radicals with O2: A Theoretical Analysis and Experimental Product Study. *Proceedings of the Combustion Institute* **2009**, *32* (1), 271–277. https://doi.org/10.1016/j.proci.2008.05.020.

(14) Noell, A. C.; Alconcel, L. S.; Robichaud, D. J.; Okumura, M.; Sander, S. P. Near-Infrared Kinetic Spectroscopy of the HO2 and C2H5O2 Self-Reactions and Cross Reactions. *The Journal of Physical Chemistry A* **2010**, *114* (26), 6983–6995. https://doi.org/10.1021/jp912129j.

(15) Atkinson, D. B.; Spillman, J. L. Alkyl Peroxy Radical Kinetics Measured Using Near-Infrared CW−Cavity Ring-down Spectroscopy. *J. Phys. Chem. A* **2002**, *106* (38), 8891–8902. https://doi.org/10.1021/jp0257597.

(16) Melnik, D.; Miller, T. A. Kinetic Measurements of the C2H5O2 Radical Using Time-Resolved Cavity Ring-down Spectroscopy with a Continuous Source. *J. Chem. Phys.* **2013**, *139* (9), 094201. https://doi.org/10.1063/1.4819474.

(17) Bossolasco, A.; Faragó, E. P.; Schoemaecker, C.; Fittschen, C. Rate Constant of the Reaction between CH3O2 and OH Radicals. *Chemical Physics Letters* **2014**, *593*, 7–13. https://doi.org/10.1016/j.cplett.2013.12.052.

(18) Zhang, D.; Zhang, R.; Allen, D. T. C–C Bond Fission Pathways of Chloroalkenyl Alkoxy Radicals. *The Journal of Chemical Physics* **2003**, *118* (4).

(19) Patchen, A. K.; Pennino, M. J.; Elrod, M. J. Overall Rate Constant Measurements of the Reaction of Chloroalkylperoxy Radicals with Nitric Oxide. *The Journal of Physical Chemistry A* **2005**, *109* (26), 5865–5871. https://doi.org/10.1021/jp050388q.

(20) Sharp, E. N.; Rupper, P.; Miller, T. A. The Structure and Spectra of Organic Peroxy Radicals. *Phys. Chem. Chem. Phys.* **2008**, *10* (27), 3955–3981. https://doi.org/10.1039/B800954F.

(21) Melnik, D.; Chhantyal-Pun, R.; Miller, T. A. Measurements of the Absolute Absorption Cross Sections of the Ã←X̃ Transition in Organic Peroxy Radicals by Dual-Wavelength Cavity Ring-Down Spectroscopy. *J. Phys. Chem. A* **2010**, *114* (43), 11583–11594. https://doi.org/10.1021/jp107340a.

(22) O'Keefe, A.; Deacon, D. A. G. Cavity Ring-down Optical Spectrometer for Absorption Measurements Using Pulsed Laser Sources. *Review of Scientific Instruments* **1988**, *59* (12), 2544–2551. https://doi.org/10.1063/1.1139895.

(23) Deev, A.; Sommar, J.; Okumura, M. Cavity Ringdown Spectrum of the Forbidden ÃE″2←X̃A2′2 Transition of NO3: Evidence for Static Jahn–Teller Distortion in the Ã State. *The Journal of Chemical Physics* **2005**, *122* (22). http://dx.doi.org/10.1063/1.1897364.

(24) Takematsu, K.; Eddingsaas, N. C.; Robichaud, D. J.; Okumura, M. Spectroscopic Studies of the Jahn-Teller Effect in the Ã2E″ State of the Nitrate Radical {NO3}. *Chemical Physics Letters* **2013**, *555* (0), 57–63. http://dx.doi.org/10.1016/j.cplett.2012.10.088.

(25) Trutna, W. R.; Byer, R. L. Multiple-Pass Raman Gain Cell. *Appl. Opt., AO* **1980**, *19* (2), 301–312. https://doi.org/10.1364/AO.19.000301.

(26) Atkinson, R.; Baulch, D. L.; Cox, R. A.; Crowley, J. N.; Hampson, R. F.; Hynes, R. G.; Jenkin, M. E.; Rossi, M. J.; Troe, J. Evaluated Kinetic and Photochemical Data for Atmospheric Chemistry: Volume I - Gas Phase Reactions of Ox, HOx, NOx and SOx Species. *Atmos. Chem. Phys.* **2004**, *4* (6), 1461–1738. https://doi.org/10.5194/acp-4-1461-2004.

(27) Fink, E. H.; Ramsay, D. A. High-Resolution Study of TheÃ2A′ → X2A″ Transition of HO2: Analysis of the 000–000 Band. *Journal of Molecular Spectroscopy* **1997**, *185* (2), 304–324. https://doi.org/10.1006/jmsp.1997.7401.

(28) Giguère, P. A. The Infra-Red Spectrum of Hydrogen Peroxide. *J. Chem. Phys.* **1950**, *18* (1), 88–92. https://doi.org/10.1063/1.1747464.

(29) L. Dodson. Thesis, California Institute of Technology, 2016.

(30) Brown, S. S.; Ravishankara, A. R.; Stark, H. Simultaneous Kinetics and Ring-down: Rate Coefficients from Single Cavity Loss Temporal Profiles. *J. Phys. Chem. A* **2000**, *104* (37), 8600–8600. https://doi.org/10.1021/jp002646j.

(31) Rupper, P.; Sharp, E. N.; Tarczay, G.; Miller, T. A. Investigation of Ethyl Peroxy Radical Conformers via Cavity Ringdown Spectroscopy of the Ã-X̃ Electronic Transition. *J. Phys. Chem. A* **2007**, *111* (5), 832–840. https://doi.org/10.1021/jp066464m.

(32) Burkholder, J. B.; Sander, S. P.; Abbatt, J. P. D.; Barker, J. R.; Huie, R. E.; Kolb, C. E.; Kurylo, M. J.; Orkin, V. L.; Wilmouth, D. M.; Wine, P. H. *Chemical Kinetics and Photochemical Data for Use in Atmospheric Studies: Evaluation Number 18*; Pasadena, CA: Jet Propulsion Laboratory, National Aeronautics and Space …, 2015.

(33) Hodges, J. T.; Looney, J. P.; Zee, R. D. van. Laser Bandwidth Effects in Quantitative Cavity Ring-down Spectroscopy. *Appl. Opt., AO* **1996**, *35* (21), 4112–4116. https://doi.org/10.1364/AO.35.004112.

(34) Yalin, A. P.; Zare, R. N. Effect of Laser Lineshape on the Quantitative Analysis of Cavity Ring-Down Signals. *Laser Physics* **2002**, *12* (8), 1065–1072.

(35) Atkinson, R.; Baulch, D. L.; Cox, R. A.; Crowley, J. N.; Hampson, R. F.; Hynes, R. G.; Jenkin, M. E.; Rossi, M. J.; Troe, J.; IUPAC Subcommittee. Evaluated Kinetic and Photochemical Data for Atmospheric Chemistry: Volume II – Gas Phase Reactions of Organic Species. *Atmospheric Chemistry and Physics* **2006**, *6* (11), 3625–4055. https://doi.org/10.5194/acp-6-3625-2006.

(36) King, M. D.; Thompson, K. C. Rate Constants for the Reaction of NO and HO2 with Peroxy Radicals Formed from the Reaction of OH, Cl or NO3 with Alkenes, Dienes and α,β-Unsaturated Carbonyls. *Atmospheric Environment* **2003**, *37* (32), 4517–4527. https://doi.org/10.1016/S1352-2310(03)00570-3.

(37) Chhantyal-Pun, R.; Kline, N. D.; Thomas, P. S.; Miller, T. A. Observation of the Ã−X̃ Electronic Transition of the β-Hydroxyethylperoxy Radical. *The Journal of Physical Chemistry Letters* **2010**, *1* (12), 1846–1852. https://doi.org/10.1021/jz1005576.

(38) Thomas, P. S.; Miller, T. A. Cavity Ringdown Spectroscopy of the NIR A∼-X∼ Electronic Transition of Allyl Peroxy Radical (H2CCH–CH2OO·). *Chemical Physics Letters* **2010**, *491* (4), 123–131. https://doi.org/10.1016/j.cplett.2010.03.073.

(39) Kaiser, E. W.; Wallington, T. J. Pressure Dependence of the Reaction Cl + C3H6. *J. Phys. Chem.* **1996**, *100* (23), 9788–9793. https://doi.org/10.1021/jp960406r.

(40) Eberhard, J.; Howard, C. J. Rate Coefficients for the Reactions of Some C3 to C5 Hydrocarbon Peroxy Radicals with NO. *J. Phys. Chem. A* **1997**, *101* (18), 3360–3366. https://doi.org/10.1021/jp9640282.

(41) Kline, N. D.; Miller, T. A. Analysis of the A∼–X∼ Electronic Transition of the 2,1-Hydroxypropylperoxy Radical Using Cavity Ringdown Spectroscopy. *Chemical Physics Letters* **2012**, *530*, 16–24. https://doi.org/10.1016/j.cplett.2012.01.056.

(42) Pushkarsky, M. B.; Zalyubovsky, S. J.; Miller, T. A. Detection and Characterization of Alkyl Peroxy Radicals Using Cavity Ringdown Spectroscopy. *The Journal of Chemical Physics* **2000**, *112* (24).

(43) Chung, C.-Y.; Cheng, C.-W.; Lee, Y.-P.; Liao, H.-Y.; Sharp, E. N.; Rupper, P.; Miller, T. A. Rovibronic Bands of the Ã←X̃ Transition of CH3OO and CD3OO Detected with Cavity Ringdown Absorption near 1.2–1.4μm. *J. Chem. Phys.* **2007**, *127* (4), 044311. https://doi.org/10.1063/1.2747616.

(44) Sarzyński, D.; Gola, A. A.; Brudnik, K.; Berkowski, R.; Jodkowski, J. T. Temperature Dependence of the Kinetic Isotopic Effect of the Reaction of Cl Atoms with C2H5Cl between 298 and 550K. *Chemical Physics Letters* **2012**, *554*, 20–26. https://doi.org/10.1016/j.cplett.2012.09.072.

(45) Guenther, A. B.; Jiang, X.; Heald, C. L.; Sakulyanontvittaya, T.; Duhl, T.; Emmons, L. K.; Wang, X. The Model of Emissions of Gases and Aerosols from Nature Version 2.1 (MEGAN2.1): An Extended and Updated Framework for Modeling Biogenic Emissions. *Geoscientific Model Development* **2012**, *5* (6), 1471–1492. https://doi.org/10.5194/gmd-5-1471-2012.

(46) Wennberg, P. O.; Bates, K. H.; Crounse, J. D.; Dodson, L. G.; McVay, R. C.; Mertens, L. A.; Nguyen, T. B.; Praske, E.; Schwantes, R. H.; Smarte, M. D.; et al. Gas-Phase Reactions of Isoprene and Its Major Oxidation Products. *Chem. Rev.* **2018**, *118* (7), 3337–3390. https://doi.org/10.1021/acs.chemrev.7b00439.

(47) Lei, W.; Zhang, D.; Zhang, R.; Molina, L. T.; Molina, M. J. Rate Constants and Isomeric Branching of the Cl–Isoprene Reaction. *Chemical Physics Letters* **2002**, *357* (1–2), 45–50. http://dx.doi.org/10.1016/S0009-2614(02)00437-2.

(48) Ragains, M. L.; Finlayson-Pitts, B. J. Kinetics and Mechanism of the Reaction of Cl Atoms with 2-Methyl-1,3-Butadiene (Isoprene) at 298 K. *The Journal of Physical Chemistry A* **1997**, *101* (8), 1509–1517. https://doi.org/10.1021/jp962786m.

(49) Lei, W.; Zhang, R.; McGivern, W. S.; Derecskei-Kovacs, A.; North, S. W. Theoretical Study of OH−O2−Isoprene Peroxy Radicals. *J. Phys. Chem. A* **2001**, *105* (2), 471–477. https://doi.org/10.1021/jp0027039.

(50) Wallington, T. J.; Dagaut, P.; Kurylo, M. J. UV Absorption Cross Sections and Reaction Kinetics and Mechanisms for Peroxy Radicals in the Gas Phase. *Chemical Reviews* **1992**, *92* (4), 667–710. https://doi.org/10.1021/cr00012a008.

(51) Glover, B. G.; Miller, T. A. Near-IR Cavity Ringdown Spectroscopy and Kinetics of the Isomers and Conformers of the Butyl Peroxy Radical. *J. Phys. Chem. A* **2005**, *109* (49), 11191–11197. https://doi.org/10.1021/jp054838q.

Chapter 4

Water Vapor Dependence of the β-Hydroxyethyl Peroxy Self Reaction

Organic peroxy radicals are widespread atmospheric intermediates that form in the oxidation of nearly every volatile organic compound. Despite the importance of these species, the impact of humidity on their chemistry remains unclear. β-Hydroxyethyl peroxy (β-HEP) is the simplest peroxy radical formed from the hydroxyl-initiated oxidation of alkenes and its chemistry provides general insight into the mechanism of alkene oxidation. It was recently reported that the rate of the β-HEP self reaction is enhanced by the presence of water vapor, suggesting that complexation of a hydroxyl-substituted organic peroxy radical with water may significantly alter its reactivity. While faster radical termination from the HO_2 self reaction through an HO_2–H_2O complex is well established, there is less experimental understanding of the fates of organic RO_2–H_2O complexes, where both radical propagating and terminating channels of the self reaction exist. Here, we present an experimental investigation of β-HEP self reaction kinetics measured as a function of water vapor concentration and temperature using multiplexed synchrotron photoionization mass spectrometry. The flexibility of this technique allows for the simultaneous, time-resolved observation of nearly every radical intermediate and stable product in the oxidation mechanism. We will discuss the impact of humidity on the rate constant and product branching ratio of the β-HEP self reaction. Evidence for the changing fate of the alkoxy radical product is also presented.

4.1 Introduction

The hydroxyl radical is the chief detergent of the atmosphere, oxidizing volatile organic compounds (VOCs) through either hydrogen abstraction or addition across a carbon-carbon double bond. The simplest example of the latter is addition to ethene to form the β-hydroxyethyl peroxy radical (β-HEP):

$$OH + CH_2CH_2 + M \rightarrow HOCH_2CH_2 + M \quad (R1)$$

$$HOCH_2CH_2 + O_2 + M \rightarrow HOCH_2CH_2O_2 + M \quad (R2)$$

where M denotes an inert third body (typically N_2 or O_2 in the atmosphere). It was recently reported by Kumbhani et al. that the self reaction rate of β-HEP radicals was enhanced by the presence of water vapor, with the sensitivity being greatest at colder temperatures.[1] Indeed, theoretical calculations support the existence of a β-HEP–H_2O complex with a binding energy of ~8.5 kcal mol^{-1},[2] which may exhibit different reactivity than the uncomplexed intermediate. Despite the prevalence of water vapor throughout the troposphere, the influence of humidity on the reactions of organic peroxy radicals has not been the subject of widespread study. The self reaction of methyl peroxy and its reaction with HO_2 have been investigated but negligible dependence on humidity was observed.[3] In contrast, the self reaction rate of inorganic HO_2 has consistently been shown to be strongly dependent on water vapor concentration.[4–10]

The self reaction of organic peroxy radicals can proceed through radical propagating (R3a) or radical terminating (R3b) channels. We schematically outline this chemistry in Figure 1. In the case of β-HEP:

$$HOCH_2CH_2O_2 + HOCH_2CH_2O_2 \rightarrow HOCH_2CH_2O + HOCH_2CH_2O + O_2 \quad (R3a)$$

$$\rightarrow HOCH_2CH_2OH + HOCH_2CHO + O_2 \quad (R3b)$$

The symbol $\alpha = k_{3a}/k_3$ is commonly defined as the branching fraction of the radical propagating channel. The alkoxy radicals (RO) from R3a have two potential fates. The first is thermal decomposition:

$$HOCH_2CH_2O + M \rightarrow HCHO + CH_2OH + M \quad (R4)$$

R4 can also occur as a prompt rather than thermal process if the RO radical is produced with sufficient energy to exceed the decomposition barrier. This commonly occurs when the RO radical is produced from the β-HEP + NO reaction, in which the peroxynitrite intermediate dissociates to yield vibrationally excited RO.[11] The RO radicals generated by

R3a are more thermalized, however, and therefore prompt decomposition is less important in the case of the self reaction. The CH_2OH radicals from the decomposition rapidly react with ambient O_2 to form a second formaldehyde and HO_2:

$$CH_2OH + O_2 \rightarrow HCHO + HO_2 \quad \text{(R5)}$$

The second fate of the RO radical is also reaction with O_2:

$$HOCH_2CH_2O + O_2 \rightarrow HOCH_2CHO + HO_2 \quad \text{(R6)}$$

Glycoaldehyde, a stable product, is generated from both the radical propagating and terminating channels of the self reaction.

An important observation is that each RO radical will yield an HO_2 radical, regardless of if the mechanism is through decomposition (R4 and R5) or reaction with O_2 (R6). In laboratory studies, measurements of the self reaction rate constant k_3 are complicated by secondary HO_2. These species serve as additional reaction partners for β-HEP (R7) or, if their concentration is great enough, they can self react (R8):

$$HOCH_2CH_2O_2 + HO_2 \rightarrow HOCH_2CH_2OOH + O_2 \quad \text{(R7)}$$

$$HO_2 + HO_2 \rightarrow H_2O_2 + O_2 \quad \text{(R8)}$$

The decay of β-HEP radicals is therefore not a simple second order process. Knowledge of the products yields of R3, whether they be stable compounds or reactive intermediates, is necessary to constrain the secondary chemistry and correct the β-HEP decay for R7.

In the study of Kumbhani et al., the self reaction decay of β-HEP in the presence of H_2O was measured using time-resolved UV detection of the peroxy radical $\tilde{B} \leftarrow \tilde{X}$ transition.[1] While their technique was also capable of detecting HO_2, they were unable to observe the HO_2 produced from the alkoxy radical chemistry, presumably due to its small steady-state concentration. No other products were detected and therefore no information could be gained about the branching fraction α, which could also depend on humidity. Nevertheless, their fits of the β-HEP decay to a chemical kinetics model optimized rate constants for R3a and R3b separately. It is unclear if a fixed value of α was assumed. Without product information, there is no sensitivity to the individual values of k_{3a} or k_{3b}. Their model included a fixed rate constant for R7 (which could also depend on H_2O), but there is no way to determine the extent of this secondary reaction from the β-HEP decays alone. We therefore interpret the self reaction rate constants reported by Kumbhani et al. as k_{obs}, defined as the observed empirical bimolecular loss rate constant of β-HEP and

β-HEP–H_2O through their self and cross reactions, as well as through their reactions with secondary HO_2 and HO_2–H_2O. We note that this differs from the definition of k_{obs} used by Kumbhani et al., which appears not to have included secondary reactions with HO_2.

The rates of R3a and R3b could be impacted to different extents by humidity; this would lead to a dependence of the effective α on water vapor concentration. Determining this sensitivity is crucial to inferring the true magnitude of the self reaction rate enhancement from measurements of k_{obs}. Kumbhani et al. have reported that k_{obs} increases with greater [H_2O].[1] If α also increases with greater [H_2O], then the true enhancement of the self reaction is less than that inferred by the increase in k_{obs}, since at least part of the faster β-HEP decay would be explained by a greater concentration of secondary HO_2. If α decreases with greater [H_2O], then the magnitude of the self reaction enhancement is even greater than the increase in k_{obs} due to a smaller relative yield of HO_2.

In this chapter, we present an investigation of the β-HEP self reaction using multiplexed synchrotron photoionization mass spectrometry (MPIMS). This technique is capable of detecting nearly every radical species and stable product in the oxidation mechanism (Figure 1). We first present our own measurements of k_{obs} as a function of temperature and water vapor concentration. Next, we use the yields of ethylene glycol (unique to the radical terminating pathway, R3b) and HO_2 (unique to the radical propagating pathway, R3a) to determine how α changes with humidity at cold temperatures. Finally, we present evidence for the influence of water vapor on the competition between decomposition of the alkoxy radicals and their reaction with O_2.

4.2 Experimental Methods

The MPIMS instrument has been described previously.[12,13] We also present a description of the instrument, including details of the low temperature reactor, in Chapter 2. Briefly, pulsed laser photolysis of a flowing gas mixture initiates radical chemistry. Neutral species effuse into a vacuum chamber through a pinhole on the side of a chemical flow reactor. The resulting molecular beam is intersected by quasi-continuous synchrotron radiation from the Chemical Dynamics Beamline at the Advanced Light Source of Lawrence Berkeley National Laboratory. The resulting cations are extracted and counted by an orthogonal-acceleration time-of-flight mass spectrometer. The data is binned to yield

a complete mass spectrum with 200 μs time spacing. These images of ion counts as a function of m/z and reaction time are acquired at discrete photoionization energies. An example of an image measured in these experiments is presented in Figure 2a. The datasets can be integrated across various axes to interpret the chemistry. An example of integration across the m/z axis to obtain the time-resolved ion signal of formaldehyde (m/z = 30) is presented in Figure 2b. By scanning the energy of vacuum ultraviolet (VUV) radiation from the synchrotron and obtaining a series of images, we add photoionization energy as an additional axis to the datasets. The absolute energy axis is calibrated daily by scanning over the 8s ← 5p atomic transition of Xe at 12.5752 eV.[14]

The radical precursor in these experiments was hydrogen peroxide. H_2O_2 vapor was photolyzed by an unfocused excimer laser (KrF, 248 nm, 4 Hz) to yield OH radicals:

$$H_2O_2 + 248\ \text{nm} \rightarrow OH + OH \qquad \text{(R9)}$$

OH would then oxidize excess ethene to form β-HEP (R1 and R2). H_2O_2 was introduced to the reactor by flowing He carrier gas through a bubbler containing a solid mixture of sand and urea hydrogen peroxide.[15] The bubbler was heated in a bath held at 40 °C to promote sublimation. The concentration of H_2O_2 in the reactor was calibrated using its known photoionization cross section at 11.2 eV.[16] Throughout a shift of experiments, we would periodically flow propene, whose cross section is also known at 11.2 eV,[17] in the absence of the photolysis. The concentration of H_2O_2 (unknown, "unk") could then be determined from the known concentration of propene (reference, "ref") via the ratio of their ion counts:[18]

$$N_{\text{unk}} = \frac{S_{\text{unk}}}{S_{\text{ref}}} \cdot \frac{\alpha_{\text{ref}} f_{\text{ref}}}{\alpha_{\text{unk}} f_{\text{unk}}} \cdot \frac{\sigma_{\text{ref}}(E)}{\sigma_{\text{unk}}(E)} \cdot N_{\text{ref}} \qquad \text{(Eqn. 1)}$$

where S_i is the ion signal and σ_i is the absolute photoionization cross section. For absolute concentration determinations in this work, only the ion signals of and cross sections to form parent cations were used. N_i is the concentration of the species in the reactor and f_i is the fractional abundance of the detected isotope. α_i is the mass discrimination factor specific to the mass of the detected ion (m_i) and is described empirically by a power law function: $\alpha_i = m_i^{\beta}$. (The value of β was determined according to experiments described in the Supplementary Material of Chapter 2 and by Savee et al.[18]) The [H_2O_2] determined by this method was typically ~5 x 10^{14} molc cm^{-3} and varied by less than ±5% throughout a day.

Water vapor was introduced to the reactor by flowing He carrier gas through a bubbler containing liquid H_2O. The bubbler was chilled in a bath held at 20 °C. The concentration of water vapor in the carrier gas flow (upstream of the reactant gas mixing region) was determined spectroscopically. Using a homebuilt spectrometer, the mid-IR absorption across several H_2O lines near 3447 cm^{-1} was recorded and fit to determine its absolute concentration.[19] Based on dilution of the H_2O / He flow by mixing with other reactant gases, the water concentration in the reactor was determined. The $[H_2O]$ was typically varied over (0–4) x 10^{16} molc cm^{-3}. This translates to a relative humidity (RH) up to ~20%, depending on the temperature.

The total pressure in the reactor was maintained at P = 30 Torr. The temperature of the reactor was set to T = 26.6 °C (room temperature experiments) or T = 3.6 °C (low temperature experiments). To achieve the latter, cold nitrogen was circulated through a jacket surrounding the stainless steel reactor tube. The low temperature reactor has been described previously[20] and additional details are provided in Chapter 2. The complete reactant mixture used to study the β-HEP self reaction was comprised of 13.3–14.3% O_2, 0–4% H_2O, 0.133–0.143% ethene, and 400–500 ppm H_2O_2 in a balance of He. Upon 248 nm photolysis of H_2O_2, the typical initial radical concentration was $[OH]_0 \approx 4$ x 10^{12} molc cm^{-3} (~0.5% photolysis fraction). Experiments used to determine the precise initial radical concentration are discussed in the next section.

4.3 Results & Discussion

4.3.1 Initial Radical Concentration

Since the decay of β-HEP radicals is concentration-dependent, it is necessary to measure the absolute initial radical concentration in order to determine k_{obs}. Each day, we performed experiments to calibrate the fraction of H_2O_2 photolyzed. The same $[H_2O_2]$ was used throughout a shift (fluctuations typically less than ±5%) and therefore this also served as a calibration of $[OH]_0$ for all experiments conducted on that particular day.

To calibrate $[OH]_0$, we photolyzed a reactant mixture containing solely H_2O_2 in a He balance. Without the presence of excess ethene, nascent OH reacts with H_2O_2:

$$OH + H_2O_2 \rightarrow HO_2 + H_2O \qquad \text{(R10)}$$

The dominant fate of HO_2 under these conditions is its self reaction (R8). To a lesser extent, HO_2 reacts with OH:

$$OH + HO_2 \rightarrow H_2O + O_2 \quad \text{(R11)}$$

The rate constant of R11 is fast ($k_{11} \approx 10^{-10}$ cm^3 molc^{-1} s^{-1}) but only has a minor impact due to the short lifetime of OH radicals with respect to R10 ($\tau \approx 1$ ms). Most OH will yield HO_2, which is subsequently lost by self reaction.

The ion signal of H_2O_2 (m/z = 34) was averaged at a photoionization energy of 11.2 eV. Since the pre-photolysis [H_2O_2] is calibrated (see previous section), we can compute a scale factor for converting ion counts to absolute concentration units from the average pre-photolysis ion signal. An example time-resolved $H_2O_2^+$ signal acquired in these experiments is presented in Figure 3a and approximates a step function. The decrease at t = 0 is due to H_2O_2 lost by both the instantaneous R9 and fast R10. A small amount of H_2O_2 will reform on a longer timescale by R8; however, we instead observe a very weak slope that is negative rather than positive. The reformation of H_2O_2 is masked by slight divergence of the excimer laser fluence as the beam propagates through the reactor that yields a gradient in the photolysis fraction (see Supplementary Material for Chapter 2).

We then tuned the photoionization energy to 13.56 eV to average the ion signals of OH (m/z = 17) and HO_2 (m/z = 33). The OH^+ signal (Figure 3b) is very short lived and approximates a delta function due the fast loss of OH by R10 and R11. The HO_2^+ (Figure 3c) signal is much longer lived and exhibits a bimolecular decay in accordance with R8.

The time-resolved ion signals of H_2O_2, HO_2, and OH were fit to a chemical kinetic model that included R8, R9, R10, and R11. The temperature-dependent parameterizations of k_8, k_{10}, and k_{11} were taken from the NASA JPL data evaluation.[21] We also added first order rate constants to describe the loss of HO_2 and OH at the walls of the reactor. The three ion signals were simultaneously fit to the model with five floated parameters: the initial $[OH]_0$, scale factors to convert HO_2^+ and OH^+ signals to absolute concentrations, and wall loss rates for HO_2 and OH. An example fit is shown in Figure 3 and yielded $[OH]_0 = 4.0 \times 10^{12}$ molc cm^{-3} (photolysis fraction of 0.48%). The optimized $[OH]_0$ was chiefly determined by two factors: the absolute decrease in [H_2O_2] upon photolysis (minor influence due to small, noisy depletion) and the bimolecular decay rate of HO_2, which is concentration-dependent (major influence). $[OH]_0$ is therefore highly sensitive to k_8.

4.3.2 Vinyl Alcohol Yield

Our determination of k_{obs} assumes that each OH radical produced from H_2O_2 photolysis eventually yields a β-HEP radical ($[OH]_0 = [\beta\text{-HEP}]_0$) through R1 and R2. However, excited β-hydroxyethyl radicals ($^*HOCH_2CH_2$) are also generated by ethene oxidation and can undergo chemically activated, bimolecular reactions with O_2 prior to collisional stabilization:

$$^*HOCH_2CH_2 + O_2 \rightarrow HO_2 + CH_2CHOH \quad \text{(R12a)}$$

$$\rightarrow OH + HCHO + HCHO \quad \text{(R12b)}$$

$$\rightarrow OH + CH_2OCHOH \text{ (epoxide)} \quad \text{(R12c)}$$

R12 includes the three pathways with the smallest energy barriers to form stable products calculated by Zádor et al.[22] These channels lead to systematic error in the measured values of k_{obs} by violating the $[OH]_0 = [\beta\text{-HEP}]_0$ assumption.

To assess the extent of the systematic error, we sought to quantify the absolute yields of some of the chemical activation products. Any regenerated OH (R12b and R12c) rapidly reacts with excess ethene and is difficult to detect. The yields of HO_2 (R12a) and formaldehyde (R12b) cannot be distinguished from their yields from the β-HEP self reaction. Furthermore, the epoxide (R12c) has the same mass as glycoaldehyde produced from the self reaction (m/z = 60). While in principle the MPIMS technique is capable of resolving isomers at the same mass through differences in their photoionization efficiency curves,[12,13] the photoionization spectrum of the epoxide is not known. Therefore, by process of elimination, vinyl alcohol (R12a, m/z = 44) appeared to be the most promising candidate to assess the extent of activated chemistry.

Experiments of ethene oxidation conducted at 10.75 eV indeed showed time-resolved ion signal at m/z = 44 (Figure 4b). The shape of the measured relative photoionization efficiency curve of m/z = 44 (Figure 4a) matches the shape of the known absolute photoionization spectrum of vinyl alcohol,[23] providing strong evidence that our m/z = 44 signal arises from this species. To determine the absolute photoionization cross section at 10.75 eV, we scaled our relative spectrum (recorded up to 12.0 eV) to match the known absolute spectrum (recorded up to 10.5 eV). The absolute concentration of vinyl alcohol ([VA]) was then determined relative to the known cross section and concentration of ethene. The ion signal of m/z = 44 (per 200 μs time bin) was averaged in the 10.75 eV

kinetics trace across 50–80 ms, over which its signal appeared constant (Figure 4b). The ion signal of ^{13}C ethene (per 200 μs time bin) was averaged across all times pre-photolysis. The [VA] yield was then calculated using Eqn. 1, with vinyl alcohol as the unknown and ^{13}C ethene as the reference.

Figure 4 outlines this procedure. We determined a yield of [VA] = 6.4 x 10^{10} molc cm^{-3} from experiments conducted at P = 30 Torr, T = 26.6 °C, 13.3% O_2, 0% H_2O, He balance, and $[OH]_0$ = 4.0 x 10^{12} molc cm^{-3}. This translates to a very small vinyl alcohol yield of 1.6%, which is well below our relative uncertainty on the absolute initial radical concentration. We therefore assumed that chemically activated processes (R12) were negligible under our conditions and that $[OH]_0 = [\beta\text{-HEP}]_0$ is a valid approximation.

4.3.3 Observed Self Reaction Rate Constant

In experiments measuring k_{obs}, the time-resolved ion signal of β-HEP was recorded at 10.75 eV and detected at m/z = 45. While the parent cation is at m/z = 77, we observed essentially no ion signal at this mass. Organic peroxy radicals larger than methyl peroxy are known to have unbound parent cation states that fragment across the C-O bond of the peroxy group to yield O_2 and an alkyl radical cation.[24] For dissociative ionization of β-HEP, this yields the β-hydroxyethyl cation at m/z = 45. β-hydroxyethyl cations could also arise from the ionization of neutral β-hydroxyethyl radicals or from dissociative ionization of the β-hydroxyethyl hydroperoxide generated by R7. We rule out the former since the lifetime of β-hydroxyethyl radicals with respect to R2 is too short ($\tau \approx$ 1–2 μs) under our conditions for this species to be detected.

We conducted several experiments to rule out contribution of β-hydroxyethyl hydroperoxide to m/z = 45. First, we measured time-resolved m/z = 45 signals at multiple photoionization energies. The kinetics exhibited rapid growth followed by a slower decay to approximately the pre-photolysis signal level; this is consistent with the expected kinetics of β-HEP and inconsistent with the expected kinetics of the hydroperoxide product. Furthermore, the shapes of the kinetic traces were identical when measured at different energies. If two species were contributing to the ion signal, then the kinetic shape would change as a function of energy, since the ratio of their partial photoionization cross sections to yield m/z = 45 would likely be energy-dependent.

Second, we measured the relative photoionization efficiency curves of m/z = 45 with solely ethene as the hydrocarbon precursor and with a mixture of $[C_2H_4]$:$[CH_3OH]$ = 0.14:0.86. In the latter case, methanol competes for OH through its oxidation:

$$CH_3OH + OH \rightarrow CH_2OH + HO_2 \quad \text{(R13)}$$

The CH_2OH radicals rapidly react with O_2 to produce HO_2 (R5). The result is a partitioning of the initial peroxy radical concentration between β-HEP and HO_2. Based on the rate constants of R1 and R13, we generated $[\beta\text{-HEP}]_0$:$[HO_2]_0$ = 0.52:0.48. These conditions promote R7 and increase the concentration of the β-hydroxyethyl hydroperoxide, relative to the case of only ethene being oxidized. If both β-HEP and the hydroperoxide ionize to m/z = 45, then the shape of the photoionization efficiency curve should change to reflect increased contribution of the hydroperoxide spectrum. Figure 5 plots the m/z = 45 spectra obtained with solely ethene and a mixture of ethene and methanol. The two curves are nearly identical, particularly up to 10.75 eV, suggesting that only one species is dissociatively ionizing to this mass. Based on the shape of the m/z = 45 kinetics discussed previously, we conclude that only β-HEP contributes to m/z = 45 signal at 10.75 eV.

Experiments were conducted at T = 26.6 and 3.6 °C and across a range of humidities to establish the dependence of k_{obs} on water vapor concentration (solely ethene as the hydrocarbon precursor). An example β-HEP ion signal is presented in Figure 6. Signals were fit to a model comprised of bimolecular decay kinetics with a baseline offset:

$$S(t) = \frac{S_0}{1 + 2k_{obs}[\beta\text{-HEP}]_0 t} + S_{base} \quad \text{(Eqn. 2)}$$

where S_0 is the initial ion signal intensity, S_{base} is the baseline intensity, and $k_{obs}[\beta\text{-HEP}]_0$ is the bimolecular decay constant. Three-parameter fits of the signals to Eqn. 2 optimized $k_{obs}[\beta\text{-HEP}]_0$, which was then divided by the calibrated initial radical concentration (under the assumption $[OH]_0 = [\beta\text{-HEP}]_0$) to obtain k_{obs}. The values of k_{obs} measured in this work are plotted in Figure 7. We see that k_{obs} is insensitive to $[H_2O]$ at T = 26.6 °C, but increases by a factor of ~3 between $[H_2O]$ = 0 and 3.7 x 10^{16} molc cm^{-3} (RH = 18%) at T = 3.6 °C. Since this is only a small change in absolute temperature, the enhancement of k_{obs} at a particular $[H_2O]$ is highly sensitive to temperature. This is consistent with the enhancement arising from a faster reaction rate of the β-HEP–H_2O complex, whose concentration will be greater at colder temperatures and highly temperature-dependent.

The decay signal arises from three processes: the self reactions of β-HEP and β-HEP–H_2O and their cross reaction. If we assume that the fraction of peroxy radicals existing as a complex is small, then the β-HEP–H_2O self reaction becomes negligible and k_{obs} can be modeled according to:[1,8]

$$k_{obs} = k_{obs}^{dry} + k_{obs}^{wet} K_{eq}[H_2O] \quad \text{(Eqn. 3)}$$

where k_{obs}^{dry} is the observed rate constant of β-HEP + β-HEP, k_{obs}^{wet} is the observed rate constant of β-HEP + β-HEP–H_2O, and K_{eq} is the equilibrium constant between β-HEP and H_2O to complex as β-HEP–H_2O. The key idea is that k_{obs} is expected to be a linear function of [H_2O] at a fixed temperature. We plot linear fits to our datasets acquired at T = 26.6 and 3.6 °C in Figure 7. Also plotted is the parameterization of k_{obs} determined by Kumbhani et al.[1] While we measured a slightly stronger water vapor dependence at 3.6 °C than that predicted by Kumbhani et al., the differences are within uncertainty and overall the results of the two studies are in excellent agreement.

4.3.4 Branching Fraction

As discussed in the introduction, the true magnitude of the self reaction rate enhancement may be stronger or weaker than that predicted by the trend in k_{obs} since α (the branching fraction to the radical propagating channel) may also depend on humidity. Larger values of α result in additional HO_2 production and faster secondary loss of β-HEP through R7 rather than through the self reaction. Since we observed a strong dependence of k_{obs} on water vapor concentration at 3.6 °C, we conducted additional studies at this temperature to measure α as a function of [H_2O].

To determine α, we measured the ion signals of ethylene glycol (detected at m/z = 62, 10.75 eV) and HO_2 (detected at m/z = 33, 11.75 eV). Ethylene glycol is a unique product of the radical terminating channel of the self reaction (R3a). HO_2 is a unique product of the radical propagating channel (R3b) and is generated regardless of whether the alkoxy radical decomposes (R4 / R5) or reacts with O_2 (R6). (Formaldehyde is also unique to the radical propagating channel but would be unsuitable for this analysis since it is only generated by decomposition and, as discussed in the next section, the fate of the alkoxy radical changes with humidity.) From the stoichiometry, the ratio of HO_2 and ethylene glycol yielded by the self reaction is related to α through:

$$\frac{[HO_2]_{yield}}{[HOCH_2CH_2OH]_{yield}} = \frac{2\alpha}{1-\alpha} \quad \text{(Eqn. 4)}$$

where the subscript $yield$ is used to denote the total concentration of this species generated by the β-HEP self reaction after the completion of chemistry.

Unfortunately, it is not possible to simply average the ion signals of HO_2 and ethylene glycol at long reaction times to determine their yields. HO_2 is reactive and has a variety of chemical loss processes (R7 and R8). Ethylene glycol is chemically stable, but exhibits considerable loss at the walls of the reactor. To determine the yields of these species, we empirically modeled their time-dependencies through a rate law composed of bimolecular production and first order loss. The production of neither species is truly bimolecular since the decay of β-HEP arises from both R3 and R7. Furthermore, in the case of HO_2, the decay is not truly first order due to its participation in R7 and R8. (We note that production of HO_2 is indeed rate-limited by the β-HEP self reaction due to the high $[O_2]$ and short lifetime of the alkoxy radical.) Despite these limitations, the time-dependencies of HO_2 and ethylene glycol could still be reasonably approximated by this empirical model. The rate law is given by:

$$\frac{d[i]}{dt} = \frac{k_{i,bi}[X]_0{}^2}{\left(1 + 2k_{total,bi}[X]_0 t\right)^2} - k_{i,loss}[i] \quad \text{(Eqn. 5)}$$

where i represents the target species, X represents the species that is self reacting to produce i, $k_{i,bi}$ is the rate constant of the X self reaction channel that yields i, $k_{tot,bi}$ is the total X self reaction rate constant, and $k_{i,loss}$ is the first order loss rate of i. If we define C_i as a scale factor between ion signal and concentration, then the ion signal is $S_i = [i] \cdot C_i$ and the rate law can be rewritten as a differential equation that describes the time-dependence of the ion signal:

$$\frac{dS_i}{dt} = \frac{C_i k_{i,bi}[X]_0{}^2}{\left(1 + 2k_{total,bi}[X]_0 t\right)^2} - k_{i,loss} S_i \quad \text{(Eqn. 6)}$$

There is no straightforward analytical solution to Eqn. 6. We therefore modeled the product ion signals by numerically integrating Eqn. 6 with $S_i(0) = 0$ as the initial condition. Three-parameter fits were performed to each signal to optimize the values $C_i k_{i,bi}[X]_0{}^2$, $2k_{total,bi}[X]_0$, and $k_{i,loss}$. Division of the first parameter by the second parameter gives

$C_i \cdot \left(k_{i,bi}/k_{tot,bi}\right) \cdot ([X]_0/2)$, which is equal to the yield of i generated by the self reaction expressed in ion signal units. This analysis was performed on kinetic traces of HO_2 and ethylene glycol to approximate their yields generated by the β-HEP self reaction; example time-resolved ion signals and fits are presented in Figure 8ab.

The ion signal yields of HO_2 and ethylene glycol were determined at each [H_2O]. Their ratio, which is proportional to $[HO_2]_{yield}/[HOCH_2CH_2OH]_{yield}$, is plotted in Figure 9a relative to the [H_2O] = 0 case. We see that this ratio decreases by ~90% across the range of [H_2O] utilized (up to RH = 18%), implying that the radical terminating channel of the β-HEP self reaction is being enhanced relative to the radical propagating channel. However, while the ratio of the ion signal yields provides a qualitative trend, the ratio of the concentration yields is necessary to use Eqn. 4 and calculate α. We determined the proportionality constant between concentration and ion signal ratios by assuming our data at [H_2O] = 0 is consistent with a prior measurement of α = 0.5 for the dry self reaction.[25] (While the prior study was conducted at 22 °C and this data was collected at 3.6 °C, we measured little difference in k_{obs} between 3.6 and 26.6 °C when [H_2O] = 0, suggesting that dry α = 0.5 is also valid at 3.6 °C.) This enabled calculation of α when [H_2O] > 0, effectively relative to the dry case. The resulting values of α are plotted as a function of water vapor concentration in Figure 9b.

The value of the branching fraction decreases from α = 0.5 under dry conditions to α ≈ 0.1 at the maximum [H_2O] = 3.7 x 10^{16} molc cm^{-3} (RH = 18%) used in experiments conducted at T = 3.6 °C. The radical terminating channel (R3b) is therefore significantly enhanced relative to the radical propagating channel (R3a) when β-HEP is complexed with water. This is consistent with enhancement of the inorganic HO_2 self reaction by water vapor,[4,9,10] which has only a radical terminating channel. Because the relative yield of secondary HO_2 decreases with increasing humidity, the true enhancement of the self reaction rate constant is even greater than the enhancement implied by the trend in k_{obs}, since a greater fraction of the β-HEP decay is now explained by the self reaction rather than secondary chemistry.

4.3.5 Fate of the Alkoxy Radical

We also explored if the fate of the alkoxy radical, generated by the radical propagating channel of the self reaction (R3a), was influenced by the presence of water vapor. Given the short lifetime of RO radicals, it seems unlikely that they would form an RO–H_2O complex prior to their removal. However, β-HEP–H_2O complexes that undergo R3a likely form product alkoxy radicals that, at least initially, are complexed as RO–H_2O. As discussed in the introduction, the fate of the alkoxy radicals is either reaction with O_2 (R6) or decomposition (R4 / R5). The former pathway produces glycoaldehyde (detected at m/z = 60, 10.75 eV) while the latter pathway ultimately yields two formaldehydes (detected at m/z = 30, 11.75 eV). The time-resolved ion signals of these species were recorded at each [H_2O] used in the T = 3.6 °C experiments. Their yields in ion signal units were determined using the analysis outlined in the previous section, fitting their kinetics to a model described by numerical integration of Eqn. 6; example datasets are shown in Figure 8cd. The formaldehyde to glycoaldehyde ion signal ratio, which is proportional to $[\mathrm{HCHO}]_{yield}/[\mathrm{HOCH_2CHO}]_{yield}$, is plotted in Figure 10 relative to the [H_2O] = 0 case.

The results indicate that the formaldehyde yield increases by ~250% relative to the glycoaldehyde yield between dry conditions and [H_2O] = 3.7 x 10^{16} molc cm^{-3} (RH = 18%). This is a significant increase, although its interpretation for the fate of the alkoxy radical is complicated by the fact that the glycoaldehyde yield from the radical terminating channel of the self reaction (R3b) also decreases. Correction of the ratio for this effect using the branching fractions determined in the previous section is not straightforward since the absolute concentrations are unknown. Nevertheless, separate experiments conducted on the β-HEP + NO reaction, in which glycoaldehyde is produced solely from the alkoxy radical chemistry, also demonstrated enhanced formaldehyde relative to glycoaldehyde upon addition of H_2O. This indicates that the changing product ratio observed in the self reaction studies is not an artifact of the decrease in α, although the results are influenced by it. Orlando et al. found that the barrier to decomposition of the RO radical is ~10–11 kcal mol^{-1} under the assumption that the activation energy for its reaction with O_2 is ~1–2 kcal mol^{-1}.[11] Our results, which demonstrate enhanced decomposition relative to the O_2 reaction, suggest the RO–H_2O complex has either a smaller decomposition barrier, greater activation energy for reaction with O_2, or some combination thereof.

4.4 Conclusions

The enhancement of the β-HEP self reaction under cold temperatures and humid conditions has been studied using multiplexed synchrotron photoionization mass spectrometry. The magnitude of the enhancement was found to be consistent with the results of a prior investigation[1] and indicates that complexation of β-HEP with water significantly increases its reactivity. Our experiments have extended the understanding of this effect by measuring the yields of the ethylene glycol, glycoaldehyde, HO_2, and formaldehyde products. We found that the radical terminating channel is significantly enhanced relative to the radical propagating channel under cold and wet conditions. Due to the relative decrease in secondary chemistry, the true enhancement of the self reaction is even greater than the trend in the observed β-HEP decay rates initially implied. We have also studied the fate of the alkoxy radical yielded by the radical propagating channel. Our results demonstrate a substantial increase in the formaldehyde to glycoaldehyde product ratio, indicating that complexation of the alkoxy radical with water promotes decomposition relative to reaction with O_2.

While studies of peroxy radical self reactions provide general insight into the reactivity of these important intermediates, the self reactions of organic peroxy radicals typically only occur under laboratory conditions, due to the large radical concentrations necessary to exceed experimental detection limits. In the real atmosphere, the fates of these species are dominated by other loss processes, such as unimolecular isomerization or bimolecular reactions with NO or HO_2. Our study has shown that the reactivity of complexes between organic peroxy radicals and water can demonstrate significantly enhanced reactivity relative to uncomplexed intermediates, at temperatures and humidities common throughout the troposphere. Future studies should explore this effect for organic peroxy radical reactions of greater atmospheric relevance.

4.5 Figures

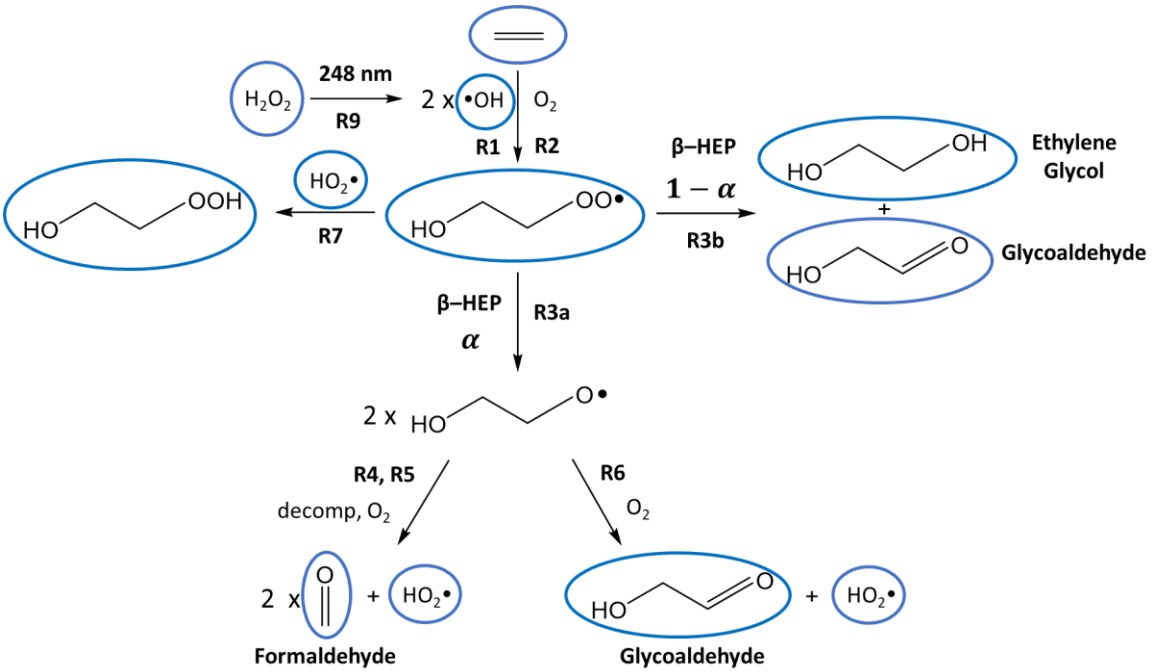

Figure 1: Schematic of oxidation chemistry studied in this chapter to investigate the water vapor dependence of the β-HEP self reaction. Circled species can be detected by the multiplexed synchrotron photoionization mass spectrometry technique. For most of the species, time-resolved ion signals can also be measured. The reaction numbers correspond to the values in the text. Not shown is the HO_2 self reaction (R8), which also occurs.

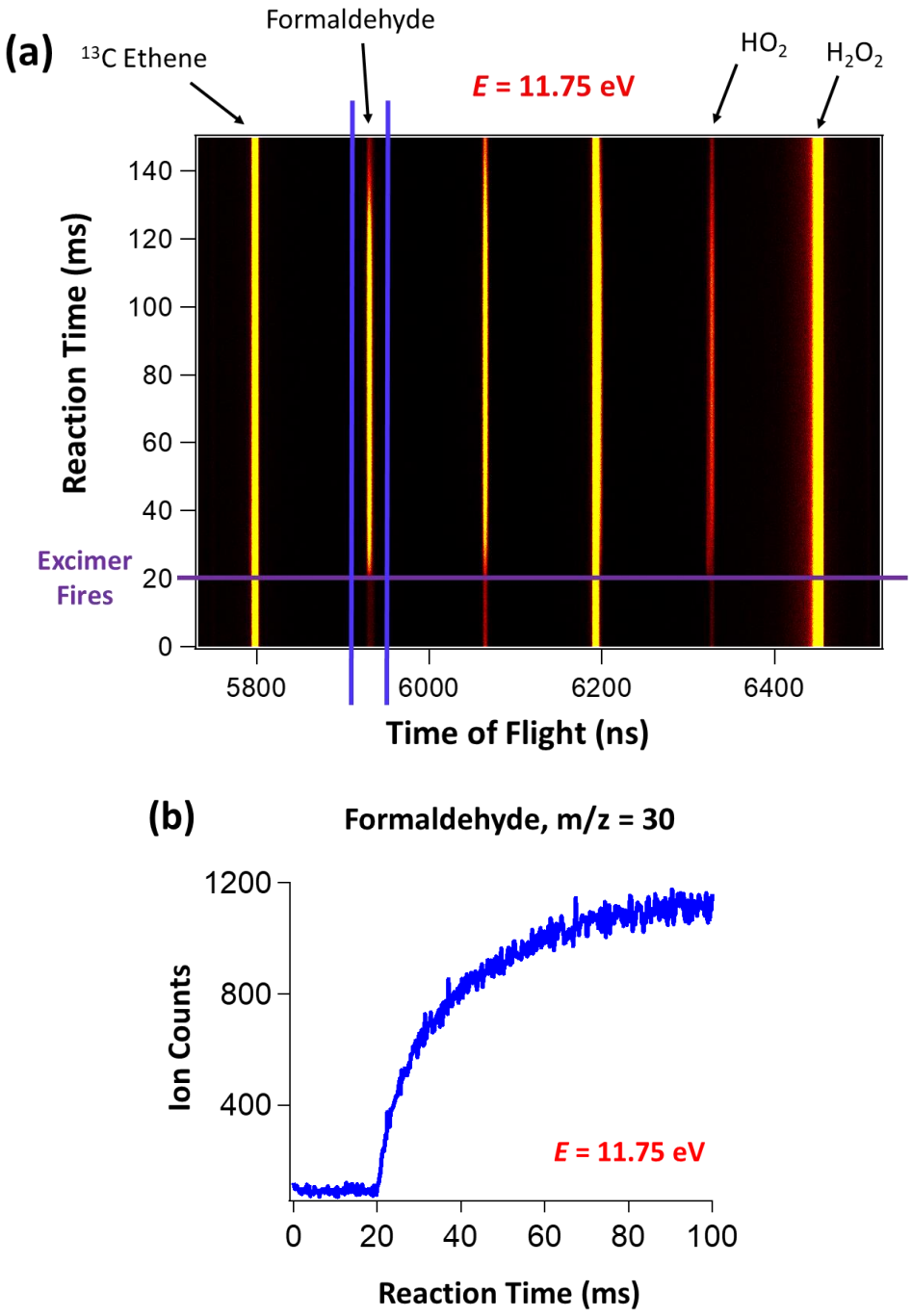

Figure 2: (a) Example image of ion counts as a function of m/z (time-of-flight) and reaction time collected in these experiments at a photoionization energy of 11.75 eV. Streaks in the image correspond to time-resolved ion signals. Various masses of relevance to these experiments are labeled. We acquire a series of these images by stepping the photoionization energy. **(b)** Example time-resolved ion signal of formaldehyde (m/z = 30) acquired by integrating across a subset of the time-of-flight axis in (a).

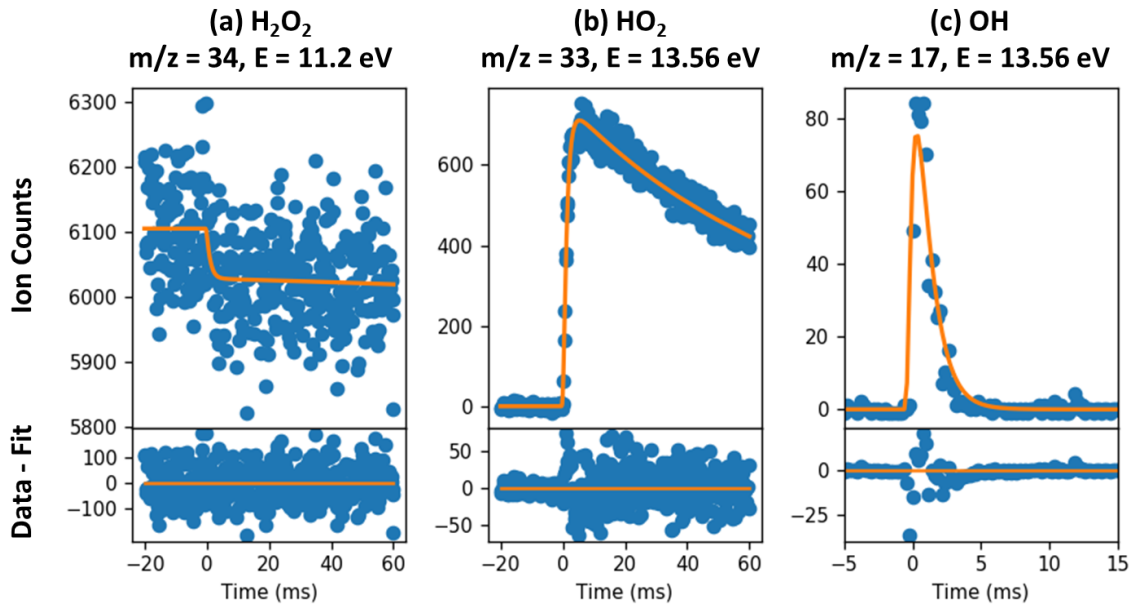

Figure 3: Example time-resolved ion signals (blue dots) of **(a)** H_2O_2, **(b)** HO_2, and **(c)** OH measured in experiments calibrating the initial radical concentration, $[OH]_0$. Example dataset was acquired by photolyzing a mixture of solely $[H_2O_2] = 4.18 \times 10^{14}$ molc cm^{-3} in a balance of He at P = 30 Torr and T = 26.6 °C. The three ion signals were simultaneously fit to a chemical kinetic model (orange curves) and optimized, which yielded $[OH]_0 = 4.0 \times 10^{12}$ molc cm^{-3} (0.48% photolysis).

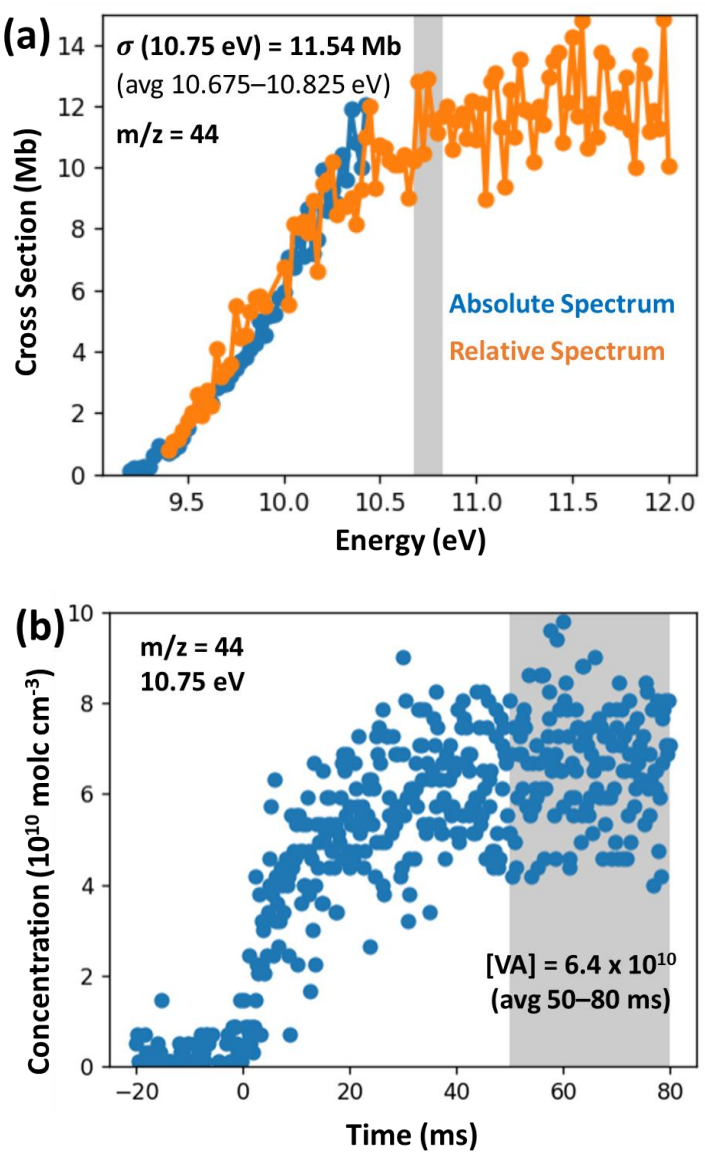

Figure 4: Summary of experiments used to determine the vinyl alcohol yield. **(a)** The relative photoionization spectrum of vinyl alcohol measured in this work (recorded up to 12.0 eV), scaled to match the known absolute spectrum (recorded up to 10.5 eV).[23] The cross section at 10.75 eV was determined by averaging over 10.675–10.825 eV. **(b)** Kinetics of vinyl alcohol measured at 10.75 eV. The vinyl alcohol yield in ion signal units was obtained by averaging over 50–80 ms. The vinyl alcohol yield in concentration units of [VA] = 6.4 x 10^{10} molc cm^{-3} was determined in reference to the known pre-photolysis concentration and cross section of ^{13}C ethene. These experiments were conducted with $[OH]_0$ = 4.0 x 10^{12} molc cm^{-3}, leading to a vinyl alcohol yield of 1.6%. The ion signal axis has been transformed to absolute concentration units.

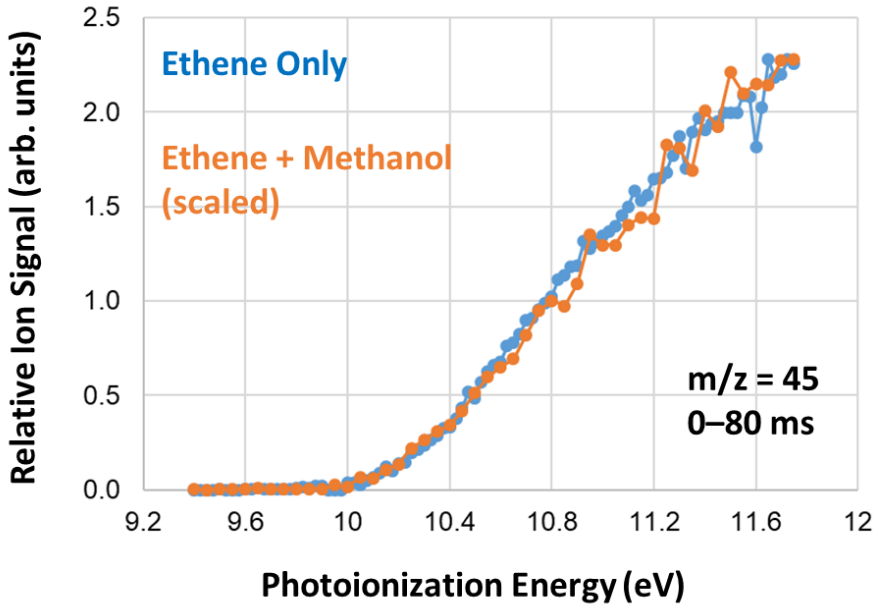

Figure 5: Relative photoionization efficiency curves of m/z = 45, integrated over 0–80 ms of reaction time after photolysis. The blue trace was collected with solely ethene as the hydrocarbon precursor and the initial peroxy radicals were all β-HEP. The orange trace was collected with a mixture of $[C_2H_4]$:$[CH_3OH]$ = 0.14:0.86 that yielded $[\beta\text{-HEP}]_0$:$[HO_2]_0$ = 0.52:0.48. The spectra are essentially identical, particularly up to 10.75 eV, suggesting that only one of either β-HEP or β-hydroxyethyl hydroperoxide is contributing to the ion signal. Based on the shape of the m/z = 45 kinetics, we conclude that only β-HEP contributes to the m/z = 45 ion signal at 10.75 eV.

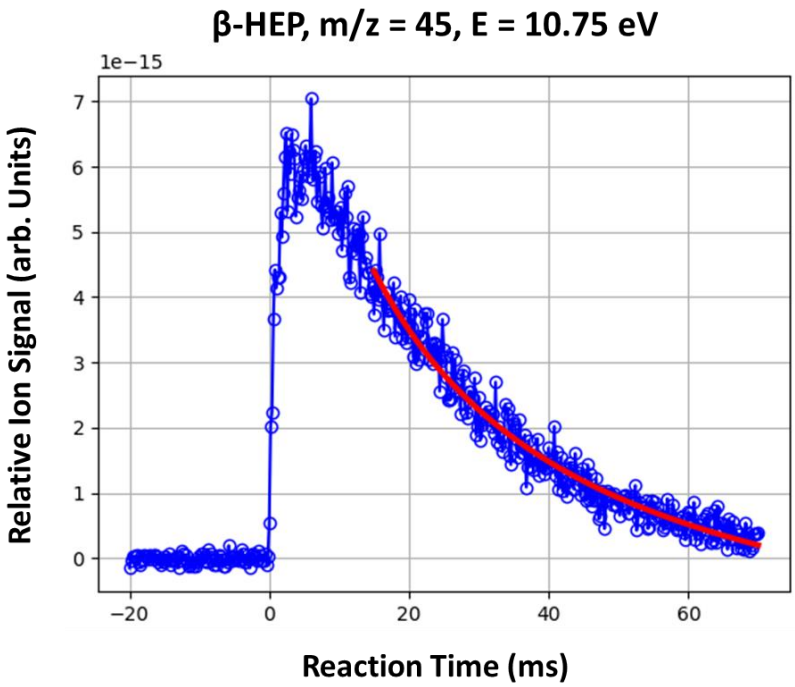

Figure 6: Representative time-resolved ion signal of β-HEP. Data (blue circles) was collected at [H_2O] = 2.8 x 10^{16} molc cm^{-3} and T = 3.6 °C (RH = 14%). A fit (red curve) was performed to Eqn. 2 (second order loss with baseline) to determine the bimolecular decay constant, which was divided by the calibrated initial radical concentration to determine k_{obs}. We began fits at 15 ms to avoid complications by the source chemistry and the temporal instrument response function.

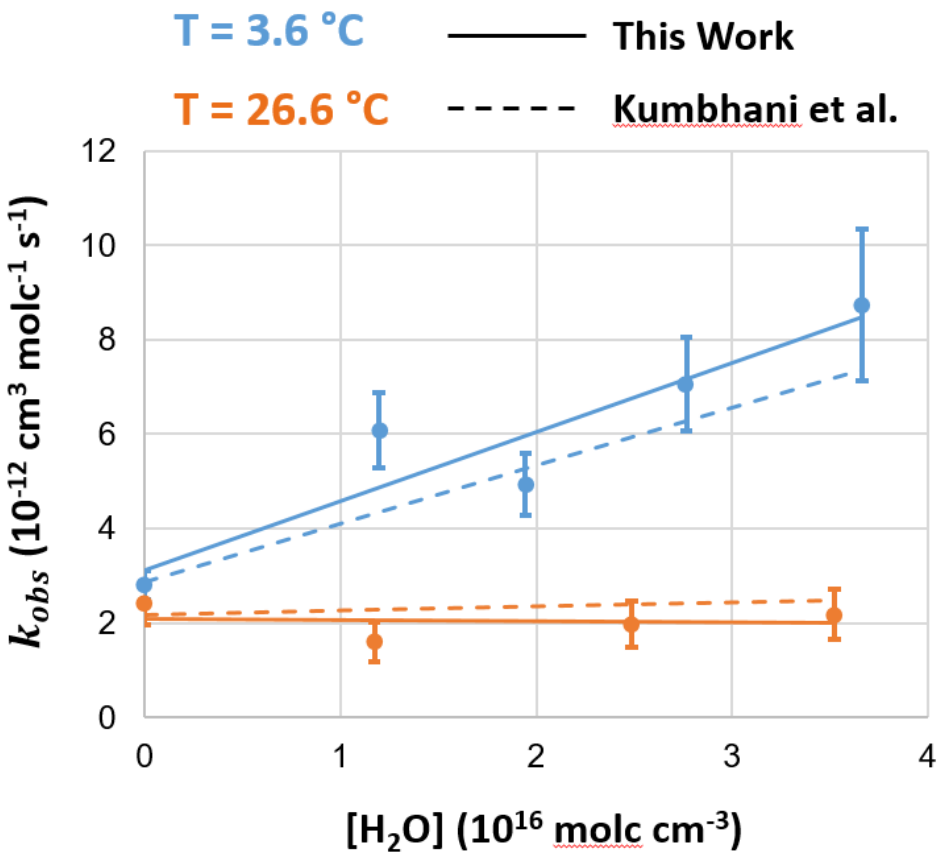

Figure 7: Values of k_{obs} measured in this work as a function of [H_2O] at temperatures of 3.6 and 26.6 °C. k_{obs} is insensitive to [H_2O] at 26.6 °C, but increases by a factor of ~3 between [H_2O] = 0 and 3.7 x 10^{16} molc cm^{-3} (RH = 18%) at 3.6 °C. Linear fits (solid lines) were performed to data collected at each temperature in accordance with Eqn. 3. The parameterization determined by Kumbhani et al.[1] is also plotted (dashed lines) and exhibits excellent agreement with our results, under the assumption that their definition of k_{obs} matches ours and encompasses loss of β-HEP by secondary HO_2.

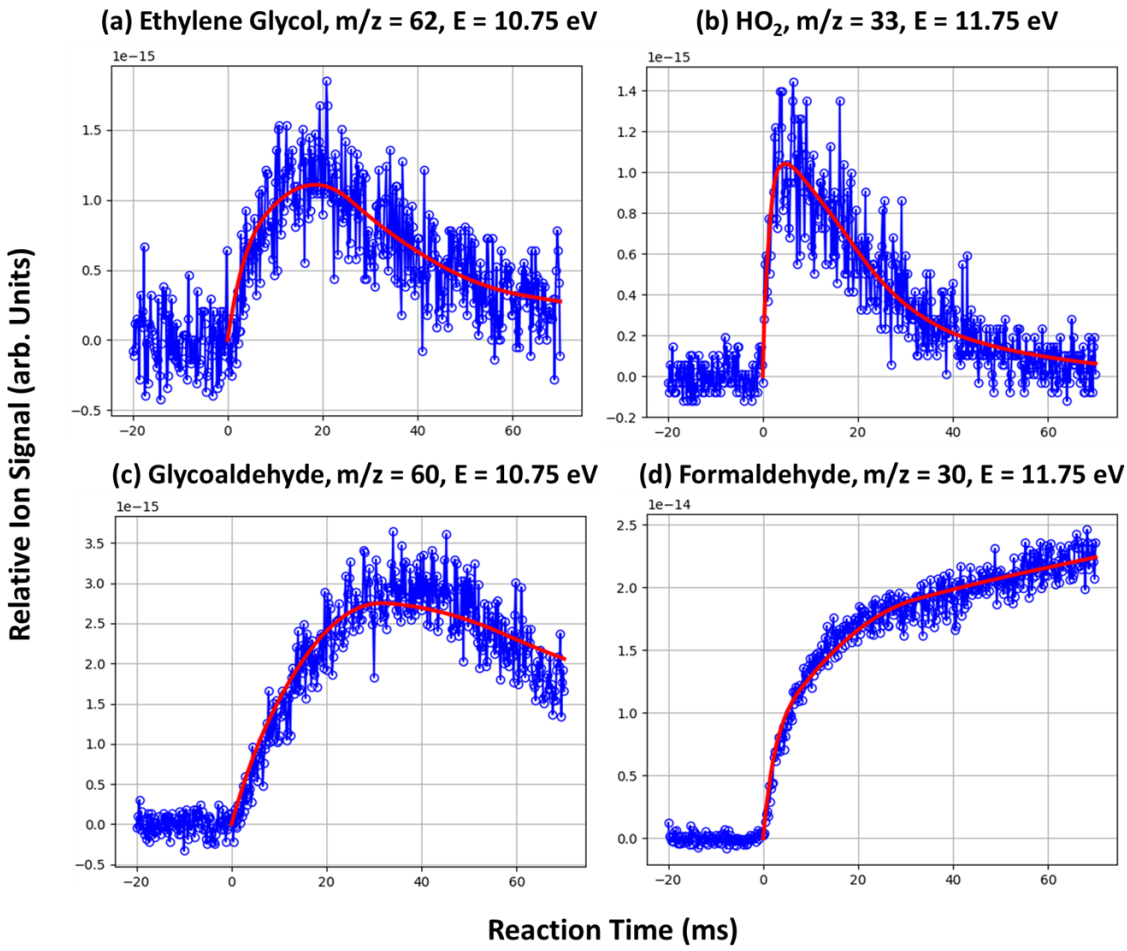

Figure 8: Representative time-resolved ion signals for the products of the β-HEP self reaction: **(a)** ethylene glycol, **(b)** HO_2, **(c)** glycoaldehyde, and **(d)** formaldehyde. Data (blue circles) was collected at $[H_2O]$ = 2.8 x 10^{16} molc cm^{-3} and T = 3.6 °C (RH = 14%). Fits (red curves) were performed through numerical integration of Eqn. 6 to determine the yield of each product from the self reaction expressed in ion signal units. The decays of ethylene glycol and glycoaldehyde at longer reaction times are attributed to heterogeneous wall loss, which was more prevalent at colder temperatures and greater relative humidity. The decay of HO_2 is attributed to its loss reactions (R7 and R8). The positive slope in the formaldehyde signal at longer reaction times arises from divergence of the photolysis laser beam and a gradient in the initial radical concentration; this effect is empirically captured by fitting a negative loss rate for this species.

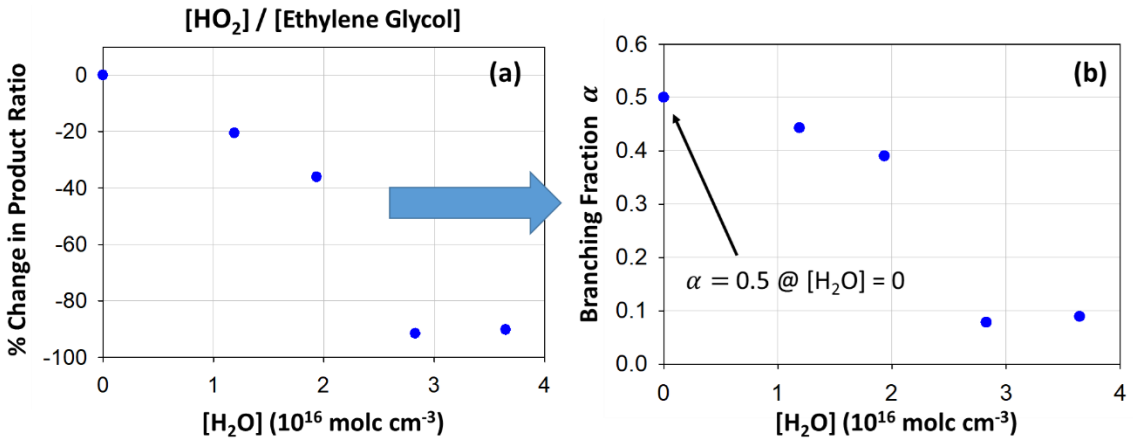

Figure 9: (a) Relative change in the HO_2 to ethylene glycol product yield ratio from the β-HEP self reaction at T = 3.6 °C. Calculated from the ratio of their yields expressed in ion signal units, relative to the $[H_2O] = 0$ case. The ratio decreased by ~90% over the range of $[H_2O]$ used in this work. **(b)** Measured values of the branching fraction to the radical propagating channel α as a function of $[H_2O]$ at T = 3.6 °C. Determined from the relative data in (a) and Eqn. 4 by assuming that α = 0.5 at $[H_2O] = 0$, as measured by Barnes et al.[25] Our results for α are therefore relative to the $[H_2O] = 0$ case. α decreases as additional water vapor is added indicating that the radical terminating channel of the self reaction is being enhanced relative to the radical propagating channel.

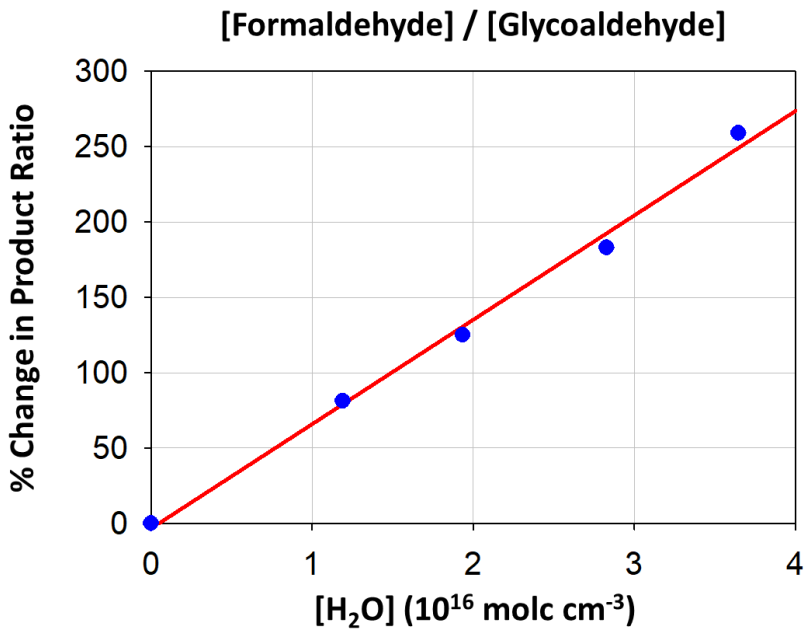

Figure 10: Relative change in the formaldehyde to glycoaldehyde product yield ratio from the β-HEP self reaction at T = 3.6 °C. Calculated from the ratio of their yields expressed in ion signal units, relative to the $[H_2O] = 0$ case. The ratio increased by ~250% over the range of $[H_2O]$ used in this work. The change in this ratio is partially influenced by the change in α, although correction for this effect is not straightforward since the absolute concentrations are unknown. Our data suggests that decomposition of the alkoxy radical is enhanced relative to its reaction with O_2 under humid conditions. The fitted trendline is empirical.

4.6 References

(1) Kumbhani, S. R.; Cline, T. S.; Killian, M. C.; Clark, J. M.; Keeton, W. J.; Hansen, L. D.; Shirts, R. B.; Robichaud, D. J.; Hansen, J. C. Water Vapor Enhancement of Rates of Peroxy Radical Reactions. *International Journal of Chemical Kinetics* **2015**, *47* (6), 395–409. https://doi.org/10.1002/kin.20917.

(2) Shirts, R. B.; Kumbhani, S. R.; Burrell, E.; Hansen, J. C. An Improved Model to Calculate Equilibrium Constants for Formation of Peroxy Radical–Water Complexes. *Theor Chem Acc* **2018**, *137* (7), 96. https://doi.org/10.1007/s00214-018-2262-8.

(3) English, A. M.; Hansen, J. C.; Szente, J. J.; Maricq, M. M. The Effects of Water Vapor on the CH3O2 Self-Reaction and Reaction with HO2. *J. Phys. Chem. A* **2008**, *112* (39), 9220–9228. https://doi.org/10.1021/jp800727a.

(4) Hamilton, E. J. Water Vapor Dependence of the Kinetics of the Self-reaction of HO2 in the Gas Phase. *J. Chem. Phys.* **1975**, *63* (8), 3682–3683. https://doi.org/10.1063/1.431772.

(5) DeMore, W. B. Reaction of Hydroperoxo Radicals with Ozone and the Effect of Water Vapor on Hydroperoxo Kinetics. *Journal of Physical Chemistry* **1979**, *83* (9), 1113–1118.

(6) Cox, R. A.; Burrows, J. P. Kinetics and Mechanism of the Disproportionation of Hydroperoxyl Radical in the Gas Phase. *Journal of Physical Chemistry* **1979**, *83* (20), 2560–2568.

(7) Sander, S. P.; Peterson, M.; Watson, R. T.; Patrick, R. Kinetics Studies of the Hydrogen Dioxide+ Hydrogen Dioxide and Deuterium Dioxide+ Deuterium Dioxide Reactions at 298 K. *The Journal of Physical Chemistry* **1982**, *86* (8), 1236–1240.

(8) Kircher, C. C.; Sander, S. P. Kinetics and Mechanism of Hydroperoxo and Hydroperoxo-d Disproportionations. *J. Phys. Chem.* **1984**, *88* (10), 2082–2091. https://doi.org/10.1021/j150654a029.

(9) Stone, D.; Rowley, D. M. Kinetics of the Gas Phase HO2 Self-Reaction: Effects of Temperature, Pressure, Water and Methanol Vapours. *Phys. Chem. Chem. Phys.* **2005**, *7* (10), 2156–2163. https://doi.org/10.1039/B502673C.

(10) Kanno, N.; Tonokura, K.; Koshi, M. Equilibrium Constant of the HO2-H2O Complex Formation and Kinetics of HO2 + HO2-H2O: Implications for Tropospheric Chemistry. *Journal of Geophysical Research: Atmospheres* **2006**, *111* (D20). https://doi.org/10.1029/2005JD006805.

(11) Orlando, J. J.; Tyndall, G. S.; Bilde, M.; Ferronato, C.; Wallington, T. J.; Vereecken, L.; Peeters, J. Laboratory and Theoretical Study of the Oxy Radicals in the OH- and Cl-Initiated Oxidation of Ethene. *J. Phys. Chem. A* **1998**, *102* (42), 8116–8123. https://doi.org/10.1021/jp981937d.

(12) Osborn, D. L.; Zou, P.; Johnsen, H.; Hayden, C. C.; Taatjes, C. A.; Knyazev, V. D.; North, S. W.; Peterka, D. S.; Ahmed, M.; Leone, S. R. The Multiplexed Chemical Kinetic Photoionization Mass Spectrometer: A New Approach to Isomer-Resolved Chemical Kinetics. *Review of Scientific Instruments* **2008**, *79* (10), 104103. https://doi.org/10.1063/1.3000004.

(13) Taatjes, C. A.; Hansen, N.; Osborn, D. L.; Kohse-Höinghaus, K.; Cool, T. A.; Westmoreland, P. R. "Imaging" Combustion Chemistry via Multiplexed Synchrotron-Photoionization Mass Spectrometry. *Phys. Chem. Chem. Phys.* **2008**, *10* (1), 20–34. https://doi.org/10.1039/B713460F.

(14) Beutler, H. Über Absorptionsserien von Argon, Krypton und Xenon zu Termen zwischen den beiden Ionisierungsgrenzen2P32/0und2P12/0. *Z. Physik* **1935**, *93* (3), 177–196. https://doi.org/10.1007/BF01365116.

(15) Assaf, E.; Fittschen, C. Cross Section of OH Radical Overtone Transition near 7028 Cm–1 and Measurement of the Rate Constant of the Reaction of OH with HO2 Radicals. *J. Phys. Chem. A* **2016**, *120* (36), 7051–7059. https://doi.org/10.1021/acs.jpca.6b06477.

(16) Dodson, L. G.; Shen, L.; Savee, J. D.; Eddingsaas, N. C.; Welz, O.; Taatjes, C. A.; Osborn, D. L.; Sander, S. P.; Okumura, M. VUV Photoionization Cross Sections of HO2, H2O2, and H2CO. *J. Phys. Chem. A* **2015**, *119* (8), 1279–1291. https://doi.org/10.1021/jp508942a.

(17) Person, J. C.; Nicole, P. P. *ANL Radiological Physics Division Annual Report*; ANL-7760; 1970; p 97.

(18) Savee, J. D.; Soorkia, S.; Welz, O.; Selby, T. M.; Taatjes, C. A.; Osborn, D. L. Absolute Photoionization Cross-Section of the Propargyl Radical. *J. Chem. Phys.* **2012**, *136* (13), 134307. https://doi.org/10.1063/1.3698282.

(19) Hui, A. O. A. Y. Atmospheric Peroxy Radical Chemistry Studied by Infrared Kinetic Spectroscopy. phd, California Institute of Technology, 2019. https://doi.org/Hui, Aileen Oyama Ah Yee (2019) Atmospheric Peroxy Radical Chemistry Studied by Infrared Kinetic Spectroscopy. Dissertation (Ph.D.), California Institute of Technology. doi:10.7907/Z9H0-1H20. http://resolver.caltech.edu/CaltechTHESIS:01172019-135430092 <http://resolver.caltech.edu/CaltechTHESIS:01172019-135430092>.

(20) L. Dodson. Thesis, California Institute of Technology, 2016.

(21) Burkholder, J. B.; Sander, S. P.; Abbatt, J. P. D.; Barker, J. R.; Huie, R. E.; Kolb, C. E.; Kurylo, M. J.; Orkin, V. L.; Wilmouth, D. M.; Wine, P. H. *Chemical Kinetics and Photochemical Data for Use in Atmospheric Studies: Evaluation Number 18*; Pasadena, CA: Jet Propulsion Laboratory, National Aeronautics and Space …, 2015.

(22) Zádor, J.; Fernandes, R. X.; Georgievskii, Y.; Meloni, G.; Taatjes, C. A.; Miller, J. A. The Reaction of Hydroxyethyl Radicals with O2: A Theoretical Analysis and Experimental Product Study. *Proceedings of the Combustion Institute* **2009**, *32* (1), 271–277. https://doi.org/10.1016/j.proci.2008.05.020.

(23) R. Caravan; D.L. Osborn. Private Communication.

(24) Meloni, G.; Zou, P.; Klippenstein, S. J.; Ahmed, M.; Leone, S. R.; Taatjes, C. A.; Osborn, D. L. Energy-Resolved Photoionization of Alkylperoxy Radicals and the Stability of Their Cations. *J. Am. Chem. Soc.* **2006**, *128* (41), 13559–13567. https://doi.org/10.1021/ja064556j.

(25) Barnes, I.; Becker, K. H.; Ruppert, L. FTIR Product Study of the Self-Reaction of β-Hydroxyethl Peroxy Radicals. *Chemical Physics Letters* **1993**, *203* (2), 295–301. https://doi.org/10.1016/0009-2614(93)85404-C.

This page intentionally left blank.

Appendix A

Implementation of Simultaneous Kinetics and Ringdown

For several of the cavity ringdown spectroscopy (CRDS) experiments described in Chapter 3 (3.3.1 and 3.3.3), kinetic processes occurred with time constants comparable to the lifetime of a photon within the cavity. To determine rate constants for these reactions, data was collected and analyzed using the Simultaneous Kinetics and Ringdown (SKaR) technique published by Brown et al.[1] The original SKaR paper assumes that the delay time between the photolysis (initiates radical chemistry) and probe (initiates a cavity ringdown decay) laser pulses is fixed at zero. In this Appendix, we show that a ringdown ratio constructed using many arbitrary delay times is equivalent to a ringdown ratio acquired with a delay time fixed at zero. This modified approach has a variety of advantages that will be discussed and was used in all SKaR experiments described in Chapter 3.

The SKaR technique is typically used with vacuum cavity ringdown times that exceed kinetic lifetimes to ensure that an entire kinetic trace can be captured within a single ringdown event. The probe laser beam is injected into the optical cavity when photolysis occurs so that all kinetic information can be observed during a single cavity decay. After many ringdown times, the signal to noise decreases substantially as intracavity power drops. When the ratio of the ringdown with kinetics is taken to the reference ringdown, the noise propagates as two noisy signals are divided. This sets a limit on the usable time range in SKaR. If the empty cavity ringdown time exceeds the kinetic lifetime, then the usable time range is often sufficient to extract a precise rate coefficient so long as one properly weights the fit to the ringdown ratio. However, achieving long ringdown times requires either a long cavity length or very high reflectivity mirrors that may be expensive or impractical to implement. One can envision an experiment in which the empty cavity ringdown time is shorter than the kinetic lifetime making the ringdown ratio too noisy to precisely extract a rate coefficient, but the ringdown with kinetics is still nonexponential.

Here, we show that by acquiring ringdown ratios at multiple delay times between the probe and photolysis lasers, one can construct a single ratio function that exhibits high signal to noise across an arbitrary number of empty cavity ringdown times. This ratio can

be fit to extract an extremely precise rate coefficient, alleviating any concerns about whether the empty cavity ringdown time is long enough to implement the SKaR technique.

Let t represent the time since photolysis was initiated (the start of kinetics) and let t_d represent the time at which the probe beam is injected into the optical cavity. Then the intensity of the ringdown acquired during a kinetic event is defined for $t \geq t_d$ by:

$$I_{on}(t) = I_{0,on} \exp\left[\frac{-c}{d}\int_{t_d}^{t} A(t')dt' - \frac{(t-t_d)}{\tau_0}\right] \quad \text{(Eqn. 1)}$$

where $I_{0,on}$ is the intensity of the ringdown at $t = t_d$, c is the speed of light, d is the distance between the cavity mirrors, τ_0 is the ringdown time in the absence of photolysis, and $A(t)$ is a function defined for $t \geq 0$ that describes absorbance at the probe wavelength after the start of kinetics. If $A(t)$ is approximately constant between t_d and a value of t by which $I_{on}(t)$ is dominated by noise, then Eqn. 1 reduces to the traditional exponential decay for a cavity with static absorbance A:

$$I_{on}(t) = I_{0,on} \exp\left[-\left(\frac{c}{d}A + \frac{1}{\tau_0}\right)(t-t_d)\right] \quad \text{(Eqn. 2)}$$

The intensity of the ringdown acquired without photolysis is defined for $t \geq t_d$ by:

$$I_{off}(t) = I_{0,off} \exp\left[-\frac{(t-t_d)}{\tau_0}\right] \quad \text{(Eqn. 3)}$$

where $I_{0,off}$ is the intensity of the ringdown at $t = t_d$. Taking the ratio of Eqn. 1 to Eqn. 3 gives the following ratio function defined for $t \geq t_d$:

$$R(t) = \frac{I_{on}(t)}{I_{off}(t)} = \frac{I_{0,on}}{I_{0,off}} \exp\left[\frac{-c}{d}\int_{t_d}^{t} A(t')dt'\right] \quad \text{(Eqn. 4)}$$

For the case that $t_d = 0$, the derivation shown thus far reduces to that presented in the original SKaR paper.[1]

Now consider that one has measured a set of ringdown ratios $\{R_i(t)\}$ with corresponding delay times $\{t_{d_i}\}$. $R_i(t)$ is defined for $t \geq t_{d_i}$ by:

$$R_i(t) = \left(\frac{I_{0,on}}{I_{0,off}}\right)_i \exp\left[\frac{-c}{d}\int_{t_{d_i}}^{t} A(t')dt'\right] \quad \text{(Eqn. 5)}$$

Without loss of generality, the sets can be reordered after collection such that $\{t_{d_i}\}$ is monotonically increasing. We show that the ratio of the ringdown ratio at any arbitrary

delay time to the ringdown ratio at the earliest delay time is a constant defined for $t \geq t_{d_i}$:

$$\frac{R_i(t)}{R_1(t)} = \frac{\left(\frac{I_{0,on}}{I_{0,off}}\right)_i \exp\left[\frac{-c}{d}\int_{t_{d_i}}^{t} A(t')dt'\right]}{\left(\frac{I_{0,on}}{I_{0,off}}\right)_1 \exp\left[\frac{-c}{d}\int_{t_{d_1}}^{t} A(t')dt'\right]} \qquad \text{(Eqn. 6)}$$

$$= \left[\frac{\left(\frac{I_{0,on}}{I_{0,off}}\right)_i}{\left(\frac{I_{0,on}}{I_{0,off}}\right)_1}\right] \exp\left[\frac{-c}{d}\left(\int_{t_{d_i}}^{t} A(t')dt' - \int_{t_{d_1}}^{t} A(t')dt'\right)\right]$$

$$= \left[\frac{\left(\frac{I_{0,on}}{I_{0,off}}\right)_i}{\left(\frac{I_{0,on}}{I_{0,off}}\right)_1}\right] \exp\left[\frac{-c}{d}\left(\int_{t_{d_i}}^{t} A(t')dt' - \int_{t_{d_1}}^{t_{d_i}} A(t')dt' - \int_{t_{d_i}}^{t} A(t')dt'\right)\right]$$

$$= \left[\frac{\left(\frac{I_{0,on}}{I_{0,off}}\right)_i}{\left(\frac{I_{0,on}}{I_{0,off}}\right)_1}\right] \exp\left[\frac{c}{d}\int_{t_{d_1}}^{t_{d_i}} A(t')dt'\right]$$

$$= C_i$$

since $t_{d_i} \geq t_{d_1}$. C_i is a constant independent of time. Therefore, a ringdown ratio measured at any arbitrary delay time differs from the ringdown ratio measured at the earliest delay time by two constant factors: (1) the initial intensities of the ringdowns and (2) how the absorbance has evolved between the two delay times.

The function $R_1(t)$ can be determined not only by direct measurement at t_{d_1} but can also be constructed iteratively via measurements of $\{R_i(t)\}$:

$$R_1(t) = \left\{ \begin{array}{ll} R_1^m(t) & \text{for} \quad t \geq t_{d_1} \\ \text{then} \quad \text{avg}\left(R_1(t), \frac{R_2^m(t)}{C_2}\right) & \text{for} \quad t \geq t_{d_2} \\ \ldots & \\ \text{then} \quad \text{avg}\left(R_1(t), \frac{R_n^m(t)}{C_n}\right) & \text{for} \quad t \geq t_{d_n} \end{array} \right\} \qquad \text{(Eqn. 7)}$$

where $R_i^m(t)$ denotes the measurement of the ringdown ratio at t_{d_i} (as opposed to its analytical expression) and n is the total number of ringdown ratios measured. The values

of C_i are determined sequentially as $R_1(t)$ is constructed, through a linear least squares optimization of

$$R_i^m(t) = C_i R_1(t) \qquad \text{(Eqn. 8)}$$

over $t \geq t_{d_i}$. That is, we first construct $R_1(t)$ for $t \geq t_{d_1}$. C_2 is then computed through a fit to Eqn. 8. Next, $R_1(t)$ for $t \geq t_{d_2}$ is updated using C_2 in Eqn. 7. This process is repeated for computing C_3 and updating $R_1(t)$ for $t \geq t_{d_3}$ and so on until all ringdown ratios have been integrated into the construction of $R_1(t)$. At each step the averaging is variance-weighted to ensure that every point in $R_1(t)$ is biased toward the ringdown ratio with the least uncertainty.

A variance-weighted fit of the constructed $R_1(t)$ to Eqn. 5 yields a precise rate coefficient for the kinetic process under study. The proposed method improves upon the original SKaR technique by taking advantage of the high signal to noise exhibited by $R_i(t)$ immediately after t_{d_i}. By measuring ringdown ratios across delay times that span several kinetic lifetimes, and which have sufficiently narrow spacing between the delays, a ringdown ratio is constructed that has excellent signal to noise across the entire kinetic timescale. This approach has two main advantages over simply averaging a large number of ringdown ratios at a single delay time: (1) Transient digitizers have a fixed number of bits which dictate the maximum precision of the A/D conversion. After a certain amount of averaging, there will be no improvements to the signal to noise of a ringdown because the limit of the transient digitizer has been reached. (2) Averaging at a single delay time results in a ringdown ratio that has the least uncertainty at early times and the greatest uncertainty at long times. Fits will therefore be biased toward changes in absorbance that occur near the beginning of a kinetic event, immediately after photolysis. The modified method creates a ringdown ratio with nearly uniform signal to noise at all times, and therefore the fit will unbiasedly represent the entire kinetic timescale. In conclusion, the modified method allows SKaR to be utilized in experiments where the ringdown time is shorter than the kinetic lifetime, but the ringdown with kinetics is still nonexponential.

(1) Brown, S. S.; Ravishankara, A. R.; Stark, H. Simultaneous Kinetics and Ring-down: Rate Coefficients from Single Cavity Loss Temporal Profiles. *J. Phys. Chem. A* **2000**, *104* (37), 8600–8600. https://doi.org/10.1021/jp002646j.

Appendix B

Kinetics and Spectroscopy of the Acetonyl Peroxy Radical

B.1 Preliminary Study

Experiments were conducted investigating the self reaction kinetics and near-IR $\tilde{A} \leftarrow \tilde{X}$ spectrum of the acetonyl peroxy radical. These measurements were performed using the pulsed cavity ringdown spectrometer described in Chapter 3. A gaseous mixture of acetone (1.1×10^{16} molc cm^{-3}), Cl_2 (5.8×10^{16} molc cm^{-3}), N_2 (47%), and O_2 (51%), was flown through the reactor at P = 100 Torr and room temperature (T ≈ 296 K). Free radical chemistry was initiated by a 351 nm excimer laser pulse, which photodissociated Cl_2 to yield Cl radicals. The initial radical concentration was not calibrated in this work, but we typically generated $[Cl]_0 \approx 10^{14}$ atoms cm^{-3} under comparable conditions.

Acetone is oxidized by Cl to generate an acetonyl radical, which associates with O_2 to form the acetonyl peroxy radical:

$$Cl + CH_3C(O)CH_3 \rightarrow CH_3C(O)CH_2 + HCl \quad (R1)$$

$$CH_3C(O)CH_2 + O_2 + M \rightarrow CH_3C(O)CH_2O_2 + M \quad (R2)$$

The dominant loss of acetonyl peroxy is through its self reaction:

$$CH_3C(O)CH_2O_2 + CH_3C(O)CH_2O_2 \rightarrow CH_3C(O)CH_2OH + CH_3C(O)CHO + O_2 \quad (R3a)$$

$$\rightarrow CH_3C(O)CH_2O + CH_3C(O)CH_2O + O_2 \quad (R3b)$$

$$\rightarrow CH_3C(O)CH_2OOCH_2C(O)CH_3 + O_2 \quad (R3c)$$

R3a terminates radical chemistry and yields stable products hydroxyacetone and methyl glyoxal. R3b propagates radical chemistry by producing alkoxy radicals, which will be discussed in greater detail below. It has historically been assumed that the accretion product (ROOR) of organic peroxy radical self reactions has negligible yield. However, a recent study of R3c measured a large ROOR yield of ~16% in acetone oxidation.[1] ROOR may be the unidentified species contributing to an elusive mystery absorption in the visible region observed in prior studies of the acetonyl peroxy self reaction.[2]

The alkoxy radical from R3b can react with O_2 (R4) or decompose (R5):

$$CH_3C(O)CH_2O + O_2 \rightarrow CH_3C(O)CHO + HO_2 \quad (R4)$$

$$CH_3C(O)CH_2O\ (+\ M) \rightarrow CH_3C(O) + HCHO\ (+\ M) \qquad (R5)$$

The HO_2 from R4 can cross react with acetonyl peroxy and complicates the interpretation of the acetonyl peroxy self reaction kinetics, since the decay is not solely due to R3. The acetyl radical yielded by R5 will typically associate with O_2 to form the acetyl peroxy radical, $CH_3C(O)O_2$. This species can also cross react with acetonyl peroxy, as well as cross react with HO_2 or self react. One of the products of each of these reactions is another alkoxy radical, $CH_3C(O)O$, which decomposes to form methyl radicals, CH_3. The methyl radicals associate with O_2 to form methyl peroxy, CH_3O_2, adding yet another peroxy radical the mixture.

In Figure 1, we present spectra of the reactive mixture acquired 140 μs and 3 ms after photolysis over 7260–7950 cm^{-1}. Immediately apparent is that the 3 ms spectrum strongly resembles the known spectrum of pure methyl peroxy.[3,4] There is essentially no evidence of another absorber, suggesting that acetonyl peroxy has mostly reacted away by 3 ms. (We cannot assess the presence of HO_2 or acetyl peroxy since the known spectra of these species do not have appreciable absorption over the probed frequency range.[5,6]) In contrast, the 140 μs spectrum demonstrates absorption arising from a mixture of methyl peroxy and a second peroxy radical, which we assume to be acetonyl peroxy. The fast formation of methyl peroxy by 140 μs is surprising given that it is a *third generation* peroxy radical according to the established mechanism described above. Our results suggest that there may be a prompt source of methyl radicals not currently taken into account by the prevailing acetone oxidation mechanism; we recommend that this possibility be explored in future studies.

To our knowledge, the 140 μs spectrum represents the first measurement of the near-IR $\tilde{A} \leftarrow \tilde{X}$ spectrum of the acetonyl peroxy radical. Unfortunately, it is not a spectrum of solely acetonyl peroxy, since the sharp features around 7383 and 7488 cm^{-1} perfectly match the frequencies of sharp features in the known methyl peroxy spectrum.[3,4] Nevertheless, we attribute the majority of the absorption to acetonyl peroxy. The broad features are typical for the spectra of larger organic peroxy radicals.

We chose to measure the spectrum of the acetonyl peroxy radical at 140 μs due to the results of kinetics modeling that indicated the acetonyl peroxy concentration would peak around this reaction time. However, for the spectra of other organic peroxy radicals

(see Chapter 3), we have previously opted to measure their pure spectra at 10 μs, which is typically after formation is complete but before any appreciable loss. For acetonyl peroxy, this was not feasible due to the slow rate constant of R1 (k_1 = 2.1 x 10^{-12} cm^3 $molc^{-1}$ s^{-1} at 298 K)[7], which limited the rate of peroxy radical formation ($\tau \approx 45$ μs). Future experiments to determine a spectrum of pure acetonyl peroxy, without interference from the products of its self reaction (i.e. methyl peroxy), are advised. We recommend two possible strategies: (1) Increase the acetone concentration to speed up the rate of R1. In this preliminary study, we prepared a tank of acetone diluted in N_2. The acetone concentration in the reactor was therefore limited by the amount of acetone vapor we could get into the tank. Alternatively, a bubbler of acetone with N_2 carrier flow could be used to introduce acetone to the reactor. A greater acetone concentration can likely be achieved with a bubbler, although the precise concentration will have greater uncertainty. (2) Reduce the radical concentration and increase the signal averaging. While this method will not speed up R1, the loss of acetonyl peroxy will slow down, and therefore it may be possible to acquire a pure spectrum prior to the production of methyl peroxy. Signal-to-noise will act as the chief limitation to this approach.

In Figure 2, we present time-resolved absorption signals recorded at 7421 and 7489 cm^{-1} over 0–10 ms. 7421 cm^{-1} is approximately located at the peak of the acetonyl peroxy spectrum and on the shoulder of a methyl peroxy band. 7489 cm^{-1} is approximately located on the shoulder of the broad acetonyl peroxy band and at the peak of a methyl peroxy band. The kinetics reflect the trends we expect from the spectra: both signals decay due to the loss of acetonyl peroxy, but the signal at 7489 cm^{-1} is longer-lived due to the greater intensity of methyl peroxy absorption at this frequency. Unfortunately, a more quantitative analysis of the acetonyl and methyl peroxy kinetics is not possible from this data alone. To elucidate the kinetics of an individual peroxy radical, future experiments should acquire reactive spectra at many more delay times. These spectra could then be fit as a linear combination of pure acetonyl and methyl peroxy spectra to separate the contributions and kinetics of each species. Due to the distinct shapes of the pure spectra and large amount of methyl peroxy, this analysis will likely have greater success than the similar analysis attempted in Chapter 3.

(1) Berndt, T.; Scholz, W.; Mentler, B.; Fischer, L.; Herrmann, H.; Kulmala, M.; Hansel, A. Accretion Product Formation from Self- and Cross-Reactions of RO2 Radicals in the Atmosphere. *Angewandte Chemie International Edition* **2018**, *57* (14), 3820–3824. https://doi.org/10.1002/anie.201710989.

(2) Hui, A. O. A. Y. Atmospheric Peroxy Radical Chemistry Studied by Infrared Kinetic Spectroscopy. phd, California Institute of Technology, 2019. https://doi.org/Hui, Aileen Oyama Ah Yee (2019) Atmospheric Peroxy Radical Chemistry Studied by Infrared Kinetic Spectroscopy. Dissertation (Ph.D.), California Institute of Technology. doi:10.7907/Z9H0-1H20. http://resolver.caltech.edu/CaltechTHESIS:01172019-135430092 <http://resolver.caltech.edu/CaltechTHESIS:01172019-135430092>.

(3) Pushkarsky, M. B.; Zalyubovsky, S. J.; Miller, T. A. Detection and Characterization of Alkyl Peroxy Radicals Using Cavity Ringdown Spectroscopy. *The Journal of Chemical Physics* **2000**, *112* (24).

(4) Chung, C.-Y.; Cheng, C.-W.; Lee, Y.-P.; Liao, H.-Y.; Sharp, E. N.; Rupper, P.; Miller, T. A. Rovibronic Bands of the Ã←X̃ Transition of CH3OO and CD3OO Detected with Cavity Ringdown Absorption near 1.2–1.4μm. *J. Chem. Phys.* **2007**, *127* (4), 044311. https://doi.org/10.1063/1.2747616.

(5) Fink, E. H.; Ramsay, D. A. High-Resolution Study of TheÃ2A′ → X2A″ Transition of HO2: Analysis of the 000–000 Band. *Journal of Molecular Spectroscopy* **1997**, *185* (2), 304–324. https://doi.org/10.1006/jmsp.1997.7401.

(6) Zalyubovsky, S. J.; Glover, B. G.; Miller, T. A. Cavity Ringdown Spectroscopy of the Ã − X̃ Electronic Transition of the CH3C(O)O2 Radical. *J. Phys. Chem. A* **2003**, *107* (39), 7704–7712. https://doi.org/10.1021/jp0305279.

(7) Burkholder, J. B.; Sander, S. P.; Abbatt, J. P. D.; Barker, J. R.; Huie, R. E.; Kolb, C. E.; Kurylo, M. J.; Orkin, V. L.; Wilmouth, D. M.; Wine, P. H. *Chemical Kinetics and Photochemical Data for Use in Atmospheric Studies: Evaluation Number 18*; Pasadena, CA: Jet Propulsion Laboratory, National Aeronautics and Space …, 2015.

B.2 Figures

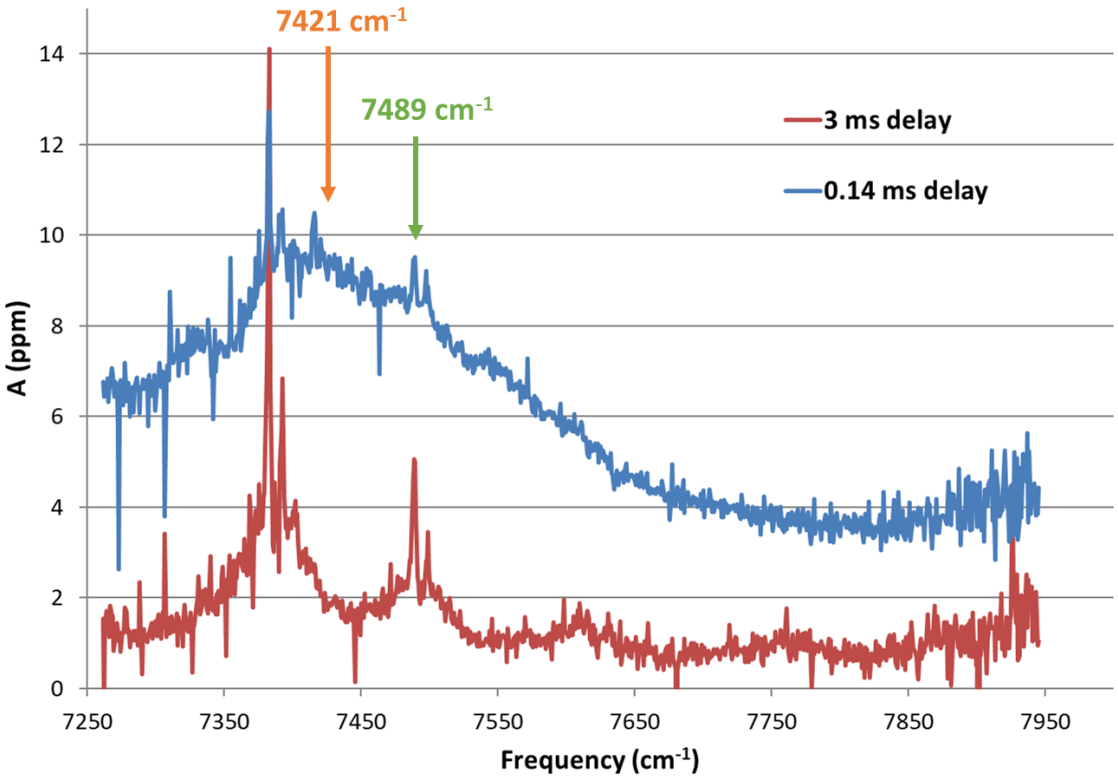

Figure 1: Near-IR absorption spectra of the reactive mixture formed upon acetone oxidation. Spectra were recorded at reaction times of 140 μs (blue) and 3 ms (red). The 140 μs spectrum represents a mixture of acetonyl and methyl peroxy. The 3 ms spectrum represents almost exclusively methyl peroxy. The frequencies used in the kinetic measurements are labeled.

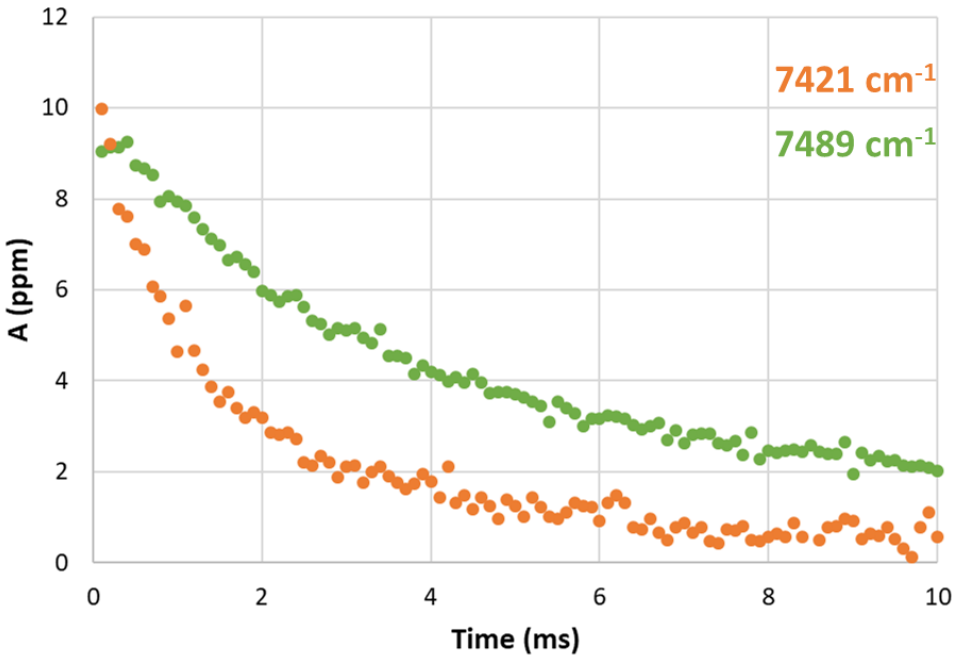

Figure 2: Time-resolved absorption signals recorded at 7421 (orange) and 7489 (green) cm^{-1} following the oxidation of acetone. The decays reflect the self reaction of acetonyl peroxy. The longer lifetime of the 7489 cm^{-1} signal is consistent with the greater intensity of methyl peroxy absorption at this frequency.

Appendix C

Photoionization Cross Sections of Some Atmospheric Molecules

The absolute photoionization spectra of ozone and glycoaldehyde have been measured in reference to the known photoionization cross sections of xenon and propene, respectively. This work was conducted using multiplexed synchrotron photoionization mass spectrometry (MPIMS).[1,2] The measurements and analysis were similar to those described in Chapter 2 to determine the absolute photoionization spectrum of methyl bromide. The unknown cross sections of a compound ("unk") were determined from the known cross sections of the reference compound ("ref") by the ratio of their ion signals:[3]

$$\sigma_{\mathrm{unk}}(E) = \sigma_{\mathrm{ref}}(E) \cdot \frac{\alpha_{\mathrm{ref}} f_{\mathrm{ref}}}{\alpha_{\mathrm{unk}} f_{\mathrm{unk}}} \cdot \frac{N_{\mathrm{ref}}}{N_{\mathrm{unk}}} \cdot \frac{S_{\mathrm{unk}}(E)}{S_{\mathrm{ref}}(E)} \qquad \text{(Eqn. 1)}$$

$\sigma_i(E)$ is the absolute photoionization cross section. We only tabulate partial cross sections to form parent cations of the neutral in this work. While approximate partial cross sections to form daughter ions of glycoaldehyde will be discussed, these may not be reproducible due to a potential dependence of relative daughter ion collection efficiency on alignment of the ion optics. α_i is the mass discrimination factor specific to the mass of the detected ion (m_i) and can be empirically described by a power law function: $\alpha_i = m_i^{\beta}$. The value of β was determined in experiments similar to those described in Chapter 2 and in a previous publication.[3] N_i is the concentration of the species in the reactor, f_i is the fractional abundance of the detected isotope, and S_i is the measured ion signal. S_i was integrated across the entire 0–150 ms observation timescale since the concentrations of the target and reference species were time-independent.

C.1 Ozone

The absolute photoionization cross sections of ozone were determined in reference to the known cross sections of xenon.[4] The literature cross sections are reported to have an accuracy of ±3%, which we assume to represent ±2 standard error. To introduce xenon to the reactor, we prepared a tank of xenon diluted in helium. The absolute xenon concentration was determined from the tank mixing ratio, flow rates, and reactor pressure.

To introduce ozone to the reactor, we followed an approach similar to that described in Chapter 2. Ozone was generated by flowing oxygen through a commercial ozonizer employing a corona discharge. Most of the O_2/O_3 flow was sent to exhaust while a portion was routed through an absorption cell upstream of the gas mixing region. The absolute ozone concentration was measured using a Hg pen-ray lamp and PMT detector to monitor its 254 nm absorption. Experiment was conducted at room temperature and 8 Torr.

We scanned the photoionization energy and measured ion counts of xenon and ozone over 12.022–14.222 eV with 25 meV steps. The measured xenon and ozone signals were interpolated onto five single energies where σ_{xenon} has been previously determined: 13.436, 13.600, 13.800, 14.000, and 14.200 eV.[4] At each of these single energies, σ_{ozone} was calculated in reference to σ_{xenon} using Eqn. 1. The results are presented in Table 1. Our analysis used the all ^{16}O isotope of ozone (m/z = 48) and the most abundant ^{132}Xe isotope of xenon (m/z = 132). Additional xenon isotopes could have been included to reduce random error, although this was not the limiting factor to the overall uncertainty of σ_{ozone}, as will be discussed below.

The shape of the relative photoionization spectrum of ozone was determined by normalizing the ion counts measured at each energy to the relative VUV photon flux recorded by a SXUV photodiode. We acquired an absolute photoionization spectrum through scaling the relative spectrum by the optimal fitted scale factor between relative ion signal and the five single energy values of σ_{ozone} discussed above. The absolute photoionization spectrum of ozone determined in this work is presented in Figure 1 and tabulated in Table 2. The single energy values of σ_{ozone} are also plotted. We note that the shape of this spectrum is normalized to the photodiode response, although the single energy cross sections are directly referenced to the literature σ_{xenon} and do not depend on the photodiode measurements.

The error budget on the single energy values of σ_{ozone} is also presented in Table 1. The uncertainty was partitioned into four categories: random error associated with the Poisson ion counting statistics, mass discrimination error associated with uncertainty on β, uncertainty associated with the absolute concentrations of xenon and ozone, and the estimated accuracy of the literature σ_{xenon}. The relative standard errors from each category can be added in quadrature to give the total relative standard error on a cross section. The

total uncertainty was typically ±7.9% (±2σ) for the single energy σ_{ozone}. Uncertainty on the absolute spectrum was slightly greater due to additional random error from each scaled point. As the error budget shows, the greatest source of uncertainty was not from the reference σ_{xenon}, but rather from the absolute concentrations. Nevertheless, the relative error associated with this category was still quite low (±6.5%, ±2σ).

C.2 Glycoaldehyde

The absolute photoionization cross sections of glycoaldehyde were determined in reference to the known cross sections of propene.[5] The literature cross sections are estimated to have an accuracy of ±20% (±2σ). To introduce propene to the reactor, we prepared a tank of propene diluted in helium. The absolute propene concentration was determined from the tank mixing ratio, flow rates, and reactor pressure. Glycoaldehyde was introduced to the reactor by flowing helium carrier gas through a bubbler containing a solid mixture of sand and glycoaldehyde dimer. The bubbler was heated in a bath held at 30 °C to promote sublimation. (This approach is similar to that described in Chapter 4 for hydrogen peroxide.) The glycoaldehyde / helium flow was routed through an absorption cell upstream of the gas mixing region. The absolute glycoaldehyde concentration was measured using a Hg pen-ray lamp and PMT detector to monitor its 185 nm absorption. Experiments were conducted at room temperature and 10 Torr.

We scanned the photoionization energy and measured ion counts of glycoaldehyde (all ^{12}C, m/z = 60) and propene (one ^{13}C, m/z = 43) over 9.662–11.512 eV in 25 meV steps. At each energy, $\sigma_{glycoaldehyde}$ was determined in reference to $\sigma_{propene}$ using Eqn. 1. We note that this approach differs from the analysis in the previous section: rather than determining the unknown cross sections at single energies and scaling a relative spectrum, the cross sections were determined at each energy relative to the reference. The shape of the resulting glycoaldehyde spectrum is therefore normalized to the shape of the propene spectrum and insensitive to the measured VUV photon flux. The absolute photoionization spectrum of glycoaldehyde is plotted in Figure 2 and tabulated in Table 3.

The recommended cross sections are an average of two scans that produced values agreeing within ~12%. These scans had the strongest absorption signals out of all datasets collected. (While we attempted other measurements, they were generally unusable due to

great uncertainty in the glycoaldehyde concentration arising from absorption that was small in comparison to the stability of the PMT.) For the recommended cross sections, the combined error associated with absolute concentrations, fluctuations between the two scans, and the mass discrimination factor was typically ±27% (±2σ). This was propagated with systematic uncertainty associated with the literature propene cross sections to give a total uncertainty that was typically ±34% (±2σ). The uncertainty on each individual cross section is included in Table 3.

The magnitude of partial cross sections to yield the parent cation is ~1 Mb; this is small in comparison to molecules of similar structure, which have cross sections of magnitude ~10 Mb over similar energy ranges (e.g. acetaldehyde[5]). To explore the reason for this difference, we analyzed the spectra of daughter ions formed in the dissociative photoionization of glycoaldehyde. As discussed previously, cross sections of daughter ions are potentially not reproducible with this apparatus. Nevertheless, we determined their absolute spectra using Eqn. 1 to assess the approximate trend and the results are plotted in Figure 3. We see that the magnitude of the total photoionization cross sections (sum of the parent and daughter ion cross sections) is ~10 Mb, suggesting that the smaller partial cross sections to form the parent cation can be explained by greater dissociative ionization.

(1) Osborn, D. L.; Zou, P.; Johnsen, H.; Hayden, C. C.; Taatjes, C. A.; Knyazev, V. D.; North, S. W.; Peterka, D. S.; Ahmed, M.; Leone, S. R. The Multiplexed Chemical Kinetic Photoionization Mass Spectrometer: A New Approach to Isomer-Resolved Chemical Kinetics. *Review of Scientific Instruments* **2008**, *79* (10), 104103. https://doi.org/10.1063/1.3000004.

(2) Taatjes, C. A.; Hansen, N.; Osborn, D. L.; Kohse-Höinghaus, K.; Cool, T. A.; Westmoreland, P. R. "Imaging" Combustion Chemistry via Multiplexed Synchrotron-Photoionization Mass Spectrometry. *Phys. Chem. Chem. Phys.* **2008**, *10* (1), 20–34. https://doi.org/10.1039/B713460F.

(3) Savee, J. D.; Soorkia, S.; Welz, O.; Selby, T. M.; Taatjes, C. A.; Osborn, D. L. Absolute Photoionization Cross-Section of the Propargyl Radical. *J. Chem. Phys.* **2012**, *136* (13), 134307. https://doi.org/10.1063/1.3698282.

(4) Samson, J. A. R.; Stolte, W. C. Precision Measurements of the Total Photoionization Cross-Sections of He, Ne, Ar, Kr, and Xe. *Journal of Electron Spectroscopy and Related Phenomena* **2002**, *123* (2), 265–276. https://doi.org/10.1016/S0368-2048(02)00026-9.

(5) Person, J. C.; Nicole, P. P. *ANL Radiological Physics Division Annual Report*; ANL-7760; 1970; p 97.

C.3 Figures

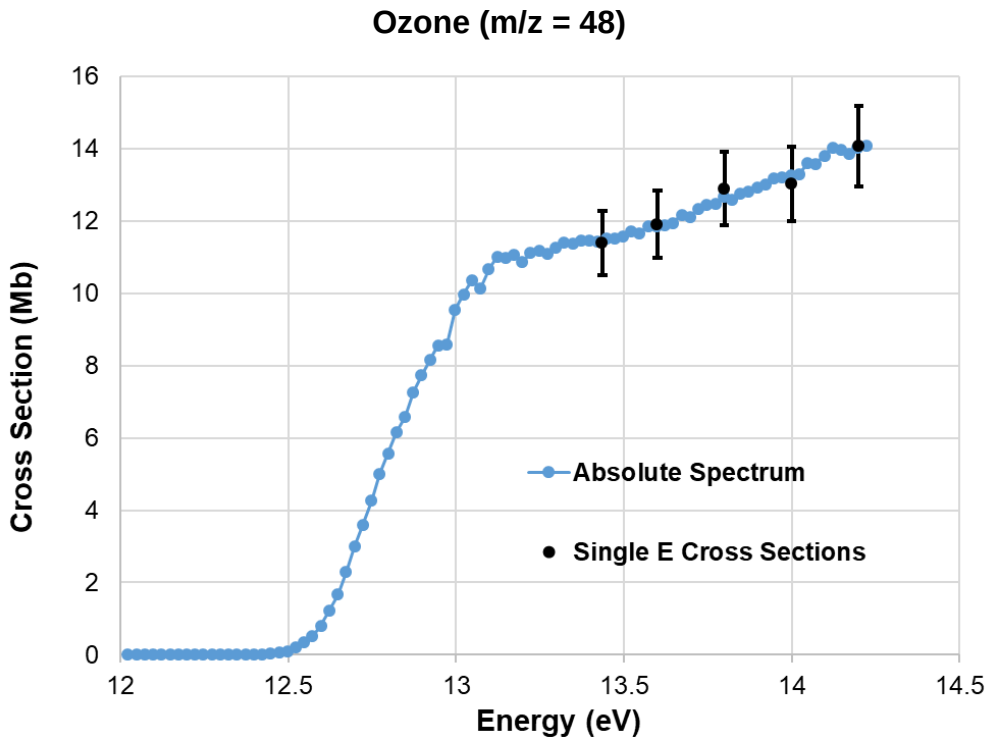

Figure 1: Absolute photoionization cross sections of ozone to form the parent cation. Obtained by scaling a relative spectrum (blue) to single energy cross sections (black) measured at 13.436, 13.600, 13.800, 14.000, and 14.200 eV (error bars are ±2σ). Spectrum was recorded with a step size of 25 meV and normalized to the relative VUV photon flux recorded by a SXUV photodiode. The single energy cross sections were determined in reference to the known cross sections of xenon. The noise level in the spectrum is much smaller than the magnitude of the single energy cross section error bars since the uncertainty is dominated by systematic errors. The data in this figure is available in Tables 1 and 2.

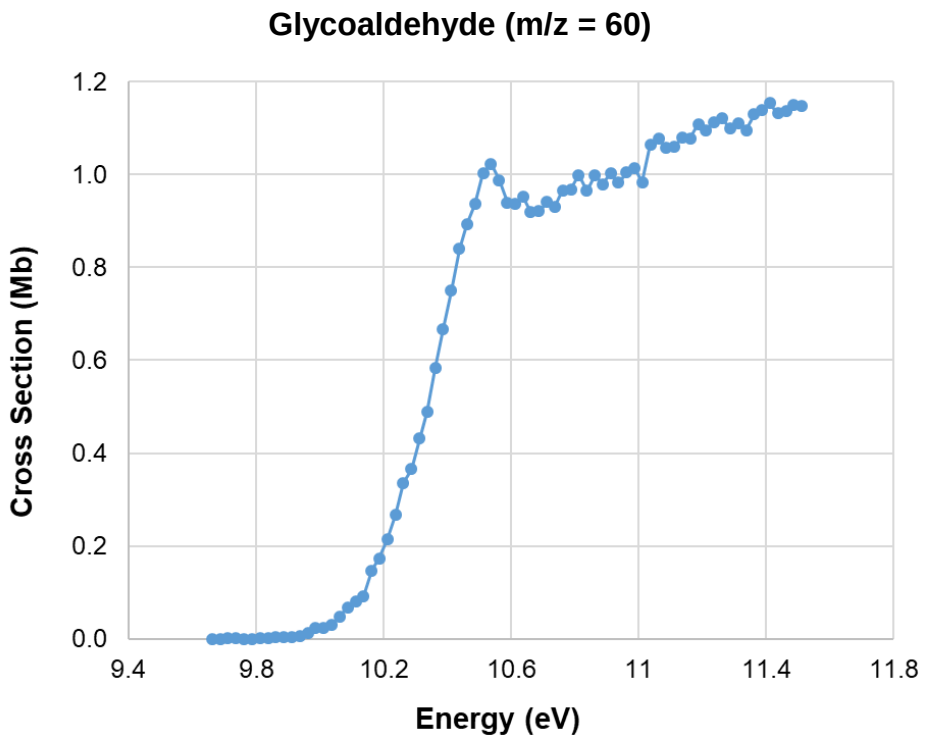

Figure 2: Absolute photoionization cross sections of glycoaldehyde to form the parent cation. Spectrum was recorded with a step size of 25 meV. The cross section at each point was determined in reference to the known cross sections of propene through Eqn. 1; the shape of the glycoaldehyde spectrum is therefore normalized to that of propene. The data in this figure is available in Table 3.

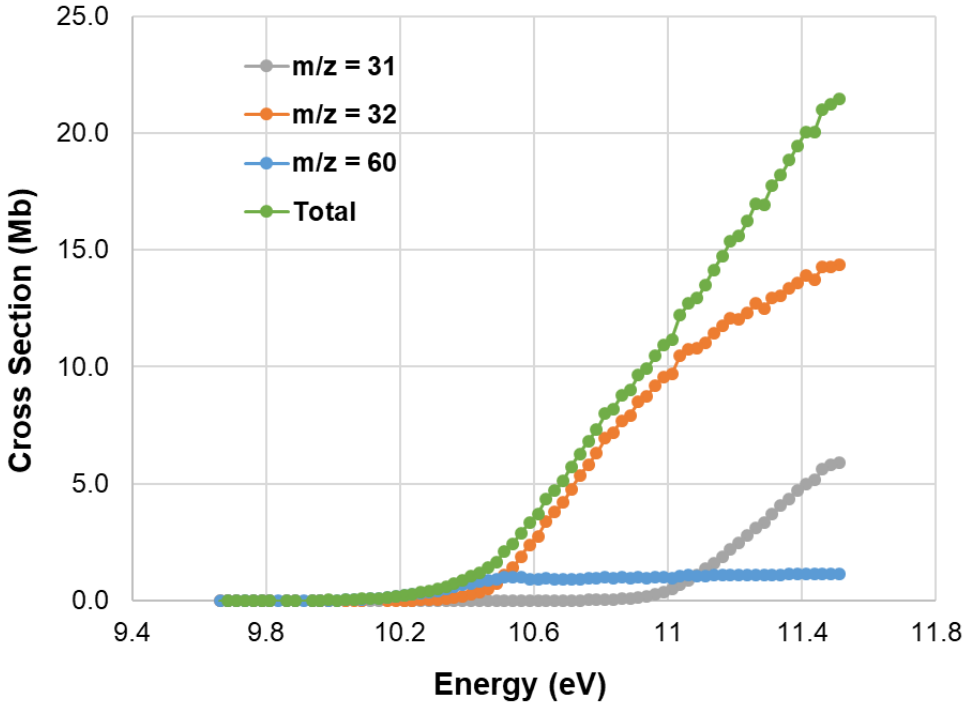

Figure 3: Partial photoionization cross sections of glycoaldehyde to form daughter cations (m/z = 31 and 32) and the parent cation (m/z = 60). The total photoionization cross section (computed as a sum across all cations) is of order of magnitude ~10 Mb. Extensive dissociative photoionization may therefore explain the unexpectedly small cross sections to form the parent cation (~1 Mb). As discussed in the text, partial cross sections to form daughter ions may not be reproducible, but were determined nevertheless to establish the approximate trend.

C.4 Tables

Table 1: Absolute photoionization cross sections of ozone determined in reference to the known cross sections of xenon. A budget of the error sources is also presented. The relative errors from each category can be added in quadrature to give the total relative error on a cross section. The fraction of the total error arising from each category is given in parentheses. Uncertainties represent ±2σ confidence.

Energy (eV)	σ_{ozone} (Mb)	Random Error	Mass Discrimination Error	Concentration Error	Reference Cross Section Error	Total Error
13.436	11.4 ± 0.9	±2.3% (9%)	±2.3% (8%)	±6.5% (68%)	±3.0% (15%)	±7.9% (100%)
13.600	11.9 ± 0.9	±2.3% (9%)	±2.3% (8%)	±6.5% (68%)	±3.0% (15%)	±7.9% (100%)
13.800	12.9 ± 1.0	±2.3% (9%)	±2.3% (8%)	±6.5% (68%)	±3.0% (15%)	±7.9% (100%)
14.000	13.0 ± 1.0	±2.3% (9%)	±2.3% (8%)	±6.5% (68%)	±3.0% (15%)	±7.9% (100%)
14.200	14.1 ± 1.1	±2.6% (11%)	±2.3% (8%)	±6.5% (67%)	±3.0% (14%)	±7.9% (100%)

Table 2: Absolute photoionization spectrum of ozone to form the parent cation. Uncertainties represent ±2σ confidence and are typically ±7.9%.

Energy (eV)	σ_{ozone} (Mb)	Energy (eV)	σ_{ozone} (Mb)	Energy (eV)	σ_{ozone} (Mb)
12.022	0	12.772	5.0 ± 0.4	13.522	11.7 ± 0.9
12.047	0.0004 ± 0.0004	12.797	5.6 ± 0.4	13.547	11.7 ± 0.9
12.072	0.0007 ± 0.0007	12.822	6.2 ± 0.5	13.572	11.8 ± 0.9
12.097	0.0004 ± 0.0004	12.847	6.6 ± 0.5	13.597	11.8 ± 0.9
12.122	0	12.872	7.3 ± 0.6	13.622	11.9 ± 0.9
12.147	0.0014 ± 0.0007	12.897	7.7 ± 0.6	13.647	11.9 ± 0.9
12.172	0.0004 ± 0.0004	12.922	8.1 ± 0.6	13.672	12.2 ± 1.0
12.197	0.0011 ± 0.0006	12.947	8.6 ± 0.7	13.697	12.1 ± 1.0
12.222	0.0028 ± 0.0013	12.972	8.6 ± 0.7	13.722	12.3 ± 1.0
12.247	0.0018 ± 0.0008	12.997	9.6 ± 0.8	13.747	12.4 ± 1.0
12.272	0.0029 ± 0.0010	13.022	10.0 ± 0.8	13.772	12.5 ± 1.0
12.297	0.0028 ± 0.0011	13.047	10.3 ± 0.8	13.797	12.7 ± 1.0
12.322	0.0028 ± 0.0010	13.072	10.1 ± 0.8	13.822	12.6 ± 1.0
12.347	0.0039 ± 0.0012	13.097	10.7 ± 0.8	13.847	12.7 ± 1.0
12.372	0.0084 ± 0.0018	13.122	11.0 ± 0.9	13.872	12.8 ± 1.0
12.397	0.012 ± 0.002	13.147	11.0 ± 0.9	13.897	12.9 ± 1.0
12.422	0.021 ± 0.003	13.172	11.1 ± 0.9	13.922	13.0 ± 1.0
12.447	0.041 ± 0.005	13.197	10.9 ± 0.9	13.947	13.2 ± 1.0
12.472	0.063 ± 0.007	13.222	11.1 ± 0.9	13.972	13.2 ± 1.0
12.497	0.100 ± 0.010	13.247	11.2 ± 0.9	13.997	13.3 ± 1.0
12.522	0.216 ± 0.019	13.272	11.1 ± 0.9	14.022	13.3 ± 1.0
12.547	0.36 ± 0.03	13.297	11.3 ± 0.9	14.047	13.6 ± 1.1
12.572	0.51 ± 0.04	13.322	11.4 ± 0.9	14.072	13.6 ± 1.1
12.597	0.80 ± 0.07	13.347	11.4 ± 0.9	14.097	13.8 ± 1.1
12.622	1.21 ± 0.10	13.372	11.4 ± 0.9	14.122	14.0 ± 1.1
12.647	1.67 ± 0.13	13.397	11.5 ± 0.9	14.147	14.0 ± 1.1
12.672	2.29 ± 0.18	13.422	11.4 ± 0.9	14.172	13.9 ± 1.1
12.697	3.0 ± 0.2	13.447	11.5 ± 0.9	14.197	14.0 ± 1.1
12.722	3.6 ± 0.3	13.472	11.5 ± 0.9	14.222	14.1 ± 1.1
12.747	4.3 ± 0.3	13.497	11.6 ± 0.9		

Table 3: Absolute photoionization spectrum of glycoaldehyde to form the parent cation. Uncertainties represent ±2σ confidence and are typically ±34%.

Energy (eV)	$\sigma_{\text{glycoaldehyde}}$ **(Mb)**	**Energy (eV)**	$\sigma_{\text{glycoaldehyde}}$ **(Mb)**	**Energy (eV)**	$\sigma_{\text{glycoaldehyde}}$ **(Mb)**
9.662	0.0001 ± 0.0002	10.287	0.37 ± 0.11	10.912	1.00 ± 0.31
9.687	0.0002 ± 0.0005	10.312	0.43 ± 0.13	10.937	0.98 ± 0.30
9.712	0.0007 ± 0.0002	10.337	0.49 ± 0.15	10.962	1.00 ± 0.34
9.737	0.0007 ± 0.0016	10.362	0.58 ± 0.18	10.987	1.01 ± 0.33
9.762	0.0002 ± 0.0005	10.387	0.67 ± 0.22	11.012	0.98 ± 0.31
9.787	0.0003 ± 0.0008	10.412	0.75 ± 0.25	11.037	1.06 ± 0.35
9.812	0.0007 ± 0.0017	10.437	0.84 ± 0.26	11.062	1.08 ± 0.38
9.837	0.0005 ± 0.0002	10.462	0.89 ± 0.29	11.087	1.06 ± 0.33
9.862	0.0034 ± 0.0021	10.487	0.94 ± 0.32	11.112	1.06 ± 0.36
9.887	0.0041 ± 0.0021	10.512	1.00 ± 0.35	11.137	1.08 ± 0.35
9.912	0.0045 ± 0.0015	10.537	1.02 ± 0.32	11.162	1.08 ± 0.36
9.937	0.0057 ± 0.0040	10.562	0.99 ± 0.33	11.187	1.11 ± 0.35
9.962	0.0129 ± 0.0040	10.587	0.94 ± 0.33	11.212	1.10 ± 0.34
9.987	0.023 ± 0.010	10.612	0.94 ± 0.29	11.237	1.11 ± 0.38
10.012	0.024 ± 0.007	10.637	0.95 ± 0.31	11.262	1.12 ± 0.37
10.037	0.031 ± 0.009	10.662	0.92 ± 0.32	11.287	1.10 ± 0.36
10.062	0.047 ± 0.021	10.687	0.92 ± 0.29	11.312	1.11 ± 0.39
10.087	0.068 ± 0.030	10.712	0.94 ± 0.32	11.337	1.10 ± 0.35
10.112	0.080 ± 0.025	10.737	0.93 ± 0.33	11.362	1.13 ± 0.38
10.137	0.092 ± 0.030	10.762	0.97 ± 0.31	11.387	1.14 ± 0.39
10.162	0.147 ± 0.051	10.787	0.97 ± 0.32	11.412	1.15 ± 0.38
10.187	0.173 ± 0.060	10.812	1.00 ± 0.35	11.437	1.13 ± 0.39
10.212	0.21 ± 0.07	10.837	0.96 ± 0.33	11.462	1.14 ± 0.39
10.237	0.27 ± 0.08	10.862	1.00 ± 0.34	11.487	1.15 ± 0.40
10.262	0.34 ± 0.11	10.887	0.98 ± 0.34	11.512	1.15 ± 0.39

Appendix D

Cold Reactor Temperature Measurements

D.1 Results & Discussion

The multiplexed synchrotron photoionization mass spectrometry (MPIMS) experiments in Chapters 2 and 4 utilized a low temperature reactor that is based on a prototype designed previously.[1] Several modifications were made to the prototype design, including a smaller pinhole (to accommodate reactor pressures ranging up to 50 Torr) and a redesign of the temperature stabilization (to achieve better control and stability). In the original prototype, a Kapton flexible heater was wrapped around the reactor tube near the coolant inlet. A thermistor was affixed to the outer tube surface directly below the heater. The temperature measured by the thermistor was stabilized using a PID feedback loop between the heater and thermistor. A second thermocouple, located within the inner tube ~2" downstream of the pinhole, continuously recorded the *in situ* temperature of the process gas. Our initial experiments with this prototype showed it was challenging to control and stabilize the process gas temperature with such a scheme, likely due to the small length of tubing (0.5") in contact with the heater.

In the redesign, we opted not to heat or measure the temperature of the outer reactor tube surface. Instead, we moved the temperature control and stabilization completely outside of the vacuum chamber, and stabilized the coolant gas temperature. After the dry house nitrogen passed through copper coils immersed in liquid nitrogen, the nitrogen coolant was passed through a second set of copper coils wrapped in heating tape. The coolant temperature was monitored immediately before entering the vacuum chamber using a thermocouple positioned directly within the gas stream. (A photograph of this setup is presented in Figure 1.) A PID feedback loop cycled power to the heating tape and stabilized the coolant to ± 0.7 °C. Optimization of the PID parameters could have produced even smaller fluctuations, but this was unnecessary for the present work: the thermal mass of the reactor buffered the process gas from fluctuations in coolant temperature, yielding an *in situ* process gas temperature that was typically stable to better than ± 0.1 °C.

During an experiment, we continuously monitored the process gas temperature using the thermocouple positioned below the pinhole. A typical temperature trace is plotted in Figure 2. In this example, the reactor temperature has been stabilized to T_{off} = 15.50 ± 0.08 °C in the absence of photolysis. When the excimer laser is firing, the temperature increases and exhibits considerable oscillations: T_{on} = 18.9 ± 0.5 °C. The increase in temperature (ΔT = 3.4 °C) could arise from several effects: (1) reaction exothermicity, (2) UV absorption by the steel reactor walls, (3) UV absorption by the thermocouple. The first two effects would lead to a real increase of the process gas temperature, while the last effect would be artificial.

To determine if the ΔT measured upon firing the photolysis laser corresponded to a true change in gas temperature, we compiled ΔT data recorded in a variety of experiments and summarize the findings in Table 1. From the 351 nm data, we see that ΔT recorded when a reaction occurs is identical to ΔT recorded with only He in the reactor. (Unfortunately, a similar experiment was not conducted at 248 nm.) This indicates that reaction exothermicity does not substantially contribute to ΔT. From both the 351 and 248 nm data, we see that ΔT recorded during active cooling (continuously flowing coolant in contact with the reactor walls) is identical to ΔT when there is no coolant. This indicates that UV absorption by the reactor walls does not substantially contribute to ΔT. (Future experiments could more firmly establish this by comparing to ΔT measured with a quartz reactor, which would not absorb 351 or 248 nm, using the same thermocouple.) We therefore assumed that the true gas temperature was equal to T_{off} (both in the presence and absence of the UV pulse) and that the recorded ΔT was entirely artificial and arose solely from UV absorption by the thermocouple. The difference in ΔT observed between 351 and 248 nm likely reflects the different fluence from the excimer laser at these wavelengths and the absorption properties of the thermocouple.

While the stability of the measured process gas temperature (T_{off}) was typically better than ± 0.1 °C, the temperature range was greater due to inhomogeneity along the flow axis. To characterize the gradient, we translated a long thermocouple probe in 0.5” steps through the reactor to acquire temperature profiles. These measurements, which were done in the absence of a UV laser pulse, were performed at pressures and bath gas compositions of relevance to the experiments described in Chapters 2 and 4. The raw data

was collected as gas temperature (T) as a function of distance above the pinhole (x). The distance axis was converted to a reaction time (t) axis by making the simplifying assumption of plug flow and numerical evaluation of the following relationship:

$$t(x) = \int_0^x \left(\frac{T(x')}{T_{STP}}\right)\left(\frac{P_{STP}}{P}\right)\left(\frac{A}{f_{STP}}\right) dx' \qquad \text{(Eqn. 1)}$$

where P is the pressure of the reactor, A is the cross sectional area of the inner tube, and f_{STP} is the total flow rate at standard temperature and pressure (T_{STP} = 0 °C and P_{STP} = 1 atm). We note that x = 0 represents the position of the pinhole and evaluation of Eqn. 1 is valid for both positive and negative values of x.

Temperature profiles, plotted as T vs t, are presented in Figures 3 and 4 for process gas temperatures that were stabilized to -3.0 and -62.6 °C, respectively (as measured by the thermocouple with a fixed position below the pinhole). We note that, when plotted in this manner, T represents the *initial* temperature (at t = 0, the time of photolysis) of a gas parcel detected at reaction time t. In both profiles, the initial gas temperature is reasonably uniform between t = 0 and t = 60 ms, which motivated the restriction of our kinetic analysis to 0–60 ms.

In Figure 3, we have added a second y-axis and also plotted ion counts of formaldehyde (a product of ethene oxidation) as a function of reaction time. This signal was measured in experiments similar to those described in Chapter 4. We see a sharp rise in formaldehyde ion signal around ~65 ms that is clearly inconsistent with the kinetic behavior observed over 0–60 ms. The sharp change appears correlated to the rapid increase in the initial temperature of gas parcels detected after 60 ms.

(1) L. Dodson. Thesis, California Institute of Technology, 2016.

D.2 Figures

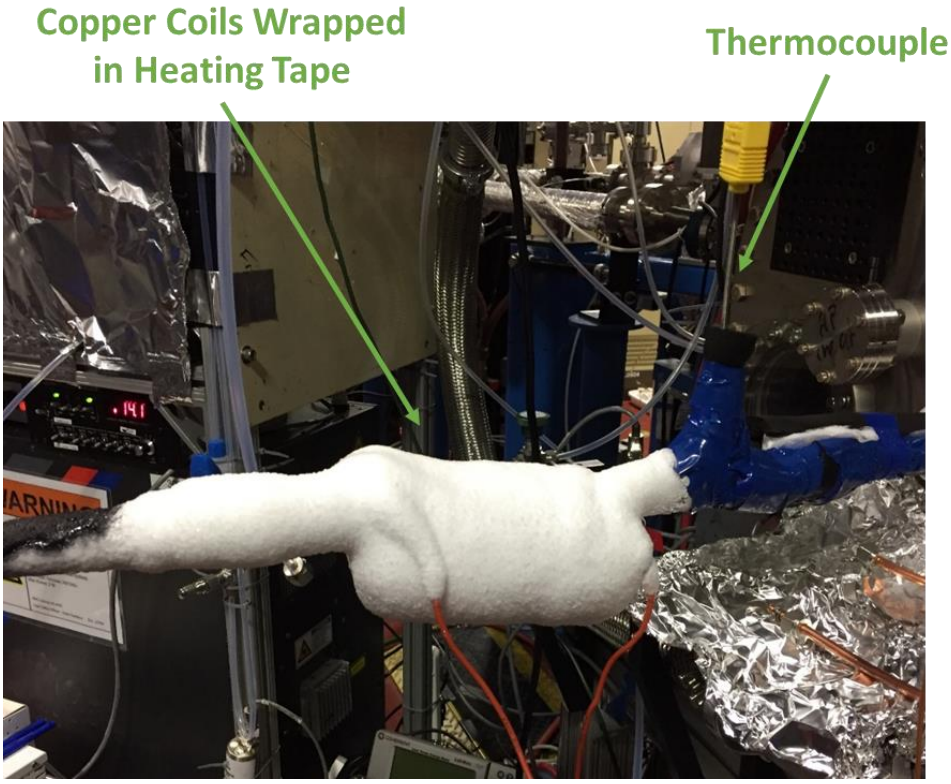

Figure 1: Picture of copper coils wrapped in heating tape and the thermocouple probe used to monitor the coolant temperature. The coolant temperature was stabilized using a PID feedback loop that toggled power to the heating tape. The photograph was taken during experiments for which the coolant temperature was ~180 K and the reactor temperature was ~210 K; the copper coils therefore appeared as an ice block due to the condensation and freezing of ambient water vapor. A Swagelok union tee was used to position the edge of the thermocouple probe directly within the stream of flowing coolant.

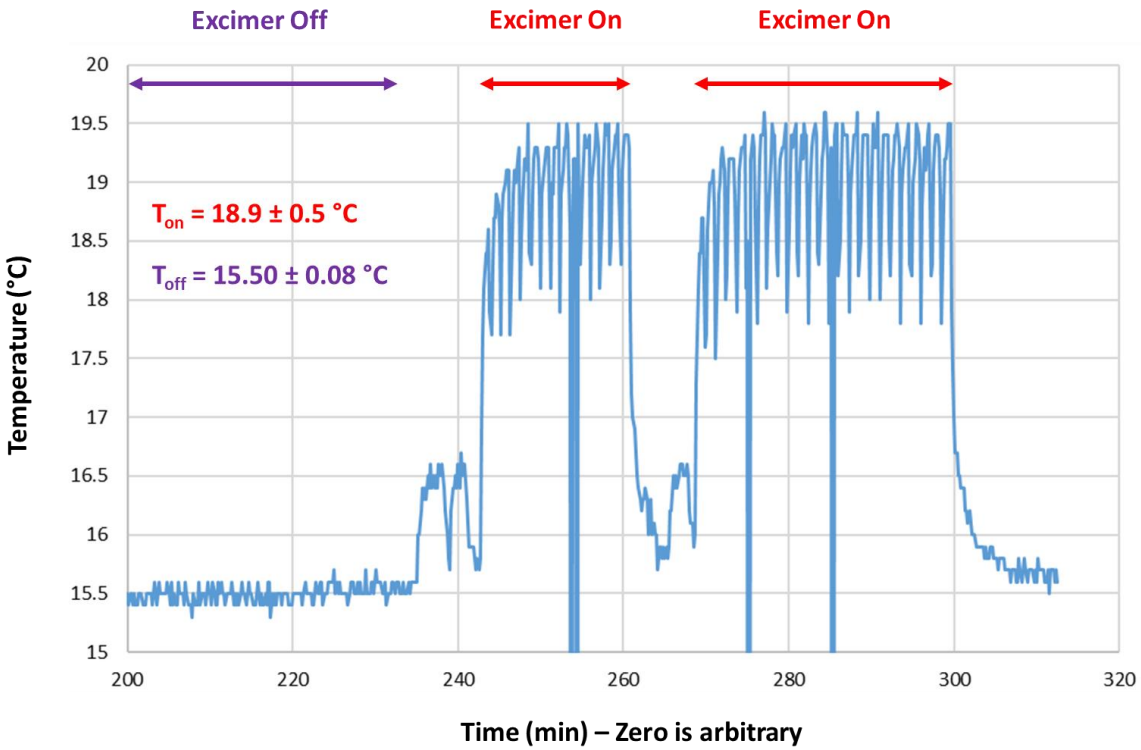

Figure 2: Example temperature time series measured by a thermocouple positioned below the pinhole and within the reactant gas stream. In the absence of the UV laser, the measured temperature was stabilized to T_{off} = 15.50 ± 0.08 °C. In the presence of the UV laser, the measured temperature oscillated around T_{on} = 18.9 ± 0.5 °C. As discussed in the text, we reason that the temperature rise and fluctuations are artificial (caused by UV absorption of the thermocouple) and that the true gas temperature is described by T_{off}, regardless of whether the UV laser is firing.

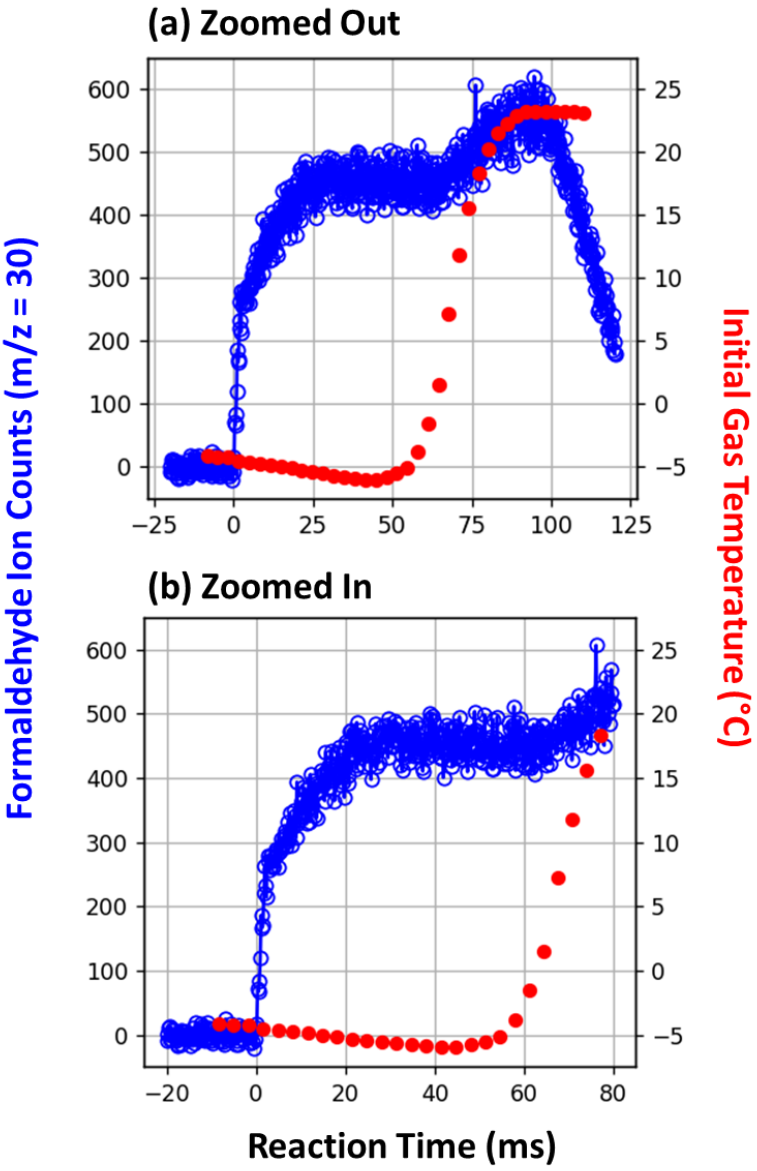

Figure 3: Temperature profile (red) measured at P = 30 Torr, 13.3% O_2, and a He balance with the process gas temperature stabilized to -3.0 °C (as measured by the thermocouple at a fixed position below the pinhole). The formaldehyde ion signal (blue) generated upon ethene oxidation under similar conditions is also plotted. The sharp rise in formaldehyde signal is correlated with the rapid increase in the initial temperature of gas parcels detected after 60 ms. (a) All data and (b) zoom in of the reaction time axis (y-axis unadjusted).

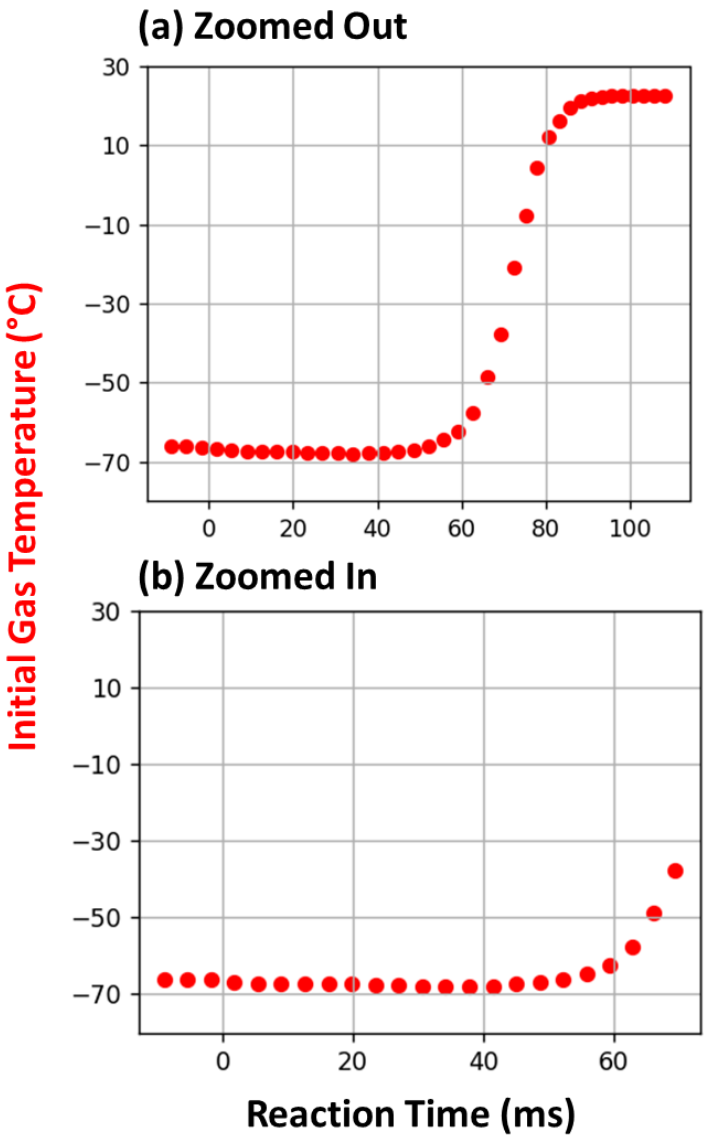

Figure 4: Temperature profile measured at P = 50 Torr, 4.5% O_2, and a He balance with the process gas temperature stabilized to -62.6 °C (as measured by the thermocouple at a fixed position below the pinhole). (a) All data and (b) zoom in of the reaction time axis (y-axis unadjusted).

D.3 Tables

Table 1: Measured temperature rises upon firing of the UV laser acquired across various representative conditions. T_{off}, T_{on}, and ΔT were determined from analysis of temperature time series similar to that presented in Figure 2. The number of laser shots (sequences) in a block of UV pulses was similar for each scan. As discussed in the text, these results were used to reason that the measured ΔT was artificial and did not represent to a true increase in the process gas temperature.

Chemistry	λ (nm)	Active Cooling?	T_{off} (°C)	T_{on} (°C)	ΔT (°C)
[a] None	351	Yes	18.8	20.5	1.7
$Cl + O_3$	351	No	26.5	28.2	1.7
$Cl + O_3$	351	Yes	-62.7	-60.9	1.8
$OH + C_2H_4$	248	No	25.6	29.3	3.7
$OH + C_2H_4$	248	Yes	15.9	19.9	4.0
$OH + C_2H_4$	248	Yes	7.8	11.4	3.6
$OH + C_2H_4$	248	Yes	-3.0	0.7	3.7

[a] Only He was flown through the reactor.

Appendix E

Code for Modeling and Fitting of Chemical Kinetics Data

A library of Python (v3.6.1) code was developed to model chemical kinetics and fit datasets acquired with the multiplexed synchrotron photoionization mass spectrometry (MPIMS) instrument at the Advanced Light Source (ALS). The code relies heavily upon algorithms from the SciPy (v0.19.0) library.[1] One of the main benefits of this code is that implementation of the photolysis gradient and temporal instrument response function are abstracted. Fits to experimental datasets are performed using the Levenberg-Marquardt algorithm to optimize various kinetic or instrument parameters.[2,3] The analysis presented in Chapter 2 utilized this code.

The code is freely available from CaltechDATA as a downloadable repository (doi: 10.22002/D1.1248),[4] which is also linked to the electronic record of this thesis and a corresponding GitHub repository. At the time of writing, the current release version is 1.2.0. If a newer version is released on GitHub in the future, the repository hosted by CaltechDATA will automatically update.

We refer to the documentation within the repository for complete details of the capabilities and implementation of the code. The repository contains multiple files:

- **ALS.py:** This file is the code library. A KineticModel class is defined with methods for fitting and plotting datasets, modeling concentration profiles (with optional photolysis gradient), performing bootstrap uncertainty simulations (to assess random errors), performing Monte Carlo uncertainty simulations (to assess systematic errors), and convolving signals with the temporal instrument response function.
- **ex_notebook_1.ipynb:** A Jupyter / IPython notebook containing documentation for ALS.py. A running example is presented throughout to demonstrate instantiation of a KineticModel object and utilization of the various methods.
- **create_model_code.py:** Contains a utility function for converting text-formatted kinetic models into Python code.

The remaining files are inputs / outputs used in the example (H_2O_2 photolysis).

(1) Oliphant, T. E. Python for Scientific Computing. *Computing in Science Engineering* **2007**, *9* (3), 10–20. https://doi.org/10.1109/MCSE.2007.58.
(2) Levenberg, K. A Method for the Solution of Certain Non-Linear Problems in Least Squares. *Quart. Appl. Math.* **1944**, *2* (2), 164–168. https://doi.org/10.1090/qam/10666.
(3) Marquardt, D. An Algorithm for Least-Squares Estimation of Nonlinear Parameters. *Journal of the Society for Industrial and Applied Mathematics* **1963**, *11* (2), 431–441. https://doi.org/10.1137/0111030.
(4) Matthew D. Smarte. *mdsmarte/ALS-Kinetic-Model: Modeling and Fitting of ALS MPIMS Kinetics*; CaltechDATA, 2019. https://doi.org/10.22002/d1.1248.